ABSTRACT

Title of Dissertation: QUANTUM SIMULATION AND DYNAMICS WITH SYNTHETIC QUANTUM MATTER

Ron Belyansky
Doctor of Philosophy, 2023

Dissertation Directed by: Professor Alexey Gorshkov
Department of Physics

Significant advancements in controlling and manipulating individual quantum degrees of freedom have paved the way for the development of programmable strongly-interacting quantum many-body systems. Quantum simulation emerges as one of the most promising applications of these systems, offering insights into complex natural phenomena that would otherwise be difficult to explore. Motivated by these advancements, this dissertation delves into several analog quantum simulation proposals spanning different fields, including high-energy and condensed matter physics, employing various synthetic quantum systems. A primary objective is the investigation of the dynamical phenomena that can be effectively studied using these simulation approaches.

The first part of the dissertation focuses on quantum simulation utilizing superconducting circuits. We demonstrate that this platform can natively realize several intriguing models including the massive Schwinger model (quantum electrodynamics (QED) in 1+1 dimensions) and various strongly interacting quantum impurity models. By studying high-energy scattering of quark and meson states within the Schwinger model, we reveal a wealth of rich phenomenology encompass-

ing inelastic particle production, hadron disintegration, as well as dynamical string formation and breaking. Furthermore, we demonstrate how the presence of a single impurity (artificial atom) can profoundly modify the properties of light-matter interactions in a waveguide, leading to anomalous transport of a single photon, strong photon decay, and the emergence of atom-photon bound states.

The second part of the dissertation focuses on quantum simulation with atomic, molecular, and optical (AMO) systems. Leveraging the tunable and long-range interactions available in platforms such as cavity-QED and trapped ions, we explore exotic regimes of quantum information dynamics. On the one hand, we demonstrate that the combination of simple and uniform all-to-all interactions together with chaotic short-range interactions can induce fast scrambling, a central feature associated with quantum black holes. On the other hand, we investigate how short-range yet non-local Rydberg interactions can strongly suppress atom tunneling in an optical lattice, resulting in frozen dynamics and Hilbert-space fragmentation. Finally, we propose a method of sympathetic cooling of neutral atoms using state-insensitive Rydberg interactions, potentially enabling longer quantum simulations and computations with this platform.

QUANTUM SIMULATION AND DYNAMICS WITH SYNTHETIC QUANTUM MATTER

by

Ron Belyansky

Dissertation submitted to the Faculty of the Graduate School of the
University of Maryland, College Park in partial fulfillment
of the requirements for the degree of
Doctor of Philosophy
2023

Advisory Committee:
Professor Zohreh Davoudi, Chair
Professor Alexey Gorshkov, Advisor, Co-chair
Professor Andrew Childs, Dean's Representative
Professor Alicia Kollár,
Professor Nathan Schine

Acknowledgments

While it is impossible to list all the people who helped me get to this point, I would like to acknowledge some of the people who had the biggest impact during my years in graduate school.

First and foremost I extend my deepest gratitude to my advisor, Alexey Gorshkov, for his unwavering support and guidance throughout this endeavor. Alexey's willingness to grant me the freedom to choose and pursue my own ideas, even when they did not always work out as intended, has been instrumental in my development as a scientist. His constant enthusiasm and fresh ideas always inspired and encouraged me.

I would like to thank the other faculty members at UMD with whom I had the privilege to collaborate and learn from: Zohreh Davoudi, Brian Swingle, Alicia Kollár, and Victor Albert. I also want to thank the members of my committee: Zohreh Davoudi, Andrew Childs, Alicia Kollár, and Nathan Schine.

During my time here I have benefited immensely from discussions and collaborations with postdocs. I want to thank especially Przemek Bienias and Seth Whitsitt, from whom I learned a lot. I was fortunate to also work with many professors outside of UMD, including Peter Zoller, Adam Kaufman, Tom Iadecola, and Niklas Mueller. The experimental collaborations with the group of Waseem Bakr as well as with Andrew Houck and Andrei Vrajitoarea have been particularly fruitful experiences.

I am also grateful to the many colleagues and friends including Rex Lundgren, Jeremy Young,

Igor Boettcher, Paraj Titum, Simon Lieu, Jim Garrison, Ali Fahimniya, Chris Baldwin, Luispe Garcia Pintos, Yidan Wang, Andrew Guo, Yaroslav Kharkov, Brayden Ware, Su-Kuan Chu, Elizabeth Bennewitz. I also thank Shuyao Gu.

Finally, I thank my family – my parents and my brother, for everything.

Table of Contents

List of Tables

List of Figures

Citations to Previously Published Work

Much of this dissertation has previously appeared in published papers. Here, we provide citations to those papers, in addition to related papers which are not presented in this dissertation.

- Chapter 2: "High-Energy Collision of Quarks and Hadrons in the Schwinger Model: From Tensor Networks to Circuit QED", R. Belyansky, S. Whitsitt, N. Mueller, A. Fahimniya, E. R. Bennewitz, Z. Davoudi, A. V. Gorshkov, arXiv preprint arXiv:2307.02522 (2023).

- Chapter 3: "Frustration-induced anomalous transport and strong photon decay in waveguide QED", R. Belyansky, S. Whitsitt, R. Lundgren, Y. Wang, A. Vrajitoarea, A. A. Houck, A. V. Gorshkov, Phys. Rev. Research 3, L032058 (2021).

- Chapter 4: "Ultrastrong light-matter interaction in a photonic crystal", A. Vrajitoarea, R. Belyansky, R. Lundgren, S. Whitsitt, A. V. Gorshkov, A. A. Houck, arXiv preprint arXiv:2209.14972 (2022).

  - Further work on using circuit QED for quantum simulation of hyperbolic space is presented in "Circuit Quantum Electrodynamics in Hyperbolic Space: From Photon Bound States to Frustrated Spin Models", P. Bienias, I. Boettcher, R. Belyansky, A. J. Kollár, A. V. Gorshkov, Phys. Rev. Lett. 128 (1), 013601 (2021), and in "Quantum Simulation of Hyperbolic Space with Circuit Quantum Electrodynamics: From Graphs to Geometry", I. Boettcher, P. Bienias, R. Belyansky, A. J. Kollár, A. V. Gorshkov, Phys. Rev. A 102, 032208 (2020).

  - Further work on the connection between driven-dissipative phase transitions and quantum error correction in cavity-QED systems is presented in "Symmetry breaking and error correction in open quantum systems", S. Lieu, R. Belyansky, J. T. Young, R. Lundgren, V. V. Albert, A. V. Gorshkov, Phys. Rev. Lett. 125, 240405 (2020).

- Chapter 5: "Minimal Model for Fast Scrambling", R. Belyansky, P. Bienias, Y. A. Kharkov, A. V. Gorshkov, B. Swingle, Phys. Rev. Lett. 125, 130601 (2020).

- Chapter 6: "Quench Dynamics of a Fermi Gas with Strong Nonlocal Interactions", E. Guardado-Sanchez, B. M. Spar, P. Schauss, R. Belyansky, J. T. Young, P. Bienias, A. V. Gorshkov, T. Iadecola, W. S. Bakr, Phys. Rev. X 11, 021036 (2021).

- Chapter 7: "Nondestructive cooling of an atomic quantum register via Rydberg interactions", R. Belyansky, J. T. Young, P. Bienias, Z. Eldredge, P. Zoller, A. V. Gorshkov, Phys. Rev. Lett., 123, 213603 (2019).

  - Further work on utilizing Rydberg interactions for quantum information applications is presented in "Asymmetric blockade and multi-qubit gates via dipole-dipole interactions", J. T. Young, P. Bienias, R. Belyansky, A. M. Kaufman, A. V. Gorshkov, Phys. Rev. Lett. 127, 120501 (2021).

Chapter 1: Introduction

1.1 Overview

The advent of quantum mechanics in the early 20th century ushered in a profound revolution in our understanding of fundamental physics. This first quantum revolution achieved tremendous success in explaining the intricate interactions at the microscopic level and also shed light on emergent effects that arise from collective quantum behavior. Moreover, quantum mechanics laid the foundation for a plethora of transformative technologies that have shaped the modern world. Semiconductors and transistors, for instance, emerged as cornerstones of modern electronics, revolutionizing computing, communication, and countless other technological domains.

The end of the 20th century marked the beginning of the ongoing *second quantum revolution* [1]. While the first quantum revolution provided the foundational principles and tools to describe the physical quantum world, the second quantum revolution ushers in the era of actively modifying and controlling quantum systems. This significant progress has been made possible through remarkable technological advancements that enabled precise control over individual quantum degrees of freedom. These include the control of individual atoms [2, 3] and ions [4], the manipulation of individual photons [5–9], as well as the control of individual quanta in solid-state systems such as quantum dots [10], Nitrogen-Vacancy centers in diamond [11], and superconducting circuits [12, 13], among others.

These remarkable advancements have sparked a quest for novel technological applications that harness the full power of quantum mechanics. Examples of such applications include unbreakable and secure quantum communication [14, 15], precise quantum sensing [16], efficient quantum simulation of natural phenomena [17, 18], as well as powerful quantum algorithms for classically hard problems [19, 20]. Achieving these applications, particularly quantum computing and simulation, requires the assembly of large-scale and strongly interacting quantum systems. Considerable efforts and resources are currently being directed towards this vision across many different platforms, such as ultra-cold atoms in optical lattices [21], Rydberg atoms arrays [22, 23], trapped ions [24, 25], superconducting circuits [26–28] and others.

The realization of a useful quantum computer or simulator poses a significant and enduring challenge due to the seemingly contradictory requirements of having a large-scale quantum many-body system that is adequately isolated from the environment, while simultaneously enabling individual control over each of its degrees of freedom. Although current systems are far removed from these goals, they nevertheless offer an exceptional playground for exploring quantum many-body physics, effectively realizing *synthetic quantum matter*. These systems, comprising tens to thousands of degrees of freedom, offer unprecedented programmability and measurement capabilities, providing novel perspectives and insights into the behavior of strongly interacting quantum matter. These remarkable developments have already instigated paradigm shifts across various areas of physics, leading to an increased emphasis on understanding highly excited [29], far-from-equilibrium [30, 31], time-dependent behavior [32], incorporating long-range and non-local interactions [33], as well as non-unitary dynamics [34–37], that are naturally available in many of these engineered quantum systems. The integration of novel measurement capabilities, in conjunction with quantum information-theoretic tools, further provides fresh perspectives and novel

approaches for understanding and exploring these intriguing phenomena [38].

Motivated by these developments, this dissertation aims to maximize the potential of current and near-term synthetic quantum matter systems, with a specific focus on quantum simulation of exotic phenomena on analog devices and the development of tools to enhance their capabilities. We employ a combination of numerical and analytical techniques, incorporating tools from quantum information, to investigate non-equilibrium dynamical phenomena that can be effectively studied on these platforms. In the remaining part of this chapter, we introduce the concept of quantum simulation and provide an overview of the main platforms employed in this dissertation, namely superconducting circuits, and atomic, molecular, and optical systems. Finally, we provide an outline of the rest of the dissertation.

1.2 Quantum Simulation

Quantum simulation can be seen as a specialized form of quantum computation aimed at replicating complex quantum phenomena on a controllable quantum system [17, 18, 39, 40]. First envisioned by R. Feynman [41] and others [42, 43] and subsequently put on more solid theoretic footing by S. Lloyd [44], quantum simulation represents perhaps the most native and promising application of quantum computers, allowing to probe complex quantum phenomena that are most likely beyond the reach of classical methods. The range of phenomena that can be addressed with quantum simulators spans various fields such as condensed matter physics, material science, high-energy and nuclear physics, as well as chemistry and biology.

Two main approaches currently exist for quantum simulation. The first uses universal digital quantum computers which work analogously to classical computers, by manipulating the infor-

mation using discrete gate operations. This approach can incorporate quantum error correction, thus realizing fault-tolerant computation and providing guarantees on the accuracy of the simulation. Current digital quantum computers are far from that goal, falling instead into the category of "Noisy Intermediate Scale Quantum" (NISQ) [45] devices.

The second approach is analog quantum simulation, reminiscent of early classical analog computers that employed electrical circuits to solve differential equations or wind tunnels to study fluid dynamics [46]. Analog quantum simulation is designed to address a single, specific problem by tailoring the interactions among the system's degrees of freedom to emulate the behavior (e.g., the Hamiltonian) of the desired model. Analog simulators are not compatible with traditional approaches to fault-tolerant quantum error correction, making them less powerful and suggesting that they will eventually be phased out in favor of digital quantum computers. However, the current advantage of analog simulation lies in its ability to access larger system sizes and longer evolution times, thanks to being designed for a specific problem, and not requiring the full controllability of digital quantum computers. This feature makes analog simulators particularly well-suited for achieving practical quantum advantage on near-term devices, especially for problems where even a qualitative answer is lacking [39]. Furthermore, unlike universal digital quantum computers, where the underlying platform is largely irrelevant, the choice of a specific platform in analog quantum simulation determines the models that can be effectively studied, as different platforms possess distinct capabilities and native interactions.

1.3 Quantum platforms

In this section, we provide a brief introduction to the main platforms employed in this dissertation, namely superconducting circuits, and atomic, molecular, and optical systems.

1.3.1 Superconducting quantum circuits

Superconducting circuits ("circuit-QED") are electrical circuits that are made out of superconducting materials and are operated at very low temperatures and powers. Several ingredients are crucial for a circuit to operate in the quantum regime [26, 47, 48]. First, although these circuits are macroscopic in size, operating them at extremely low powers ensures that only a small number of electrons or Cooper pairs are relevant to their behavior. Second, superconducting circuits are typically operated at temperatures as low as a few millikelvins ($T \sim \mathrm{mK}$), which significantly suppresses thermal fluctuations (characterized by $k_B T$) relative to the characteristic excitation energies (characterized by $\hbar\omega$ with frequency ω in the microwave range) of the circuits. Last, superconducting materials exhibit zero electrical resistance, eliminating a major source of decoherence found in ordinary metals, even at low temperatures.

Essentially all circuits are made using a combination of three basic components, shown in Fig. 1.1: capacitors and inductors which are linear elements, as well as Josephson junctions, which provide nonlinearity. The dynamics of a circuit are described by the canonically conjugate variables, current I and voltage V. Alternatively, it is often more useful to work with the charge $\pi(t) = \int^t I(t')dt'$ and flux $\phi(t) = \int^t V(t')dt'$. This is particularly true when considering Josephson junctions, as the current through these junctions is most naturally expressed in terms of the superconducting phase difference across the junction, which is proportional to the flux. Upon

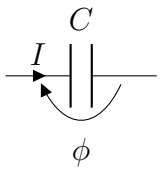

(a) Capacitor with capacitance C and current-voltage-flux relation: $I = C\dot{V} = C\ddot{\phi}$.

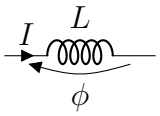

(b) Inductor with inductance L and current-voltage-flux relation: $\dot{I} = V/L \rightarrow I = \phi/L$.

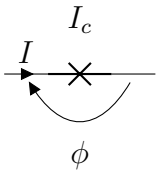

(c) Josephson junction with critical current I_c and current-flux relation: $I = I_c \sin\left(\frac{4e^2}{\hbar}\phi\right)$.

Figure 1.1: Building blocks of circuit QED.

quantization, these classical variables are promoted to quantum operators that satisfy the canonical commutation relation $[\hat{\phi}, \hat{\pi}] = i\hbar$, playing the role of position and momentum operators.

Circuit-QED systems offer a range of distinct advantages that make them highly attractive for quantum information processing and simulation. One notable advantage is their ability to realize artificial atoms with customizable properties that can be precisely designed and controlled [47, 49–51]. Moreover, the fundamental degrees of freedom in circuit-QED architectures, namely the charge π and flux ϕ, realize a local infinite bosonic Hilbert space. This property makes circuit-QED well-suited for simulating theories with bosonic content, avoiding the overhead from encoding quantum oscillators into qubits. Another compelling feature is the potential for achieving very strong coupling between different subsystems [52–54]. Circuit-QED systems can exhibit significantly stronger interactions, scaling with up to a factor of α^{-2} stronger compared to the couplings between real atoms and photons, where $\alpha \approx 1/137$ is the fine-structure constant [52]. These advantageous characteristics of circuit-QED are leveraged in Chapters 2 to 4 to explore exotic regimes of light-matter interactions and simulate relativistic bosonic field theories.

1.3.2 Atomic, molecular, and optical systems

The field of atomic, molecular, and optical (AMO) physics focuses on the study of matter, such as atoms, ions, or molecules, and their interactions with light. Within this broad field, the investigation of arrays of atoms and ions holds particular significance for quantum computing and simulation applications. These arrays, which can vary in geometries and dimensions, can be assembled using optical lattices [21, 55, 56] or optical tweezers [57–59] in the case of neutral atoms, and using electrical fields in the case of ions [24, 25]. Quantum information can be stored in their internal states and manipulated using external electromagnetic fields.

These platforms offer several advantages for quantum computing and simulation. One notable advantage is that atoms or ions of the same species are exactly identical, unlike circuit-QED where fabrication disorder may pose challenges. Furthermore, their ground-state manifolds provide a means to store quantum information with extremely long coherence times [60, 61]. Additionally, these systems can exhibit long-range interactions, enabling the exploration of phenomena beyond traditional locality constraints. These interactions are also highly programmable and can be tuned using additional external fields. These advantageous features will be further explored in Chapters 5 to 7, where the programmability and long-range interactions of these platforms are leveraged for various applications. We proceed with a short description of the possible interactions in these systems, focusing on Coulomb (phonon) mediated interactions for trapped ions as well as Rydberg and cavity (photon) mediated interactions for neutral atoms.

We begin by discussing how interactions between qubits stored in the internal levels of ions can be generated via the Coulomb force, arising due to the electric charges of the ions. When confined in a trap, the ions form a crystal-like structure, with each ion occupying a well-defined

position, with the Coulomb repulsion balanced by external confinement force. The motion of the ions away from their equilibrium position can be described by harmonic normal modes (phonons). These collective vibration modes can be coupled to the internal levels of the ions via microwave or optical fields. For example, using two Raman transitions with virtual absorption and emission of phonons can lead to generic interactions of the form [62]

$$H_{\text{int}} = \sum_{i,j} J_{ij} Z_i Z_j, \tag{1.1}$$

where Z_i is the Pauli-z matrix acting on the internal qubit degree of freedom of ion i. The couplings J_{ij} may take different forms. For instance, when coupling only to the center-of-mass mode, the couplings are approximately constant, i.e., $J_{ij} \sim J_0$ [63–66]. In more general cases, the couplings exhibit power-law decay, such as $J_{ij} \sim J_0/|i-j|^\alpha$ with $0 \leq \alpha < 3$. It is also possible to generate completely arbitrary J_{ij} by employing N^2 lasers for N ions [67].

We now turn our attention to interactions among neutral atoms. In their electronic ground state and when far apart from each other, neutral atoms do not exhibit significant interactions. Strong interactions can nonetheless be induced by exciting one or more of their valence electrons to Rydberg states, corresponding to states with large principal quantum numbers n [23]. Due to the large spatial extent of the electronic wavefunction, these states exhibit highly exaggerated properties including long lifetimes and large dipole moments. These dipole moments give rise to strong dipole-dipole interactions between pairs of atoms. For two atoms with dipole moments $\boldsymbol{\mu}_1$ and $\boldsymbol{\mu}_2$ separated by a distance $\boldsymbol{R}$, the dipole-dipole interaction potential is given by [23]:

$$V_{dd} = \frac{\boldsymbol{\mu}_1 \cdot \boldsymbol{\mu}_2}{R^3} - \frac{3(\boldsymbol{\mu}_1 \cdot \mathbf{R})(\boldsymbol{\mu}_2 \cdot \boldsymbol{R})}{R^5}. \tag{1.2}$$

When the atoms are excited to states with angular momenta that differ by ± 1, Eq. (1.2) provides the leading contribution to the interactions, scaling as C_3/R^3. However, when the atoms are excited

to the same Rydberg state, these dipole-dipole interactions in Eq. (1.2) vanish. Instead, the leading order interactions are van der Waals (vdW), scaling as C_6/R^6, which are obtained from Eq. (1.2) via second-order perturbation theory. Both the dipole-dipole and the vdW interactions can be used to engineer more complex interactions by careful choices of the Rydberg states together with additional microwave and optical dressing [68–70].

Finally, neutral atoms can also interact when placed in an optical cavity. In this configuration, atoms interact with the quantized light modes of the cavity by absorbing and emitting photons. The specific nature of these light-atom interactions depends on various factors, including the cavity geometry, the number of participating cavity modes, and the internal level structure of the atoms [71–73]. When the cavity modes are far detuned from the atomic transitions, the cavity can be effectively eliminated, and the system can be described solely in terms of the atoms with effective interactions among them [74–79]. For instance, in the case of a single-mode cavity, cavity-assisted Raman transitions can lead to interactions of the form described in Eq. (1.1), with a uniform coupling strength $J_{ij} \sim J_0$ [74, 78].

1.4 Outline of dissertation

In Chapters 2 to 4 we study quantum simulation with the circuit-QED platform.

In Chapter 2, we investigate the scattering dynamics of lattice quantum electrodynamics in 1+1 dimensions, with the aim of studying nonperturbative, out-of-equilibrium dynamics of high-energy particle collisions on quantum simulators. Working in the bosonized formulation of the model, an analog circuit-QED implementation is proposed that is native to the platform, hence requires minimal ingredients and approximations, and enables practical schemes for particle wavepacket

preparation and evolution. Furthermore, working in the thermodynamic limit, uniform-matrix-product-state tensor networks are used to construct multi-particle wavepacket states, evolve them in time, and detect outgoing particles post-collision. This facilitates the numerical simulation of scattering experiments in both confined and deconfined regimes of the model at different energies, giving rise to rich phenomenology, including inelastic production of quark and meson states, meson disintegration, and dynamical string formation and breaking.

In Chapter 3, we study the propagation of photons in a one-dimensional environment consisting of two noninteracting species of photons frustratingly coupled to a single spin 1/2. The ultrastrong frustrated coupling leads to an extreme mixing of the light and matter degrees of freedom, resulting in the disintegration of the spin and a breakdown of the "dressed-spin," or polaron, description. Using a combination of numerical and analytical methods, we show that the elastic response becomes increasingly weak at the effective spin frequency, showing instead an increasingly strong and broadband response at higher energies. We also show that the photons can decay into multiple photons of smaller energies with a nearly maximal allowed probability and that the spin induces strong anisotropic photon-photon interactions.

In Chapter 4, we explore many-body phenomena with a single artificial atom coupled to the many discrete modes of a photonic crystal. This work is a collaboration with the experimental group of A. A. Houck from Princeton University. The experiment reaches the ultrastrong light-matter coupling regime using the circuit-QED paradigm, by galvanically coupling a highly nonlinear fluxonium qubit to a tight-binding lattice of microwave resonators. Using matrix-product-state simulations, we show that in this regime, the transport of a single photon is strongly modified by the presence of multi-photon bound states, owing to interactions that break particle number conservation, in good agreement with the experimental observations. The experiment was performed

by A. Vrajitoarea in the group of A. A. Houck from Princeton University. The contribution of the author of this dissertation consisted of the initial planning as well as the theoretical and numerical modeling of the experiment.

Next, Chapters 5 to 7 describe quantum simulation and tools for atomic, molecular, and optical systems.

In Chapter 5, we study quantum information scrambling in spin models with both long-range all-to-all and short-range interactions. We argue that a simple global, spatially homogeneous interaction together with local chaotic dynamics is sufficient to give rise to fast scrambling, which describes the spread of quantum information over the entire system in a time that is logarithmic in the system size. This is illustrated in two tractable models: (1) a random circuit with Haar random local unitaries and a global interaction and (2) a classical model of globally coupled nonlinear oscillators. We use exact numerics to provide further evidence by studying the time evolution of an out-of-time-order correlator and entanglement entropy in spin chains of intermediate sizes. These results pave the way towards experimental investigations of fast scrambling and aspects of quantum gravity with quantum simulators.

In Chapter 6, we report on the experimental realization of strong nonlocal interactions in a 2D Fermi gas in an optical lattice using Rydberg dressing. This work is a collaboration with the experimental group of W. Bakr at Princeton University. The system is approximately described by a t-V model on a square lattice where the fermions experience isotropic nearest-neighbor interactions and are free to hop only along one direction. To probe the interplay of nonlocal interactions with tunneling, we investigate the short-time-relaxation dynamics of charge-density waves in the gas. We find that strong nearest-neighbor interactions slow down the relaxation. Our work opens the door for quantum simulation of systems with strong nonlocal interactions such as extended

Fermi-Hubbard models. The experiment was performed by E. Guardado-Sanchez, B. M. Spar and P. Schauss in the group of W. S. Bakr. The contribution of the author of this dissertation consisted of the initial planning as well as the theoretical and numerical modeling of the experiment.

In Chapter 7, we propose a protocol for sympathetically cooling neutral atoms without destroying the quantum information stored in their internal states. This is achieved by designing state-insensitive Rydberg interactions between the data-carrying atoms and cold auxiliary atoms. The resulting interactions give rise to an effective phonon coupling, which leads to the transfer of heat from the data atoms to the auxiliary atoms, where the latter can be cooled by conventional methods. This can be used to extend the lifetime of quantum storage based on neutral atoms and can have applications for long quantum computations. The protocol can also be modified to realize state-insensitive interactions between the data and the auxiliary atoms but tunable and nontrivial interactions among the data atoms, allowing one to simultaneously cool and simulate a quantum spin model.

Finally, Appendices A to F provide technical details that were omitted from Chapters 2 to 7.

Chapter 2: High-Energy Collision of Quarks and Hadrons in the Schwinger Model: From Tensor Networks to Circuit QED

2.1 Introduction

Scattering processes in nuclear and high-energy physics play an essential role in studies of hadronic and nuclear structure and of exotic phases of matter, and in searches for new particles and interactions. Current and future frontiers are the Large Hadron Collider, the Relativistic Heavy-Ion Collider [80, 81], the Electron-Ion Collider [82, 83], and neutrino-nucleus scattering at the Deep Underground Neutrino Experiment [84–87]. Collisions in these experiments involve hadronic initial states and complex many-particle final states. In addition, scattering proceeds in a multistage process and may encompass a wide range of phenomena, including the formation of exotic matter [81, 88], such as quark-gluon plasma [89, 90], thermalization [91, 92], quark and hadron fragmentation [93, 94], and quark-gluon-plasma hadronization [95, 96]. Ideally, such rich phenomenology should be grounded in first-principles quantum-chromodynamics (QCD) descriptions. While perturbation theory and QCD factorization [97–100], as well as the nonperturbative method of lattice QCD [101–109], have brought about impressive advances, a full understanding of scattering processes in QCD at all stages and energies is still lacking.

First-principles simulations of high-energy particle scattering are considered a prime appli-

cation for quantum computers and simulators [110–121]. A central challenge is that realistic scattering experiments involve a vast range of spatial and temporal scales, placing their simulation beyond the capabilities of current digital quantum computers. Analog quantum simulators may enable simulating larger Hilbert spaces and longer times, but concrete proposals are lacking for analog simulation of scattering processes in quantum field theories. At the same time, classical tensor-network methods have been shown to successfully capture ground-state [122], and to some degree dynamical [123], phenomena in gapped theories, including scattering processes [124–127], particularly in $1+1$ dimensions, but their reach remains limited in simulating general scattering problems in quantum field theories. This Chapter advances both analog quantum simulation and tensor-network-based classical simulation for a prototypical model of QCD, the lattice Schwinger model, i.e., lattice quantum electrodynamics (QED) in 1+1 dimensions. Previous tensor-network [124, 125, 128–139] and quantum-simulation [140–164] studies of the model focused on formulations involving fermion (or qubit) degrees of freedom (with or without gauge fields). Motivated to address, more generally, theories with bosonic content, here we instead consider the bosonic dual of the theory, a particular type of a massive Sine-Gordon model.

Our first objective is to propose an analog circuit-QED implementation of the bosonized lattice Schwinger model. Recently, the bosonic dual was shown to be approximately realizable by circular Rydberg states [165]. In contrast, we will show that circuit QED's basic components, its native bosonic degrees of freedom, and the available ultrastrong coupling [53, 54] allow the model to be implemented in a simple circuit with minimal ingredients and approximations, making it particularly suitable for near-term quantum simulation. Our second objective is a numerical exploration of high-energy real-time scattering phenomenology in the model. We work in the nonperturbative regime, near the confinement-deconfinement critical point and in the thermodynamic limit, using

uniform matrix product states (uMPS) [166], which in turn allows for the construction [126, 127] and collision of numerically-exact quasiparticle wave packets in the interacting theory at various energies, resulting in nontrivial inelastic effects. In contrast, earlier works were limited to elastic scattering at either weak (nearly free fermions) [125] or strong (nearly free bosons) [124] coupling regimes. We focus on a detailed spatial, temporal, and momentum-resolved diagnostic of elastic and inelastic processes of quark and meson states, involving phenomena such as meson disintegration, dynamical string formation and breaking, and the creation of quark and (excited) meson states. We also investigate the role of entanglement in high-energy scattering [124, 167–174].

2.2 Model and circuit-QED implementation

The massive Schwinger model has the Lagrangian density

$$\mathcal{L} = \bar{\psi}(i\gamma^\mu \partial_\mu - e\gamma^u A_\mu - m)\psi - \frac{1}{4} F_{\mu\nu} F^{\mu\nu}, \tag{2.1}$$

where $\psi(x,t)$ is a 2-component Dirac spinor, $\gamma^0 = \sigma^z, \gamma^1 = i\sigma^y$ with σ^z, σ^y being the Pauli matrices, m is the mass, e is the electric charge, and $A_\mu(x,t)$ and $F_{\mu\nu}(x,t)$ are the gauge field and the field-strength tensor, respectively. Equation (2.1) is dual to a bosonic scalar field theory with the Hamiltonian [175, 176]

$$H = \int dx \left[\frac{\Pi^2}{2} + \frac{(\partial_x \phi)^2}{2} + \frac{M^2 \phi^2}{2} - u \cos(\beta\phi - \theta) \right], \tag{2.2}$$

where $\phi(x)$ and $\Pi(x)$ are the scalar field and conjugate momentum, respectively, $M = e/\sqrt{\pi}$, $\beta = \sqrt{4\pi}$, and $u = \frac{e^\gamma}{2\pi}\Lambda m$, where γ is Euler's constant and Λ is a UV scale (we assume $\hbar = c = 1$ throughout, where c is the speed of light). Finally, $\theta \in (-\pi, \pi]$, with its origin explained in Ref. [176] and Appendix A.1.1. We work with a lattice discretization of Eq. (2.2) given by

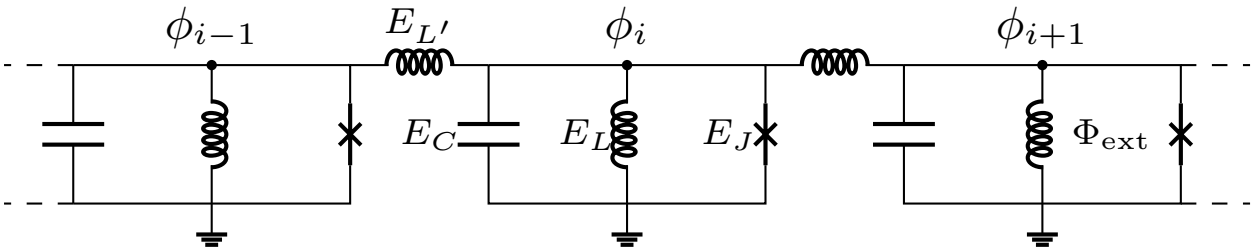

Figure 2.1: Lumped-element circuit diagram that realizes Eq. (2.3).

$$H = \chi \sum_x \left[\frac{\pi_x^2}{2} + \frac{(\phi_x - \phi_{x-1})^2}{2} + \frac{\mu^2 \phi_x^2}{2} - \lambda \cos(\beta \phi_x - \theta) \right], \tag{2.3}$$

where x labels lattice sites, $[\phi_x, \pi_y] = i\delta_{xy}$, $\chi = 1/a$, $\mu^2 = M^2 a^2$, $\lambda = u a^2$, and a is the lattice spacing. We set $a = 1$, with the continuum limit corresponding to $\mu, \lambda \to 0$. Quantities are assumed in lattice units throughout.

Remarkably, Eq. (2.3) can be exactly realized in a simple superconducting circuit, shown in Fig. 2.1. The circuit can be regarded as a chain of inductively coupled fluxoniums [177]. It consists of nodes i, each corresponding to a lattice site with a local bosonic degree of freedom described by flux ϕ_i and charge π_i, composed of a parallel arrangement of a capacitor, an inductor, and a Josephson junction with respective energies E_C, E_L, and E_J [26]. Further, nodes are coupled by inductors with energy $E_{L'}$. The circuit parameters are related to those of Eq. (2.3) via $\chi = \frac{8E_C}{\beta^2}$, $\frac{E_{L'}\beta^4}{8E_C} = 1$, $\mu^2 = \frac{E_L \beta^4}{8E_C}$, $\lambda = \frac{E_J \beta^2}{8E_C}$, and $\theta = \Phi_{\text{ext}} - \pi$, where Φ_{ext} is a tunable external flux threading each loop, and $\beta \neq 0$ can be chosen arbitrarily (see Appendix A.2.1 for the full derivation). In fact, when $\beta \neq \sqrt{4\pi}$, the circuit describes a more general model known as the massive Thirring-Schwinger model [178]. In Appendix A.2.2, we present a method for preparing initial wave packets of bosonic particles using two ancillary qubits, hence providing a complete protocol for preparation and evolution of mesonic wave packets for a scattering experiment. Measurements of the local field ϕ_x [179] or the output field at the edges [180, 181] can be performed using standard techniques.

To gain insight into the anticipated phenomenology, we proceed with a numerical study of the collision dynamics in the lattice Schwinger model. While quantitative predictions for the continuum theory require an extrapolation procedure [135, 182], here only fixed, but sufficiently small, values of μ and λ are considered. The model has two dimensionless parameters, the ratio e/m, corresponding to μ/λ in Eq. (2.3), and the angle θ representing a constant background electric field $E_\theta = \frac{e}{2\pi}\theta$. Gauss's law, $\partial_x E = e\psi^\dagger\psi$, ties the total electric field $E_T = E_\theta + E$ to the dynamical charges, and equals $E_T = \frac{e}{\sqrt{\pi}}\phi$ in the bosonic dual [183].

Two regimes will be studied near the $\mathbb{Z}_2$ critical point, shown in Fig. 2.2 as (b) and (c). Point (b) is in the deconfined phase [red line at $\theta = \pi$ in Fig. 2.2(a) terminating at the Ising critical point], where the ground state is two-fold degenerate [Fig. 2.2(b,i)]. Here, fundamental excitations are "half-asymptotic" [176] fermions ("quarks"), appearing as topological kinks in the bosonic dual [see Fig. 2.2(b,ii)]. Point (c) in Fig. 2.2(a) is in the confined phase, with a unique ground state [Fig. 2.2(c,i)] and quark-antiquark bound-state ("meson") excitations.

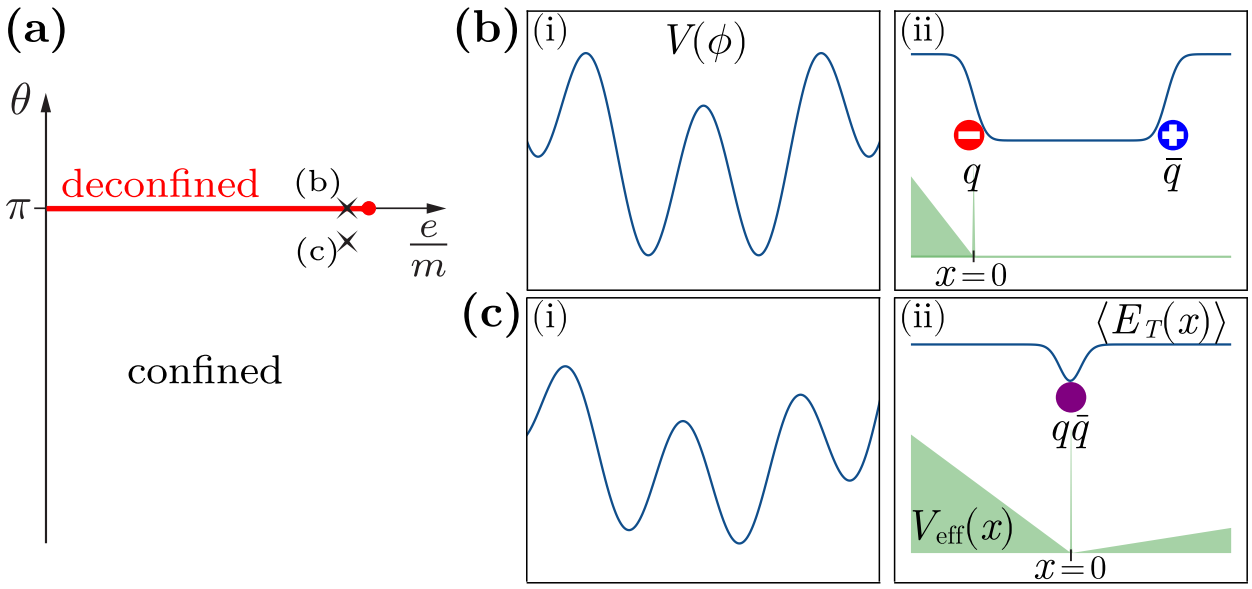

Figure 2.2: (a) Sketch of the phase diagram of the massive Schwinger model as a function of e/m (corresponding to μ/λ) and θ. The red dot is the Ising critical point, where the deconfined phase (red line) terminates. Points (b) and (c) correspond to the two regimes considered in the Chapter. Panels (b,i) and (c,i) show the corresponding scalar potential $V(\phi) = \frac{1}{2}\mu^2\phi^2 - \lambda\cos\left(\sqrt{4\pi}\phi - \theta\right)$ [Eq. (2.3)]. Panels (b,ii) and (c,ii) show both the effective potential between the quarks [Eq. (2.4)] (green) and the electric/scalar-field distributions (blue) due to the quarks and mesons.

2.3 Quark-antiquark scattering

We first consider quark-antiquark scattering in the deconfined phase [Fig. 2.2(b)]. Constructing a uMPS representation of the two ground states [184], we use the uMPS quasiparticle ansatz [185, 186] to obtain single-particle energy-momentum eigenstates with dispersion $\mathcal{E}(p)$ and momenta $p \in [-\pi, \pi)$ (see Appendix A.3.1). From this, we construct two Gaussian wave packets, localized in momentum and position space, centered at opposite momenta $\pm p_0$. The initial state consists of a finite nonuniform region of 150–300 sites containing the two wave packets, and is surrounded (on the left and the right) by the uniform vacuum [we choose the vacuum with positive E_T, i.e., the right minimum of Fig. 2.2(b,i)]. We then time-evolve this state under the Hamiltonian in Eq. (2.3), while dynamically expanding the nonuniform region [187–189] up to 600–1300

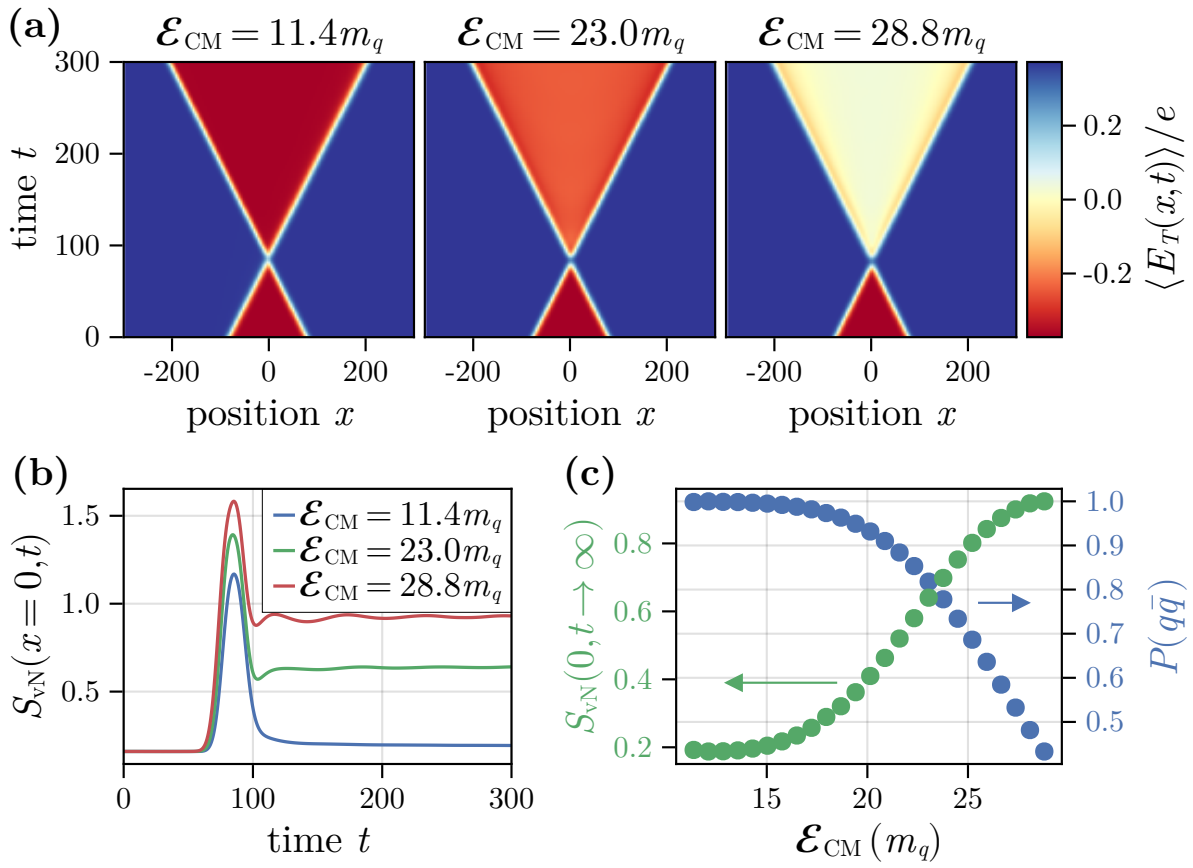

Figure 2.3: Quark-antiquark scattering in the deconfined phase. (a) Time evolution of the electric field for different center-of-mass energies. (b) Time evolution of the von Neumann entanglement entropy for a cut at $x = 0$, for the same three collisions as in (a). (c) Elastic scattering probability (right, blue) and asymptotic von Neumann entanglement entropy for the $x = 0$ cut (left, green) as a function of the center-of-mass energy. The parameters are $\mu^2 = 0.1$ and $\lambda = 0.5$ [see Eq. (2.3)].

sites (see Appendix A.3.2 for a more detailed description). By working near the critical point, where the quark mass $m_q \equiv \mathcal{E}(p = 0)$ (i.e., the gap) is small, one can consider momenta up to $|p_0| \lesssim 0.8$. These are sufficiently small to keep the physics in the long-wavelength regime of the lattice model, where the dispersion is approximately relativistic $\mathcal{E}(p) \approx (p^2 + m_q^2)^{\frac{1}{2}}$, but highly relativistic center-of-mass (CM) energies $\mathcal{E}_{\rm CM} \equiv 2\mathcal{E}(p_0) \lesssim 30 m_q$ are achieved.

Figure 2.3(a) shows the space-time distribution of the electric field for collisions at three representative energies, $\mathcal{E}_{\rm CM}/m_q = 11.4$, 23.0, and 28.8. Initially, the quark and antiquark are sep-

arated, resembling Fig. 2.2(b,ii), with electric field between the charges equal in magnitude but opposite in sign to the field outside [the two regions correspond to the two degenerate ground states in Fig. 2.2(b,i)]. Under time evolution, the two charges propagate ballistically, shrinking the negative-field region until they collide. During the collision, the particles bounce off each other and reverse their propagation direction elastically, the sole process at lower energies. Specifically, as can be seen in Fig. 2.3(a), at the lowest energy, $\mathcal{E}_{\rm CM}/m_q = 11.4$, the post-collision value of E_T between the charges is practically equal to the pre-collision value. For the higher-energy collisions, $\mathcal{E}_{\rm CM}/m_q = 23.0$ and 28.8, an increase of the post-collision electric field is observed, signalling additional charge production.

While our numerical approach does not rely on strong- or weak-coupling expansion, the relevant scattering channels can be understood from weak-coupling arguments as follows. In Appendix A.1.2, we derive, in the nonrelativistic limit, an effective potential between opposite charges at the lowest order in e/m starting from Eq. (2.1), which reads (in the center-of-mass frame)

$$V_{\rm eff}(x) = \frac{e^2}{2}\left(|x| - \frac{\theta}{\pi}x\right) + \frac{e^2}{4m^2}\delta(x)\,. \tag{2.4}$$

Here, x is the distance between charges. For $\theta \neq \pi$, one recovers linear confinement [Fig. 2.2(c,ii)] [129, 176, 183, 190], while at $\theta = \pi$, charges experience short-range *repulsion* due to the delta function in Eq. (2.4) [Fig. 2.2(b,ii)]. This implies the absence of stable bound states (mesons) in the deconfined phase, which is confirmed numerically in Appendix A.1.2. All possible scattering channels are, therefore, (even-numbered) multi-quark states. The lowest-order channel after the elastic one ($q\bar{q} \to q\bar{q}$) is the four-quark production ($q\bar{q} \to q\bar{q}q\bar{q}$), exhibiting quark fragmentation. In the latter case, the two inner particles screen the electric field produced by the outer two, consistent with the two rightmost panels in Fig. 2.3(a).

Elastic and inelastic processes are also distinguished by the production of von Neumann entanglement entropy [$S_{\rm vN}(x,t) = -\,\mathrm{tr}(\rho_{>x}(t)\ln\rho_{>x}(t))$ with $\rho_{>x}(t)$ being the reduced density matrix for sites $y > x$] across the collision point ($x = 0$), shown in Fig. 2.3(b) as a function of time. Figure 2.3(c) also shows the asymptotic ($t \to \infty$) entanglement generated as a function of the collision energy. The entanglement entropy is maximal during the collision but quickly approaches a constant afterwards. At lower energies, it nearly returns to its pre-collision (vacuum) value. A small increase is observed because different momentum components of the wave packets acquire slightly different elastic scattering phase shifts, making the two scattered wave packets slightly entangled [127]. At higher energies, however, significant net entanglement is generated, indicating inelastic particle production [111].

Finally, we compute elements of the momentum-resolved scattering S-matrix by projecting the post-collision state onto a basis of asymptotic two-particle states (see Appendix A.3.3 for details). This basis is constructed from the single-particle wavefunctions, requiring the particles to be widely separated to ensure orthogonality and avoid interaction effects. For $2 \to 2$ scattering, this is guaranteed sufficiently far from the collision point, but not for higher-order scattering. From this, we obtain the elastic scattering probability $P(q\bar{q})$, displayed in Fig. 2.3(c), as a function of the collision energy.

The elastic scattering probability is near unity at lower energies, decreasing monotonically, falling below 0.5 around $\mathcal{E}_{\rm CM}/m_q \gtrsim 28$. Interestingly, the energy required for significant inelastic scattering is many times the threshold energy ($\mathcal{E}_{\rm CM} = 4m_q$). While we did not obtain the precise contribution of the four-quark (or higher-quark-number) states [1], the decrease of $P(q\bar{q})$ confirms

[1] Projecting the state on four widely-separated quarks basis states resulted in a negligible contribution. This does not mean that four particle states are absent from Fig. 2.3, but suggests that they are not spatially separated to be recorded as single-particle states.

the presence of significant inelastic scattering, consistent with the increase in entanglement entropy in Fig. 2.3(b) and the screening of E_T in Fig. 2.3(a).

2.4 Meson-meson scattering

We next consider scattering in the confined phase [Fig. 2.2(c)] at $\theta = \pi - \varepsilon$. We choose $\varepsilon \ll 1$, which gives rise to weak confinement of quarks, but keeps us close to the critical point (all other parameters are unchanged). In contrast to the deconfined regime, the interplay of high-energy and weak confinement yields rich behavior following the collision. There are multiple stable meson excitations, which are labeled by π_j ($j = 1, 2, ...$), with increasing masses m_{π_j}. Here, we consider $\pi_1\pi_1$ collisions, with meson wave packets prepared similarly as before, centered at $p_0 = \pm 0.6$ with $\mathcal{E}_{\rm CM}/m_{\pi_1} = 6.84$ (5.95) for $\varepsilon = 0.04$ (0.07).

The electric-field evolution for the two collisions is displayed in Fig. 2.4(a,i). Before the collision, the background electric field is only locally disturbed by the charge-neutral mesons [Fig. 2.2(c,ii)], unlike in the deconfined case where the presence of free quarks can lead to electric-field screening at arbitrary long distances. After the collision, the mesons partially fragment into a quark-antiquark pair. The quarks are joined by an electric-field string which screens the background electric field (light-blue regions) inside the collision cone. As the quarks travel outward, their kinetic energy gets converted into the potential energy of the string. Eventually, they turn and propagate back in the opposite direction [see also Fig. 2.4(c)] causing a second collision. Weaker confinement $\varepsilon = 0.04$ allows the quarks to propagate farther.

Next, we project the time-evolved state onto two-particle components, focusing on the lightest two mesons π_1, π_2, and the quark-antiquark pair $q\bar{q}$. While the latter are not true (i.e., asymptotic)

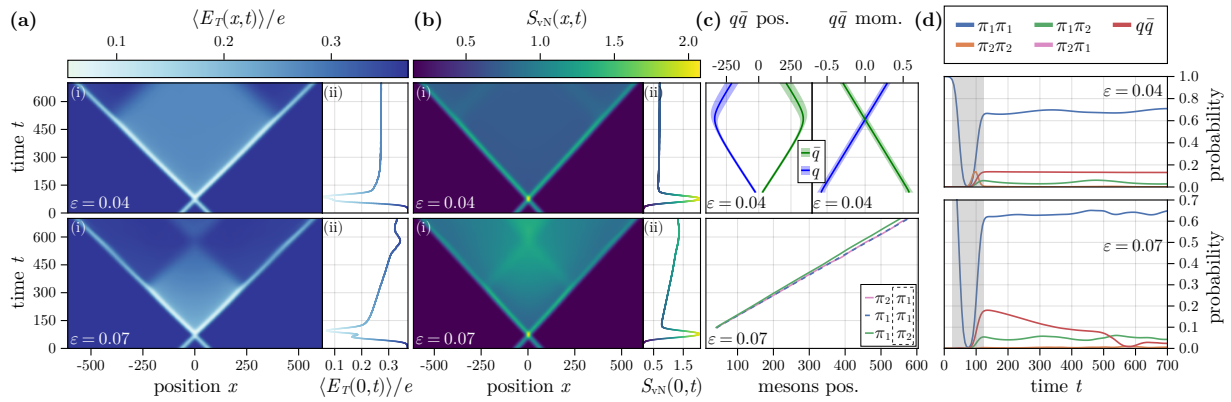

Figure 2.4: Meson-meson scattering in the confined phase. (a) Time evolution of the electric field for different $\theta = \pi - \varepsilon$ at all positions x [panels (i)] and at $x = 0$ [panels (ii)] with $\mu^2 = 0.1$ and $\lambda = 0.5$ as in Fig. 2.3. The wave packets are centered at $p_0 = \pm 0.6$, corresponding to $\mathcal{E}_{\mathrm{CM}}/m_{\pi_1} = 6.84, 5.95$ for $\varepsilon = 0.04, 0.07$. (b) Time evolution of the von Neumann entanglement entropy at all positions x [panels (i)] and at $x = 0$ [panels (ii)]. (c) Momenta and positions (mean $\pm$ std. extracted from a Gaussian fit of the projected distributions) of the quarks for $\varepsilon = 0.04$ (top) and the mean positions of the right-moving mesons for $\varepsilon = 0.07$ (bottom). (d) Probabilities of two-particle states $\mu\nu$ ($\mu, \nu \in [\pi_1, \pi_2, q, \bar{q}]$) where μ/ν is the particle on the left/right. The curves for $\pi_1\pi_2$ and $\pi_2\pi_1$ overlap due to the reflection symmetry of the initial state. Near the initial collision (shaded region), as well as near the secondary collision at $t \sim 550$ for $\varepsilon = 0.07$, the state cannot be captured by a basis of asymptotic particles.

quasiparticles, at weak confinement $\varepsilon \ll 1$, (anti)quarks can be approximately described by the modified quasiparticle ansatz of Ref. [127]. This requires a uMPS representation of the electric-flux string, which we approximate by its lowest energy state, a so-called "false-vacuum" state [191, 192], corresponding to the second (local) minimum in Fig. 2.2(c,i).

Figure 2.4(d) shows the probabilities of the $\pi_1\pi_1$ (blue), $\pi_2\pi_2$ (orange), $\pi_1\pi_2$ (green), and $\pi_2\pi_1$ (pink) combinations (where in state $\mu\nu$, the particle μ/ν is on the left/right), and of the quark-antiquark state (red). One can observe significant flavor-conserving elastic scattering, $\pi_1\pi_1 \to \pi_1\pi_1$, a smaller probability of exciting one of the outgoing mesons, $\pi_2\pi_1$ and $\pi_1\pi_2$ (this smaller probability increases with stronger confinement $\varepsilon = 0.07$), and a substantial $q\bar{q}$ component. Interestingly, for $\varepsilon = 0.07$, the $q\bar{q}$ component is decreasing in time, indicating string breaking [129, 193], which is also visible in the gradual increase of the bipartite entanglement entropy

in Fig. 2.4(b,i) [see also Fig. 2.4(b,ii)], and in the gradual reduction of the electric-field screening [Fig. 2.4(a,ii)]. At a late time $t = 700$, asymptotic two-particle states account for about 90% (76%) of the state at $\varepsilon = 0.04$ (0.07) [2].

The projection onto the asymptotic two-particle basis also provides the full momentum, and consequently position, distributions of the particles. Figure 2.4(c) shows the mean and standard deviation of the positions and momenta of the quarks, and the mean positions of the mesons, computed from fits of these distributions to a Gaussian form. The mean momenta of the quarks are approximately $\langle p(t) \rangle \propto \pm t$, in agreement with the expectation from the linear potential of Eq. (2.4). Their extracted positions in Fig. 2.4(c) are consistent with the boundaries of the screened-field region in Fig. 2.4(a,i) and with the localized increase in the entanglement entropy in Fig. 2.4(b,i). From the mean position of the mesons, Fig. 2.4(c), one can see that the heavier meson π_2 has a slightly lower average velocity compared to π_1, as expected.

2.5 Discussion and outlook

First-principles numerical explorations and quantum simulations of dynamics in strongly interacting quantum field theories are starting to shed light on the rich phenomenology of particle collisions in real time. As a step toward this goal, using *ab initio* numerical uMPS computations and working with a bosonized formulation of the Schwinger model, we analyzed the real-time dynamics of high-energy particle scattering in the nonperturbative regime of QED in 1+1 dimensions. We also proposed an analog circuit-QED implementation of the bosonized Schwinger model. This implementation requires minimal ingredients and no approximations (besides a lattice discretization), in

[2] We verified that the missing wavefunction weight is not accounted for by three or four widely-separated particle basis states.

contrast to previous circuit-QED proposals based on a quantum-link model [162]. We studied both the confined and deconfined regimes of the model, exhibiting a multitude of phenomena, including inelastic particle production, meson disintegration, and dynamical string formation and breaking.

In addition to the local electric-field and entanglement observables, the single-particle excitations allowed us to obtain complete time-resolved momentum and position distributions of the outgoing $2 \to 2$ scattered particles. To account for higher-order scattering beyond this two-particle characterization, it appears necessary to include states where two particles can be close, which could potentially be accomplished using the two-particle uMPS ansatz from Ref. [194]. This might also shed light on the nontrivial transient dynamics in Fig. 2.4(d). It would also be interesting to explore the energy dependence of string-breaking dynamics [195] as well as the possibility of formation of excited string states and their characterization beyond the false-vacuum approximation.

Ultimately, tensor-network methods are limited by entanglement growth, motivating quantum simulations using the proposed circuit-QED implementation for high-energy collisions. The proposed implementation can also be used to study quench dynamics. For example, the Schwinger mechanism or dynamical topological phase transitions can be studied in quenches of the θ parameter [143, 196], which can be accomplished using time-dependent flux control [26].

Finally, our circuit-QED implementation applies to other bosonic theories [197–200], including the ϕ^4 theory (achieved in the $\beta \to 0$ limit) in 1+1 or 2+1 dimensions and generalizations of the bosonized Schwinger model, including to multi-flavor fermions [176, 201] and to Thirring interactions [178]. In the latter case, sufficiently strong Thirring interactions give rise to attractive short-range interactions between quarks in the deconfined phase, as shown in Appendix A.1.2, leading to stable meson particles and hence qualitatively different scattering dynamics.

Chapter 3: Frustration-Induced Anomalous Transport and Strong Photon Decay in Waveguide QED

3.1 Introduction

Photons propagating in one-dimensional environments are a fundamental building block for quantum optics and waveguide quantum electrodynamics (QED). While interaction among photons is inherently negligible, strong effective interactions can be induced by coupling the light to atoms, or "impurities". Such photon-photon interactions are a crucial ingredient in many technologies ranging from quantum communication to quantum computation and metrology [26, 53, 54, 202]. Even a single two-level-atom (or a spin-1/2) can induce non-trivial behavior, perfectly reflecting photons whose energy matches the two-level gap Δ, while being transparent for other photons [203–206].

This picture can be greatly modified when the light-matter coupling is increased to the so-called ultrastrong coupling (USC) regime of waveguide QED [207–212]. This regime has been recently of great experimental and theoretical interest [26, 53, 54, 213, 214], and has been experimentally realized in superconducting quantum circuits [180, 215–218], allowing the exploration of quantum many-body physics with a *single* artificial atom [219]. The hallmark feature of USC regime is the breakdown of the rotating-wave approximation and the description of light and matter as separate

entities, which must instead be described by hybridized excitations.

Nevertheless, most light-matter systems do admit an intuitive interpretation in terms of quasi-particles whose behavior closely resembles the bare constituents of the system. For a two-level atom coupled to a 1D continuum, such a hybridized description is given in terms of a "dressed spin" or a polaron [220–222]. The strong dressing of the spin by photons leads to a dramatic Lamb shift of the bare spin frequency Δ to a renormalized value $\Delta_R \ll \Delta$ [223], the energy of the polaron excitation. The propagation of photons in the system can be understood in terms of scattering of free photons off the polaron, with the scattering resonance being shifted from Δ to Δ_R [208, 212]. This renormalized frequency emerges as the natural intrinsic energy scale of the system, with all non-trivial physics, such as photon-photon interactions, occurring in the vicinity of Δ_R. This intuition can be formalized with the well-known variational polaron transformation, which has been widely successful in describing both static and dynamical observables in various spin-boson systems [212, 224–231].

In this Chapter, we introduce a regime of light-matter interaction where the dressed-spin quasi-particle description of the combined light-matter system qualitatively breaks down. This is induced by ultrastrong frustrated interactions between a single two-level atom and two different species of photons in one dimension [232, 233]. We use matrix-product-state (MPS) numerics together with field-theoretical calculations to study the propagation of a single photon in the system. At weaker couplings, the elastic scattering shows a peaked response at a renormalized value $\Delta_R < \Delta$, consistent with the polaron interpretation. However, at larger couplings, this resonance becomes increasingly weak, and instead there is an emergent *increasingly* large and broadband response at large frequencies $\omega > \Delta_R$. We also find that inelastic processes, where the photon decays into several smaller-energies photons, can be as important or even *dominate* the elastic scattering. This

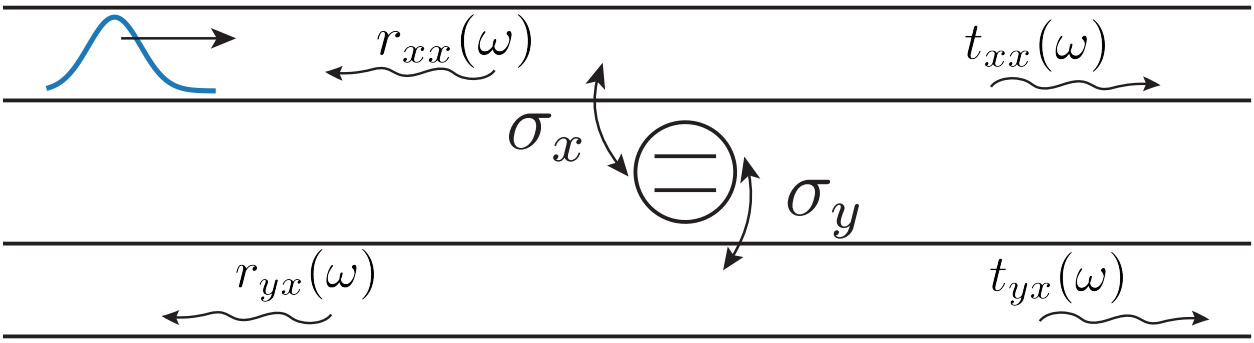

Figure 3.1: Schematic of the model, where a single spin-1/2 is coupled locally to two independent electromagnetic fields, represented here as two separate waveguides.

decay rate does not peak in the vicinity of Δ_R, in contrast to the polaron scenario, but saturates close to its allowed maximum and persists at very high energies, exceeding even the bare gap Δ. Both the elastic and inelastic results show that the induced photon-photon interactions can be highly anisotropic, being dominated by interactions between photons of different species.

The model we study is closely related to the problem of a spin coupled to two competing Ohmic baths. The ground-state phase diagram and the spin properties in such a system were originally studied in the context of quantum impurities in magnetically ordered backgrounds [232–237], where it was observed that the two competing baths result in the preservation of coherence in the spin dynamics, which was named "quantum frustration of decoherence" [232, 233]. Here we are instead interested in the dynamics of the photons.

3.2 Model

We consider a single spin-1/2 that is coupled, via two non-commuting operators, to two species of propagating photons in one-dimension, as shown in Fig. 3.1, and as described by the Hamiltonian [232, 233] ($\hbar = 1$)

$$\hat{\mathcal{H}} = \sum_{i=x,y} \left[\int dz \left(\frac{q_i(z)^2}{2} + \frac{(\partial_z \phi_i(z))^2}{2} \right) \right] - \frac{\Delta}{2} \hat{\sigma}_z + \pi \sqrt{\alpha_x} q_x(0) \hat{\sigma}_x + \pi \sqrt{\alpha_y} \partial_z \phi_y(0) \hat{\sigma}_y. \quad (3.1)$$

The two photon species have a linear dispersion $\omega_k = |k|$ and are described by the scalar fields $\phi_i(z)$ satisfying $[q_i(z), \phi_j(z')] = -i\delta_{ij}\delta(z - z')$. Here, $q_i(z)$ and $\phi_i(z)$ could represent the charge and flux degrees of freedom of two superconducting transmission lines [208], and the spin degree of freedom can be a qubit that is coupled capacitively to one transmission line and inductively to the other [238]. We note that our results would apply equally well to other geometries, such as a spin coupled to two semi-infinite leads [209], or a spin coupled to two polarizations of a single waveguide as in Ref. [239]. In Eq. (3.1), α_i ($i = x, y$) are the dimensionless coupling constants, which, for the rest of the Chapter, we assume to be equal ($\alpha_x = \alpha_y \equiv \alpha$).

The Hamiltonian in Eq. (3.1) needs to be supplemented with an ultraviolet cutoff ω_c. The latter can be used to define, via a renormalization group (RG) procedure [233], a renormalized spin frequency Δ_R, implicitly given by

$$\Delta_R = \frac{\Delta}{1 + 2\alpha \log(\omega_c/\Delta_R)}. \tag{3.2}$$

This quantity, first derived in Refs. [232, 233], is close to the bare spin frequency Δ for small $\alpha \to 0$, and it decreases as α is increased, approaching 0 as $\alpha \to \infty$. As we show in the next section, for intermediate coupling strengths $\alpha \lesssim 0.4$, Δ_R plays an important role in the photon dynamics, where it can be interpreted as the splitting of the dressed spin, whereas this picture breaks down for larger α.

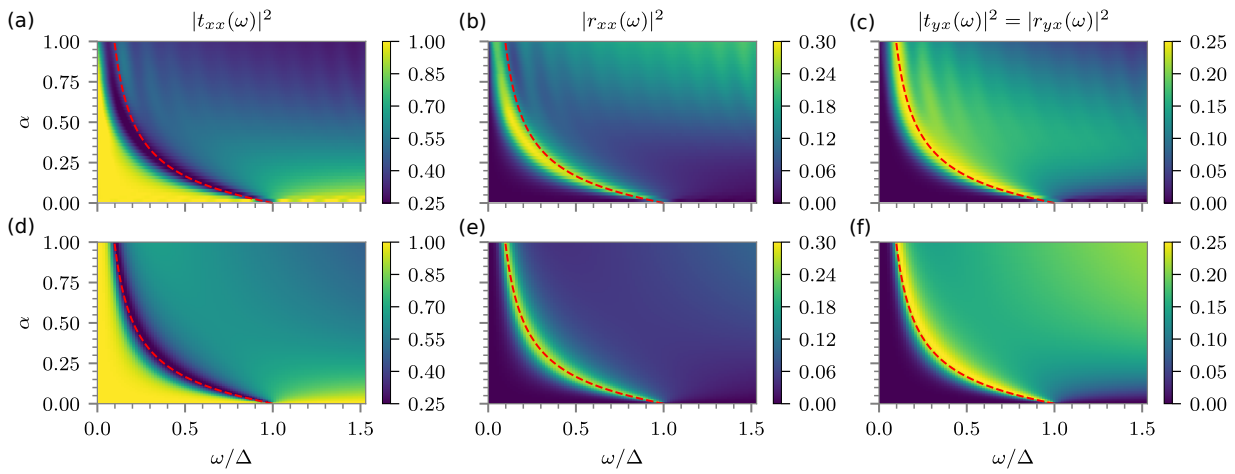

Figure 3.2: Numerical (a,b,c) and analytical (d,e,f) elastic scattering coefficients corresponding to Fig. 3.1, as a function of the incoming frequency ω and coupling constant α. The red dashed line corresponds to Δ_R from Eq. (3.2). The cutoff is $\omega_c = 10\Delta$. The oscillating behavior in the numerical plots at large α is a finite-size effect due to the scattering being very broad in space-time.

3.3 Anomalous transport

We begin by considering the elastic scattering of a single photon. Without loss of generality, we assume an incoming x photon that can scatter elastically in four different ways, as shown in Fig. 3.1. We computed the scattering coefficients both numerically, using an MPS-based approach, and analytically, with diagrammatic perturbation theory. In order to simulate the system numerically, we use an orthogonal polynomials mapping [240, 241] that transforms Eq. (3.1) into a one-dimensional tight-binding model with only local interactions (see Appendix B.2). We first use the density matrix renormalization group method to find the ground state of the system and then create a broad-in-frequency single-photon wavepacket on top of it. This state is then evolved for sufficiently long times so that the scattering process has ended. From the resulting state, we extract the elastic probabilities [242], shown in the top row of Fig. 3.2, as a function of the incoming frequency ω and coupling constant α.

In order to gain analytical insight into the problem, we use the fact that the elastic S-matrix can be written in terms of spin susceptibilities [209, 210, 215, 243–246]. For the setup in Fig. 3.1, we find (Appendix B.3)

$$r_{\alpha\beta}(\omega) = -i2\pi\alpha\omega\chi_{\alpha\beta}(\omega), \quad t_{\alpha\beta}(\omega) = \delta_{\alpha\beta} + r_{\alpha\beta}(\omega), \tag{3.3}$$

where the spin susceptibilities $\chi_{\alpha\beta}(\omega)$ are given by the Fourier-transformed retarded Green's function

$$\chi_{\alpha\beta}(\omega) = -\frac{i}{4}\int_0^\infty dt e^{i\omega t}\left\langle[\hat{\sigma}_\alpha(t), \hat{\sigma}_\beta(0)]\right\rangle, \tag{3.4}$$

evaluated in the ground state. Equations (3.3) and (3.4) are exact for a single incoming photon, but they can be understood intuitively within linear response formalism. The scattering of a β photon acts as a perturbation $\hat{\sigma}_\beta(0)$ on the spin, and the response $\hat{\sigma}_\alpha(t)$ of the spin describes the emission of an α photon.

The advantage of writing the elastic S-matrix in the form of Eqs. (3.3) and (3.4) is that it allows the use of powerful field-theoretical methods. In particular, we use an Abrikosov psuedo-fermion representation of the spin to perturbatively compute Eq. (3.4) to leading order in α, and employ the Dyson equation to sum an infinite subset of diagrams, as in the random-phase-approximation of the Coulomb gas [247]. We then use the Callan-Symanzik equation together with the RG flow equations from Refs. [232, 233] to improve upon the perturbative results, taking into account the non-perturbative Lamb shift in Eq. (3.2). The end result is (see Appendix B.4 for derivation)

$$\chi_{xx}(\omega) = \frac{(-\Delta + i\pi\alpha\omega)/2}{\Delta^2 - \omega^2\left[\pi^2\alpha^2 + \left(1 + 2\alpha\log\left(\frac{\omega_c}{\omega}\right)\right)^2\right] - i2\pi\alpha\Delta\omega}, \tag{3.5}$$

$$\chi_{xy}(\omega) = \frac{-i\omega(1 + 2\alpha\log(\omega_c/\omega))/2}{\Delta^2 - \omega^2\left[\pi^2\alpha^2 + \left(1 + 2\alpha\log\left(\frac{\omega_c}{\omega}\right)\right)^2\right] - i2\pi\alpha\Delta\omega}. \tag{3.6}$$

These forms for the susceptibility have a peak near Δ_R with a width of order $\tau^{-1} \sim \alpha\Delta_R$, where

τ is the lifetime of a spin excitation. At small α, both expressions reduce to narrows peaks at Δ, since $\Delta_R \to \Delta$ and $\tau^{-1} \to 0$ for $\alpha \to 0$. The resulting transmission and reflection probabilities are shown in the bottom row of Fig. 3.2.

We find excellent qualitative agreement between the numerical and analytical results, particularly for $\alpha \lesssim 0.5$. At very small α, we have the standard situation in waveguide QED [203–206], where only photons at $\omega \approx \Delta$ are coupled to the spin and experience scattering, being equally split among the four channels in Fig. 3.1, and the rest are simply transmitted. As α is increased, the location of the resonance drastically decreases, in excellent agreement with the RG predicted Δ_R in Eq. (3.2) (red dashed lines in Fig. 3.2).

For $\omega \ll \Delta_R$, Fig. 3.2 shows perfect transmission for all α, indicating that modes with frequencies smaller than Δ_R are effectively uncoupled from the impurity. This regime is qualitatively similar to that of the usual unfrustrated spin-boson model [223] and the Kondo problem [248]. In the latter, for energies smaller than the Kondo temperature (the equivalent of Δ_R), the impurity is screened and essentially disappears from the problem [246, 248, 249].

The $\omega > \Delta_R$ regime, on the other hand, is drastically different than in these paradigmatic models and the standard ultrastrong waveguide QED systems (see Appendix B.6 for a more detailed comparison to the case when the coupling operator to both waveguides is the same). Surprisingly, we find that, at large α, there is very little transmission, even for $\omega \gg \Delta_R$. For $\alpha \lesssim 0.4$, the system still admits the effective polaron description, since the strongest elastic response for all scattering channels in Fig. 3.2 is still concentrated near Δ_R. This picture changes dramatically for $\alpha \gtrsim 0.4$, where the reflection $|r_{xx}(\omega)|^2$, for example, instead of monotonically decreasing away from the resonance at Δ_R, first decreases but then starts increasing for $\omega > \Delta_R$. This behavior is more easily seen in the numerical plots but is nonetheless qualitatively consistent with the ana-

lytical solution. In particular, from Eq. (3.5) we see that, at large α and $\omega \gg \Delta_R$, $\chi_{xx}(\omega)$ decays *sublinearly* $\sim \omega^{-1} \log^{-2}(\omega_c/\omega)$, as was also pointed out in Refs. [232, 233]. Hence, the reflection coefficient [$\sim \omega\chi_{xx}(\omega)$ from Eq. (3.3)] *increases*, while the transmission *decreases*, in that regime. At even higher couplings $\alpha \gtrsim 0.5$, the numerical results show that the Δ_R resonance in $|r_{xx}(\omega)|^2$ becomes increasingly *weaker*, becoming less intense than the extremely *broadband* response at higher frequencies. All this implies that the spectral weight of the spin [$\sim \mathrm{Im}(\chi_{xx}(\omega))$] becomes increasingly spread out over larger energies instead of having a sharp peak at Δ_R. This anomalous behavior of the elastic reflection and transmission at large α, bearing no resemblance to a two-level system, constitutes the first of the two main results of this work.

Another interesting aspect in Fig. 3.2 is the behavior of the inter-species scattering, $|t_{yx}(\omega)|^2$, where the Δ_R resonance becomes extremely broad on the $\omega > \Delta_R$ side (note that $\chi_{xy}(\omega)$ [Eq. (3.6)] approaches a constant for large α and $\omega \gg \Delta_R$). This implies that the incoming x photon can be efficiently converted into a y photon in a wide range of energies. The inter-species scattering at large α shows significant disagreement between the numerical and analytical results, with the analytics suggesting that $|t_{yx}(\omega)|^2$ increases as ω is increased away from the Δ_R resonance. The numerics do not show such an increase, but rather show that $|t_{yx}(\omega)|^2$ approaches zero for very large ω and α. As we discuss in the next section, the discrepancy in $|t_{yx}(\omega)|^2$ (as well as in $|r_{xx}(\omega)|^2$ and $|t_{xx}(\omega)|^2$) at large α is due to the lack of certain kind of $\mathcal{O}(\alpha^2)$ diagrams in the susceptibility calculation and is related to the presence of substantial inelastic scattering.

3.4 Photon decay

As is well-known, ultrastrong coupling can give rise to number-non-conserving inelastic processes. The probability of such processes is, however, typically much weaker than the elastic rate and is usually peaked at the vicinity of the polaron energy Δ_R [209, 244, 246]. As we now show, these two expectations are strongly invalidated due to the strong frustration in our model, which constitutes the second main unexpected result of this work.

Conservation of probability implies that $|t_{xx}(\omega)|^2 + |r_{xx}(\omega)|^2 + 2|t_{yx}(\omega)|^2 = 1 - \gamma(\omega)$, where nonzero $\gamma(\omega)$ signifies that the initial x photon of energy ω can decay into multiple photons of smaller energies. Direct computation using Eqs. (3.3), (3.5) and (3.6) yields $\gamma(\omega) = 0$, which is certainly incorrect. In fact, the numerical plots in Fig. 3.2 show that the total inelastic scattering rate approaches ≈ 0.5 (for $\omega \gtrsim 0.5\Delta$ and $\alpha \gtrsim 0.6$). In those regimes, a photon is therefore as likely to *decay* as to be scattered elastically. Note that the continuity equation in Eq. (3.3) constrains that $\max[\gamma] = 0.5$, implying that the scattering is nearly *maximally inelastic* in that regime.

To get a deeper understanding of the inelastic scattering, we perform additional numerical simulations and analytical computations. Numerically, we use narrower wavepackets in order to probe the dependence of the outgoing particles on the energy of the incoming photon. After the scattering event, we record the total number of elastically and inelastically scattered photons in each waveguide (Appendix B.2), shown in Fig. 3.3 for six wavepackets with different mean energy. The first observation from Fig. 3.3 is that the inelastic emission is highly anisotropic, giving rise to significantly more y photons than x photons, for an initial x wavepacket. Since the scattering process cannot change the state of the spin, the leading-order inelastic process involves four (one incoming and three outgoing) photons and is therefore of order α^2 [209]. It is precisely those

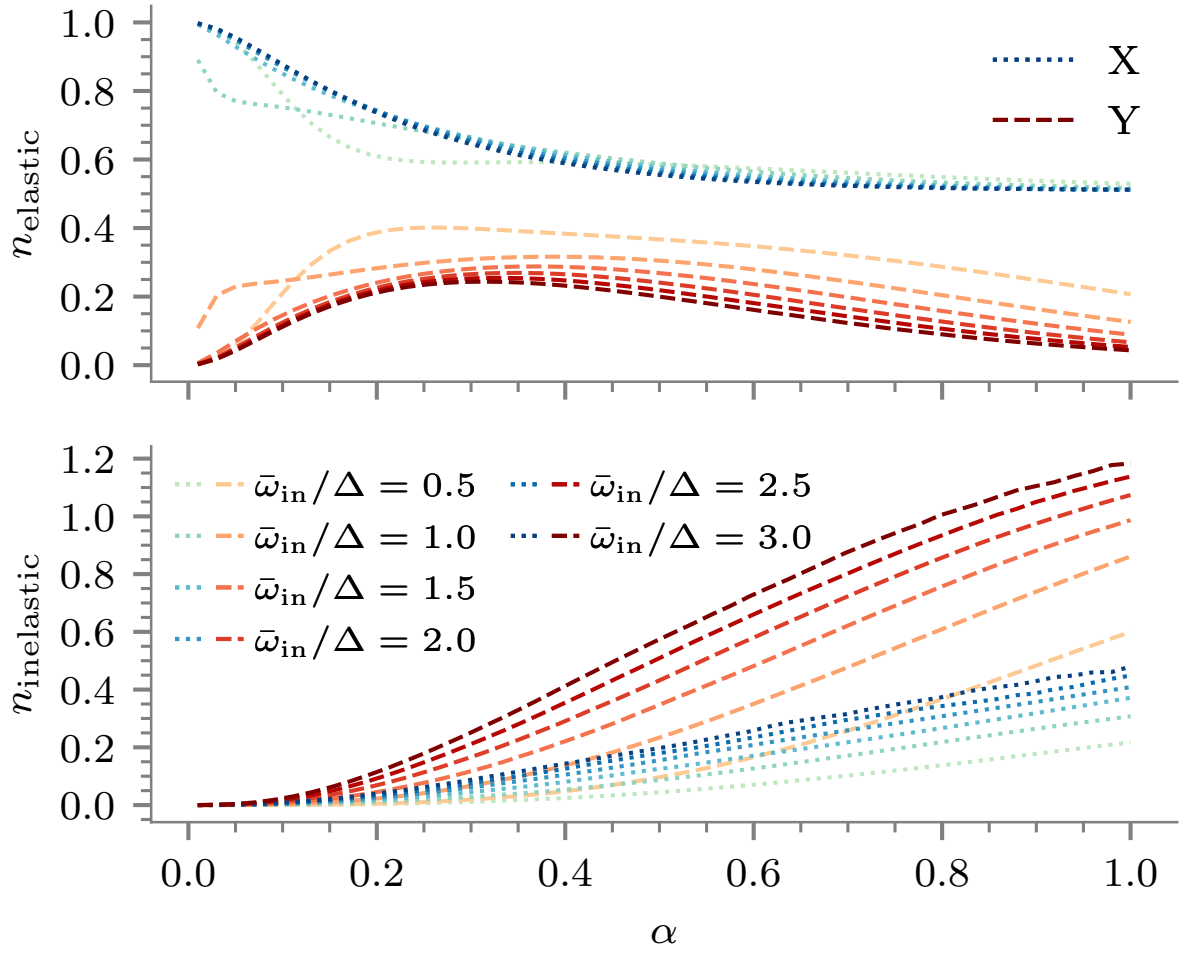

Figure 3.3: Numerically computed total number of elastic (a) and inelastic (b) particles produced in each waveguide as a function of α for six different incoming wavepackets. The wavepackets are single-particle Gaussians centered at $\bar{\omega}_{in}$ with a standard deviation of 0.2Δ. $\omega_c = 10\Delta$.

diagrams which are missing in the susceptibilities in Eqs. (3.5) and (3.6), explaining also why the analytics become inaccurate for $\alpha \gtrsim 0.5$ where nearly half of the scattering is inelastic. The four leading-order inelastic processes are $x \to \{xxx, yyy, xxy, xyy\}$. We denote the probability of these processes by $\gamma_{\mu_1\mu_2\mu_3}(\omega_1, \omega_2, \omega_3; \omega)$ where μ_i specifies the flavor of the outgoing photon (x or y) and ω_i its frequency. Energy conservation constrains $\omega_1 + \omega_2 + \omega_3 = \omega$. We have computed the leading order diagrams contributing to these processes, and the expressions are provided in Appendix B.5.

We find that the leading-order expression for γ_{xxx} exactly matches that [209] of the standard unfrustrated spin-boson model. Moreover, three of the four processes are elegantly related to each other to leading order, as follows:

$$\gamma_{yyy} = \gamma_{xxx}\frac{\omega^2}{\Delta_R^2}, \quad \gamma_{xxy} = \gamma_{xxx}\frac{\omega_3^2}{\Delta_R^2}. \tag{3.7}$$

The first of these demonstrates that an incoming x photon with energy $\omega > \Delta_R$ is more likely to decay into three y photons, as opposed to three x photons. The second relation shows that the γ_{xxy} process is more likely to occur than γ_{xxx} provided that the energy of the y photon satisfies $\omega_3 > \Delta_R$. However, it is far less likely compared to γ_{yyy} because if $\omega_3 \approx \omega$, energy conservation would require $\omega_1 \approx \omega_2 \approx 0$ and this would highly suppress its probability. The remaining process, γ_{xyy}, does not have a simple relation to the other three, but we have verified by direct numerical integration that its total cross-section is of the same order as the one for γ_{xxy}, and both of these are significantly less important than γ_{yyy}. In short, all this demonstrates that, in the regime $\omega \gg \Delta_R$, photons of one flavor decay dominantly to the other. This agrees qualitatively with Fig. 3.3, since even the smallest energy wavepacket ($\bar{\omega}_{in}/\Delta = 0.5$) is in the regime of $\omega > \Delta_R$ for $\alpha \gtrsim 0.2$ (see Fig. 3.2). In fact, for almost all the wavepackets and the range of α in Fig. 3.3, we have $\omega \gg \Delta_R$.

Figure 3.3 also shows that the number of elastic y photons goes to zero at large α and ω, consistent with $t_{yx}(\omega) \to 0$ in that regime, as we discussed in the previous section. Interestingly, this says that the inter-species scattering can be *completely inelastic*, while also dominating over the intra-species scattering, as we have just shown. Remarkably, we also see that the number of inelastically produced photons continues to rise as a function of $\bar{\omega}_{in}$, suggesting that $\gamma(\omega)$ remains close to 0.5 even for $\omega > \Delta \gg \Delta_R$. This behavior is consistent with the anomalous elastic scattering we identified in the previous section, but we nonetheless expect that $\gamma(\omega)$, as well as the

nontrivial elastic scattering $[r_{xx}(\omega), t_{yx}(\omega)]$, would eventually decay to zero as $\omega \to \infty$. While all the presented analytical and numerical results are qualitatively independent of the high-energy cutoff, we conjecture that the exact location of this decay may be nonuniversal and may depend on the precise cutoff function for a given physical system. In Appendix B.6, we compare these results to the situation where the two waveguides in Fig. 3.1 couple to the spin via the same operator, $\hat{\sigma}_x$, showing that, without the frustrated coupling, the inelastic processes are comparatively negligible and the anomalous elastic transport is absent.

3.5 Summary and outlook

In this Chapter we have shown that ultrastrong frustrated coupling between a two-level system and free photons in 1D leads to novel behavior such as anomalous photon transport and maximal photon decay. This behavior bears no resemblance to scattering off a two-level system and hence indicates the breakdown of the polaron quasi-particle description. Instead, this is reminiscent of non-Fermi liquid behavior of quantum impurity models in strongly correlated electron systems [244, 246].

While in this Chapter we have focused solely on the equal couplings case $\alpha_x = \alpha_y$, we expect our main results, namely the anomalous transport and strong photon decay, to remain qualitatively valid even in the presence of anisotropic couplings, provided they are both large and similar in magnitude. On the other hand, if the couplings are strongly asymmetric, say $\alpha_x \gg \alpha_y$, the behavior of the system would resemble more the unfrustrated model. The weaker coupling in such a case can be thought of as an unwanted source of dissipation acting on the spin, which would necessarily be present experimentally. Such unwanted dissipation can be similarly included in our model

by adding a third waveguide with coupling $\alpha_3 \ll \alpha_x \approx \alpha_y$. In superconducting circuits, such additional dissipation channels can be made negligible compared to the desired couplings [180, 215], and thus should not qualitatively affect our results.

Future theoretical work can investigate what kind of effective spin-spin interactions as well as novel phases of hybrid light-matter systems can be engineered by adding multiple impurities. The numerical and analytical methods developed in this Chapter can also be immediately applied in a variety of other situations, such as photons with more exotic dispersions. It would also be interesting to develop protocols that make use of the unusual properties of the light-matter system in this Chapter for entanglement generation, single-photon switches and routers, and frequency conversion, among other applications. Finally, our work may also shed light and inspire future studies on the problems of heat and energy transport, relevant for quantum thermodynamics and quantum chemistry, where similar models to the one studied here appear [250, 251].

Chapter 4: Ultrastrong Light-Matter Interaction in a Photonic Crystal

4.1 Introduction

Manipulating and studying the behavior of quantum systems composed of interacting particles, such as cold atoms [22, 252] or trapped ions [25], can help gain insight into fascinating many-body phenomena. Efforts have begun to develop synthetic materials in quantum optical platforms, harnessing the atom-light interface to extend interactions between atoms beyond the free-space limit using photonic structures [253], or to mediate interactions between photons through a non-linear atomic medium [254].

The strong hybridization of an atom with the band structure of a photonic crystal creates unique atom-photon dressed states, where the photonic excitation is exponentially localized at the atom position [255]. The first detection of a single-photon bound state has been achieved in the microwave domain, by coupling a superconducting qubit to a stepped impedance waveguide [256]. It is even possible for multiple photons to be simultaneously localized by a single emitter [257–260], the formation of multi-excitation bound states lying at the heart of many interacting quantum systems [261–263].

Assembling a chain of atoms coupled through their localized photonic modes offers a promising platform for simulating a wide range of quantum spin models with tunable long-range interactions [264, 265]. Realizations of these quantum simulators have been explored with atomic systems

embedded in nanophotonic waveguides [253, 266] and with superconducting circuits [179, 267–269]. Implementing such a large-scale system while maintaining a high level of control over the atomic elements is a challenging task on par with current efforts in building quantum information processors. An alternative direction to building a quantum optical simulator is to couple only a *single* atom to the *many* harmonic degrees of freedom in the crystal, which are energetically resolved and bestowed with strong photon-photon interactions inherited from the atom nonlinearity. This requires engineering the interaction to be large enough to observe significant many-body effects, in which the single-particle description becomes insufficient.

Circuit quantum electrodynamics (cQED) is an ideal platform for pushing the light-matter coupling [52] to novel frontiers in quantum optics [53, 54]. When the coupling strength becomes a sizable fraction of the excitation energies of the noninteracting system, the rotating wave approximation (RWA) is no longer valid and the resurgence of counterrotating terms gives rise to fascinating phenomena, such as the formation of an entangled atom-photon ground state [270]. This regime, termed the ultrastrong coupling regime, has been demonstrated with a superconducting flux qubit coupled to a single-mode microwave resonator [271, 272], displaying spectroscopic deviations from the standard Jaynes-Cummings model. Recent experiments have also reached the nonperturbative deep-strong coupling regime [273], where the physics is fully captured by the quantum Rabi model.

Extending the ultrastrong coupling regime to a discrete or continuous spectrum of harmonic modes provides an exciting avenue for exploring quantum impurity models in condensed matter physics [207–209, 211]. Connecting qubits to high-impedance transmission lines [216–218], the coupling strength can exceed the free spectral range and allow many discrete modes to hybridize with the qubit, offering insights into the enhanced down-conversion of a single photon [274] and

many-body localization [275]. Ultrastrong coupling to the electromagnetic continuum of a transmission line was also achieved [180, 215] where the qubit emission rate into the waveguide becomes a significant fraction of its frequency. Realization of the ultrastrong light-matter interaction in a structured multimode vacuum, with band edges, would provide a platform to explore unique phenomena beyond spin-boson models with linear waveguides [228, 231, 242].

In this Chapter we achieve the ultrastrong light-matter coupling regime in a photonic crystal waveguide where many-body effects arise from interactions that break particle number conservation and allow the direct observation of multi-particle bound states with a single-excitation probe. Our platform employs a highly nonlinear artificial atom with engineered control over its internal energy levels and over its coupling to the photonic crystal. We implement this model with superconducting circuits and reach the ultrastrong coupling regime using a galvanic connection. As predicted [242], the breakdown of the RWA converts the transport of a single photon into a many-body problem, where multi-photon bound states participate in the dynamics. This platform also harnesses the discrete multimode structure of the metamaterial to microscopically probe the photonic modes and their underlying correlations using well-established quantum optics techniques. We probe the photon-photon interactions mediated by the artificial atom through a multimode fluorescence measurement and observe the broadband emission of entangled pairs of photons.

4.2 Waveguide QED model

Our quantum optical model depicted in Fig. 4.1a consists of a multi-level artificial atom coupled to a photonic crystal waveguide with a finite-bandwidth dispersion. The discrete waveguide is represented as an array of coupled cavities, where the impurity is directly dipole-coupled to one

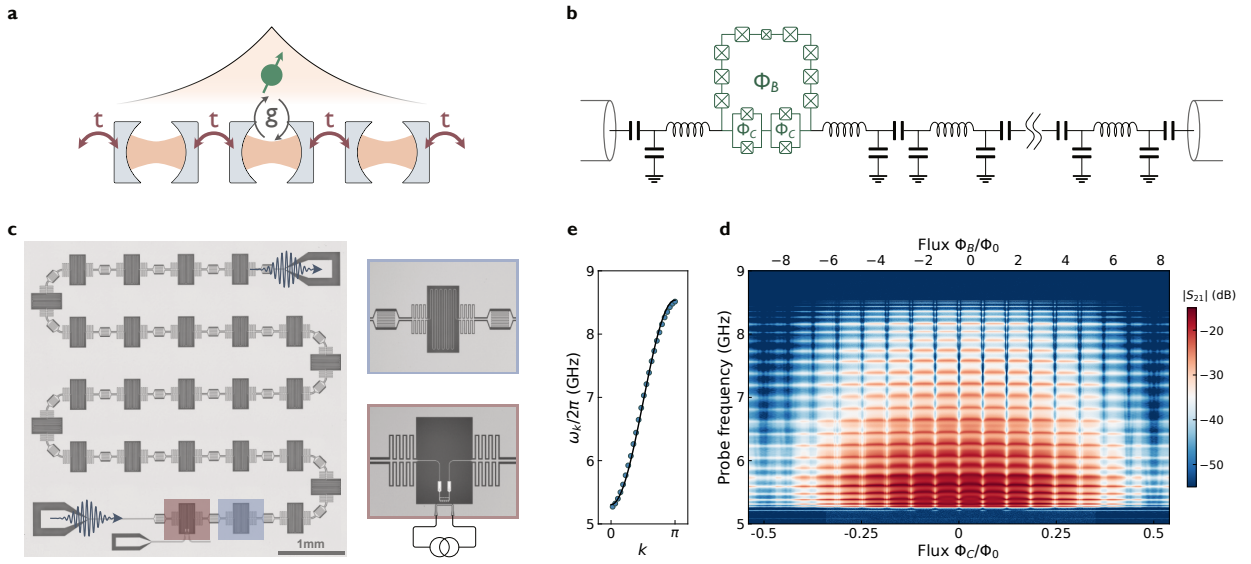

Figure 4.1: Photonic crystal platform. Atom-photon dressed bound states are explored in the waveguide quantum electrodynamics model illustrated in **a**. The physical system, shown in **b**, consists of a fluxonium artificial atom galvanically coupled to a tight-binding lattice of photons implemented as a lumped-element metamaterial. The fluxonium energy levels and its coupling inductance to the metamaterial are tuned in-situ with the externally applied magnetic flux Φ_{B} and Φ_{C}, respectively. The photonic crystal device is patterned on a large-area superconducting circuit. As shown in the optical microscope image in **c**, each of $M = 26$ unit cells is defined by a microwave resonator (blue), and the fluxonium circuit is coupled to the edge resonator (red). **d.** The dressed eigenmodes of the metamaterial are spectroscopically probed in transmission as the qubit resonance and its coupling are tuned with the magnetic flux bias. **e.** The eigenmode frequencies, measured when the qubit is far detuned, match the theoretical energy dispersion $\omega_k = \omega_c - 2J\cos(k)$ (solid line) for a 1D tight-binding chain of cavities, with a resonance frequency ω_c, coupled with a tunneling rate J. Here $k = n\pi/(M+1)$, with $n = 1, \ldots, M$, labels the eigenmodes in the order of increasing energy.

cavity site. The Hamiltonian is given by

$$\mathbf{H}/\hbar = \sum_{j=0}^{M-1} \omega_j a_j^\dagger a_j - \sum_{\langle i,j \rangle} J_{ij} \left(a_i^\dagger a_j + a_j^\dagger a_i \right) + \sum_l \varepsilon_l |l\rangle\langle l| + \sum_{l,l'} g_{ll'} \sigma_{ll'} \left(a_0^\dagger + a_0 \right). \quad (4.1)$$

The first two terms represent the tight-binding model for the photonic metamaterial, where $a_j^\dagger$ is the bosonic creation operator for a photon in the cavity site j. Each cavity has a bare resonance frequency ω_j and is coupled to its nearest neighbours with a tunneling rate J_{ij}. The third term describes the energy spectrum ε_l of the uncoupled atom in its eigenbasis $|l\rangle$. The last term in the Hamiltonian describes the coupling between the atomic dipole transitions $\sigma_{ll'} = |l\rangle\langle l'| + |l'\rangle\langle l|$ and

the local cavity field in the site $j = 0$. For the range of coupling strengths g_{01} investigated in this Chapter, the counterrotating contributions to the dipolar coupling are purposefully retained.

Adopting the cQED platform, we have implemented the device show in Fig. 4.1b, with a circuit diagram (Fig. 4.1c) that directly maps to our physical model (see Appendix C.2). The photonic metamaterial consists of a linear chain of $M = 26$ lumped-element microwave resonators with bare frequencies $\omega_j/2\pi \simeq 6.9\,\text{GHz}$ and nearest-neighbor capacitive couplings $J_{ij}/2\pi \simeq 814.4\,\text{MHz}$. We employ the fluxonium circuit [276] as our highly nonlinear quantum impurity. The qubit consists of a Josephson junction with energy $E_J/h = 8.1\,\text{GHz}$, shunted by a capacitor and an inductor, defined by a charging and inductive energy $E_C/h = 3.3\,\text{GHz}$ and $E_L/h = 5.5\,\text{GHz}$, respectively. Given its large anharmonicity and non-trivial selection rules, this circuit becomes an ideal choice for realizing a multi-level artificial atom whose energy spectrum and dipole matrix elements can be controlled in-situ using an external magnetic flux Φ_B threading the fluxonium loop.

This choice of superconducting qubit and coupling topology is favorable for reaching the ultrastrong coupling regime [52, 53, 277]. The fluxonium circuit is galvanically coupled to a lattice site by sharing a portion of its shunt-inductor, thereby coupling the resonator current to the phase drop $|\varphi\rangle\langle\varphi|_q$ across the Josephson junction. This becomes analogous to a magnetic dipole interaction of the atom with the resonator magnetic field dB, with the dipole moment defined in the fluxonium eigenbasis $d_{ij} = \langle i|\varphi\rangle_q \langle\varphi|_q |j\rangle$. The normalized inductive coupling strength takes the general form $g_{ij}/\omega_0 \propto \beta_L \sqrt{Z_\text{vac}/Z_r}\alpha^{-1/2} d_{ij}$, where β_L is the relative inductive participation ratio, $Z_\text{vac} = \sqrt{\mu_0/\varepsilon_0} \simeq 377\,\Omega$ is the vacuum impedance, Z_r is the resonator impedance, and $\alpha \simeq 1/137$ is the fine structure constant (see Appendix C.2). To achieve large coupling strengths, we operate the fluxonium near the sweet spot $\Phi_\text{B} = \Phi_0/2$, where $\Phi_0 = h/2e$ is the magnetic flux quantum.

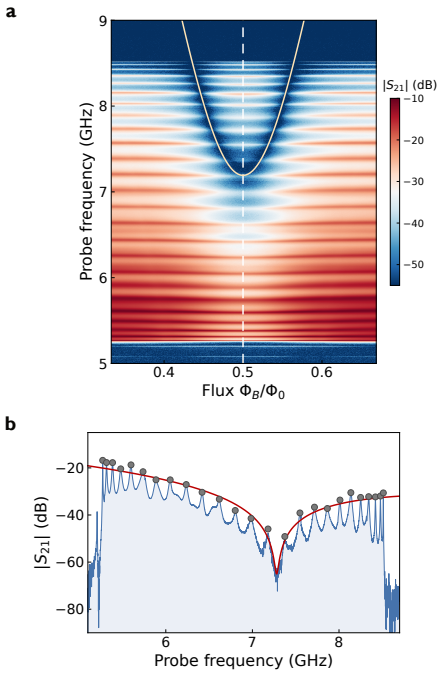

Figure 4.2: Spectroscopy near the impurity resonance. **a.** The coupled impurity-metamaterial system is characterized by measuring the magnitude of microwave transmission as a function of probe frequency. The fluxonium transition (solid curve) is tuned in resonance with the lattice passband by varying the external flux (Φ_B) through the qubit loop. **b.** The elastic scattering mediated by the qubit leads to a decrease in transmission, as highlighted by the trace at the flux sweet spot $\Phi_B = \Phi_0/2$ (dashed line cut in **a.**). The extracted amplitudes for each resonance peak (gray circles) are fitted to the transmission coefficient $|T|^2$ (solid red curve) for a single photon propagating in a 1D waveguide, scattered by a two-level emitter.

At this bias point, the dipole moment for the ground to first excited state transition reaches its maximum value. Remarkably, the inductive coupling scales inversely with the fine structure constant [52], allowing us to effortlessly reach the ultrastrong coupling regime. This is in contrast with capacitive coupling of a superconducting qubit or coupling a Rydberg atom to a cavity, where the small fine structure constant fundamentally limits the interaction strength. Furthermore, we control the qubit-metamaterial coupling by implementing the shared inductor as a chain of five superconducting quantum interference device (SQuID) loops threaded by a magnetic flux Φ_{C}. The SQuIDs are operated in the linear regime and jointly act as a flux-tunable inductor.

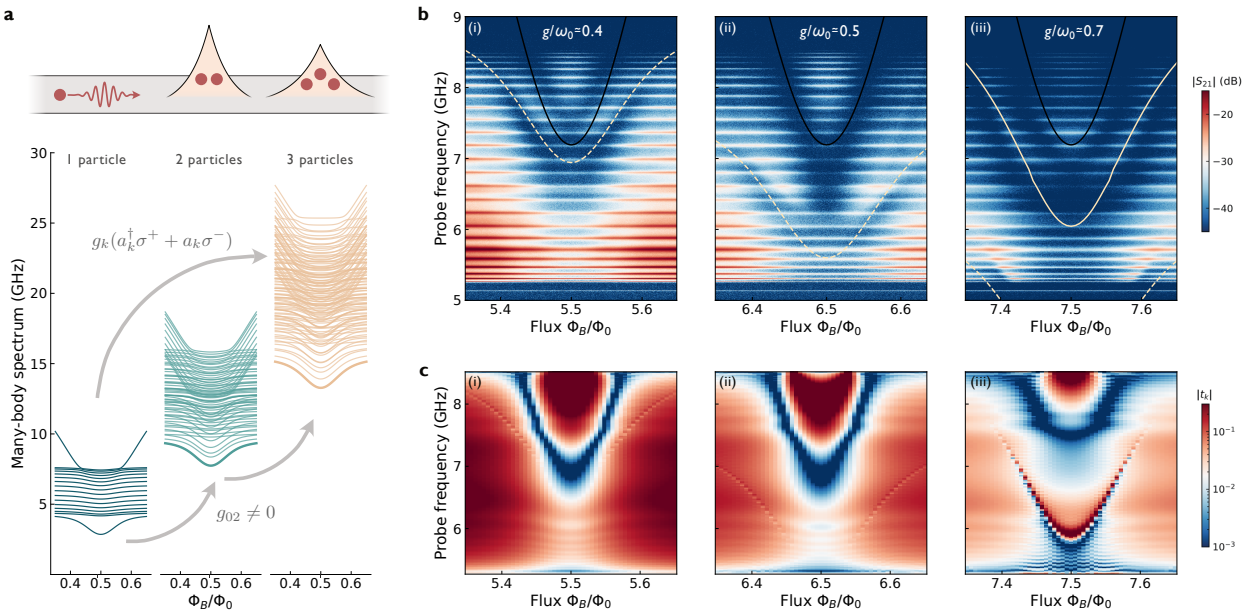

Figure 4.3: Many-body scattering dynamics of a single propagating photon. **a.** If the artificial atom is restricted to a two-level system and the RWA approximation is valid, the multi-particle eigenstates of the joint system form isolated bands of fixed-excitation manifolds. In the full model, these particle sectors are coupled through counter-rotating terms and parity-breaking transitions to higher fluxonium states, as highlighted by arrows. The multiphoton bound states scatter a single propagating photon as they enter the single-particle band, see upper diagram where the photons are represented as red dots. **b.** This nonperturbative effect is captured in the measured transmission amplitude of a weak probe tone for increasing values of the SQuID coupler inductance which leads to an increased light-matter coupling (normalized coupling strength at the flux sweet spot is listed at the top of each plot). In addition to the main fluxonium transition resonance (solid black curve), we observe the two-photon and three-photon bound states entering the passband. The yellow theory curves are the calculated energy levels from diagonalizing the full model Hamiltonian. The dashed yellow curve corresponds to the calculated two-photon state, while the solid yellow curve (above the measured three-photon resonance) corresponds to the calculated three-photon state. **c.** The appearance of these additional multiparticle resonances are validated with MPS scattering simulations of the transmission amplitude t_k. The faint resonance that gets shifted down in frequency as we increase the coupling strength qualitatively follows the calculated energy for the two-photon bound state, while the strong Fano-like resonance in (iii) matches the calculated energy for the three-photon bound state.

4.3 Nonperturbative transport of a single photon

The single-photon transport measurements are performed by applying a weak probe field and recording the amplitude of the transmitted field through the photonic crystal. The probe frequency

is varied over a broad range that covers the full dispersive band of the lattice. The transmission spectrum, shown in Fig. 4.1d, reveals a set of frequency-resolved resonances which correspond to the lattice modes hybridized with the fluxonium internal states. As the external magnetic bias is varied, we observe periodic disturbances in the resonance spectrum with two distinct modulation periods. The short and long periods coincide with the insertion of an additional flux quantum through the large fluxonium loop and the smaller SQuID loops, respectively. This large asymmetry ($\Phi_B/\Phi_C \approx 16$) allows independent control over the fluxonium spectrum and its coupling strength with the metamaterial. The transmission measurements are focused at flux bias values $\Phi_B \approx (2n+1)\Phi_0/2$ where the fluxonium resonance, corresponding to the transition from the ground state to the first excited state, enters the lattice band. Going to larger bias values, by increasing n, we are accessing increasing values of the coupling strength g_{01}/ω_0. In Fig. 4.2a we show the transmission spectrum centered around $\Phi_B \approx \Phi_0/2$, where the coupler SQuID is biased around its lowest inductance value. Tuning the qubit frequency $\varepsilon_{01} = \varepsilon_1 - \varepsilon_0$ across the photonic crystal spectrum leads to a clear extinction in the transmission amplitude for modes in the vicinity of the fluxonium resonance. This is explained by the destructive interference between the incoming probe field and the forward propagating field radiated by the qubit [206]. Additionally, we observe that the dressed lattice modes are displaced in frequency upon tuning the qubit into the band, in agreement with previous multimode experiments [216, 217]. The fluxonium circuit parameters are inferred from matching the flux dependence of the ε_{01} transition to the data.

The coupling between the impurity and its environment is characterized by the spontaneous emission rate Γ_1 of the artificial atom into the photonic crystal waveguide. To quantify this rate of energy exchange, we fit the transmission spectrum at the flux sweet spot (Fig. 4.2b) to the model of a two-level system coupled to a one-dimensional waveguide. In the weak-driving limit, the trans-

mission coefficient is given by $T(\omega) = 1 - \frac{1}{2}\Gamma_1/(\Gamma_2 + i\Delta)$ [206, 278], where Γ_1 is the total emission rate, Γ_2 is the decoherence rate, and $\Delta = \omega_p - \varepsilon_{01}$ is the detuning of the probe tone. From this simple model, we estimate a spontaneous emission rate $\Gamma_1/2\pi \simeq 6.18\,\text{GHz}$. This places our platform in the many-body regime, a combination of multi-mode and ultrastrong regimes. The multimode aspect is supported by the coupling rate exceeding the lattice mode spacing $\Gamma_1 > \delta\omega_k$ [217, 279], while the ultrastrong signature is justified by the coupling being a significant fraction of the qubit frequency $\Gamma_1/\omega_{01} \simeq 0.85$ [180]. We quantify this coupling regime in terms of Γ_1 since it is readily available from the transmission spectrum, but similar conditions can be written in terms of the Rabi coupling strength g_{01} [208]. This presents a picture of an impurity simultaneously exchanging excitations with many environmental modes, involving interaction processes that do not conserve the total number of particles. While this regime of light-matter interaction is still under active investigation and has thus far been discussed in linear waveguide models [209, 211, 279], we put forward a different picture that highlights the ultrastrong coupling physics and correlated nature in our structured multimode system.

In the presence of band-edges in the photonic crystal dispersion, the ultrastrong coupling regime introduces nonperturbative modifications to the propagation of a single photon. To understand the transmission of a single photon in our setting, we begin the discussion from the simple limit, not relevant for our experiment, where only the two lowest energy levels ($|0\rangle, |1\rangle$) of the fluxonium are accounted and we neglect the counter rotating terms in Eq. (4.1). In that case, the Hamiltonian conserves the total excitation number $N = \sum_j a_j^\dagger a_j + |1\rangle\langle 1|$, and the full eigenstate spectrum (see Fig. 4.3a) consists of bands of scattering and bound states, for each integer N. The scattering of a single incoming photon is therefore confined to the single-excitation sector. The higher excitation eigenstates do not participate in the dynamics, even if they are energetically

accessible and lie within the single particle band. The situation changes when the light-matter interaction is increased so that the counter-rotating terms in Eq. (4.1) cannot be neglected. The Hamiltonian no longer conserves the total excitation number, but it conserves the parity $e^{i\pi N}$, meaning that the counter-rotating terms only couple sectors of the same parity (see Fig. 4.3a). This remaining parity symmetry is broken due to the multi-level structure of the fluxonium, and the small coupling between states $|0\rangle$ and $|2\rangle$ from nontrivial selection rules.

The counter-rotating terms and the parity breaking couplings have a striking effect on the scattering dynamics, particularly when the higher excitation bound states appear inside the single-particle band. These localized bound states hybridize with the single-particle scattering states, leading to Fano-like resonances in the scattering spectra [242]. We directly observe this effect by probing the transmission through the lattice at larger coupling strengths achieved by increasing the inductance of the shared SQuID coupler. The flux dependent values for the coupling inductor, used for estimating the normalized coupling strength g_{01}/ω_0, are inferred from the redshift in the lowest lattice eigenmode (see Appendix C.2). In Fig. 4.3b(i),(ii), we observe these additional resonances coming from the two-particle bound state, while for even stronger coupling the three-particle bound state also appears in the band, seen in Fig. 4.3b(iii). While the counter-rotating terms are also present in Fig. 4.2a, we only start to observe the multi-particle bound states in Fig. 4.3b owing to the stronger inductive coupling that pushes these states to lower energy manifolds until they overlap with the single-particle band. The observed resonances are in qualitative agreement with the calculated spectrum (solid and dashed curves in Fig. 4.3b) for the full model using the Hamiltonian parameters of the circuit. The diminished transmission amplitude around the bound state frequencies reveals how these multi-particle states strongly scatter a single photon. Note that the resonance in Fig. 4.3b(iii) coming from the three-particle bound state is much

more pronounced than the two-particle equivalent. This arises from the fact that the coupling between the three-particle bound state and the single-particle scattering states comes from the strong counter-rotating terms, whereas the two-particle bound state resonances are the result of the weak parity breaking terms.

We consolidate these transmission measurements with simulations of the scattering dynamics using the matrix product state (MPS) representation of the many-body wavefunction. The simulations capture the observed reflections at the bound state frequencies, as shown in Fig. 4.3c. Additionally, we compare these numerical results with simulations of the simplified RWA model (see Appendix C.3) and confirm that the bound state resonances are visible in the transmission spectrum only when counter-rotating terms are included in the Hamiltonian. It becomes clear from our experimental observations and numerical results that the RWA waveguide QED model, where single photons are only reflected when resonant with the atom [203], fails to explain the pronounced bound-state scattering, providing the signature feature of ultrastrong coupling physics in our platform.

4.4 Stimulated emission of entangled photons

To further explore the multimode dynamics in our strongly interacting system, we shift our focus to the inelastic response to a coherent drive, probing the system beyond the single-photon level. Early work reaching the strong coupling regime in a multimode cavity has observed the phenomena of multimode fluorescence [280], where strongly driving the dressed qubit leads to emission over many modes close in frequency to the Rabi sidebands. In our platform, owing to the enhanced light-matter coupling, we observe complex multimode emission over the entire lattice passband,

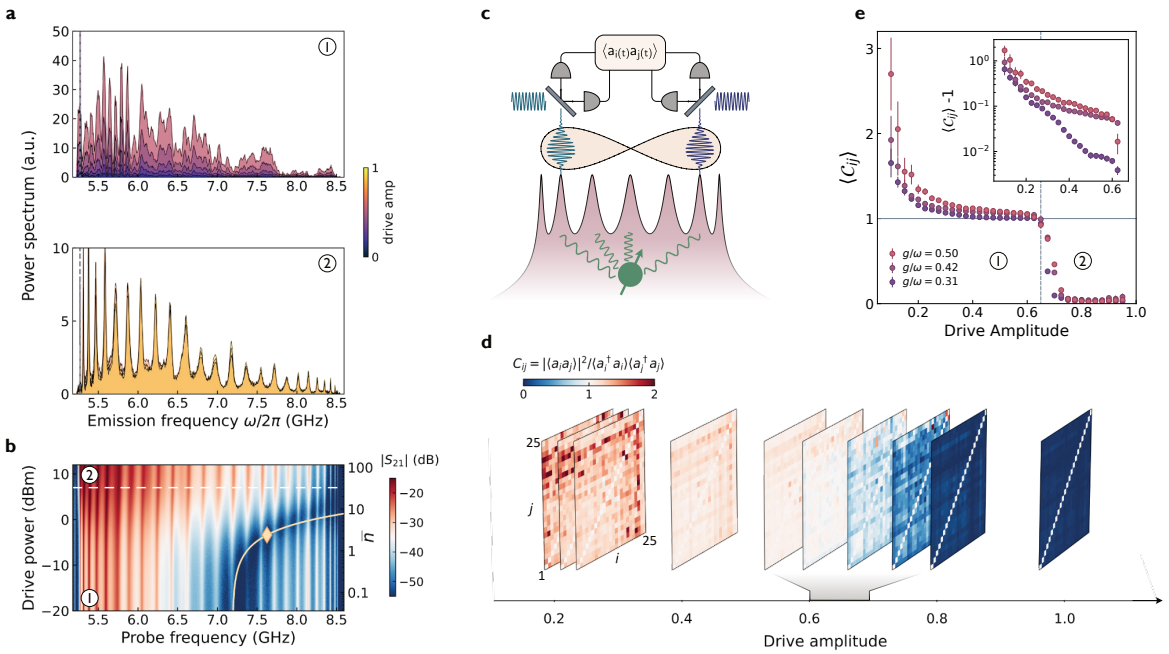

Figure 4.4: Fluorescence of multimode correlated states. The coupling with the highly nonlinear impurity leads to effective interactions between the modes of the photonic crystal. These interactions are reflected in the multimode fluorescence shown in **a**. Driving the lowest lattice mode (vertical line) leads to inelastic emission over the entire passband, inferred from the measured power spectrum. Two emission regimes are present over the range of applied drive amplitudes: ① in the weak drive limit, the fluorescence spectrum displays broad peaks that closely overlap with the dressed lattice modes, ② in the strong drive limit, the emission profile decreases in amplitude and has sharp peaks at the unperturbed mode frequencies. **b.** A two-tone transmission measurement reveals that the transition to the second emission regime (horizontal dashed line) coincides with the qubit resonance being Stark shifted out of the passband (solid theory line) from populating the driven lattice mode with an average of $\bar{n}$ photons. The marker (diamond) highlights the lowest drive amplitude used in the experiment to observe fluorescence signal above the noise floor of the amplifier chain. **c.** The quantum correlations between the emitted microwave photons are quantified using the extracted second order moments in a dual-heterodyne measurement. **d.** We determine if any pair of modes are entangled by measuring their squeezing correlations C_{ij} (for $i \neq j$) as a function of drive amplitude. **e.** Averaging these correlations across the multimode spectrum reveals that pairs of entangled photons are being emitted in the weak drive regime ①, as justified by the Hillery-Zubairy criterion $\langle C_{ij} \rangle > 1$. Error bars represent one standard deviation; where absent, they are smaller than the data points.

at much lower drive powers. In Fig. 4.4a, as we drive the lowest lattice mode, the measured power spectrum reveals two distinct emission regimes for varying drive amplitudes. For low drive strengths there is a broad emission profile with a subset of the fluorescence peaks close in frequency

to the dressed lattice modes. At higher drive strengths there is a dramatic decrease in the emission signal, and the fluorescence spectrum reveals sharp peaks that match the unperturbed lattice modes shown in Fig. 4.1d. The transition between these two emission regimes is investigated with a two-tone spectroscopic measurement, where we monitor the transmission over the lattice band with a weak probe and vary the power of the additional fixed-frequency drive used in the fluorescence experiment. In Fig. 4.4b, we observe that above the threshold drive strength, which separates the two emission regimes, the qubit experiences a large frequency shift that pushes its resonance outside the passband of the photonic crystal. This corresponds to an ac-Stark shift induced by populating the driven mode with a coherent state having an average number of $\bar{n}$ photons (see Appendix C.2.3), and we use this measurement to provide an estimate for $\bar{n}$. We find that in the weak drive regime, to observe fluorescence above the noise threshold we need to insert $\bar{n} \geq 3$ photons, and we transition into the strong drive regime with $\bar{n} > 40$ photons. Given the large system size and the number of inserted photons, numerically reproducing the steady state nonlinear response in Fig. 4.4a is a fascinating but challenging task which we leave for future work. These stimulated multiphoton processes, in which photons injected in the lowest lattice mode are being converted to photons in other modes, arise from the qubit-induced interactions between the modes. Detuning the qubit transition away from the band leads to a diminished photon nonlinearity and thus a dramatic decrease in the fluorescence signal. The simultaneous fluorescence of all modes for a fixed drive power is intriguing in itself, as it suggests the emergence of multimode correlations.

Quantifying the entanglement in such a large system is challenging, measuring the full density-matrix becomes experimentally impractical, and we need to adopt methods accessible with realistic resources. We characterize the quantum state of the multimode output and the underlying correlations by analyzing the moments of the propagating microwave fields [281], where the observables

are quadratic in the mode creation and annihilation operators. The amplified output signal is split into two separate heterodyne detection setups, with separate local oscillators selectively tuned in frequency to simultaneously measure the conjugate quadrature components for every pair of propagating modes emitted from the lattice. This allows us to extract the second order moments of the complex field amplitudes and evaluate the field correlations by subtracting the amplifier noise moments (see Appendix C.4). We examine the entanglement structure by employing the Hillery-Zubairy criterion [282], which states that any (pure or mixed) two-mode separable state, defined by the bosonic annihilation operators a and b, satisfies the condition $|\langle ab\rangle|^2 \leq \langle a^\dagger a\rangle\langle b^\dagger b\rangle$. When the quantum correlations on the left hand side become larger than the product of intensities, the state is identified as entangled, favoring a superposition of states that differ by a photon in each mode similar to a two-mode squeezed state. This is a sufficient but not necessary condition for entanglement, as there are other classes of two-mode entangled states that satisfy the above separability inequality. This entanglement criterion is tested on our multimode state by measuring the squeezing correlations $C_{ij} = |\langle a_i a_j\rangle|^2/\langle a_i^\dagger a_i\rangle\langle a_j^\dagger a_j\rangle$ for the fields emitted at every lattice mode frequency. In Fig. 4.4d, we highlight the evolution of the full correlation matrix as a function of the pump tone amplitude (see Appendix C.4). Our global measure of entanglement $\langle C_{ij}\rangle$ is extracted from averaging all $i \neq j$ mode-pair correlations for each matrix. The dependence of this metric on the pump amplitude is displayed in Fig. 4.4e for three distinct values of the coupling strength. We find that, in the low drive strength regime, the two-mode correlations are on-average above one, which violates the separability criterion. This reveals how the nonlinear wave-mixing processes stimulated by the pump tone lead to inelastic emission of entangled pairs of photons.

4.5 Outlook

In this Chapter we have demonstrated the ultrastrong coupling of a highly nonlinear emitter to a photonic crystal waveguide, where multi-photon bound states modify the transmission of photons in the lattice and provide a new avenue for exploring nonlinear quantum optics at the single-photon level [242, 283]. Similar to the single-mode picture, the ground state contains a multimode cloud of virtual photons centered around the emitter [208]. Harnessing the full control over the emitter's coupling to its environment, these vacuum fluctuations can be converted into single-photon radiation by modulating the coupling strength [228], a process which is again mediated by the photon bound states. This platform can also be extended to the frustrated ultrastrong coupling of an impurity to two competing baths [284], where the dressed-spin quasiparticle description breaks down and the induced photon-photon interactions can be highly anisotropic. Exploiting the intrinsic three-wave mixing nonlinearity of the fluxonium circuit, this multimode platform can also be employed as a quantum simulator in synthetic dimensions, where frequency-selective drives can induce inter-mode particle hopping and blockade-induced interactions [285].

Finally, the multimode correlation measurements presented in this Chapter can become a useful technique for probing entanglement in large-scale quantum systems, further expanding the quantum optics toolbox for characterizing strongly-correlated photonic materials [254]. The sharp change in the squeezing correlations observed in Fig. 4.4 could in fact be indicative of a driven-dissipative phase transition between the two inelastic emission regimes [286]. Furthermore, this pumped nonlinear system can be used as a broadband correlated reservoir for quantum communication applications, where the correlated photon fields can drive distant qubit nodes and distribute entanglement in a quantum network [287, 288]. This stimulated reservoir can also be potentially

used as a source of multimode squeezed light in boson sampling experiments for demonstrating quantum computational advantage [289]. A particularly intriguing prospect would be to provide strong evidence that an experiment of the type shown in Fig. 4.4, which we were unable to reproduce theoretically due to the large Hilbert space involved, is itself a demonstration of a quantum advantage.

Chapter 5: Minimal Model for Fast Scrambling

5.1 Introduction

The study of quantum information scrambling has recently attracted significant attention due to its relation to quantum chaos and thermalization of isolated many-body systems [290–292] as well as the dynamics of black holes [293–296]. Scrambling refers to the spread of an initially local quantum information over the many-body degrees of freedom of the entire system, rendering it inaccessible to local measurements. Scrambling is also related to the Heisenberg dynamics of local operators, and can be probed via the squared commutator of two local and Hermitian operators W_1, V_r, at positions 1 and r respectively,

$$\mathcal{C}(r,t) = -\frac{1}{2}\left\langle [W_1(t), V_r]^{\,2} \right\rangle , \tag{5.1}$$

where $W_1(t)$ is the Heisenberg evolved operator. The growth of the squared commutator corresponds to $W_1(t)$ increasing in size and complexity, leading it to fail to commute with V_r. In a local quantum chaotic system, $\mathcal{C}(r,t)$ typically spreads ballistically, exhibiting rapid growth ahead of the wavefront and saturation behind, at late times [297–299].

Of particular interest are the so-called fast scramblers, systems where $\mathcal{C}(r,t)$ reaches $O(1)$ for all r in a time $t_s \propto \log(N)$, with N being the number of degrees of freedom. Among the best known examples are black holes, which are conjectured to be the fastest scramblers in nature [294–

296, 300], as well as the Sachdev-Ye-Kitaev (SYK) [301, 302] model and other related holographic models [303–306].

Recent advances in the development of coherent quantum simulators have enabled the study of out-of-equilibrium dynamics of spin models with controllable interactions [17], making them ideal platforms to experimentally study information scrambling. Several experiments have already been performed [307–312], probing scrambling in either local or non-chaotic systems. The experimental observation of fast scrambling remains challenging however, particularly because few systems are known to be fast scramblers, and those that are, like the SYK model, are highly non-trivial, involving random couplings and many-body interactions. Some recent proposals suggested that spin models with non-local interactions can exhibit fast scrambling [313–315], albeit with complicated and inhomogeneous interactions.

In this Chapter, we argue that the simplest possible global interaction, together with chaotic dynamics, are sufficient to make a spin model fast scrambling. We consider spin-1/2 chains with Hamiltonians of the form

$$\mathcal{H} = \mathcal{H}_{\text{local}} - \frac{g}{\sqrt{N}} \sum_{i<j} Z_i Z_j, \tag{5.2}$$

where Z_i is the Pauli z operator acting on site i and $\mathcal{H}_{\text{local}}$ is a Hamiltonian with only local interactions that ensures that the full $\mathcal{H}$ is chaotic. We note that such global interactions are ubiquitous in ultracold atoms in optical cavities [74–76, 316, 317], and also in ion traps [63–66].

We first show that this effect is generic, by studying two models, a random quantum circuit and a classical model, both designed to mimic the universal dynamics of Eq. (5.2). We then provide numerical evidence for fast scrambling for a particular time-independent quantum Hamiltonian. Finally, we discuss possible experimental realizations.

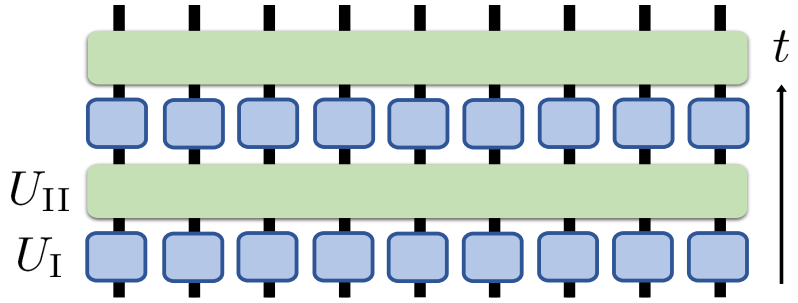

Figure 5.1: Diagram of the random circuit. As given in Eq. (5.3), each blue square is an independent Haar-random unitary $U_{H,i}$ acting on site i, and the green rectangle is the global interaction U_{II}.

5.2 Random circuit model

As a proof-of-principle, we consider a system of N spin-1/2 sites, with dynamics generated by a random quantum circuit (see Fig. 5.1) inspired by the Hamiltonian in Eq. (5.2). While less physical than the Hamiltonian model, it has the advantage of being exactly solvable while providing intuition about generic many-body chaotic systems with similar features.

The time-evolution operator is $U(t) = (U_{\mathrm{II}}U_{\mathrm{I}})^t$ where a single-time-step update consists of the two layers

$$U_{\mathrm{I}} = \prod_{i=1}^{N} U_{H,i}, \qquad U_{\mathrm{II}} = e^{-i\frac{g}{2\sqrt{N}}\sum_{i<j} Z_i Z_j}, \tag{5.3}$$

where each $U_{H,i}$ is an independent Haar-random single-site unitary. The two layers in Eq. (5.3) are motivated by the two terms in Eq. (5.2), with the Haar-random unitaries replacing $\mathcal{H}_{\text{local}}$.

We are interested in the operator growth of an initially simple operator $\mathcal{O}$. At any point in time, the Heisenberg operator $\mathcal{O}(t) = U^\dagger(t)\mathcal{O}U(t)$ can be decomposed as $\mathcal{O}(t) = \sum_{\mathcal{S}} a_{\mathcal{S}}(t)\mathcal{S}$, where $\mathcal{S}$ is a string composed of the Pauli matrices and the identity, forming a basis for $SU(2^N)$. As in random brickwork models [318, 319] and random Brownian models [298], the Haar-averaged probabilities $\langle a_{\mathcal{S}}^2(t)\rangle$, encoding the time evolution of $\mathcal{O}(t)$, themselves obey a linear equation

$$\left\langle a_{\mathcal{S}}^2(t+1)\right\rangle = \sum_{\mathcal{S}'} W_{\mathcal{S},\mathcal{S}'} \left\langle a_{\mathcal{S}'}^2(t)\right\rangle . \tag{5.4}$$

Here, $W_{\mathcal{S},\mathcal{S}'}$ is a $4^N \times 4^N$ stochastic matrix describing a fictitious Markov process [320, 321]. The average probabilities $\langle a_{\mathcal{S}}^2(t)\rangle$ fully determine the growth of the average of $\mathcal{C}(t)$ in Eq. (5.1) (see Appendix D). Because of the Haar unitaries and the simple uniform interaction in Eq. (5.3), $W_{\mathcal{S},\mathcal{S}'}$ is highly degenerate and only depends on the total weights of the strings $\mathcal{S}, \mathcal{S}'$, counting the number of non-identity operators, i.e $w(\mathcal{S}) = \sum_i (1 - \delta_{\mathcal{S}_i,1})$, and on the number of sites where both $\mathcal{S}$ and $\mathcal{S}'$ are non-identity, i.e $v(\mathcal{S},\mathcal{S}') = \sum_i (1-\delta_{\mathcal{S}_i,1})(1-\delta_{\mathcal{S}'_i,1})$, and is given by (see Appendix D.1 for derivation)[1]

$$W(w,w',v) = \left(\frac{1}{3}\right)^{w+w'} \sum_{k=0}^{v} \binom{v}{k} \sum_{l=0}^{k} \binom{k}{l} \times \left[\cos^2\left(\frac{2l-k}{\sqrt{N}} g\right)\right]^{N-k-(w+w'-2v)} \left[\sin^2\left(\frac{2l-k}{\sqrt{N}} g\right)\right]^{w+w'-2v} . \tag{5.5}$$

If we further assume that $\mathcal{O}$ starts out as a single site operator on site 1, then throughout the evolution, $\langle a_{\mathcal{S}}^2(t)\rangle$ only depend on the total operator weight w, and the weight on site 1, which we denote by $w_1 \in \{0,1\}$. We thus introduce the operator weight probability h_t at time t,

$$h_t(w,w_1) = \left\langle a_{\mathcal{S}}^2(t)\right\rangle 3^w \binom{N-1}{w-w_1}, \tag{5.6}$$

which gives the probability of $\mathcal{O}(t)$ having total weight w and weight w_1 on site 1.

The time evolution of $h_t(w,w_1)$ is given by the master equation

$$h_{t+1}(w,w_1) = \sum_{w_1'=0,1} \sum_{w'=w_1'}^{N-1+w_1'} \mathcal{R}(w,w_1,w',w_1') h_t(w',w_1'), \tag{5.7}$$

where the $2N \times 2N$ matrix $\mathcal{R}$ is (see Appendix D.2)

[1] The term with $2l = k, w+w'-2v = 0$ is assumed to be $0^0 = 1$. See Appendix D.1.

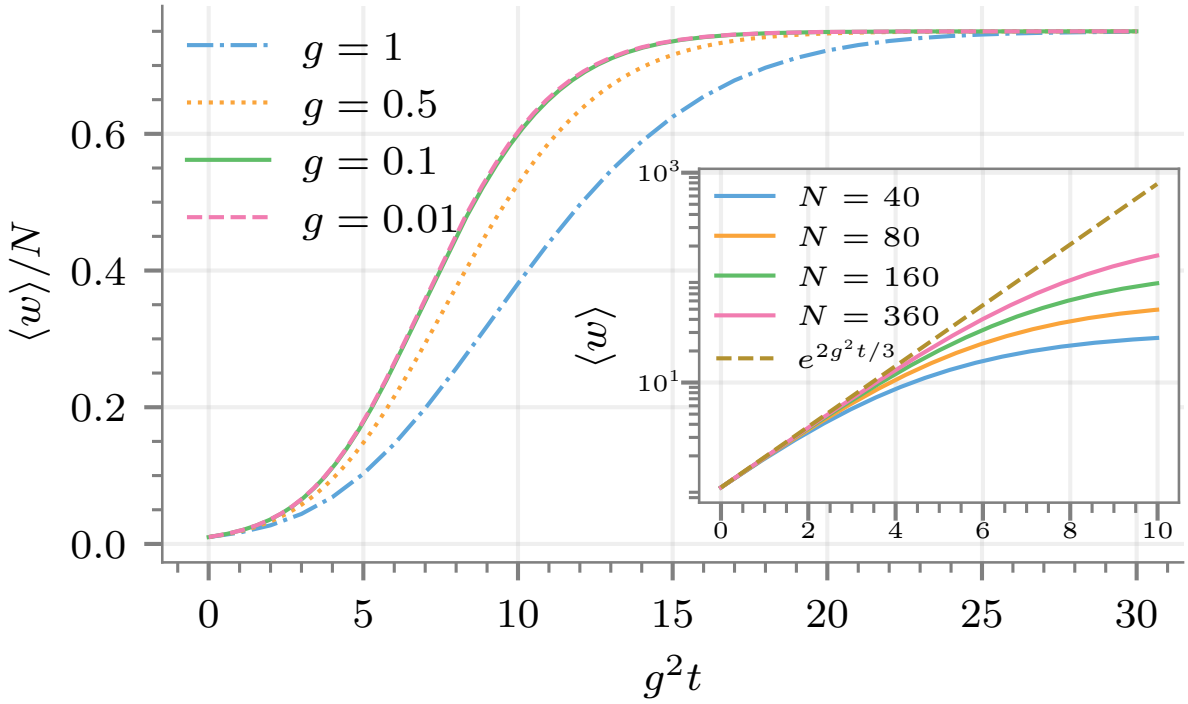

Figure 5.2: Normalized mean operator weight $\langle w(t) \rangle / N = \frac{1}{N} \sum_w w\, h_t(w)$ as a function of time for different g and $N = 100$, computed using Eq. (5.7). For small enough g, all the curves collapse to a single curve as a function of $g^2 t$, as implied by Eq. (5.10). The inset shows the initial exponential increase of $\langle w(t) \rangle$ for different system sizes N and $g = 0.1$.

$$\mathcal{R}(w, w_1, w', w_1') = 3^w \sum_{m=0}^{\min\{w-w_1, w'-w_1'\}} \binom{w' - w_1'}{m} \times \binom{N - 1 - w' + w_1'}{w - w_1 - m} W(w, w', m + w_1 w_1'). \quad (5.8)$$

The transition matrix $\mathcal{R}$, scaling only linearly with N, allows us to efficiently simulate the dynamics for large system sizes (see Fig. 5.2).

To proceed analytically, we Taylor-expand Eq. (5.5) to leading order in g, which gives rise to a closed master equation for the total operator weight probability $h_t(w) \equiv h_t(w, 0) + h_t(w, 1)$,

$$\frac{h_{t+1}(w) - h_t(w)}{g^2} = \frac{2w}{9N}(1 - 3N + 2w)h_t(w) \tag{5.9}$$
$$+ \frac{2w(w+1)}{9N}h_t(w+1) + \frac{N - w + 1}{3N}2(w-1)h_t(w-1),$$

which is similar to random Brownian models [298, 322] and shows that, at $O(g^2)$, w can change by at most ± 1 in a single step. Assuming that $h(w,t)$ varies slowly with respect to $g^2 t$ and w, we can approximate the above equation by a Fokker-Planck equation (rescaling time $\tau = g^2 t$)

$$\partial_\tau h(w,\tau) = -\partial_w(D_1(w)h(w,\tau)) + \partial_w^2(D_2(w)h(w,\tau)), \tag{5.10}$$

where the drift and diffusion coefficients are (dropping higher order terms $O(1/N, w/N)$)

$$D_1(w) = \frac{2}{3}\left(w - \frac{4w^2}{3N}\right), \qquad D_2(w) = \frac{w}{3} - \frac{2w^2}{9N}. \tag{5.11}$$

This equation describes the rapid growth of an initially localized distribution, followed by a broadening and finally saturation (see Fig. 5.2 and Appendix D.5 for more details). At early time, the $\frac{2}{3}w$ term in the drift coefficient dominates, giving rise to exponential growth of the mean operator weight $\langle w(t)\rangle \sim e^{2g^2 t/3}$, which agrees with the full numerical solution of the master equation, as can be seen in Fig. 5.2. The mean weight is related to the infinite-temperature squared-commutator in Eq. (5.1) (averaged over different circuits) via $\langle \mathcal{C}(t)\rangle = \frac{4}{3}\langle w(t)\rangle / N$ (Appendix D.4). Since $\langle w(t)\rangle$ grows exponentially with time, $\langle w(t)\rangle$ reaches $O(N)$ and $\langle \mathcal{C}(t)\rangle$ reaches $O(1)$ when $t = \frac{3}{2g^2}\log(N)$, thus establishing that this model is fast scrambling. Note that the $1/\sqrt{N}$ normalization in Eqs. (5.2) and (5.3) is crucial. Had we chosen instead $1/N$ ($g \to g/\sqrt{N}$), the Lyapunov exponent would have been $\frac{2g^2}{3N}$ and the scrambling time would have been $t \sim N\log(N)$.

5.3 Classical Model

Let us now consider a different setting that also allows to probe the basic timescales involved, and shows that randomness is not required. A convenient tractable choice is a classical model consisting of globally coupled non-linear oscillators. Note that the analogs of out-of-time-order correlators (OTOCs) have been studied in a variety of classical models [314, 323–327] and have been shown to capture the scrambling dynamics of quantum models like the SYK model [328–330].

Consider a $2N$-dimensional phase space with coordinates q_r (positions) and p_r (momenta) for $r = 1, \cdots, N$ with canonical structure specified by the Poisson brackets $\{q_r, p_s\}_{PB} = \delta_{rs}$. The Hamiltonian is $\mathcal{H}_c = K + V_2 + V_4$ where

$$K = \sum_{r=1}^{N} \frac{p_r^2}{2}, \qquad V_4 = \frac{\Omega_3^2}{4} \sum_{r=1}^{N} q_r^4, \tag{5.12}$$

$$V_2 = \frac{\Omega_1^2}{2} \sum_{r=1}^{N-1} (q_{r+1} - q_r)^2 + \frac{\Omega_2^2}{2\sqrt{N}} \left(\sum_{r=1}^{N} q_r \right)^2 . \tag{5.13}$$

The timescales for the growth of perturbations under $\mathcal{H}_c$ dynamics may be understood in two stages. First, $K + V_2$ can be solved exactly; this combination of terms provides the non-locality. The remaining V_4 term renders the dynamics chaotic, provided Ω_3 is large enough. The dynamics of $K + V_2$ causes a localized perturbation to spread to every oscillator with non-local amplitude $1/N$ in a time of order $1/N^{1/4}\Omega_2$. Then conventional local chaos can amplify this $1/N$-sized perturbation to order-one size in a time of order $\lambda^{-1} \ln N$, where λ is some typical Lyapunov exponent.

At the quadratic level, the uniform mode, $Q = \frac{1}{N} \sum_r q_r$, is decoupled from the remaining

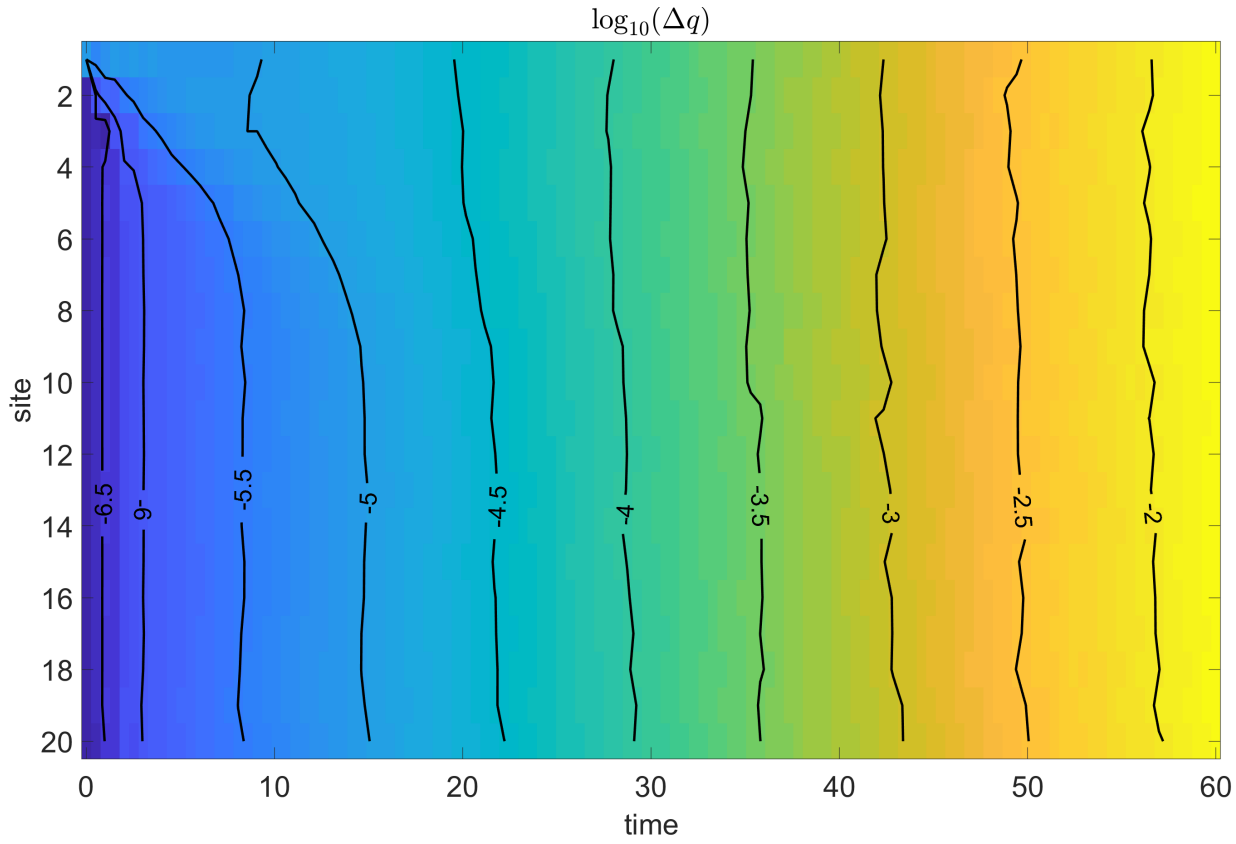

Figure 5.3: $\log_{10} \Delta q_r(t)$ for $N = 20$, $\epsilon = 10^{-5}$, $\Omega_1 = \Omega_2 = 1$, and $\Omega_3 = 2$. The labeled black lines are contours of constant $\log_{10} \Delta q$. Early time ballistic growth is visible in the upper left corner while at later times the system exhibits spatially uniform exponential growth in time.

modes of the chain. Hence, the propagation of any perturbation is a superposition of the motion due to the local Ω_1 terms and the special dynamics of the uniform mode. Since the local terms cannot induce non-local perturbations, we may focus on the dynamics of the uniform mode. The uniform mode's equation of motion is $\frac{d^2Q}{dt^2} = -\sqrt{N}\Omega_2^2 Q$ with solution

$$Q(t) = Q(0)\cos\left(N^{\frac{1}{4}}\Omega_2 t\right) + \frac{\frac{dQ}{dt}(0)}{N^{\frac{1}{4}}\Omega_2}\sin\left(N^{\frac{1}{4}}\Omega_2 t\right). \tag{5.14}$$

A localized perturbation on site 1 with zero initial time derivative can be written as $\delta\vec{\mathbf{q}}(0) = \epsilon\left([\hat{\mathbf{e}}_1 - \hat{\mathbf{u}}_0] + \hat{\mathbf{u}}_0\right)$, where $\hat{\mathbf{u}}_0 = [1, \cdots, 1]^T/N$ represents the uniform mode, $\hat{\mathbf{e}}_1 = [1, 0, \cdots, 0]^T$, and $\hat{\mathbf{e}}_1 - \hat{\mathbf{u}}_0$ is orthogonal to the uniform mode. The orthogonal mode evolves in a local fashion, hence $\delta\vec{\mathbf{q}}(t) = \epsilon\left(\text{local piece} + \hat{\mathbf{u}}_0\cos\left(N^{\frac{1}{4}}\Omega_2 t\right)\right)$. For oscillators far from the initial local

perturbation, the dynamics is given by

$$\delta q_{r\gg 1}(t) = \frac{\epsilon}{N}\Big[\cos\Big(N^{\frac{1}{4}}\Omega_2 t\Big) - 1\Big]. \tag{5.15}$$

Thus, after a time $\pi/N^{\frac{1}{4}}\Omega_2$, any localized perturbation has spread to distant sites with amplitude ϵ/N.

The inclusion of V_4 renders the equations of motion non-linear and the system chaotic in at least part of the phase space. We leave a detailed study of the classical chaotic dynamics of this model to the future, but as can be seen in Fig. 5.3, a numerical solution of the equations of motion displays sensitivity to initial conditions.

The precise protocol is as follows. We compare the dynamics of two configurations, $\vec{\mathbf{q}}^{(1)}$ and $\vec{\mathbf{q}}^{(2)}$, averaged over many initial conditions. The initial condition of configuration one has each oscillator start at rest from a random amplitude drawn uniformly and independently from $[-1, 1]$. Configuration two is identical to configuration one except that $q_1^{(2)}(0) = q_1^{(1)}(0) + \epsilon$ for $\epsilon = 10^{-5}$. Both configurations are evolved in time and the difference $\Delta q_r(t) = |q_r^{(2)}(t) - q_r^{(1)}(t)|$ is computed and averaged over 4000 different initial conditions. Figure 5.3 shows this average of Δq_r for $N = 20$ with $\Omega_1 = 1$, $\Omega_2 = 1$, and $\Omega_3 = 2$. Because the system can generate an ϵ/N-sized perturbation on all sites in a short time, the subsequent uniform exponential growth implies that any local perturbation will become order one on all sites after a time $\sim \lambda^{-1} \log \frac{N}{\epsilon}$.

The above analysis corresponds to the classical limit of coupled quantum oscillators where some effective dimensionless Planck's constant vanishes, $\hbar_{\text{eff}} \to 0$. In the opposite limit of large N at fixed $\hbar_{\text{eff}}$, the dynamics of quantum OTOCs can be obtained from the corresponding classical Lyapunov growth up to a timescale of order $\log \frac{1}{\hbar_{\text{eff}}} \ll \log N$. At later times, one needs to consider fully quantum local dynamics. If one imagines breaking the system up into local clusters and if

each cluster can be viewed as a quantum chaotic system with random-matrix-like energy levels, a dynamical system not unlike the random circuit model above is obtained.

5.4 Chaos and level statistics

Having established fast scrambling in both the random circuit and the classical model, we now return to the quantum spin model of Eq. (5.2). We first examine whether such a model is chaotic, which is a necessary condition for it being fast scrambling. For the local Hamiltonian part, we consider the mixed-field Ising chain

$$\mathcal{H}_{\text{local}} = -J \sum_i Z_i Z_{i+1} - h_x \sum_i X_i - h_z \sum_i Z_i. \tag{5.16}$$

A standard approach to identify a transition from integrability to quantum chaos is based on a comparison of energy-level-spacing statistics with Poisson and Wigner-Dyson distributions. Another convenient metric is the average ratio of consecutive level spacings [331] $\langle r \rangle$, where $r = \min(r_n, 1/r_n)$, $r_n = \delta_n/\delta_{n-1}$, $\delta_n = E_n - E_{n-1}$, and E_n are the eigenvalues ordered such that $E_n \geq E_{n-1}$.

As was already suggested in Ref. [332] for a similar model, we find that the longitudinal field is unnecessary, and the full system can have Wigner-Dyson statistics even for $h_z = 0$, in which case $\mathcal{H}_{\text{local}}$ is integrable. The resulting Hamiltonian reads

$$\mathcal{H} = -J \sum_i Z_i Z_{i+1} - h_x \sum_i X_i - \frac{g}{\sqrt{N}} \sum_{i<j} Z_i Z_j. \tag{5.17}$$

Average adjacent-level-spacing ratio changes from $\langle r \rangle_{Pois} \approx 0.38$ for Poisson level statistics to $\langle r \rangle_{GOE} \approx 0.53$ for Wigner-Dyson level statistics in the Gaussian Orthogonal Ensemble (GOE) [331]. In the vicinity of $g \to 0$, $\langle r \rangle$ (see Fig. 5.4) shows proximity to Poisson statistics, while, for $|g| \gtrsim 0.25$, the level statistics agree with those of the GOE.

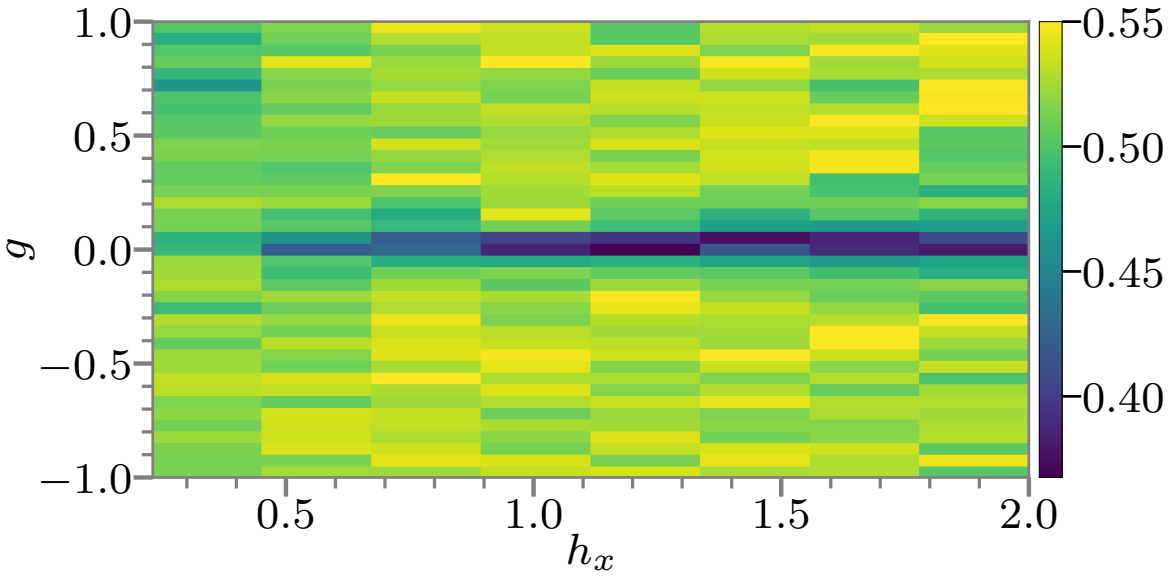

Figure 5.4: Average adjacent-level-spacing ratio $\langle r \rangle$ for the model in Eq. (5.17) with $J = 1$. Data corresponds to a system of $N = 15$ spins with periodic boundary conditions for fixed momentum and Z-reflection symmetry blocks of the Hamiltonian.

5.5 Out-of-time-order correlator and entanglement growth

We now study the dynamics of an OTOC and entanglement entropy in the spin chain. We consider the following OTOC

$$F(r,t) = \mathrm{Re}[\langle Z_1(t) Z_r Z_1(t) Z_r \rangle], \tag{5.18}$$

which is related to Eq. (5.1) by $\mathcal{C}(r,t) = 1 - F(r,t)$. The expectation value is evaluated in a Haar-random pure state, which approximates the infinite-temperature OTOC, but enables us to reach larger systems sizes [333].

In Fig. 5.5(a), we show the OTOC for an open chain of $N = 20$ spins for both the local model, governed by $\mathcal{H}_{\text{local}}$ only, and the non-local model in Eq. (5.17), which includes the global interaction. In the local case, the OTOC spreads ballistically, forming a linear light cone. In

contrast, in the non-local case, the spreading is super-ballistic and $F(r \gg 1, t)$ is approximately independent of r, as expected for a fast scrambler. As we discussed in the context of the classical model, a necessary condition for fast scrambling is that, before the onset of exponential growth, the decay of correlations with N should be at most algebraic ($\mathcal{C} \propto N^{-\alpha}$) and not exponential. In Fig. 5.5(b), we verify that this is the case for the non-local model, showing that $\mathcal{C} \propto N^{-1}$ between the two ends of the chain after a fixed time.

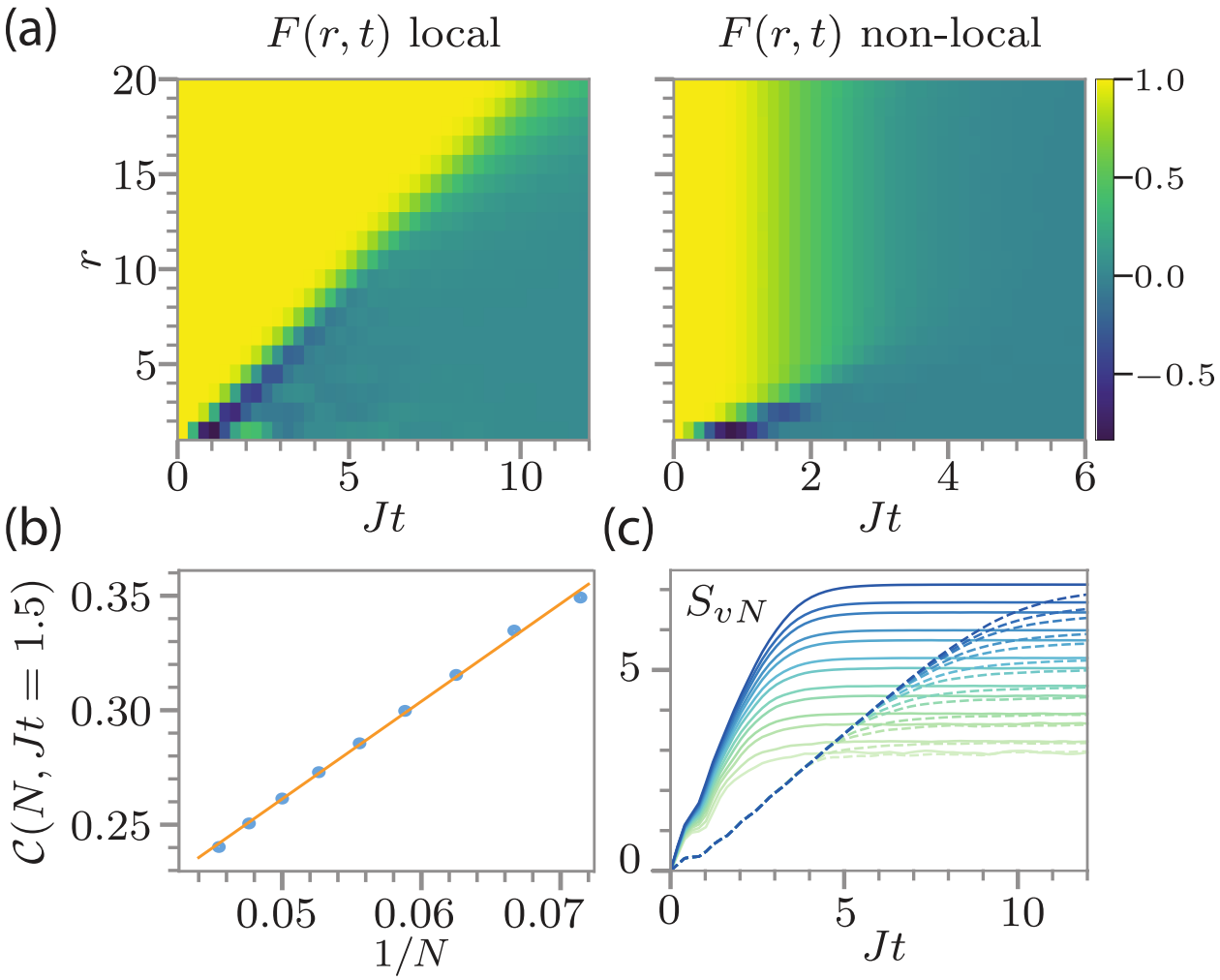

Figure 5.5: (a) Time evolution of the OTOC for the (left) local and (right) non-local models. (b) $1 - F(N, t)$ after a fixed evolution time for the non-local model (for different system sizes N), showing a linear dependence on $1/N$. The orange line is a linear fit. (c) Half-cut entanglement-entropy growth starting from the $+\hat{\mathbf{y}}$ state for local (dashed) and non-local (solid) models. The color indicates the system size, starting from $N = 10$ (light green) until $N = 22$ (dark blue). For all plots, $J = 1, h_x = 1.05$ and $h_z = 0.5, g = 0$ ($h_z = 0, g = -1$) for the local (non-local) models.

Figure 5.5(c) shows the half-cut entanglement entropy following a quench starting from the $+\hat{y}$ state for both models. For the local model, the entanglement grows linearly in time before saturating, whereas the non-local model shows a significant speed up. Moreover, in the non-local model, the growth rate clearly increases with the system size, further supporting our claim.

5.6 Experimental realization

The Hamiltonian in Eq. (5.17), and many variations of it, can be experimentally realized in a variety of platforms. A natural realization is with Rydberg dressing of neutral atoms [334–337]. The spin can be encoded in two ground states with one of them dressed to two Rydberg states such that one of the Rydberg states leads to all-to-all interactions and the second to nearest-neighbor interactions. Other similar spin models can be realized with cavity-QED setups, using photon-mediated all-to-all interactions [74, 75, 338, 339] of the XX or XXZ-Heisenberg form [313, 315] together with nearest-neighbor interactions achieved by Rydberg-dressing one of the grounds states [79, 340]. Other possibilities include a chain of coupled superconducting qubits, with all-to-all flip-flop interactions mediated via a common bus [341–343] or trapped ions [63–66, 344].

5.7 Conclusion and outlook

In this Chapter, we argued that a single global interaction together with local chaotic dynamics is sufficient to give rise to fast scrambling. While fast scrambling is intrinsically difficult to study numerically, our numerical evidence, together with the semi-classical analysis and the exactly solvable random circuit, provide a compelling argument in favor of our claim. Our models do not require disordered or inhomogeneous couplings and are within reach of current state-of-the-

art quantum simulators. Thus, an experimental implementation of the spin model could test our claims on much larger systems sizes, something that may very well be impossible to do on a classical computer. This can pave the way towards experimental investigations of aspects of quantum gravity.

Future theoretical work may include a more systematic analysis of the N-dependence of various timescales, e.g. for entanglement growth, and of the behaviour of the OTOC at low temperatures. It is also interesting to investigate whether similar conclusions can be reached without perfectly uniform global interactions, for example with power-law decaying interactions.

Chapter 6: Quench Dynamics of a Fermi Gas with Strong Non-Local Interactions

6.1 Introduction

Ultracold gases are a versatile platform for studying quantum many-body physics [345]. The ability to engineer and control the interactions in these systems has played an important role in observing novel phases of matter including crossover fermionic superfluids [346] and dipolar supersolids [347–349] and in studying out-of-equilibrium dynamical processes such as thermalization [350]. Recent efforts have focused on degenerate quantum gases with long-range interactions including those of magnetic atoms [347, 350–352] and polar molecules [353, 354]. These systems may be distinguished from other quantum platforms with long-range interactions including ions [25, 355], Rydberg atoms [23], polar molecules in optical tweezers [356, 357] and atoms in optical cavities [72], in that the particles are itinerant. This can lead to an interesting interplay between interactions, kinetic energy and quantum statistics. Rydberg dressing has been proposed as an alternative route to realize quantum gases with tunable long-range interactions [336, 358, 359]. Experimental demonstrations of Rydberg dressing [360–369] have been performed with localized atoms or quantum gases of heavy atoms where observation of motional effects has been elusive.

However, the combination of motion and Rydberg dressing can lead to novel phenomena and

shed new light on the many-body physics of spinless and spinful fermionic systems with power-law interactions. In 1D, Rydberg dressing leads to quantum liquids with qualitatively new features relative to the Tomonaga-Luttinger liquid paradigm [370]. In 2D, topological Mott insulators can be emulated by placing atoms on a Lieb lattice [371]. Compared to contact or on-site interactions, the long-range interactions between Rydberg-dressed atoms makes it easier to achieve the low filling factors required for quantum Hall states [335, 372]. The interplay between hole motion and antiferromagnetism—believed to be at the heart of high-temperature superconductivity—can be studied in Rydberg-dressed atomic lattices emulating the $t-J_z$ model [373]. In 3D, one can achieve exotic topological density waves [374], topological superfluids [375], and metallic quantum solid phases [376].

Here we investigate Rydberg dressing of lithium-6, a light fermionic atom. Its fast tunneling in an optical lattice allows us to study the quench dynamics of itinerant fermions with strong, purely off-site interactions.

Atoms in a quantum gas resonantly coupled to a Rydberg state experience strong van der Waals interactions many orders of magnitude larger than their kinetic energy for typical interatomic spacings, hindering access to the interesting regime where the two energy scales compete. At the same time, the population of atoms in the Rydberg state decays on a timescale of tens of microseconds, short compared to millisecond motional timescales. Rydberg dressing addresses both of these issues. Using an off-resonant coupling, the atoms are prepared in a laser-dressed eigenstate $|g_{\mathrm{dr}}\rangle \approx |g\rangle + \beta\,|r\rangle$ of predominant ground state ($|g\rangle$) character and a small Rydberg ($|r\rangle$) admixture, where $\beta = \frac{\Omega}{2\Delta} \ll 1$, Ω is the coupling strength, and Δ is the laser detuning from the transition frequency. This enhances the lifetime of the dressed atom by a factor of $1/\beta^2$ relative to the bare Rydberg state lifetime. On the other hand, the interaction between two atoms a distance

r apart is reduced in strength and can be approximately described by a tunable softcore potential $V(r) = V_{\text{max}}/(r^6 + r_c^6)$ with strength $V_{\text{max}} \sim \beta^3\Omega$ and range $r_c \sim (|C_6/2\Delta|)^{1/6}$, where C_6 is the van der Waals coefficient for the Rydberg-Rydberg interaction. Early experiments with 3D quantum gases were limited by rapid collective atom loss attributed to a blackbody-induced avalanche dephasing effect [360–362, 366]. Nevertheless, Rydberg dressing has been successfully used to entangle atoms in optical tweezers [363], perform electrometry in bulk gases [368], and study spin dynamics [364, 367, 369].

In this Chapter, we report on the single-photon Rydberg dressing of a 2D ^{6}Li Fermi gas in an optical lattice in the presence of tunneling. This results in a lattice gas of fermions with strong, non-local interactions. We characterize the interaction potential using many-body Ramsey interferometry [364]. A careful study of the lifetime of spin-polarized gases shows different behavior compared to previous Rydberg dressing realizations, with the lifetime depending strongly on the density but not on the atom number at fixed density. We also observe that the presence of tunneling in the system has no effect on the lifetime. Finally, we use this platform to realize a 2D coupled-chain $t-V$ model consisting of interaction-coupled chains and study the short-time quench dynamics of charge-density wave states, finding that the strong attractive interactions inhibit the motion of the atoms.

Theoretical studies of the 1D $t - V$ model [377, 378] have shown that it can exhibit Hilbert-space fragmentation (HSF) [379, 380], in which dynamical constraints "shatter" the Hilbert space into exponentially many disconnected subspaces. Like many-body localization (MBL) [381, 382] and quantum many-body scars [383, 384], HSF is a mechanism whereby isolated quantum systems can fail to reach thermal equilibrium after a quantum quench [385]. In the $t-V$ model, HSF arises in the limit of strong interactions, where the number of "bond" excitations, i.e., nearest-neighbor

pairs of fermions, joins the total fermion number as a conserved quantity. Our mixed-dimensional $t - V$ model inherits properties of the 1D version, including the HSF in the limit $t/V \to 0$. Our quench results demonstrate experimentally how HSF impacts the short-time relaxation dynamics for nonzero t/V.

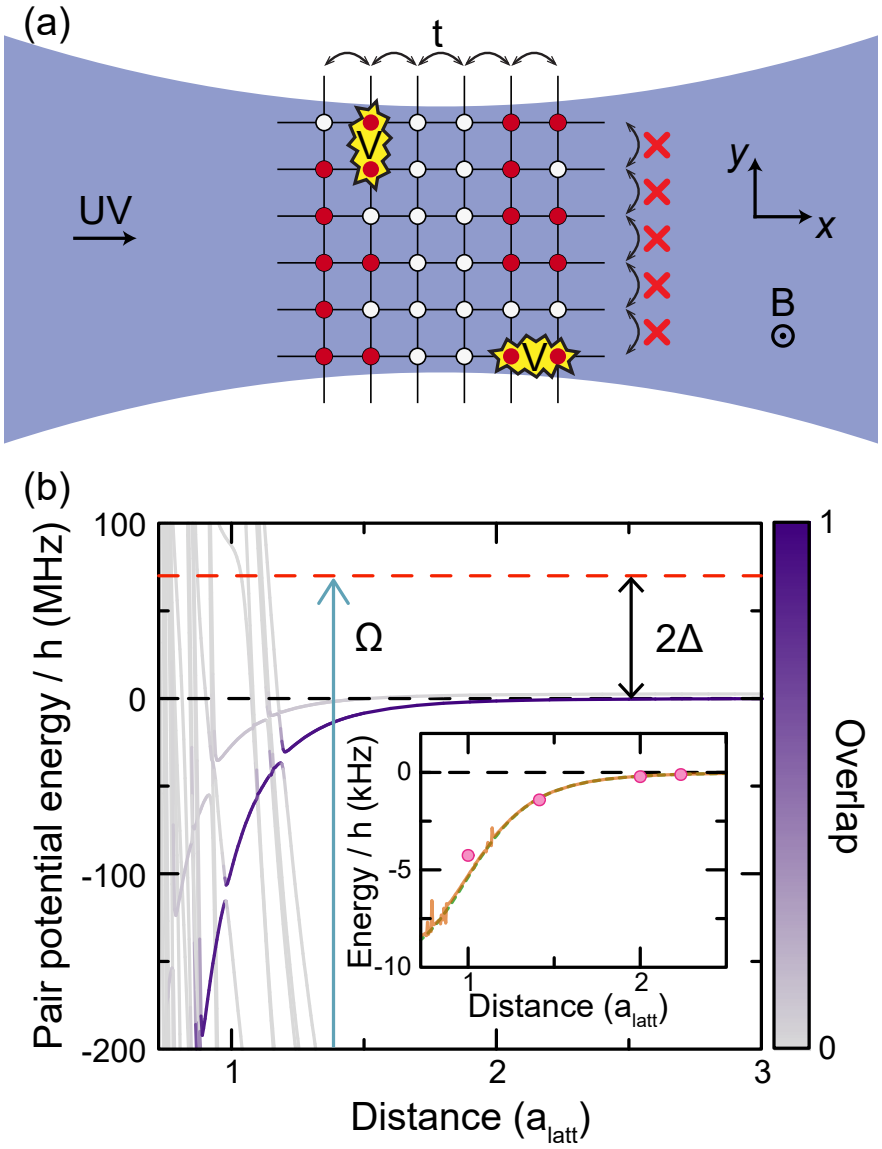

Figure 6.1: Realization of a $t-V$ model with Rydberg dressing. (a) The Rydberg dressing beam propagates along the x-direction of the lattice, effectively decoupling 1D chains in the y-direction due to a differential light shift. Hopping of fermions (red dots) along the x-direction is unaffected. Interactions are isotropic. (b) ^{6}Li pair potentials for dressing to the state $|28P, m_l = 0, m_s = -1/2\rangle$ calculated using [386]. The color of the lines represents the overlap with the target pair-state ($|28P, 0, -1/2\rangle \otimes |28P, 0, -1/2\rangle$) coupled via the laser with Rabi coupling Ω and detuning Δ from the target state. Inset: Calculated dressed potential for $\Omega = 2\pi \times 7.66\,\mathrm{MHz}$ and $\Delta = 2\pi \times 35\,\mathrm{MHz}$ taking into account the overlaps to all pair potentials (orange solid line). The dashed green line represents the expected dressed potential for a simple van der Waals potential with $C_6 = h \times 90.19\,\mathrm{MHz}\,\mathrm{a}_{\mathrm{latt}}^6$. Pink points are the interaction at each lattice distance taking into account the wavefunction spread of the atoms.

6.2 Experimental system and theoretical model

Our system consists of a degenerate Fermi gas of ^{6}Li atoms in a square optical lattice of spacing $a_{\text{latt}} = 752\,\text{nm}$ (Fig. 6.1a) [387]. We apply a $591.8(3)\,\text{G}$ [1] magnetic field perpendicular to the 2D system. We load spin-polarized gases prepared in a state that may be labeled at high fields as $|nl, m_l, m_s, m_I\rangle = |2S, 0, -1/2, 1\rangle = |1\rangle$, or alternatively $|2S, 0, -1/2, -1\rangle = |3\rangle$ depending on the measurement. We have control over the initial density profile by employing a spatial light modulator. Using a $231\,\text{nm}$ laser beam with linear polarization parallel to the magnetic field and propagating along the lattice x-direction, we couple the ground state atoms to the $|28P, 0, -1/2\rangle$ Rydberg state (Appendix E.1). By tuning the intensity and the detuning of the dressing light [2], we have real-time control over the isotropic soft-core interaction potential between the atoms in the gas (Fig. 6.1b).

The lattice system is described by a single-band spinless fermion Hamiltonian

$$\hat{H} = -t \sum_{\langle i,j \rangle} (\hat{c}_i^\dagger \hat{c}_j + \text{h.c.}) + \sum_{i \neq j} \frac{V_{ij}}{2} \hat{n}_i \hat{n}_j + \sum_i \delta_i \hat{n}_i, \tag{6.1}$$

where t is a tunneling matrix element, V_{ij} is the off-site interaction [Eq. (E.3)) and Fig. 6.1b(inset)] and δ_i is the potential due to single-particle light shifts contributed by the lattice and Rydberg dressing beams. Since our dressing beam is tightly focused with a waist of $16.1(4)\,^-\text{m}$, the change in δ between rows in the y-direction, which is orthogonal to the beam propagation axis, is much larger than t (for typical experiments presented in Section 6.4, the minimum change in δ between rows is $> 3t$ near the intensity maximum of the Rydberg dressing beam). On the other hand,

[1] $1\,\text{Gauss} = 1 \times 10^{-4}\,\text{Tesla}$

[2] The laser is locked to an ultralow expansion glass cavity and we can set the detuning with an uncertainty of $\sim 2\pi \times 200\,\text{kHz}$ by referencing to resonant blowing of a sparse system at very low intensity which is limited by the linewidth of the laser.

because of the large Rayleigh range of the beam ($\sim 3.5\,\mathrm{mm}$), the variation of δ along the beam propagation direction (x-direction) is negligible. To first approximation, we drop the light shift term and the hopping along the y-direction. Thus, we can rewrite our Hamiltonian as a coupled-chain $t-V$ model of the form

$$\hat{H} = -t \sum_{\langle i,j \rangle_x} (\hat{c}_i^\dagger \hat{c}_j + \text{h.c.}) + \sum_{i \neq j} \frac{V_{ij}}{2} \hat{n}_i \hat{n}_j. \tag{6.2}$$

6.3 Characterization of the system

6.3.1 Rydberg-dressed interaction potentials

In order to characterize the Rydberg dressing interaction potentials, we perform many-body Ramsey interferometry between states $|1\rangle$ and $|2\rangle = |2S, 0, -1/2, 0\rangle$ following the procedure introduced in Ref. [364]. Starting from a spin-polarized band insulator of atoms prepared in state $|1\rangle$ in a deep lattice that suppresses tunneling, a $\pi/2$ radiofrequency pulse prepares a superposition of state $|1\rangle$ and $|2\rangle$, which acquire a differential phase during a subsequent evolution for time T in the presence of the dressing light. Unlike Ref. [364], the splitting between the hyperfine ground-states of ^{6}Li is comparable to the detuning Δ of the dressing laser (Fig. 6.2a), and both states are significantly dressed by the light (App. E.2). First, we obtain the spatial profile of the Rabi coupling strength $\Omega(i,j)$ by measuring the population of $|2\rangle$ after a $\pi/2 - T - \pi/2$ pulse sequence using a detuning $\Delta = 2\pi \times 100\,\mathrm{MHz}$. The large detuning is chosen so that the interactions, whose strength scales as $1/\Delta^3$, are negligible, while the single-particle light shifts that scale as $1/\Delta$ lead to a large differential phase during the evolution. From these measurements, we extract the waist of the beam ($16.1(4)\,^-\mathrm{m}$) and measure Rabi couplings up to $\Omega = 2\pi \times 9.48(8)\,\mathrm{MHz}$ (Fig. 6.2b). The

measured spatial profile of the Ramsey fringe frequency confirms the rapid variation of δ_i along the y-direction, while no variation of δ_i is observed along the x-direction within the statistical uncertainty of the measurement (~ 1 kHz).

To probe interactions in the system, we switch to a smaller detuning $\Delta = 2\pi \times 35\,\mathrm{MHz}$. We measure density correlations of state $|1\rangle$ ($C(\mathbf{r}) = \langle n_1(\mathbf{r}) n_1(0)\rangle - \langle n_1(\mathbf{r})\rangle \langle n_1(0)\rangle$) after a spin-echo pulse sequence ($\pi/2 - T - \pi - T - \pi/2$) which eliminates differential phases due to the light shift. Fig. 6.2c shows the measured correlations after different evolution times T compared to the theoretical expectation (Appendix E.3). Fig. 6.2d depicts the evolution of the nearest-neighbor and next-nearest-neighbor correlations with the correlation offset $C(\infty)$ subtracted. This offset is attributed to correlated atom number fluctuations in the images [364]. We find good agreement with the theoretical model, which predicts a nearest-neighbor (next-nearest-neighbor) attractive interaction $|V_{10}| = h\times$4.2(2) kHz ($|V_{11}| = h\times$1.37(6) kHz) (Fig. 6.1b)

6.3.2 Lifetime

To probe coherent many-body physics in our system, the lifetime τ of the sample has to be larger than the interaction and tunneling times. Atoms resonantly excited to a Rydberg state are lost from our system on a timescale of tens of microseconds for several reasons: photon recoils due to spontaneous emission and large forces due to anti-trapping optical potentials and due to interactions with other Rydberg atoms. Due to its Rydberg admixture, an isolated dressed atom decays with a lifetime $\tau_{\text{eff}} = \tau_0/\beta^2$, where τ_0 is the lifetime of the Rydberg state determined by radiative and blackbody-driven transitions to other states. Previous experiments with frozen 2D and 3D systems have observed much shorter lifetimes than τ_{eff} [360–362, 364, 366]. A simplified model used to

explain these experiments considers a blackbody-driven decay of the dressed state to a pure Rydberg state of opposite parity. The first such contaminant appears in the system on a timescale $\tau_c = \tau_{\text{BB}}/(N\beta^2)$ where τ_{BB} is the blackbody lifetime of the Rydberg state and N is the number of atoms in the system. This atom interacts with other dressed atoms through resonant state-exchange characterized by a C_3 coefficient, broadening the Rydberg line. In particular, other atoms at a certain facilitation radius $(|C_3/\Delta|)^{1/3}$ will be resonantly excited, leading to avalanche loss of all the atoms from the trap. Experiments in 2D have indeed observed a collective lifetime close to τ_c and a bimodal atom number distribution in lifetime measurements [364]. We have not observed such bimodality in our 2D systems, and the lifetime does not depend strongly on N at fixed density (Appendix E.4). In this regard, our 2D ^{6}Li experiments are closer to ^{87}Rb experiments with 1D chains where the avalanche mechanism is suppressed to some extent [367].

The atom number decay in a frozen system of 7 by 7 sites is shown in Fig. 6.3a. The decay is not exponential, indicating a density-dependent lifetime which we extract by fitting different sections of the decay curve. For dressing to $|28P\rangle$, $\tau_0 = 30.5\,\mu$s [388]. We measured the density-dependent lifetime for $\Omega = 2\pi \times 9.25(8)$ MHz at three different detunings, $\Delta = 2\pi \times (30, 40, 60)$ MHz (Fig. 6.3b). Around half-filling, the collective lifetime is $\sim 0.3\tau_{\text{eff}}$ for $\Delta = 2\pi \times 30$ MHz and approaches τ_{eff} for the smallest densities ($n \sim 0.1$). For comparison, perfect avalanche loss would predict $\tau_c = 0.08\tau_{\text{eff}}$.

Next, we measure the lifetime of the dressed gas in the presence of tunneling, which has been a topic of theoretical debate [389, 390]. We measure the density-dependent lifetime for different lattice depths, spanning the frozen gas regime to a tunneling of 1.7 kHz (Fig. 6.3c). We do not observe any change of the lifetime with tunneling. A potential concern in this measurement is that the tunneling along the x-direction may be suppressed by uncontrolled disorder in δ_i. We rule this

out by preparing a sparse strip of atoms and observing its tunneling dynamics. As expected for a clean dressed system, the tunneling dynamics along the x-direction is almost identical to the case without the dressing light, while the dynamics is frozen along the y-direction (Fig. 6.3c inset). Combining the results of our interferometry and lifetime measurements, we achieve a lifetime of several interaction times measured by the figure of merit $V_{10}\tau/\hbar \sim 20$ [367] for a mobile system with $n = 0.5$.

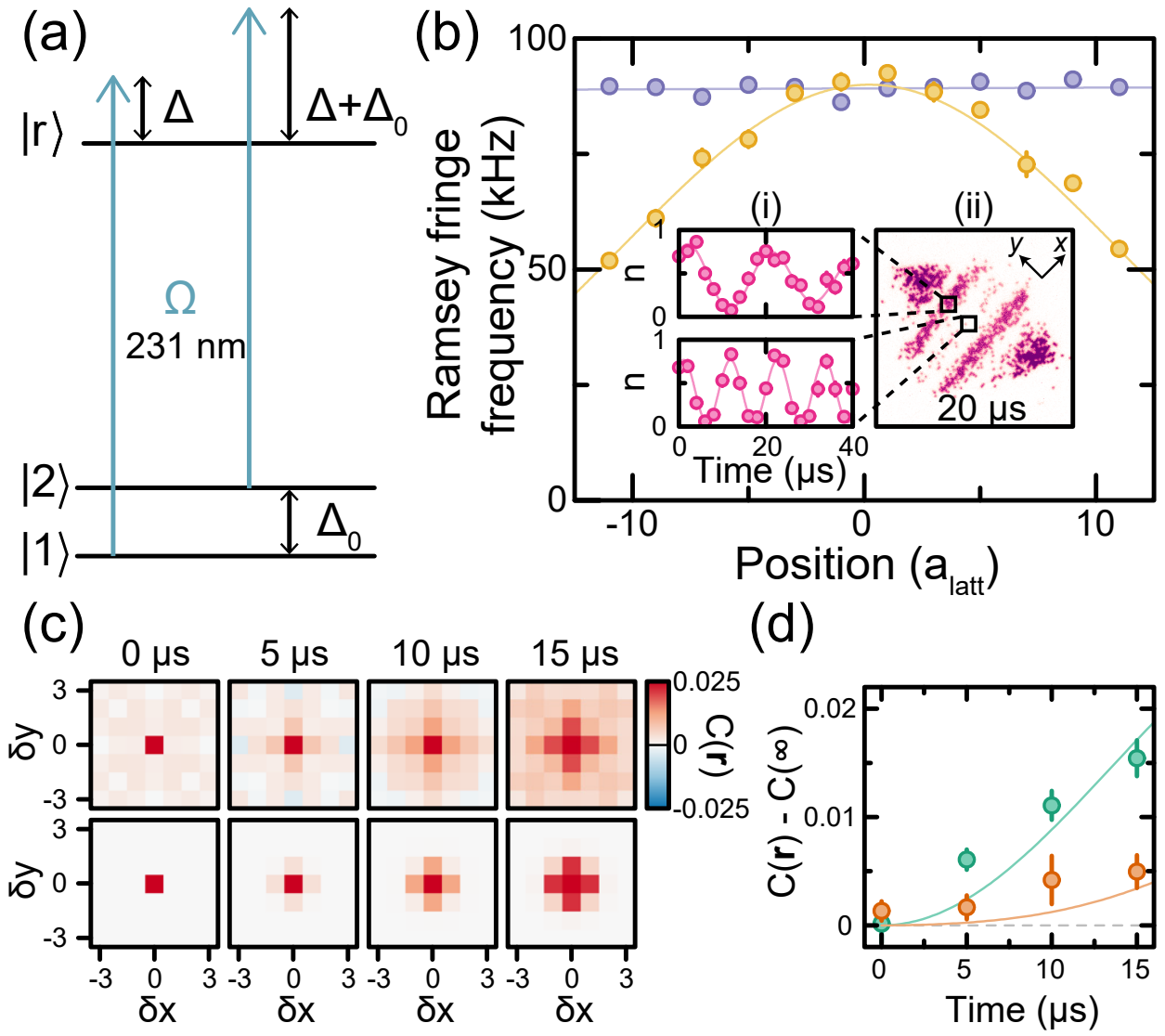

Figure 6.2: Measuring Rydberg dressed interactions with many-body Ramsey interferometry. (a) Energy level diagram for ^{6}Li showing that the dressing of the other hyperfine ground state cannot be ignored. Here $\Delta/2\pi$ is varied between 30 MHz and 100 MHz while $\Delta_0/2\pi = 75.806(1)$ MHz. (b) Ramsey fringe frequency measured at a detuning of $\Delta = 2\pi \times 100$ MHz at different positions in the cloud. The frequency is almost constant along the propagation direction of the beam (purple). In the transverse direction (yellow), it varies rapidly as expected for a tightly focused Gaussian beam. Insets: (i) Ramsey oscillations at two representative positions in the cloud. (ii) Sample image of one spin state in the cloud at $T = 20$ s. (c) Spin correlations for different spin-echo pulse times at $\Omega = 2\pi \times 7.66(7)$ MHz and $\Delta = 2\pi \times 35$ MHz. Measurement (top) and theoretical expectation (bottom). (d) Nearest (green) and next-nearest (orange) neighbor correlations after subtracting $C(\infty)$. Lines correspond to the expected correlations. Experimental error bars correspond to standard error of the mean.

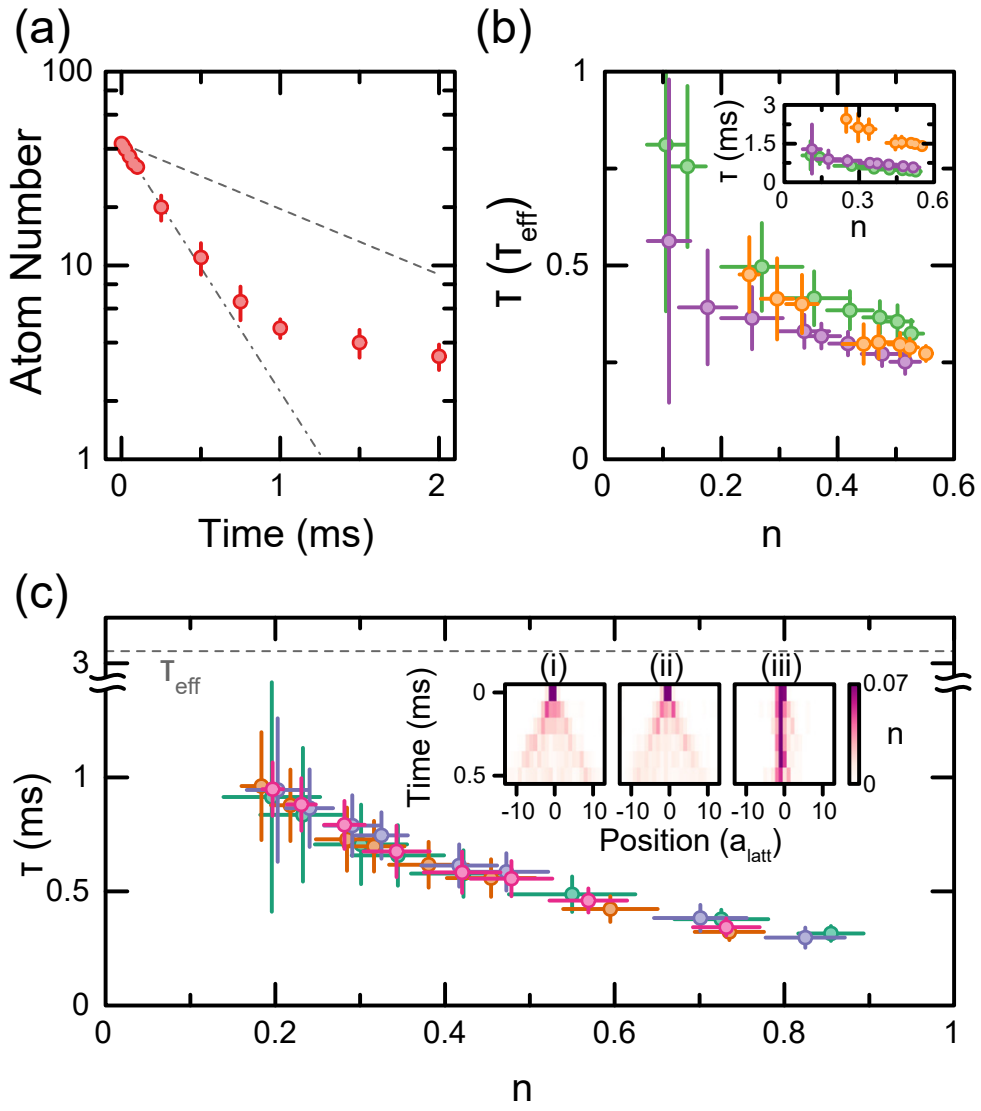

Figure 6.3: Lifetime of itinerant Rydberg dressed fermions. (a) Atom number vs. dressing time for a frozen gas. The red circles correspond to measurements on a system of 7 by 7 sites. Dashed-dotted line corresponds to an exponential fit to the first 5 data points and dashed line corresponds to the expected single-particle dressed lifetime τ_{eff}. (b) Measured lifetime in a frozen gas in units of τ_{eff} vs. the initial density for $\Omega = 2\pi \times 9.25(8)\,\text{MHz}$ and $\Delta = 2\pi \times (30\,(\text{green}), 40\,(\text{purple}), 60\,(\text{orange}))\,\text{MHz}$. Inset: Same measurements in units of ms. (c) Lifetime vs. initial density for different tunnelings: $0.01\,\text{kHz}$ (green), $0.25\,\text{kHz}$ (purple), $1.0\,\text{kHz}$ (orange), and $1.7\,\text{kHz}$ (pink). The data is taken with $\Omega = 2\pi \times 6.04(8)\,\text{MHz}$, $\Delta = 2\pi \times 30\,\text{MHz}$. Insets: (i) Tunneling dynamics of atoms sparsely initialized on a strip along the y-direction with no dressing light. From this data, we extract a tunneling rate $t = h \times 1.7\,\text{kHz}$. (ii) Same measurement in the presence of the dressing light. (iii) Same measurement in the presence of the dressing light but with the strip along the x-direction. Experimental error bars correspond to standard error of the mean.

6.4 Quench Dynamics

To probe the interplay of interactions and tunneling in our system, we use light patterned with a spatial light modulator to initialize the system in a charge density wave state of atoms in state $|3\rangle$. The initial density pattern approximates a square wave with period $\lambda = 4\,\mathrm{a_{latt}}$ and width $w = 7\,\mathrm{a_{latt}}$, with the average density oscillating between $n \sim 0$ and $n \sim 0.7$. (see Figs. 6.4a-b). Dynamics in a lattice with $t = h \times 1.7\,\mathrm{kHz}$ is initiated by suddenly turning off the patterning potential while keeping walls in the y-direction as in [391]. We average the density profiles over the non-hopping direction and observe a qualitative change in the dynamics as we increase V/t (here $V \equiv |V_{10}|$) from 0 to 2.9(2) (Fig. 6.4c). To emphasize the evolution of the pattern, we scale the data to account for atom loss during the evolution (Appendix E.5). In the non-interacting quench, we observe that the phase of the charge density wave inverts at a time $\sim \hbar/t$ as is expected for a coherent evolution [392]. For strong interactions, the decay of the charge density wave slows down and the system retains a memory of its initial state for longer times.

This can be understood as an interplay between two conservation laws: the intrinsic U(1) particle number ($\hat{N} = \sum_x \hat{n}_x$) conservation as well as an emergent conservation of the number of bonds $\hat{N}_b = \sum_x \hat{n}_x \hat{n}_{x+1}$. The latter becomes a conserved quantity when the longer range interactions are ignored, and in the limit of infinite V/t. States of the form $|...0011001100...\rangle$ along the hopping direction, which the imprinted density pattern attempts to approximate, would be completely frozen in the limit of infinite V/t [377]. For a large but finite V, moving a single atom (and hence breaking a bond) costs an energy of up to $3V$, which is energetically unfavorable, and hence leads to reduced relaxation dynamics.

To quantify the difference in the dynamics of the different quenches, we employ two different

methods. The first is to fit a sinusoid of the form $n(x,t) = A\sin(2\pi x/\lambda + \phi) + B$ to determine the amplitude of the wave relative to its mean, A/B (Fig. 6.4d). The fit is restricted to $|x| \leq 6\,\mathrm{a_{latt}}$, and ϕ is fixed by the initial pattern. The second method is to calculate the autocorrelation function

$$\rho(t) = \frac{\mathrm{cov}_x(n(x,0), n(x,t))}{\text{œ}_x(n(x,0))\text{œ}_x(n(x,t))}, \tag{6.3}$$

where cov_x and σ_x are the covariance and the standard deviation respectively (Fig. 6.4e).

Further confirmation that the slower decay of the charge density waves is an interaction effect is obtained by varying the average density in the initial state. Fig. 6.5 shows these initial states and their time evolution for $V/t = 2.9(2)$. As the average density of the initial state is decreased, it approaches a "sparse" limit where the probability of having two neighboring atoms is negligible. In this regime, the system is effectively non-interacting and we recover the phase inversion during the evolution. Since these measurements are done at fixed power of the dressing light, they rule out disorder-induced localization as a mechanism for arresting the dynamics.

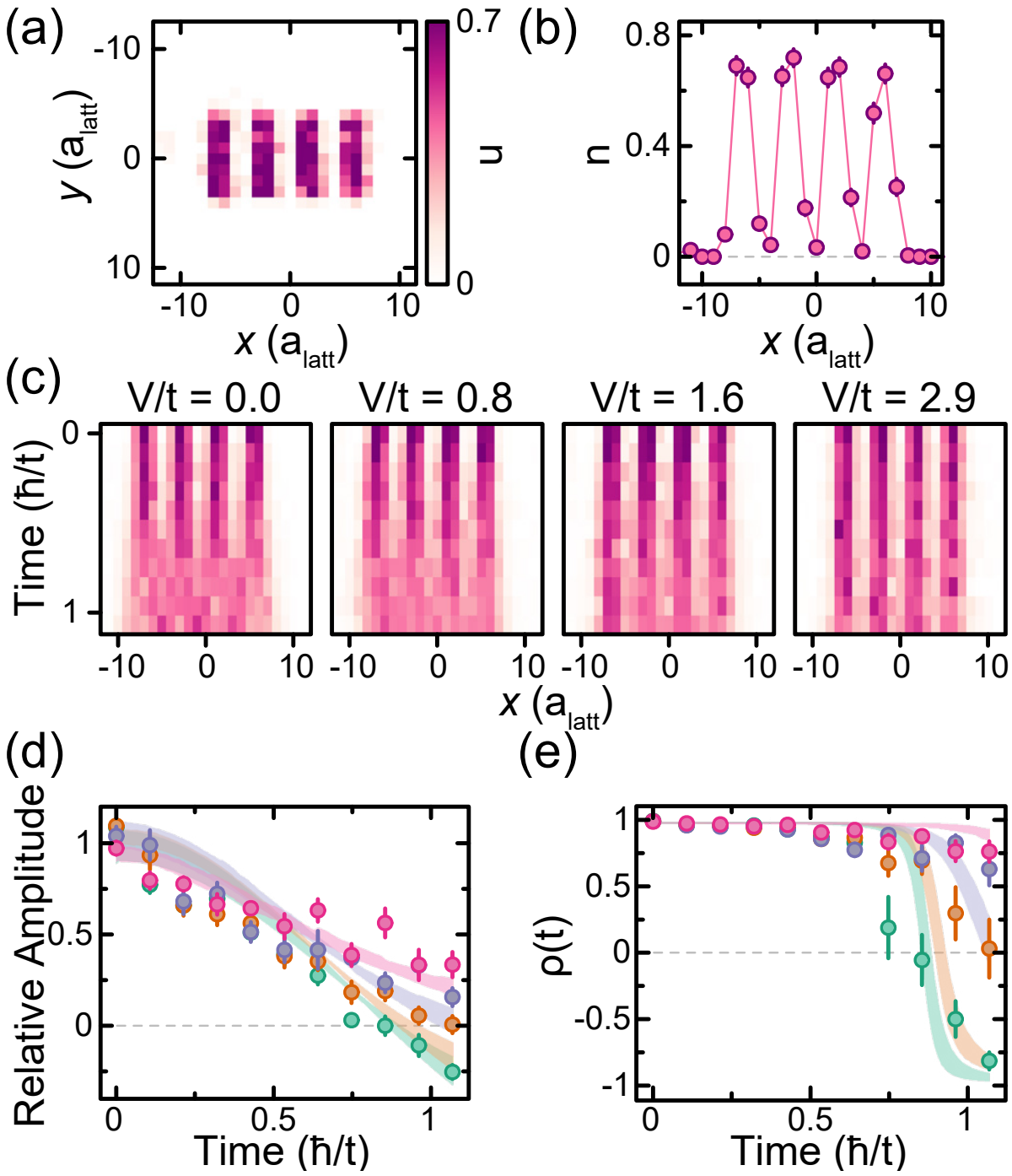

Figure 6.4: Interaction dependence of quench dynamics of a charge density wave. (a) Average initial state density profile for the quench measurements. (b) Density profile averaged along the y-direction of the initial state shown in (a). (c) Density profile time evolution for interactions $V/t = [0, 0.78(7), 1.61(8), 2.9(2)]$. Color scale is the same as in (a). (d) Fitted relative amplitude of density profile vs. time. Colors (green, orange, purple, and pink) correspond to the interactions in (c) from lowest to highest. (e) Autocorrelation function of the density pattern. Colors are same as in (d). Shaded curves correspond to numerical simulations. Experimental error bars correspond to standard error of the mean.

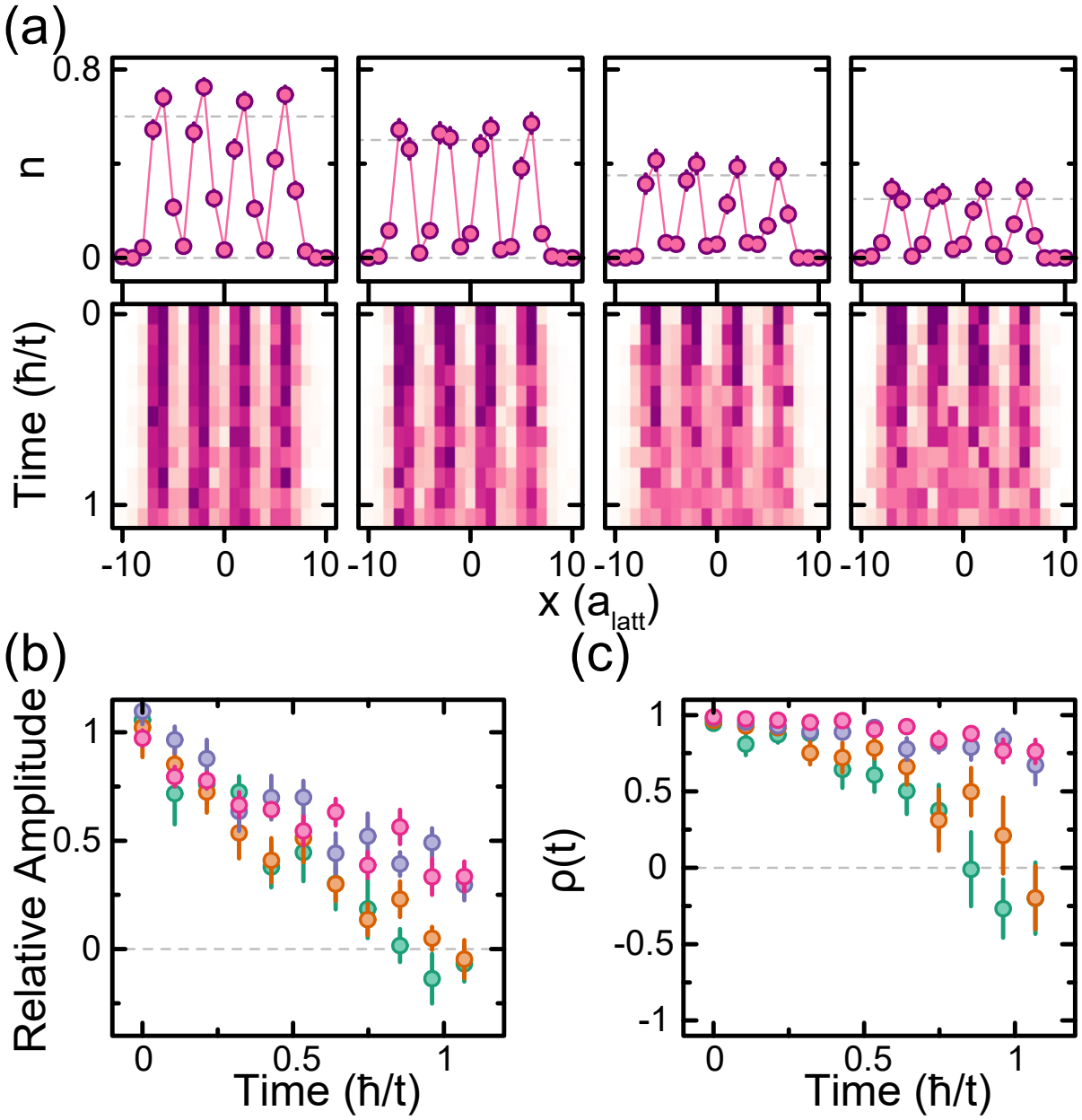

Figure 6.5: Density dependence of quench dynamics. (a) (top) Initial state density profiles. (bottom) Corresponding time evolution of each initial state for $V/t = 2.9(2)$. Colorbar is same as Fig. 6.4a with limits set by dotted lines on top panel. (b) Fitted relative amplitude of density profiles vs. time. Colors (green, orange, purple, and pink) correspond to the initial states in (a) from low to high density. (c) Autocorrelation function of the density pattern. Colors are same as in (b). Experimental error bars correspond to standard error of the mean.

6.5 Numerical simulations

We use exact diagonalization to simulate the quench dynamics of our experiment. As the simulation for the full experimental 2D system ($\sim 7 \times 21$) is computationally intractable, we compare instead to numerics on a 2×11 $t-V$ model with only nearest-neighbor interactions and no tunneling along the y-direction and find qualitative agreement with the measurements.

We account for atom loss during the experiment via a Lindblad master equation $\partial_t \hat{\rho} = -i(\hat{H}_{\text{eff}}\hat{\rho} - \hat{\rho}\hat{H}_{\text{eff}}^\dagger) + \Gamma \sum_i \hat{a}_i \hat{\rho} \hat{a}_i^\dagger$. Here, $\hat{H}_{\text{eff}} = \hat{H} - i\frac{\Gamma}{2}\hat{N}$ is the effective non-Hermitian Hamiltonian [$\hat{H}$ is the $t-V$ Hamiltonian from Eq. (6.2)] and the second term describes quantum jumps corresponding to atom loss with rate Γ. We solve the master equation using the quantum trajectory approach [36]. Note that the anti-Hermitian term in $\hat{H}_{\text{eff}}$ is a constant due to the particle number conservation, and hence it can be neglected since $\hat{H}_{\text{eff}}$ and $\hat{H}$ generate the same dynamics (up to the normalization, which only serves to determine the timings of the quantum jumps).

The initial state for each trajectory is sampled directly from the experimental data taken at $t = 0$. We pick a 2×9 region centered on 2 of the 4 density peaks from the experimental images (Fig. 6.4a). In order to reduce boundary effects, we add empty sites on each end of the chain. We average the resulting dynamics over the different trajectories, whose number is comparable to the number of experimental snapshots. Next, we analyze the averaged simulated dynamics using the same methods we use for the experimental data. Fig. 6.4 shows the comparison of the experiments with these numerical simulations. We find good qualitative agreement with this small 2D coupled-chain numerical model.

The 2D nature of the system is important for fully understanding the relaxation time-scales in our system. In particular, in a one-dimensional system, moving a single atom from the initial

"...00110011..." pattern (and hence breaking a bond) costs an energy V. However, in the coupled-chain $t-V$ model with isotropic interaction, breaking a bond now costs up to $3V$ for the idealized initial charge density wave state. We thus expect the 2D system to have slower relaxation rate compared to a 1D system with the same interaction strength.

To verify this, we perform additional numerical simulations on a single chain of 21 atoms. Similarly to our 2D simulation, we sample 1×19 arrays from the experimental snapshots at $t = 0$ and add empty sites at the ends. We find that the atoms spread quicker than they do in the ladder geometry and have worse agreement with the experimental results. Fig. 6.6 shows a comparison between the 1D and 2D coupled-chain numerical simulations on the one hand and the experimental data on the other. This comparison highlights the importance of the interchain interactions in order to fully understand our system.

The remaining discrepancy between some of the numerical and experimental results could be attributed to several factors. First, we are only able to simulate a smaller system than in the experiment. We expect that adding additional chains could further slow down the relaxation dynamics. Second, our modeling of the atom loss via a Lindblad master equation assumes that the decay rate is exponential. However, as we showed in Sec. 6.3.2, the decay rate is actually non-uniform in space and time, and depends on the density.

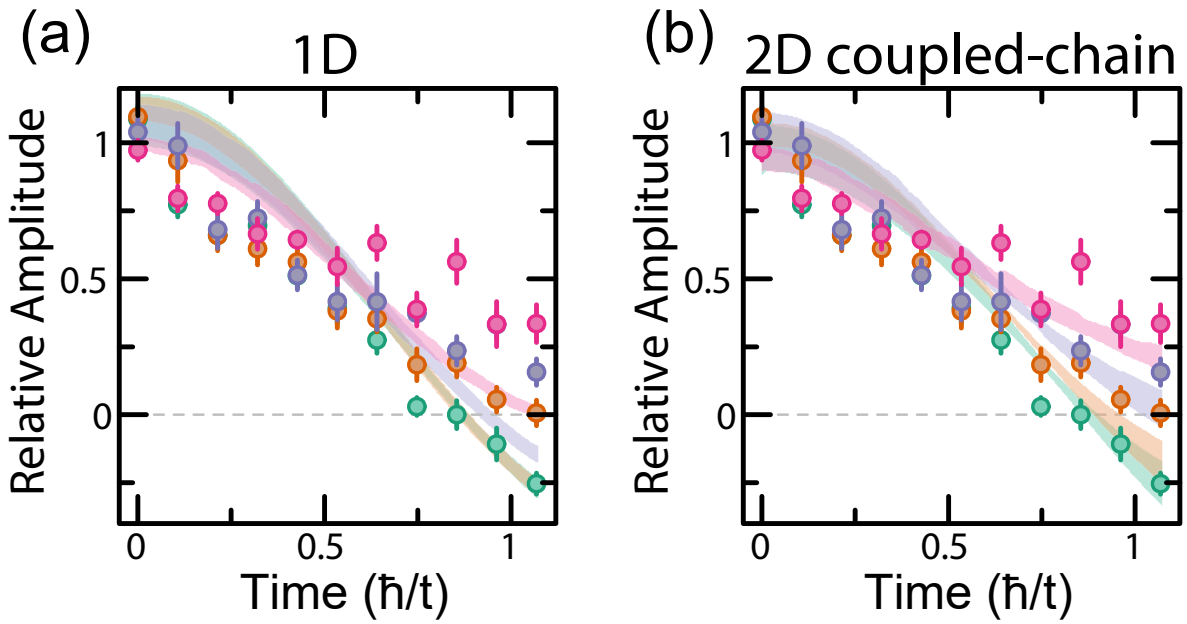

Figure 6.6: Role of interchain couplings in slowing down charge density wave relaxation. Numerical simulations of a $t-V$ model with tunneling t along only one direction and isotropic nearest-neighbor interactions V. (a) Fitted relative sinusoid amplitude to observed (circles) and calculated quench dynamics of 1×21 systems (shaded regions). The colors represent the different interaction strengths $V/t = [0\ (\text{green}), 0.78(7)\ (\text{orange}), 1.61(8)\ (\text{purple}), 2.9(2)\ (\text{pink})]$ explored in the experiment. (b) Same comparison as in (a) but for calculations done on 2×11 systems. This is Fig. 4d. Experimental error bars correspond to standard error of the mean.

6.6 Conclusions

Our results present a new frontier in quantum simulations of itinerant lattice models with strong off-site interactions. By working with larger r_c/a, spinless fermion models may be used to explore equilibrium phases such as topological Mott states [393] or cluster Luttinger liquid phases [370]. Moreover, the system considered in this Chapter provides a platform for the experimental realization of models prevalent in theoretical studies of non-equilibrium dynamics. For example, the 1D $t-V$ model can be mapped to the XXZ spin chain, which has long been studied in the context of many-body localization [394–396]. This model and variants thereof have also been proposed to harbor dynamical phases intermediate between full MBL and thermalization [397–399]. Our

work lays the foundation for future studies of such phenomena, as well as other non-equilibrium dynamical regimes including prethermalization [400]. Furthermore, the close spacing between the hyperfine ground states of ^{6}Li also opens the door for the simultaneous dressing of two spin states and the exploration of extended Fermi-Hubbard models.

The present experiment has allowed us to start probing coherent dynamics in $t - V$ models, which we plan to continue to explore especially upon improving the interaction-lifetime figure of merit. For example, for small but finite $t/|V|$, it is possible to access a complex hierarchy of timescales for quench dynamics that depends crucially on the initial state [378].

Our work motivates further theoretical and experimental exploration of the mixed-dimensional models in the context of both the non-equilibrium dynamics and ground-state physics [401] such as meson formation. Another promising direction based on the interplay of Rydberg-dressing and atomic motion is vibrational dressing [402, 403], non-destructive cooling [404], an exploration of multi-band physics, as well as the use of microwave-dressed Rydberg states, allowing for both attractive and repulsive dressed $1/r^3$ dipole-dipole interactions [70].

There are several possible approaches to improve the interaction-lifetime figure of merit. Enhancement of the Rabi coupling by over an order of magnitude may be achieved using a build-up cavity [405]. For a single-particle system, the figure of merit scales with Ω at fixed β, while further enhancement of the collective lifetime is expected in this regime due to shrinking facilitation radii for increasing Δ. Increasing Ω by a factor of 10 at fixed β leads to facilitation radii that are a factor of $10^{1/3}$ smaller. For almost all states coupled to by blackbody radiation, the facilitation radii become less than one site. If collective loss is completely inhibited, the combined effect is to enhance the figure of merit by a factor of ~ 30. The principal quantum number used in this experiment was chosen to keep the range of the interaction on the order of one site. Relaxing this constraint or

alternatively using a larger lattice spacing would allow using longer-lived Rydberg states at higher principal quantum number. Using electric fields to tune close to a Förster resonance results in deep potential wells that may be exploited to enhance the figure of merit by a factor of $|\Delta|/\Omega$ [69] and potentially allow us to achieve repulsive interactions. Finally, the single particle lifetime can be improved and the collective black-body induced atom loss may be completely eliminated by operating at cryogenic temperatures improving the figure of merit by a factor of ~ 6 for fixed dressing laser parameters.

Chapter 7: Nondestructive Cooling of an Atomic Quantum Register via State-Insensitive Rydberg Interactions

7.1 Introduction

In recent years, neutral atoms stored in individual traps [57–59, 406–408] have emerged as a powerful resource for quantum information and quantum technologies [367, 383, 409–412]. Considerable effort is currently being invested in developing neutral atom traps that are insensitive to the internal state of the atom [407, 413–415]. These so-called magic traps attempt to achieve what is naturally available with trapped ions, since the trapping of the latter relies on the net charge of the ion, and hence is independent of its internal electronic state. The magic trapping of neutral atoms reduces heating and dephasing associated with the fact that different electronic states may have different trapping potentials. Nevertheless, even with such magic trapping conditions, heating of the motional degrees of freedom of the atoms can occur because of, for example, the shaking of the atomic array due to laser intensity noise [416], mechanical forces from Rydberg interactions [23, 417, 418], or incoherent light scattering [419].

Such heating of the atomic motion, when combined with state-dependent Rydberg mediated gates, generally leads to reduced fidelities and loss of coherence, which is particularly problematic for long quantum simulations or computations [420–422]. It is therefore desirable to develop

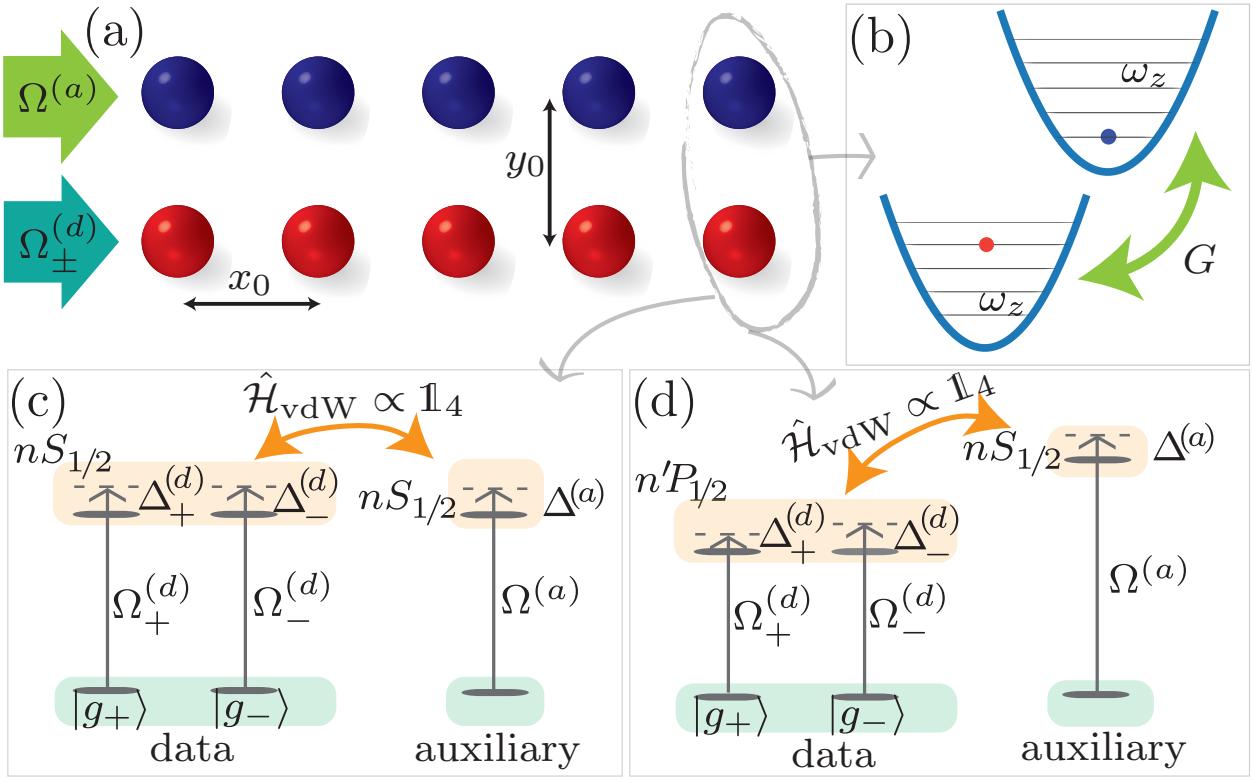

Figure 7.1: Schematic of the phonon-swap protocol. (a) For each data atom (red, bottom) we place another auxiliary atom (blue, top) at an equal distance y_0. We assume a 1D chain of data and auxiliary atoms, with a lattice spacing of x_0. (b) The Rydberg interactions give rise to effective coupling G between the vibrational modes of the data and auxiliary atoms. (c,d) Two schemes that lead to spin-insensitive interactions between the data and the auxiliary atoms: in (c), the ground states of all atoms are weakly coupled to Rydberg $S_{1/2}$ states. In (d), the data atoms are coupled to $n'P_{1/2}$ states and the auxiliary to $nS_{1/2}$, where $|n - n'| \gg 1$.

schemes to cool the atomic motion without destroying the quantum information stored in the internal states. The conventional laser cooling techniques [423–425] are not suitable for this task since they involve optical pumping which, in general, destroys the quantum information.

Several approaches for this problem have already been proposed in the past, from immersing the atomic lattice in a superfluid [426] to using cavity-assisted cooling [427]. It has also been shown that alkaline-earth atoms can be laser-cooled without destroying the quantum information provided it is stored in the nuclear spin [428].

In this Chapter, we introduce two schemes for achieving state-insensitive interactions between

neutral atoms, another natural and useful tool of trapped ions. We further show how to use these interactions to realize a state-preserving cooling procedure, inspired by sympathetic cooling of trapped ions [429, 430]. In contrast to the protocols in Refs. [426, 427], ours requires only ingredients and capabilities that are already present in many neutral atoms experiments: auxiliary atoms and Rydberg interactions.

The scenario we have in mind is the following: we assume one starts with a quantum data register composed of an array of N atoms, each in an individual trap, cooled to the vibrational ground state and optically pumped to a particular ground state. Each atom encodes a two-level system in its ground states. One then uses Rydberg interactions to perform a quantum computation or simulation, during which the atoms are heated. To cool the data register we introduce N auxiliary atoms, one for each data atom [see Fig. 7.1(a)], that have been precooled using any of the standard methods. The data and auxiliary atoms can then be coupled via Rydberg interactions, implementing a *phonon-swap* gate – a coherent exchange of vibrational quanta. A key requirement of this protocol is for the interactions between the auxiliary and data atoms to be insensitive to the internal state of the data atoms. Unlike the Coulomb interaction between ions which naturally satisfies this requirement, the Rydberg interactions between neutral atoms are inherently state-dependent. As we show in this Chapter, a careful choice of the Rydberg states can nevertheless satisfy this requirement.

Another requirement is that the phonon-swap interactions should not induce unwanted state-dependent couplings between the data atoms. In the first of our two schemes [see Fig. 7.1(c,d)], the interactions between any pair of atoms (data-data and data-auxiliary) are independent of the internal state. This scheme consists of pausing the quantum computation or simulation, performing the phonon-swap, and then resuming the computation or simulation. In the second scheme, the data

and auxiliary atoms are addressed separately, which allows one to design state-insensitive data-auxiliary interactions but tunable data-data interactions. As an example, we show how this can be used to implement the phonon-swap while simultaneously performing a quantum simulation of a spin model on the data atoms. Finally, for both of the above schemes, one can laser cool the auxiliary atoms during the phonon-swap. Due to the quantum Zeno effect [431], this has the additional advantage of preventing certain coherent heating mechanisms, such as those due to the Rydberg interactions, from taking place at all. We leave the detailed study of such a scheme for future work.

7.2 Phonon-swap for two atoms

Let us first consider the case of two atoms: a two-level data atom "d" and a single-level auxiliary atom "a". The two atoms are each trapped in a three-dimensional harmonic potential separated by a distance $\mathbf{r}$. In recent experiments [57, 423–425, 432, 433], the confinement along two directions (x, y) is often much stronger than along the third (z), i.e. the trap frequencies satisfy $\omega_x, \omega_y \gg \omega_z$. For simplicity, we focus on cooling the weakest direction (z). Cooling the two components perpendicular to the inter-atomic axis is a trivial generalization of this section. The third component [y direction in Fig. 7.1(a)] requires more care but can be cooled via an adiabatic protocol (see Appendix F.3).

The Hamiltonian consisting of both the vibrational and the internal degrees-of-freedom is ($\hbar = 1$) $\hat{\mathcal{H}} = \omega_z(\hat{d}^\dagger\hat{d} + \hat{a}^\dagger\hat{a}) + \hat{\mathcal{H}}_s + \hat{\mathcal{H}}_{\text{int}}(\mathbf{r})$, where $\hat{d}\,(\hat{a})$ is the phonon annihilation operator of the data (auxiliary) atom along the z direction; $\hat{\mathcal{H}}_s$ acts on the internal (spin) degree-of-freedom of the data atom, and $\hat{\mathcal{H}}_{\text{int}}(\mathbf{r})$ describes the interaction between the two atoms that, in principle, couples

motion and spin. Since we want to preserve the spin state of the data atom, the phonon dynamics should be decoupled from the spin, i.e. we want $\hat{\mathcal{H}}_{\text{int}} = \mathbb{1}_{\text{internal}} \otimes V(r)$ to be an identity operator on the internal states. As we later show, by weakly laser-dressing the ground states with Rydberg states, it is possible to obtain effective interactions of such form, where $V(r) = \frac{\mathcal{A}}{r^6+R_c^6}$ for coupling $\mathcal{A}$ and blockade radius R_c.

For now, let us assume these interactions and Taylor-expand them to second order in the small quantum fluctuations on top of the macroscopic separation r_0, which we assume to be along one of the strongly confined directions [Fig. 7.1(a)]. This gives rise to a quadratic Hamiltonian (Appendix F.2),

$$\hat{\mathcal{H}}_{\text{ph},2} = \omega_z(\hat{d}^\dagger\hat{d} + \hat{a}^\dagger\hat{a}) - \frac{G}{2}\left[(\hat{d}+\hat{d}^\dagger)^2 + (\hat{a}+\hat{a}^\dagger)^2\right] + G(\hat{d}+\hat{d}^\dagger)(\hat{a}+\hat{a}^\dagger), \tag{7.1}$$

where $G = \frac{3\mathcal{A}}{M\omega_z r_0^8}\frac{1}{[1+(R_c/r_0)^6]^2}$ is the phonon coupling strength and M is the atomic mass. In the regime where $\omega_z \gg G$, only the number-conserving terms are relevant, giving a "beam splitter" interaction (in the rotating frame) $\hat{\mathcal{H}}_{\text{ph},2} = G(\hat{a}^\dagger\hat{d} + \hat{d}^\dagger\hat{a})$. This Hamiltonian effectuates a state-transfer between the two vibrational modes in a time of $t_s = \frac{\pi}{2G}$, swapping the phonons of the data atom with those of the auxiliary atom. This cools the data atom down to the initial phonon occupancy of the auxiliary atom.

7.3 Phonon-swap for 1D chain

The discussed protocol can be easily generalized for an ensemble of atoms. We simply associate each data atom with a cold auxiliary atom. For concreteness, we consider a chain of data atoms with a lattice constant x_0, separated by a distance of y_0 from a chain of cold auxiliary atoms [Fig. 7.1(a)]. The many-body Hamiltonian is quadratic with approximate power-law decaying

hopping between the sites (Appendix F.4)

$$\hat{\mathcal{H}}_{\text{ph},1D} = \sum_{i\neq j} \frac{G}{\eta^8 |i-j|^8} (\hat{a}_i^\dagger \hat{a}_j + \hat{d}_i^\dagger \hat{d}_j) + \sum_{ij} \frac{G}{[\eta^2 (i-j)^2 + 1]^4} (\hat{a}_i \hat{d}_j^\dagger + \hat{a}_i^\dagger \hat{d}_j) \tag{7.2}$$

where $\eta \equiv \frac{x_0}{y_0}$. Here we defined G in terms of the smallest distance between a data atom and its auxiliary, i.e. y_0 (see Fig. 7.1). Clearly, as $\eta \to \infty$, it is sufficient to consider only the nearest-neighbor data-auxiliary interactions. In such a case, we recover the situation in the previous section: each data-auxiliary pair perfectly swaps their phonons after a time of $t_s = \frac{\pi}{2G}$. If we also take into account next-nearest-neighbor data-auxiliary interactions, we find (see Appendix F.4) that the average phonon occupancy of the data atoms is

$$\bar{n}_d(t) = \frac{\bar{n}_a(0) + \bar{n}_d(0)}{2} - \frac{\bar{n}_a(0) - \bar{n}_d(0)}{2} J_0\left[\frac{4Gt}{(1+\eta^2)^4}\right] \cos(2Gt), \tag{7.3}$$

where $\bar{n}_d(t)$ ($\bar{n}_a(t)$) is the average occupancy of data (auxiliary) atoms at time t and $J_0(z)$ is a Bessel function of the first kind. Equation (7.3) is quantitatively accurate (see Fig. 7.2) at short time-scales, when the effects of the long-range interactions are less important. As $\eta \to \infty$ we have $J_0 \to 1$ which reproduces the case of independent pair-wise phonon-swaps. Moreover, $t_s = \frac{\pi}{2G}$ is still the nearly optimal swap time (see Fig. 7.2) and even with $\eta = 1$ we can still achieve a high-efficiency swap. Assuming for simplicity that the auxiliary atoms are initially in the vibrational ground state, we obtain a swap efficiency of $1 - \frac{\bar{n}_d(t_s)}{\bar{n}_d(0)} = \frac{1}{2} + \frac{1}{2} J_0(\frac{\pi}{8}) \approx 98\,\%$. Furthermore, Eq. (7.3) remains qualitatively accurate even at longer time-scales. As $t \to \infty$ we have $J_0 \to 0$ and we see that the mean phonon occupancy of all atoms is the average of the total initial number of phonons, as expected.

The above discussion concludes that to cool an atomic register consisting of many atoms in arbitrary geometries and dimensions, we simply perform the phonon-swap as if all the data-auxiliary pairs are independent. The many-body interactions only lead to a small degradation in the swap

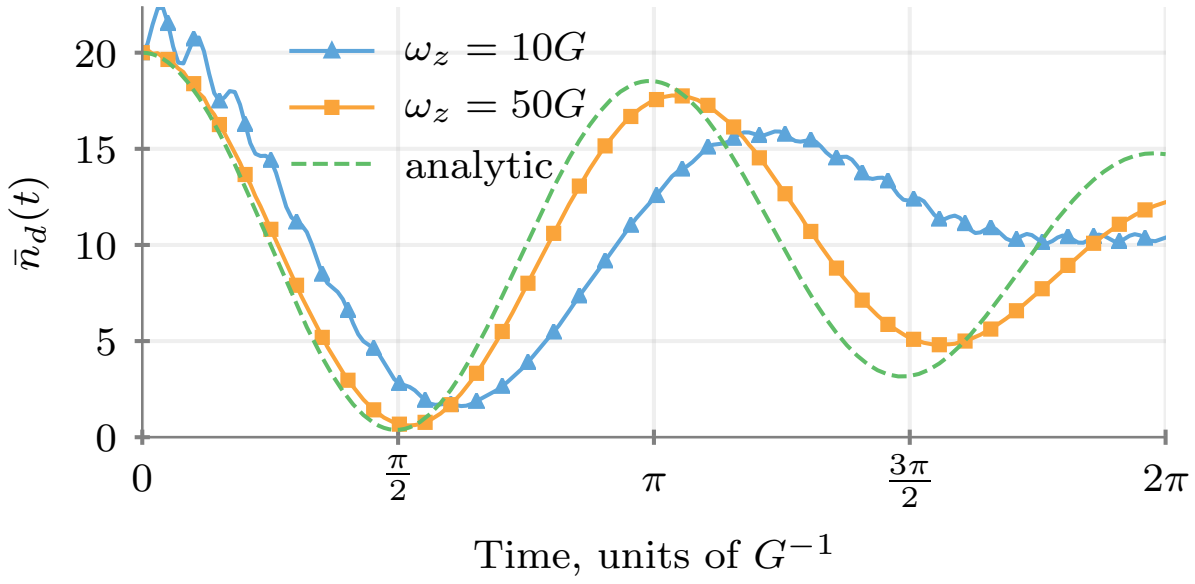

Figure 7.2: The average number of phonons in the data atoms as a function of time computed numerically (solid lines) for different values of ω_z for two chains of 50 atoms, including the counter-rotating terms in Eq. (7.1), and using Eq. (7.3) (dashed line). Here, $\eta = 1, \bar{n}_d(0) = 20, \bar{n}_a(0) = 0$.

efficiency.

7.4 State-insensitive Rydberg interactions

We now turn to discuss how to obtain the spin-independent interactions by utilizing the van-der-Waals (vdW) couplings between Rydberg states. Specifically, we concentrate on alkali atoms and consider weakly laser-admixing two hyperfine ground states (see Appendix F.5 for an explicit example) representing the spin-1/2, $|g_+\rangle, |g_-\rangle$, to Rydberg states $|r_+\rangle, |r_-\rangle$, depicting the magnetic sublevels of either $S_{1/2}$ or $P_{1/2}$ manifolds, as shown in Fig. 7.1(c,d). The vdW couplings $\hat{\mathcal{H}}_{\text{vdW}}$ between the Rydberg states then give rise to effective interactions between the dressed ground states. The relevant Hamiltonian is $\hat{\mathcal{H}} = \sum_{i=1,2}(\hat{\mathcal{H}}_A^{(i)} + \hat{\mathcal{H}}_L^{(i)}) + \hat{\mathcal{H}}_{\text{vdW}}$ where $\hat{\mathcal{H}}_A^{(i)} = -\Delta_+^{(i)} |r_+^{(i)}\rangle \langle r_+^{(i)}| - \Delta_-^{(i)} |r_-^{(i)}\rangle \langle r_-^{(i)}|$ and $\hat{\mathcal{H}}_L^{(i)} = \frac{\Omega_+^{(i)}}{2} |g_+^{(i)}\rangle \langle r_+^{(i)}| + \frac{\Omega_-^{(i)}}{2} |g_-^{(i)}\rangle \langle r_-^{(i)}| + \text{H.c.}$ are the atomic and laser Hamiltonians, respectively, in the rotating frame within the rotating wave approximation. Here, $\Omega_\pm^{(i)}$ are Rabi frequencies and $\Delta_\pm^{(i)} \gg \Omega_\pm^{(i)}$ the laser detunings. Note that for the auxiliary atoms, it is sufficient to consider a single ground state and hence a single laser. However, we must take into account all the states in the Rydberg manifold because, in general, $\hat{\mathcal{H}}_{\text{vdW}}$ may contain both diagonal and off-diagonal matrix elements. This fact has been used previously to construct tunable spin-spin interactions [68, 69]. A sufficient condition to obtain spin-independent interactions is for $\hat{\mathcal{H}}_{\text{vdW}}$ to be proportional to an identity, together with a suitable choice of the laser parameters. We show below two simple schemes using $S_{1/2}$ and $P_{1/2}$ states that satisfy well this requirement.

The vdW Hamiltonian between two atoms in either $S_{1/2} + S_{1/2}$, $S_{1/2} + P_{1/2}$ or $P_{1/2} + P_{1/2}$ in the Zeeman basis has the following form (see Appendix F.1) [1]

[1] For $nS_{1/2} + n'S_{1/2}$ with $n \neq n'$, there are additional terms corresponding flip-flop interactions where the atoms swap their principle quantum numbers. The magnitude of these unwanted interactions is smaller than the unwanted n-preserving spin-dependent interactions of Eq. (7.4).

$$\hat{\mathcal{H}}_{\text{vdW}} = \frac{C_6}{r^6}\mathbb{1}_4 - \frac{C_6^{(a)} + C_6^{(b)} - C_6^{(c)} - C_6^{(d)}}{r^6}\mathcal{D}_0(\theta,\phi), \tag{7.4}$$

$$C_6 \equiv \frac{2}{27}\Big[C_6^{(a)} + 4C_6^{(b)} + 2(C_6^{(c)} + C_6^{(d)})\Big], \tag{7.5}$$

where the $C_6^{(p)}$ coefficients correspond to the four different channels describing the possible (L, J) quantum numbers of the intermediate states and $\mathcal{D}_0(\theta,\phi)$ is a traceless matrix that depends on the angles between the interatomic and quantization axes. The channels for $S_{1/2}+S_{1/2}$ and $S_{1/2}+P_{1/2}$ are shown in Table 7.1.

	$S_{1/2}+S_{1/2}$	$S_{1/2}+P_{1/2}$
(a)	$S_{1/2}+S_{1/2} \to P_{1/2}+P_{1/2}$	$S_{1/2}+P_{1/2} \to P_{1/2}+S_{1/2}$
(b)	$S_{1/2}+S_{1/2} \to P_{3/2}+P_{3/2}$	$S_{1/2}+P_{1/2} \to P_{3/2}+D_{3/2}$
(c)	$S_{1/2}+S_{1/2} \to P_{3/2}+P_{1/2}$	$S_{1/2}+P_{1/2} \to P_{3/2}+S_{1/2}$
(d)	$S_{1/2}+S_{1/2} \to P_{1/2}+P_{3/2}$	$S_{1/2}+P_{1/2} \to P_{1/2}+D_{3/2}$

Table 7.1: The four channels describing the dipole-allowed virtual processes $(L_1, J_1)+(L_2, J_2) \to (L_1', J_1')+(L_2', J_2')$ that lead to vdW interactions.

7.5 Phonon-swap with $S + S$ states

The first scheme uses the fact that for a pair of atoms in $nS_{1/2}$ states, the second term in Eq. (7.4) approximately vanishes [68, 434]. This can be seen from Table 7.1, which shows that the difference between the four channels is only in the fine structure of the intermediate states. In the limit of vanishing fine structure, we have $C_6^{(a)} = C_6^{(b)} = C_6^{(c)} = C_6^{(d)}$. This can also be understood intuitively: the vdW interactions arise from second-order perturbation theory, where the two electrons undergo virtual transitions to intermediate states allowed by the selection rules. If we neglect the fine structure, we are free to use the uncoupled basis ($|L, m_L\rangle \otimes |S, m_S\rangle$) for the intermediate levels. Since $S_{1/2}$-states are proportional to electronic spin states with definite m_S, i.e.

$\left|S_{1/2}, m_J = \pm\frac{1}{2}\right\rangle = |L=0, m_L=0\rangle \otimes \left|S=\frac{1}{2}, m_S=\pm\frac{1}{2}\right\rangle$ and because the dipole-dipole interactions do not act on the electronic spin, the vdW couplings cannot mix states with different m_J. The correction to this scales as $\Delta_{\text{FS}}/\delta$, where Δ_{FS} is the fine structure splitting and δ the energy difference to the intermediate states.

Neglecting these small corrections, and to fourth order in the small parameter $\epsilon = \Omega/2\Delta$, the effective spin-spin interactions between any two data atoms are given by

$$\hat{\mathcal{H}}_{\text{int}}(r) = \text{diag}\big(\tilde{V}_{++} \quad \tilde{V}_{+-} \quad \tilde{V}_{-+} \quad \tilde{V}_{--}\big). \tag{7.6}$$

In the case of data-auxiliary interactions, we have a 2×2 version of Eq. (7.6). In both cases, the matrix elements are

$$\tilde{V}_{\mu\nu} = \left(\frac{\Omega_\mu^{(1)}\Omega_\nu^{(2)}}{4\Delta_\mu^{(1)}\Delta_\nu^{(2)}}\right)^2 \frac{C_6}{r^6 - \frac{C_6}{\Delta_\mu^{(1)}+\Delta_\nu^{(1)}}}, \tag{7.7}$$

which are spin-independent (i.e. $\tilde{V}_{++} = \tilde{V}_{+-} = \tilde{V}_{-+} = \tilde{V}_{--}$) for a suitable choice of the laser parameters. A trivial example consists of the two laser fields being identical.

The cooling protocol with this scheme would thus consist of stopping the quantum simulation or computation, weakly coupling the ground states of both the data and auxiliary atoms to $nS_{1/2}$ states, and waiting for a time of t_s. As an example, Rb atoms separated by $2.36\,\mu\text{m}$, and weakly coupled to $60S_{1/2}$ ($C_6/2\pi \approx 138.5\,\text{GHz}\,\mu\text{m}^6$) with $\Omega/2\pi = 100\,\text{MHz}$[2] and $\Delta/2\pi = 200\,\text{MHz}$ would experience a phonon coupling of $G/2\pi \approx 1.48\,\text{kHz}$ assuming a trap frequency of $\omega_z/2\pi = 15\,\text{kHz}$. G is about an order of magnitude smaller than the trap frequency and about two orders of magnitude larger than the effective decay rate $\epsilon^2\Gamma_{60S}/2\pi \approx 0.043\,\text{kHz}$, where Γ_{60S} is the decay rate of $60S_{1/2}$ states. The deviation of $\hat{\mathcal{H}}_{\text{vdW}}$ from identity, which we define by the ratio of the

[2]This can be achieved by a two-photon transition with one of the lasers tightly focused through an objective, or by using a build-up cavity. One can also use stronger interactions together with optimal control techniques to reduce the Rabi frequency.

operator norms of the two terms in Eq. (7.4), is, in this case, ≈ 0.027. This error can be reduced by driving the two atoms to different principal quantum numbers, [Fig. 7.3(b)]. This generally reduces the C_6 coefficient [Fig. 7.3(a)], but it can nevertheless be sufficiently strong. For instance, $74S_{1/2} + 64S_{1/2}$ yields $C_6/2\pi \approx 29\,\mathrm{GHz}\,\mu\mathrm{m}^6$ (a factor of five smaller than for $60S_{1/2} + 60S_{1/2}$) with an error of ≈ 0.003 (an order of magnitude smaller).

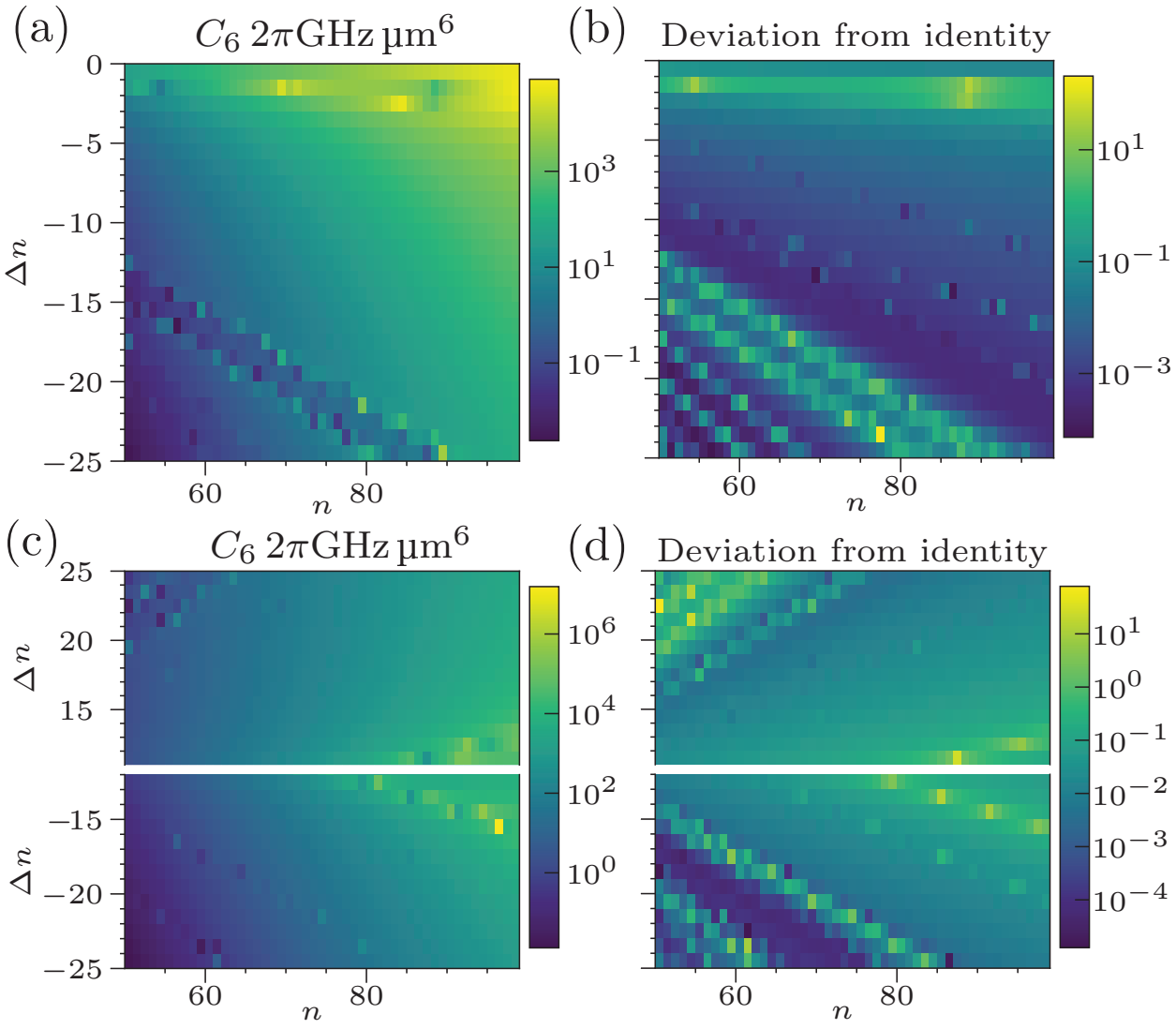

Figure 7.3: (a,c) The spin-insensitive interaction strength C_6 and (b,d) deviation from identity for (top) $nS_{1/2}+n'S_{1/2}$ and (bottom) $nS_{1/2}+n'P_{1/2}$ as a function of n and $\Delta n = n' - n$ for Rb atoms. In the case of $nS_{1/2} + n'P_{1/2}$, we take $\min|\Delta n| = 10$.

7.6 Phonon-swap with $S + P$ states

This brings us to the second scheme, in which the auxiliary atoms are coupled to $nS_{1/2}$ states, while the data atoms to $n'P_{1/2}$ states, where $|\Delta n| = |n' - n| \gg 1$ in order to ensure that the dipolar interactions between them can be ignored [335]. Such a configuration not only gives spin-independent data-auxiliary interactions, as we will explain below, but also gives rise to tunable spin-spin interactions between the data atoms [68]. To see why $S_{1/2} + P_{1/2}$ gives rise to $\hat{\mathcal{H}}_{\text{vdW}} \propto \mathbb{1}$, note that channels (a, c), as well as (b, d), in Table 7.1 only differ by the fine structure in one of the terms. In the limit of vanishing fine structure, the four channels cancel each other pair-wise, eliminating $\mathcal{D}_0(\theta, \phi)$ in Eq. (7.4).

Intuitively, the same argument as in the $S_{1/2} + S_{1/2}$ case shows that there cannot be any mixing between states involving different m_J of the $S_{1/2}$ atom. Hence, in the absence of fine structure in the intermediate manifold, the $S_{1/2}$ atom is effectively decoupled and $\hat{\mathcal{H}}_{\text{vdW}}$ must at least be block-diagonal. Within this approximation, we can understand why the remaining off-diagonal matrix elements also vanish by focusing solely on the $P_{1/2}$ atom. For each possible sub-channel of the $P_{1/2}$ atom [Fig. 7.4], there are exactly two processes that can couple its $m_J = +\frac{1}{2}$ and $m_J = -\frac{1}{2}$ states. These two processes, however, precisely destructively interfere. The resulting spin

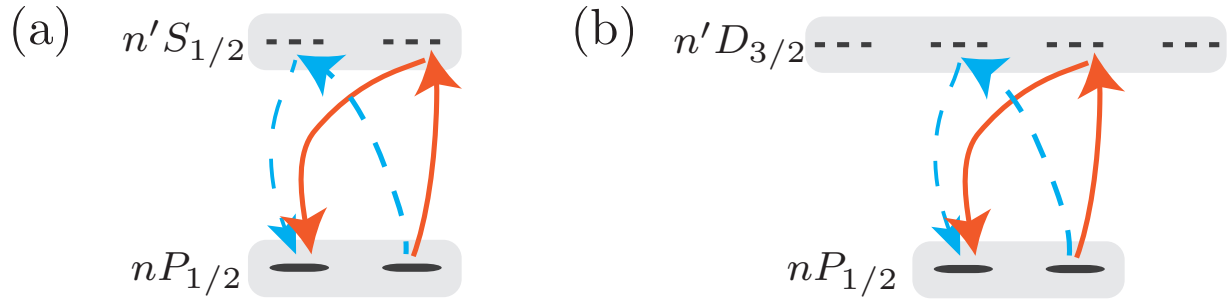

Figure 7.4: The four virtual transitions that can couple the $m_J = 1/2$ magnetic state to $m_J = -1/2$, in the $P_{1/2}$ manifold.

interactions between the data and auxiliary atoms have the same form as in Eqs. (7.6) and (7.7). The corresponding C_6, and the error due to the spin-dependent couplings, are shown in Fig. 7.3(c,d), respectively.

The data atoms, on the other hand, experience non-trivial spin-spin interactions due to the $P_{1/2} + P_{1/2}$ vdW couplings. For the configuration in Fig. 7.1 (quantization axis parallel to inter-atomic axis), the $\mathcal{D}_0(\theta, \phi)$ matrix reads

$$\mathcal{D}_0(0, \phi) = \frac{2}{81} \begin{pmatrix} 1 & 0 & 0 & 0 \\ 0 & -1 & -4 & 0 \\ 0 & -4 & -1 & 0 \\ 0 & 0 & 0 & 1 \end{pmatrix}, \tag{7.8}$$

which gives rise to the following spin-1/2 Hamiltonian for the data atoms:

$$\hat{\mathcal{H}} = \sum_{ij} J_z^{ij} \hat{S}_z^{(i)} + J_{zz}^{ij} \hat{S}_z \hat{S}_z + \left(J_{+-}^{ij} \hat{S}_+^{(i)} \hat{S}_-^{(j)} + \text{H.c.} \right), \tag{7.9}$$

where $\hat{S}_\alpha^{(i)}$ are the spin-1/2 operators of atom i and $J_{\mu\nu}^{ij}$ are coefficients that depend on the geometry, laser parameters, and Rydberg interactions [68]. This approach can be extended to generate other spin-1/2 models, for instance in two dimensions [68], with simultaneous cooling.

7.7 Summary and outlook

We have presented a protocol for sympathetically cooling Rydberg atoms without destroying the quantum information stored in their internal states. This can have applications for future Rydberg-based quantum computers and simulators as well as other quantum technologies. Note that while we focused here on the weak coupling regime ($G \ll \omega_z$), which inevitably limits the phonon-swap time to $\sim 1/G \gg 1/\omega_z$, it is possible to speed it up by working in the strong coupling regime $G \sim \omega_z$ and employing optimal control techniques [435–437]. Furthermore, while we used vdW interactions, state-insensitive interactions can also be realized with dipole-dipole interactions and

microwave dressing of Rydberg states [438]. Finally, our state-insensitive interactions schemes could potentially be used in other contexts, such as generating non-classical states [439] and novel phases of matter [440] combining motional and electronic degrees-of-freedom.

Appendix A: Supplemental Material for Chapter 2

A.1 The Massive Thirring-Schwinger model

In this section, we discuss the massive Thirring-Schwinger model, realized in our circuit-QED proposal, including its bosonization, Hamiltonian formulation, and the presence of quark-antiquark bound states for different parameters.

A.1.1 Hamiltonian and bosonic dual

Consider the Lagrangian density for the so-called massive Thirring-Schwinger model

$$\mathcal{L} = \bar{\psi}(i\partial\!\!\!/ - eA\!\!\!/ - m)\psi - \frac{1}{4}F_{\mu\nu}F^{\mu\nu} - \frac{1}{2}g(\bar{\psi}\gamma^{\mu}\psi)(\bar{\psi}\gamma_{\mu}\psi)\,, \tag{A.1}$$

which for $g = 0$ reduces to the massive Schwinger model investigated in this study [Eq. (2.1) in Section 2.2], while $e = 0$ yields the massive Thirring model [178, 441]. The gauge fields can be eliminated using Gauss's law [176], which, after fixing the gauge to $A_1(x) = 0$, reads

$$\partial_x E = -\partial_x^2 A_0 = e\rho, \tag{A.2}$$

where $\rho(x) = \psi^{\dagger}(x)\psi(x)$ is the charge-density operator. The solution to this equation is

$$A_0(x) = a_0 - \frac{e\theta}{2\pi}x - \frac{e}{2}\int dx'\,\rho(x')|x - x'|, \tag{A.3}$$

where a_0 and θ are integration constants. As argued in Ref. [176], physics depends on θ only modulo 2π, and so a suitable range for this variable is $\theta \in (-\pi, \pi]$. The Hamiltonian can be

derived in the standard fashion, noting the expression for the electric field from Eq. (A.2) with A_0 given in Eq. (A.3). In the charge-zero subspace $\int dx\, \rho(x) = 0$, the (normal-ordered) Hamiltonian of the Thirring-Schwinger model becomes

$$H = \int dx\ :\psi^\dagger \gamma^0 \left(-i\gamma^1 \partial_x + m\right) \psi : -\frac{e^2\theta}{2\pi} \int dx\, x\ :\rho(x): \\ -\frac{e^2}{4} \int dx \int dx'\, |x - x'| :\rho(x)\rho(x'): + \frac{g}{2} \int dx :\left[\rho(x)^2 - \left(\psi^\dagger(x)\gamma^0\gamma^1\psi(x)\right)^2\right] . \quad \text{(A.4)}$$

Our conventions are such that $\{\gamma^\mu, \gamma^\nu\} = 2\eta^{\mu\nu}$, with metric signature $\eta^{00} = -\eta^{11} = +1$. The two-component spinor operators, $\psi(x,t) \equiv (\psi_1(x,t), \psi_2(x,t))^T$, satisfy the canonical anticommutation relations $\{\psi_a(x,t), \psi_b^\dagger(x',t)\} = \delta_{ab}\delta(x - x')$, where $a, b = 1, 2$. The model described above can be shown to be dual to a bosonic theory with the Hamiltonian [175, 176, 178, 441]

$$H = \int dx \left[\frac{\Pi^2}{2} + \frac{(\partial_x\phi)^2}{2} + \frac{M^2(\phi + \theta/\beta)^2}{2} - u\cos(\beta\phi)\right] , \quad \text{(A.5)}$$

where $[\phi(x), \Pi(y)] = i\delta(x - y)$ and $[\Pi(x), \Pi(y)] = [\phi(x), \phi(y)] = 0$. The model parameters are related to those in the fermionic model as follows:

$$M = \frac{e}{\sqrt{\pi}} \frac{1}{\sqrt{1 + g/\pi}}, \quad u = \frac{e^\gamma}{2\pi}\Lambda m, \quad \beta = \sqrt{\frac{4\pi}{1 + g/\pi}} , \quad \text{(A.6)}$$

with γ being the Euler's constant and $\Lambda \gg e, m$ being a UV hard momentum cutoff, see Ref. [441] for details. Furthermore, the following relation holds between the fermionic current $\overline{\psi}\gamma^\mu\psi$ and the bosonic field ϕ [441]:

$$\overline{\psi}\gamma^\mu\psi \ = \ -\frac{\beta}{2\pi}\epsilon^{\mu\nu}\partial_\nu\phi. \quad \text{(A.7)}$$

Here, $\epsilon^{\mu\nu}$ is the Levi-Civita tensor. Now, using $\partial_x E = e\overline{\psi}\gamma^0\psi$ [see Eq. (A.2)], one arrives at $\frac{e\beta}{2\pi}\phi = E$, which relates the scalar field ϕ to the electric field E. It is more convenient to work with a shifted ϕ: $\phi \to \phi - \theta/\beta$, such that the Hamiltonian is

$$H = \int dx \left[\frac{\Pi^2}{2} + \frac{(\partial_x \phi)^2}{2} + \frac{M^2 \phi^2}{2} - u \cos(\beta\phi - \theta) \right], \tag{A.8}$$

and the relation to the electric field is now $\frac{e\beta}{2\pi}\phi = E + \frac{e\theta}{2\pi} \equiv E_T$, which in the limit $g = 0$ reproduces the relation presented in Chapter 2 between the total electric field E_T and the bosonic field of the massive Schwinger model. When $g = 0$, Eq. (A.8) reduces to Eq. (2.2) in Section 2.2. Finally, note that the dimensionless coupling e/m in the fermionic theory corresponds to the combination $\Lambda M/u$ in the bosonic theory [442].

A.1.2 Quark-antiquark interactions and bound states

In this section, we derive an effective quark-antiquark Hamiltonian in the nonrelativistic limit in perturbation theory and use this Hamiltonian to confirm the existence of quark-antiquark bound states (mesons). We also study the meson bound states using nonperturbative tensor-network computation of the low-lying spectrum.

A.1.2.1 Derivation of effective Hamiltonian

The goal is to derive an effective interaction Hamiltonian between a quark and an antiquark to leading order in the interactions e and g. For $g = 0$, an analogous computation was discussed by Coleman in Ref. [176]. The idea is that, in the weak-coupling limit in which $e/m, g \ll 1$, one can restrict the physics to subspaces with fixed particle number, e.g., vacuum, quark-antiquark state, etc. [1], since transitions between states with different particle numbers are higher order in the coupling strength [176]. This means that, in this limit, the full Hamiltonian can be assumed to be almost block-diagonal in the Fock basis. This mimics a nonrelativistic limit in which one can de-

[1] Recall that we have restricted the model to the net zero electric-charge sector.

fine an '*effective*' potential describing interactions in each fixed-particle sector, with well-defined quantum-mechanical operators $\hat{x}$ and $\hat{p}$ which would have been meaningless otherwise. Relativistic corrections in the dynamics can be included using standard quantum-mechanical perturbation theory, while corrections in the kinematics can be included by incorporating higher-order terms in p/m, where p is the typical momentum in the system. Such a notion of an effective Hamiltonian is useful to get a qualitative understanding of the nature of quark-antiparticle interactions in such a limit, and to make analytic predictions for the expected spectrum that can be compared against exact numerics.

To start with, we keep the kinematics relativistic but constrain our analysis to the two-particle sector only. A nonrelativistic expansion in p/m will be performed at the end. First, note that the quadratic piece of the Hamiltonian in Eq. (A.4), $H_0 \equiv \int dx \ : \psi^\dagger \gamma^0 \left(-i\gamma^1 \partial_x + m\right) \psi \ :$, can be diagonalized by a standard mode expansion:

$$\psi_a(x) = \int \frac{dk}{\sqrt{4\pi E_k}} e^{ikx} \left[u_a(k) b(k) + v_a(-k) c^\dagger(-k)\right], \tag{A.9}$$

where $E_k \equiv \sqrt{k^2 + m^2}$ with $k \equiv k^1 = -k_1$, and $u(k)$ and $v(k)$ are two-component spinor wave functions that satisfy the classical Dirac equation for positive and negative frequencies, respectively: $(\not{k} - m)u(k) = (\not{k} + m)v(k) = 0$ (here, $\not{k} = E_k\gamma^0 - k\gamma^1$). The creation operators for quarks and antiquarks satisfy the canonical anticommutation relations $\{b(k), b^\dagger(k')\} = \{c(k), c^\dagger(k')\} = \delta(k - k')$. Further, the following representation of Dirac matrices is used for explicit computations, $\gamma^0 = \sigma^z$ and $\gamma^1 = i\sigma^y$, so that the spinor wavefunctions are given by $u(k) = \begin{pmatrix} \sqrt{m + E_k} \\ \frac{k}{\sqrt{m+E_k}} \end{pmatrix}$ and $v(k) = \begin{pmatrix} \frac{k}{\sqrt{m+E_k}} \\ \sqrt{m + E_k} \end{pmatrix}$, leading to the free-fermion Hamiltonian

$$H_0 = \int dk \, E_k \left[b^\dagger(k) b(k) + c^\dagger(k) c(k)\right]. \tag{A.10}$$

A quark-antiquark state in the noninteracting limit can be written as

$$|p,q\rangle = b^\dagger(p)c^\dagger(q)|0\rangle, \tag{A.11}$$

where $|0\rangle$ is the Fock vaccum of H_0 and where the quark (antiquark) has momentum p (q). Following Coleman [176], one can now *define* the reduced center-of-mass Hamiltonian as the operator H_{eff}, whose matrix elements in the two-particle sector are given by

$$\langle p',q'|H|p,-p\rangle = \delta(p'+q')\langle p'|H_{\text{eff}}|p\rangle. \tag{A.12}$$

The effective Hamiltonian H_{eff} is a function of a conjugate pair of operators $[\hat{x},\hat{p}] = i$, where $\hat{x}$ is the displacement between the quark and the antiquark and $|p\rangle$ is a single-particle momentum eigenstate, $\hat{p}|p\rangle = p|p\rangle$, with normalization $\langle p'|p\rangle = \delta(p-p')$. In the absence of interactions, one has

$$\langle p',q'|H_0|p,-p\rangle \;\; = 2\sqrt{m^2+p^2}\,\delta(p-p')\delta(p'+q') \quad \Rightarrow \quad H_{\text{eff}} = 2\sqrt{m^2+\hat{p}^2}\,. \tag{A.13}$$

To compute $\langle p',q'|H|p,-p\rangle$ in the interacting case, one can insert Eq. (A.9) into Eq. (A.4) to obtain

$$\begin{aligned}\langle p'|H_{\text{eff}}|p\rangle = {} & 2\sqrt{m^2+p^2}\,\delta(p-p') - \frac{e^2\theta}{4\pi^2}\int dx\, x\, e^{i(p-p')x} \\ & + \frac{e^2}{8\pi E_{p'}E_p}\left(m^2+p'p+E_{p'}E_p\right)\int dx\,|x|\,e^{i(p-p')x} \\ & + \frac{e^2}{8\pi}\frac{m^2}{E_{p'}^2E_p^2} - \frac{g}{2\pi E_{p'}E_p}\left(m^2+p'p+E_{p'}E_p\right).\end{aligned} \tag{A.14}$$

Note that all interaction terms are of the form

$$\langle p'|\hat{O}|p\rangle = f_1(p')f_2(p)\int\frac{dx}{2\pi}\,g(x)\,e^{i(p-p')x} \tag{A.15}$$

for some functions f_1, f_2, and g [for the last line of Eq. (A.14), $g(x) = \delta(x)$]. This allows any interaction term $\hat{O}$ to be written as follows:

$$
\begin{aligned}
\hat{O} &= \left(\int dp' \, |p'\rangle\langle p'|\right) \hat{O} \left(\int dp \, |p\rangle\langle p|\right) \\
&= \int dp' \int dp \, |p'\rangle f_1(p') f_2(p) \int \frac{dx}{2\pi} \, g(x) \, e^{i(p-p')x} \langle p| \\
&= f_1(\hat{p}) \int dp' \int dp \, |p'\rangle \left(\int dx \, g(x) \langle p'|x\rangle\langle x|p\rangle\right) \langle p| f_2(\hat{p}) \\
&= f_1(\hat{p}) \left(\int dp' \, |p'\rangle\langle p'|\right) g(\hat{x}) \left(\int dx \, |x\rangle\langle x|\right) \left(\int dp \, |p\rangle\langle p|\right) f_2(\hat{p}) \\
&= f_1(\hat{p}) g(\hat{x}) f_2(\hat{p}) \, . \qquad \text{(A.16)}
\end{aligned}
$$

Equation (A.15) is used in the second equality, and the identity $e^{i(p-p')x} = 2\pi\langle p'|x\rangle\langle x|p\rangle$ is used in the third equality. Finally, the effective Hamiltonian can be written as

$$
\begin{aligned}
H_{\text{eff}} &= 2\left(m^2 + \hat{p}^2\right)^{1/2} - \frac{e^2\theta}{2\pi}\hat{x} + \frac{e^2}{4}\frac{m}{m^2+\hat{p}^2}\delta(\hat{x})\frac{m}{m^2+\hat{p}^2} \\
&\quad + \frac{e^2}{4}\left[|\hat{x}| + \frac{\hat{p}}{(m^2+\hat{p}^2)^{1/2}}|\hat{x}|\frac{\hat{p}}{(m^2+\hat{p}^2)^{1/2}} + \frac{m}{(m^2+\hat{p}^2)^{1/2}}|\hat{x}|\frac{m}{(m^2+\hat{p}^2)^{1/2}}\right] \\
&\quad - g\left[\delta(\hat{x}) + \frac{\hat{p}}{(m^2+\hat{p}^2)^{1/2}}\delta(\hat{x})\frac{\hat{p}}{(m^2+\hat{p}^2)^{1/2}} + \frac{m}{(m^2+\hat{p}^2)^{1/2}}\delta(\hat{x})\frac{m}{(m^2+\hat{p}^2)^{1/2}}\right] . \qquad \text{(A.17)}
\end{aligned}
$$

The lengthy expression in Eq. (A.17) can be simplified by considering the nonrelativistic limit. Note that, when momentum and energy are large enough for particle creation, $\langle\hat{p}^2\rangle \gtrsim m^2$, non-particle-conserving, i.e., inelastic, transitions can occur, and, in such a regime, it is not particularly useful to consider an effective potential between a quark and an antiquark. However, since our interest is in an effective interaction between static or slow-moving quark and antiquark—in particular, for investigating the presence of bound states—the matrix elements between states with different particle numbers will be reduced by kinematic constraints. Note that this limit is only applicable when the dimensionless coupling constants e/m and g are small enough, since large

couplings result in binding- or scattering-energy scales large enough to violate these assumptions. Based on this discussion, H_{eff} can be expanded in $p/m \ll 1$ to obtain a simpler effective Hamiltonian at leading order in p/m, e/m, and g:

$$H_{\text{eff}} = 2m + \frac{\hat{p}^2}{m} + \frac{e^2}{2}\left(|\hat{x}| - \frac{\theta}{\pi}\hat{x}\right) + \frac{e^2}{4m^2}\delta(\hat{x}) - 2g\delta(\hat{x}). \tag{A.18}$$

In taking the large-m limit, the dimensionless combination e/m is kept fixed. For the Schwinger model, $g = 0$, this gives Eq. (2.4) in Chapter 2. Note that the electric ($e \neq 0$) and the Thirring ($g \neq 0$) interactions contribute short-range terms which compete with each other. In the confined phase ($\theta \neq \pi$), the linear potential guarantees quark-antiquark bound states, which are the fundamental excitations, regardless of the short-range interactions. However, in the deconfined phase ($\theta = \pi$), quarks are free particles (as long as $x > 0$, i.e., the quark is to the left of the antiquark). Here, the presence of bound states depends on the delta-function term in Eq. (A.18). When $g > g_c \equiv \frac{e^2}{8m^2}$, the delta-function term is negative, giving rise to attractive short-range interactions, implying the existence of at least one bound state. For $g < g_c$ (including the $g = 0$ case considered in Chapter 2), on the other hand, the delta function is repulsive, prohibiting any bound states from forming.

As a nontrivial check on this expression, consider the Thirring model, $e = 0$, which is an integrable quantum field theory whose spectrum is known exactly [443, 444]. The effective Hamiltonian in this case is simply

$$H_{\text{eff}} = 2m + \frac{\hat{p}^2}{m} - 2g\delta(\hat{x})\,. \tag{A.19}$$

This is a standard problem in introductory quantum mechanics (see e.g., Ref. [445]). For $g > 0$, there is a single bound state with energy

$$E_{\text{bound}} = 2m(1 - \frac{g^2}{2}). \tag{A.20}$$

The exact Thirring model with $g > 0$ has N bound states, where N is the largest integer smaller than $1 + 2g/\pi$, and the energy of the nth bound state is given by [443]

$$E_n = 2m \sin\left(\frac{n\pi/2}{1 + 2g/\pi}\right), \quad n = 1, 2, .., N\,. \tag{A.21}$$

For small g, there is a single bound state ($n = 1$) with energy given, at leading order in g, by Eq. (A.20).

A.1.2.2 Numerical verification

To go beyond the perturbative results, we make use of the variational uMPS quasiparticle ansatz [see Appendix A.3.1 and Eq. (A.35)] to verify the existence of the bound states. In the deconfined phase, quarks are topological "kinks" [176], and are numerically described by the topological uMPS ansatz, whereas the mesons, if they exist, would be described by the topologically trivial uMPS ansatz (see Appendix A.3). The energy minimization of the topological uMPS ansatz yields the quark mass m_q, and the minimization of the topologically trivial uMPS ansatz returns an energy which we denote m_π. To determine if this corresponds to a meson eigenstate, we plot the ratio m_π/m_q in Fig. A.1 as a function of g. If the meson exists, that ratio needs to satisfy $m_\pi/m_q < 2$, since the bound-state energy must be below the two-particle continuum beginning at $2m_q$. Furthermore, plotting this ratio for different values of the bond dimension D of the uMPS ansatz can signify the existence or absence of the meson. This is because, if the meson exists, its wavefunction will be localized, and so the ansatz energy m_π should be rather insensitive to D and will quickly converge to the true meson mass as D is increased [186].

Figure A.1 reveals a critical $g_c \approx 1$ (for the parameters used in Chapter 2) above which $m_\pi/m_q < 2$. This region clearly shows insensitivity to D, signaling that the ansatz properly

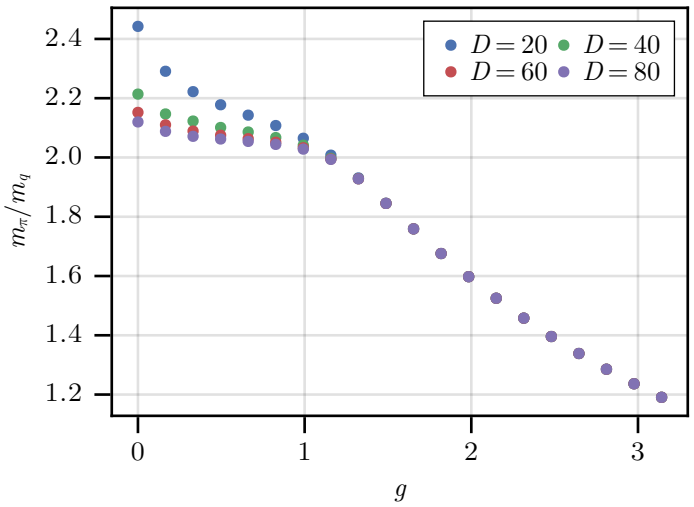

Figure A.1: Ratio of the meson mass m_π to the quark mass m_q in the deconfined phase ($\theta = \pi$) as a function of the Thirring interaction strength g, for different bond dimensions D. The energies are calculated using the variational principle with the uMPS quasiparticle ansatz [see Eq. (A.35)] using the same parameters as in Chapter 2 ($\chi = 1, \mu^2 = 0.5$, and $\lambda = 0.1$).

captures the nature of the bound-state wave function even for smaller bond dimensions. Below g_c, on the other hand, $m_\pi/m_q > 2$, and a qualitatively different behavior is observed as a function of D, signaling sensitivity to the choice of bond dimension. All this indicates that the bound state in the deconfined phase only exists for sufficiently large g, in agreement with the analytical prediction in the previous section. For small $g < g_c$, the minimization of the topologically trivial uMPS ansatz results in a two-particle state that is not an eigenstate, but is rather a superposition of many eigenstates from the continuum. The two particles in that state are forced together into a small region of size $\sim \log(D)$, and hence as D is increased, the particles are allowed to spread, which decreases their interaction energy and makes the energy of the variational ansatz approach the bottom of the two-particle band at $2m_q$.

A.2 Circuit-QED implementation

In this section, we derive the circuit-QED Hamiltonian from a lumped-element model and present a scheme for preparing meson excitations.

A.2.1 Hamiltonian derivation

Consider the circuit diagram in Fig. A.2, which is a more detailed version of Fig. 2.1. Here, each unit cell consists of a capacitor with capacitance C, an inductor with inductance L, and a Josephson junction with critical current I_c, in parallel, representing a general rf-SQUID circuit, which includes the fluxonium as a special case [446]. Each L-J loop is threaded by an external flux Φ_{ext}, and different unit cells are coupled together via inductors with inductance L'. Node fluxes are labeled by ϕ_i, branch fluxes by ϕ_C^i, ϕ_J^i, and ϕ_L^i, for the corresponding elements within node i, and the inter-node branch fluxes coupling nodes i and $i+1$ by $\phi_{L'}^{i,i+i}$. The branch currents are related to the branch fluxes by $I_C^i = C\ddot{\phi}_i$, $I_L^i = \phi_L^i/L$, $I_{L'}^{i,i+1} = \phi_{L'}^{i,i+1}/L'$, and $I_J^i = I_c \sin(\phi_J^i)$, for the capacitor, inductors, and the Josephson junction, respectively [2].

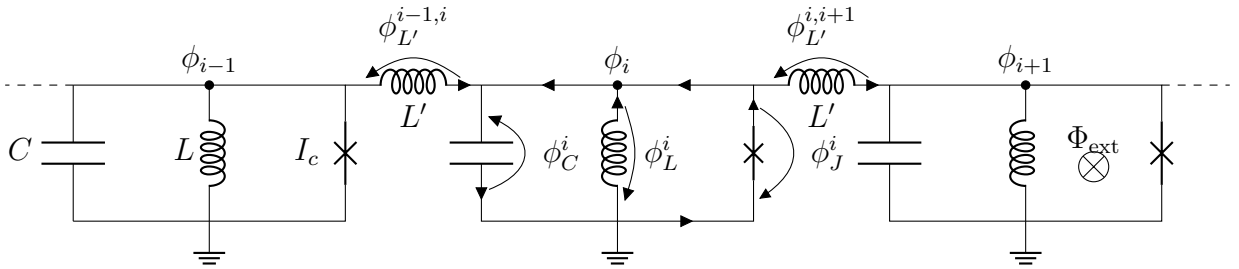

Figure A.2: Circuit diagram implementing the massive Thirring-Schwinger model. An external flux Φ_{ext} threads each L-J loop.

The Hamiltonian of the circuit can be derived by standard means. The capacitor branch fluxes

[2] We work in units where $\hbar = 1$ and the reduced flux quantum $\Phi_0/2\pi = \hbar/(4e^2) = 1$. This e is not to be confused with the e of the Schwinger model.

are chosen to be equal to the node fluxes $\phi_C^i = \phi_i \,\forall\, i$. Flux quantization yields the remaining branch fluxes: $\phi_J^i + \phi_C^i = \Phi_{\text{ext}}$, $\phi_C^i + \phi_L^i = 0$, $\phi_J^{i-1} + \phi_C^i + \phi_{L'}^{i-1,i} = 0$. Current conservation gives $I_{L'}^{i-1,i} - I_C^i + I_L^i + I_J^i - I_{L'}^{i,i+1} = 0$, which, together with the above, yields the equation of motion

$$-C\ddot{\phi}_i - \frac{1}{L}\phi_i + I_c \sin(\Phi_{\text{ext}} - \phi_i) + \frac{1}{L'}(\phi_{i-1} - 2\phi_i + \phi_{i+1}) = 0. \tag{A.22}$$

The corresponding Lagrangian is

$$\mathcal{L} = \sum_i \left[\frac{C\dot{\phi}_i^2}{2} - \frac{(\phi_i - \phi_{i-1})^2}{2L'} - \frac{\phi_i^2}{2L} - I_c \cos(\phi_i - \Phi_{\text{ext}}) \right]. \tag{A.23}$$

Defining the conjugate momentum $\pi_i = \frac{\partial \mathcal{L}}{\partial \dot{\phi}_i} = C\dot{\phi}_i$ and imposing the canonical commutation relations $[\phi_i, \pi_j] = i\delta_{ij}$, we obtain the Hamiltonian

$$H = \sum_i \left[4E_C \pi_i^2 + \frac{E_{L'}(\phi_i - \phi_{i-1})^2}{2} + \frac{E_L \phi_i^2}{2} + E_J \cos(\phi_i - \Phi_{\text{ext}}) \right], \tag{A.24}$$

where we defined the energies

$$E_C = \frac{1}{8C}, \quad E_{L'} = \frac{1}{L'}, \quad E_L = \frac{1}{L}, \quad I_J = E_J. \tag{A.25}$$

Redefining $\phi_i \to \beta\phi_i$ and $\pi_i \to \pi_i/\beta$, we obtain

$$H = \chi \sum_i \left[\frac{\pi_i^2}{2} + \frac{(\phi_i - \phi_{i-1})^2}{2} + \frac{\mu^2 \phi_i^2}{2} - \lambda \cos(\beta\phi_i - \theta) \right], \tag{A.26}$$

which is Eq. (2.3) of Section 2.2 with

$$\chi = \frac{8E_C}{\beta^2}, \quad \frac{E_{L'}\beta^4}{8E_C} = 1, \quad \mu^2 = \frac{E_L \beta^4}{8E_C}, \quad \lambda = \frac{E_J \beta^2}{8E_C}, \quad \theta = \Phi_{\text{ext}} - \pi. \tag{A.27}$$

Recall that the parameters of the bosonized lattice Hamiltonian are

$$\chi = \frac{1}{a}, \quad \mu^2 = M^2 a^2, \quad \lambda = u a^2. \tag{A.28}$$

Equations (A.27) and (A.28) together constitute a dictionary between the parameters of the bosonized massive Thirring-Schwinger model and those of the circuit-QED Hamiltonian.

A.2.2 Experimental meson–wave-packet preparation

In this section, we describe a scheme for preparing initial wave packets, focusing on meson excitations. The quarks, being topological excitations, do not couple to local operators, hence their preparation is left to future work. Our proposal goes as follows. We assume the system [i.e., Eq. (A.26)] is cooled down to its ground state in the confined phase. We add two ancillary qubits [111] far away from each other. Initializing the qubits in the excited state and coupling them to the system will result in the decay of the two qubit excitations into the system, producing two wave packets of quasiparticles. Choosing a weak coupling will ensure that multi-particle states are not be excited.

To see this, first note that, in terms of the quasiparticle degrees of freedom, Eq. (A.26) can be re-expressed as follows:

$$H = \sum_j \sum_k \omega_{k,j} \Psi^\dagger_{k,j} \Psi_{k,j} + \text{interactions}, \tag{A.29}$$

where k is a label for the eigenstates assuming open boundary conditions. $\Psi^\dagger_{k,j}$ and $\Psi_{k,j}$ are the creation and annihilation operators for the jth meson with energy $\omega_{k,j}$, i.e.,

$$\Psi^\dagger_{k,j} |\text{vac}\rangle = |\pi_{k,j}\rangle , \tag{A.30}$$
$$\Psi_{k,j} |\text{vac}\rangle = 0, \tag{A.31}$$

where $|\pi_{k,j}\rangle$ are the meson quasiparticles.

Next, consider, for simplicity, a single qubit (e.g., a transmon or a fluxonium [447]) with frequency Δ, coupled at position $i = L$. The addition to Eq. (A.26) is

$$H_{\text{qubit}} = \frac{\Delta}{2}\sigma_z + g(t)\sigma_x(a_L + a^\dagger_L), \tag{A.32}$$

where $a_i, a^\dagger_i = \frac{\phi_i \pm i\pi_i}{\sqrt{2}}$ are the creation and annihilation operators satisfying $[a_i, a^\dagger_j] = \delta_{ij}$, and $g(t)$ is the coupling (which can be controlled in time using a tunable coupler [49]). In terms of mesonic

quasiparticles, the entire Hamiltonian [Eq. (A.26) plus Eq. (A.32)] can be written as

$$H = \sum_j \sum_k \omega_{k,j} \Psi^\dagger_{k,j} \Psi_{k,j} + \sum_j \sum_k \left[g(t) \lambda_{k,j} \Psi^\dagger_{k,j} \sigma_- + \text{H.c.} \right] + \frac{\Delta}{2} \sigma_z, \tag{A.33}$$

under a rotating-wave approximation (RWA) that assumes only a single excitation in the combined qubit-system and hence ignores interactions from Eq. (A.29). $\lambda_{k,j} \equiv \langle \pi_{k,j} | \, a_L + a_L^\dagger \, | \text{vac} \rangle$ is a matrix element that depends on the overlaps of a_L and $a_L^\dagger$ between the vacuum $|\text{vac}\rangle$ and the meson eigenstates $|\pi_{k,j}\rangle$. Turning on $g(t)$, the (initially) excited qubit will decay into the system, producing a mesonic wave packet. The central momentum and the shape of the resulting wave packet can be controlled by choosing the qubit frequency Δ and the time dependence of the qubit-system coupling $g(t)$, as described in the Supplementary Methods of Ref. [448]. Placing the qubit at the (left) right edge can ensure that only (right-)left-moving excitations are created. The matrix element $\lambda_{k,j}$ can either be calculated numerically or accounted for (prior to performing the actual scattering experiment) using measurements of the resulting wave-packet shape and a feedback loop. The wave-packet shape can be determined from, for example, local measurements of the fields ϕ_x [179] or from spectroscopic measurements of the transmitted amplitude at the other edge of the system [180, 181].

An important subtlety is that the qubit generically couples to all mesons in the theory. If there is more than a single meson flavor, this will result in an undesired superposition of wave packets of different mesons. To mitigate this issue, this scheme can be combined with adiabatic state preparation. One can first tune the system to a parameter regime where there is only a single meson particle. A simple example is the free-boson limit with $\lambda = 0$. More generally, the "phase diagram" in Fig. A.3, obtained using the uMPS methods of Appendix A.3.1, shows the region in the $\{\lambda, \theta\}$ parameter space with only a single meson particle for $\mu^2 = 0.1$. This phase diagram is

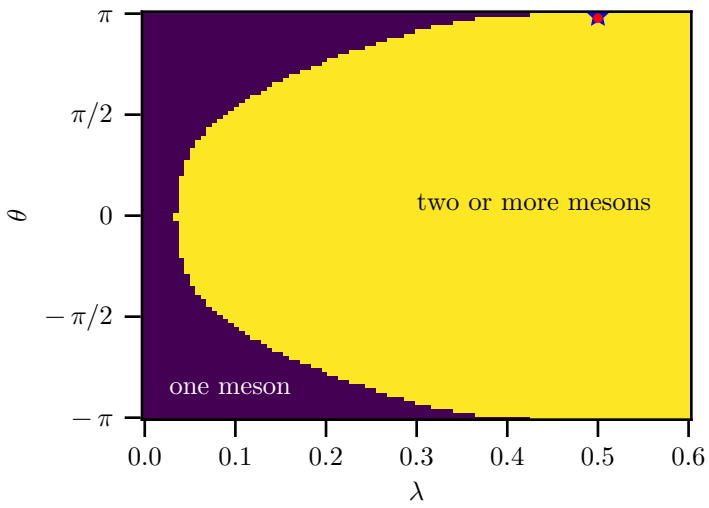

Figure A.3: Number of mesons in the confined phase. Purple (yellow) region corresponds to one (two or more) mesons. The two regions are determined by obtaining the two lowest eigenvalues above the ground state using the topologically trivial MPS quasiparticle ansatz (see Appendix A.3.1). The single (two or more) meson region correspond to the second eigenvalue being bigger (smaller) than twice the lowest eigenvalue (mass of the fundamental meson). The remaining parameters are $\chi = 1$ and $\mu^2 = 0.1$ as in Chapter 2. The star and circle indicate the parameters used in Chapter 2 [$\lambda = 0.5$ and $\theta = \pi - 0.04$ (star) or $\theta = \pi - 0.07$ (circle)]. The vertical axis range is $[-\pi + 0.001, \pi - 0.001]$ so as to avoid the deconfined phase at $\theta = -\pi, \pi$.

consistent with the perturbative result of Coleman [176], predicting the existence of one meson for $|\theta| \gtrsim \pi/2$ in the limit $\lambda/\mu \to 0$ (i.e., the strong-coupling limit of the original Schwinger model). After preparing the meson wave packets in the single-meson regime, one can adiabatically tune λ and θ to their desired regime, preparing in this way the fundamental mesons of the interacting theory. Tuning both θ and λ can be accomplished using external time-dependant flux control. In order to be able to tune λ, each Josephson junction in Fig. A.2 can be replaced by a SQUID, a loop composed of two junctions, realizing an effective single flux-tunable junction [26]. Designing the two loops (the L-J loop from Fig. A.2 and the SQUID loop) to be asymmetric in size allows one to control both $\lambda(\Phi_{\text{ext}})$ and $\theta(\Phi_{\text{ext}})$ with a single external flux [180, 181, 215].

A.3 Numerical Methods

In this section, we provide more details on the uniform-matrix-product-state methods, describing the wave-packet preparation and particle detection.

A.3.1 Uniform Matrix Product States

We begin with a general review of uniform matrix product states (see Ref. [166] for more details). A uniform matrix product state (uMPS), describing a translationally invariant state, is graphically represented as

$$|\Psi(A)\rangle = \cdots - A - A - A - A - A - \cdots \quad , \tag{A.34}$$
$$\qquad\qquad\qquad\quad s_{n-1} \quad s_n \quad s_{n+1}$$

where A^s is a $D \times D$ matrix for each basis index s. When dealing with a bosonic theory, even the local Hilbert space is infinite dimensional and needs to be truncated. For the parameters used in Chapter 2, we found the local energy basis to be an efficient choice, i.e., the local (single-site) part of the Hamiltonian in Eq. (A.26) was diagonalized using a very large Fock-state basis (of $\sim$ 2000 levels), keeping only the lowest d eigenstates (we found $d = 12$ to be sufficient for the scattering considered in Chapter 2). The full Hamiltonian was then projected on this truncated local eigenbasis, and the ground state was subsequently found using variational methods [184].

The quasiparticle excitations on top of the ground state can be described with the MPS quasiparticle ansatz [184–186]

$$|\Phi_p(B)\rangle = \sum_n e^{ipn} \cdots - A_L - A_L - B - \tilde{A}_R - \tilde{A}_R - \cdots \, . \tag{A.35}$$
$$\qquad\qquad\qquad\quad \cdots \quad s_{n-1} \quad s_n \quad s_{n+1} \quad \cdots$$

This state is written in the so-called mixed canonical form, with the ground-state tensors A_L and $\tilde{A}_R$ in the left- and right-orthonormal forms, respectively. A_L and $\tilde{A}_R$ can either represent the same

ground state for a topologically trivial excitation, in which case they are related by a gauge transformation (i.e $A_L = C^{-1}A_R C$ for a $D \times D$ matrix C), or different degenerate ground states for a topological excitation in case of a spontaneously broken symmetry. The variational optimization of the B tensor reduces to an eigenvalue problem for each $p \in [-\pi, \pi)$, providing both the dispersion relation $\mathcal{E}(p)$ and the p-dependent eigenvectors $B(p)$.

The dispersion relation is shown in Fig. A.4 for the three parameter regimes studied in Chapter 2: the deconfined phase where $\theta = \pi$, and the confined phase where $\theta = \pi - \varepsilon$ with $\varepsilon = 0.04, 0.07$. At low energies (insets), the dispersion is well approximated by the relativistic relation $\mathcal{E}(p) \approx \sqrt{m^2 + p^2}$, where m is the mass of the particle [obtained from $m \equiv \mathcal{E}(p = 0)$].

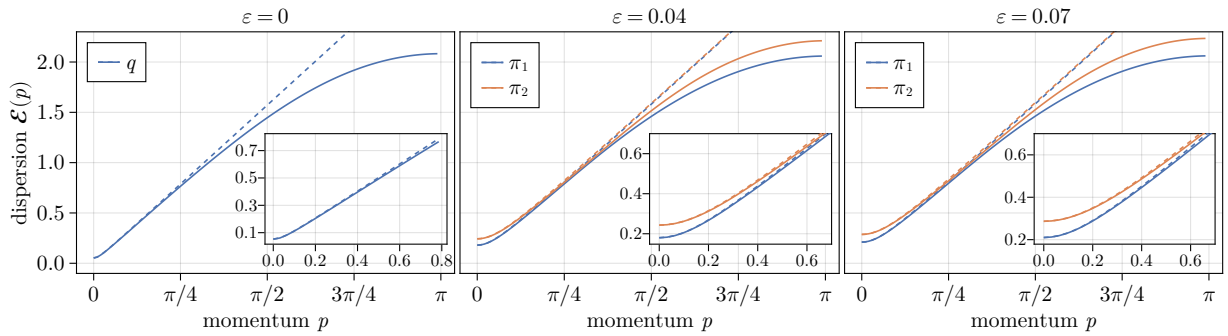

Figure A.4: Dispersion relation as a function of (positive) momentum for the three parameter regimes considered in Chapter 2 [with $\mathcal{E}(-p) = \mathcal{E}(p)$]. Solid lines are the numerical uMPS results [obtained using Eq. (A.35)], and dashed lines are the relativistic approximations $\mathcal{E}(p) \approx \sqrt{m^2 + p^2}$, where m is $\mathcal{E}(p = 0)$ for the corresponding particle: quarks q in the deconfined phase ($\varepsilon = 0$) and mesons π_j in the confined phase with $\varepsilon = 0.04, 0.07$ (only the lightest two mesons corresponding to $j = 1, 2$ are shown). Insets show a zoom in the low-energy regime.

A.3.2 MPS wave-packet preparation

In this section, we describe the numerical procedure for preparing initial wave-packet states using the uMPS quasiparticles. We follow a procedure similar to the one in Refs. [126, 127] albeit with some differences that are explained below. Using the momentum quasiparticle eigenstates in

Eq. (A.35), a localized wave packets can be built as

$$|\Psi_{\mathrm{wp}}\rangle = \int_{-\pi}^{\pi} dp\, c_p\, |\Phi_p(B(p))\rangle = \sum_n \cdots$$ 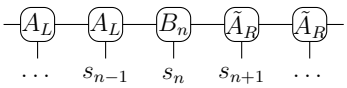 $$\cdots\,, \tag{A.36}$$

where

$$B_n \equiv \int_{-\pi}^{\pi} dp\, c_p\, e^{ipn} B(p). \tag{A.37}$$

Here, $c_p \sim e^{-(p-p_0)^2/(2\sigma^2)}$, which is a Gaussian function centered at p_0 with width σ. We use $\sigma = 0.12$ for the quark-antiquark wave packets (Fig. 2.3) and $\sigma = 0.06$ for the meson wave packets (Fig. 2.4).

As first discussed in Ref. [126], there are several caveats with this approach. First, because the $B(p)$ tensors are determined from an eigenvalue problem for each momentum p, they come with random phases, preventing the phase coherence needed for building localized wave packets. To deal with this issue, we fix the global phase of each $B(p)$ such that one specifically chosen tensor element in each is real and positive. Second, one needs to fix the gauge redundancy of the $B(p)$ tensors (i.e., invariance of $|\Phi_p(B(p))\rangle$ under $B^s(p) \to B^s(p) + Y\tilde{A}_R^s - e^{ip}A_L^s Y$ for any $D \times D$ matrix Y). The choices used when solving the variational minimization problem, the so-called left or right gauge fixing conditions, are inherently very asymmetric. To deal with this issue, we employ the "reflection symmetric" gauge choice of Ref. [127] as it is applicable for both topologically trivial and nontrival excitations. Together, this approach is simpler and does not require any approximations or conditions on the wave-packets' width, unlike the methods of Refs. [126, 127]. The final wave packet ends up slightly shifted from its intended location [which is $n = 0$ for the choice of c_p in Eq. (A.37)], which can be corrected by centering it based on $\mathrm{argmax}\|B_n\|$, as discussed in the following.

Finally, we note that, to evaluate Eq. (A.37), one has to sample a finite grid of momenta p with

resolution Δp, and the B_n are, therefore, periodic with period $N_p = \frac{2\pi}{\Delta p}$, i.e., $B_{n+N_p} = B_n$. We choose N_p large enough so that the wave packet comfortably fits inside a single period (we used $N_p = 400$), which we take to be centered around $n^* = \mathrm{argmax}\|B_n\|$. Of this N_p-sized interval of B_n tensors, we only keep $N < N_p$ tensors that satisfy $\|B_n\|/\|B_{n^*}\| \geq \epsilon$ for some chosen threshold ϵ (we used $\epsilon = 10^{-3}$), which we label by $n \in [i+1, i+N]$ for a chosen i along the uMPS chain. The integral in Eq. (A.36) becomes a finite sum and can be analytically expressed as

$$
\begin{aligned}
|\Psi_{\mathrm{wp}}\rangle =& \cdots - \boxed{A_L} - \boxed{M_{i+1}} - \boxed{M_{i+2}} - \cdots - \boxed{M_{i+N}} - \boxed{\tilde{A}_R} - \cdots , \\
M_{i+1} =& \begin{pmatrix} A_L & B_{i+1} \end{pmatrix}, \quad M_{n\in[i+2,i+N-1]} = \begin{pmatrix} A_L & B_n \\ 0 & \tilde{A}_R \end{pmatrix}, \quad M_{i+N} = \begin{pmatrix} B_{i+N} \\ \tilde{A}_R \end{pmatrix}.
\end{aligned}
\tag{A.38}
$$

To create the initial two-particle state, this procedure can be carried out twice to create two wave packets with opposite momenta. Given that A_L is related to A_R by a gauge transformation, i.e., $A_L C = C A_R$, the states are then glued together using the matrix C^{-1}. The result is a nonuniform window of tensors surrounded by the uniform ground state. Note that the bond dimension of the tensors in Eq. (A.38) is not uniform, as some have the value D and others $2D$. Finally, the one-site time-dependent variational principle (TDVP) [449] is used to evolve the state in time, which does not change the bond dimensions. Hence, prior to the time-evolution, we expand the bond dimensions of all the tensors to a uniform value $D' \geq 2D$. For the quark-antiquark scattering (Fig. 2.3), we found that $D = 20$ and $D' = 50$ were sufficient for convergence at late times, while the meson-meson scattering in the confined phase required a larger bond dimension ($D = 40$ and $D' = 100$). During the time evolution, we only update the tensors inside the nonuniform window [187–189]. To decide whether to extend the window, at each time step, we compute the entanglement entropy across the bonds at the edges of the window and compare that to the entropy of the vacuum, extending the window by a site if the relative difference is greater than a specified

threshold (which we chose to be 0.02).

A.3.3 Particle detection

In this section, we describe how the scattering matrix can be computed by projecting on multi-particle basis states. As long as the particles are well separated, one can use Eq. (A.35) to build multi-particle states, akin to the asymptotic "out" states in the definition of the S-matrix. For example, a two-particles state, with a particle on the left with momentum p_1 and a particle on the right with momentum p_2, is expressed as

$$|\Phi_{p_1,p_2}\rangle = \sum_{n_1 \in W_L} \sum_{n_2 \in W_R} e^{ik_1 n_1} e^{ik_2 n_2} \cdots$$

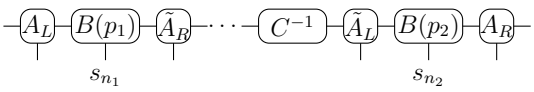

$$\cdots . \qquad \text{(A.39)}$$

The sums are restricted such that the two excitation tensors B appear in disjoint regions W_L and W_R and are separated by some minimum number r of vacuum tensors, ensuring that there are no interactions between the particles (we found $r = 40$ to be sufficient for both meson and quark scattering in Chapter 2). Moreover, since we are projecting on a time-evolved state where the particles are constrained to a finite window of the uMPS, we further restrict the sums to the sites within this nonuniform window. Using the left gauge-fixing condition for the left-most B tensor, and the right gauge-fixing condition for the right-most B tensor [166], ensures that overlaps where either of the B tensors is outside of the window are exactly zero. The finite sums in Eq. (A.39) can then be summed exactly and expressed as a single MPS, similarly to Eq. (A.38).

To compute the full n-particle momentum distribution (for $n = 2$, $S_{p_1,p_2} \equiv \langle \Phi_{p_1,p_2} | \psi(t) \rangle$, where $|\psi(t)\rangle$ is the time-evolved state), M_p^n contractions need to be performed, where M_p is the desired number of p samples (i.e., the equivalent of N_p in the incoming wave-packet construction). This can be sped up by precomputing partial contractions. For example, for the two-particle case,

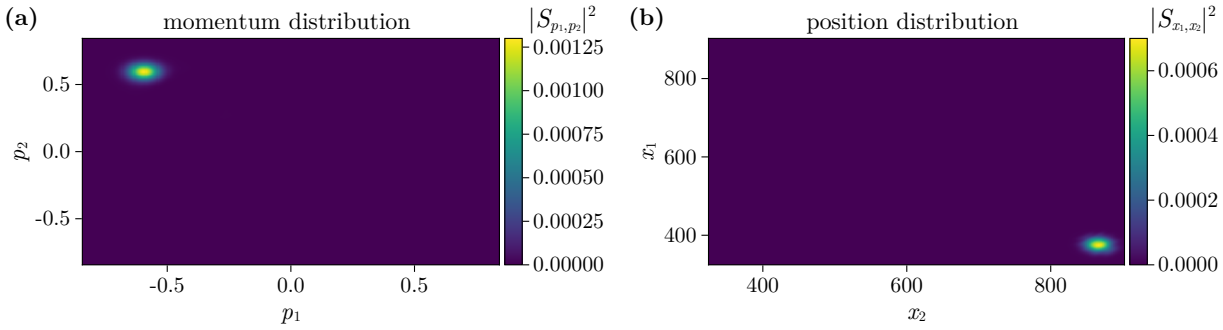

Figure A.5: (a) Momentum and (b) position probability distributions of observing a $\pi_1\pi_1$ meson pair at $t = 345$ following the $\pi_1\pi_1$ collision at $\varepsilon = 0.07$ in Fig. 2.4.

we compute the partial left and right contractions for each value of p, which scale as $\sim M_p|W_L|$ and $\sim M_p|W_R|$, respectively. Then, the $\sim M_p^2$ contractions are very efficient since the remaining tensor network is of length ~ 1. As an example, Fig. A.5 depicts the result of projecting the state following the meson-meson collision (this process is depicted in Fig. 2.4 of Section 2.4) on the lightest meson-meson ($\pi_1\pi_1$) two-particle basis. From the momentum distribution, the position distribution (S_{x_1,x_2}) is computed by a Fourier transform. For this to work, it is crucial that the phases of the $B(p)$ tensors are fixed prior to the projection, as described in Appendix A.3.2. To avoid multiple unphysical copies due to the periodicity of the discrete Fourier transform, we choose the number of p samples, M_p, to be larger than the window size (we used $M_p = 400$ for the quark-antiquark scattering and $M_p = 1300$ for the meson-meson scattering). Finally, fitting Gaussians to the marginals of these distributions produces the information plotted in Fig. 2.4(c) of Section 2.4.

Appendix B: Supplemental Material for Chapter 3

B.1 Renormalized spin frequency

In this section, we reproduce the derivation [233] of the crossover energy scale between weak and strong coupling, the equivalent of the Kondo temperature, which we associate with the renormalized spin frequency Δ_R in Eq. (3.2).

We employ the renormalization group (RG) procedure as used in Ref. [233]. Let us denote the cutoff at some energy scale l by $\Lambda(l)$ (such that $\Lambda(0) \equiv \omega_c$ is the original cutoff of the problem). The RG procedure consists of integrating out the high-energy modes, and thus redefining the cutoff from Λ to $\Lambda - d\Lambda$. This leads to the RG flow equations for the coupling constants α and $h \equiv \Delta/\Lambda$ [233] (that can also be derived from perturbation theory in α)

$$\frac{\mathrm{d}\alpha}{\mathrm{d}l} = -2\alpha^2, \tag{B.1}$$

$$\frac{\mathrm{d}h}{\mathrm{d}l} = (1-2\alpha)h, \tag{B.2}$$

where $dl = -d\Lambda/\Lambda$, which implies that $l = \log\left(\frac{\omega_c}{\Lambda}\right)$.

The equation for α can be readily solved,

$$\alpha(l) = \frac{\alpha(0)}{1 + 2l\alpha(0)}. \tag{B.3}$$

Plugging Eq. (B.3) into the differential equation for h we find

$$h(l) = \frac{e^l \Delta/\omega_c}{1 + 2\alpha(0) l}. \tag{B.4}$$

Note that both the cutoff Λ and Δ are decreasing as function of l. Equivalently, h increases from its initial value of $h(0) = \Delta/\omega_c$. Eventually, we have $h(l^*) \approx 1$, which occurs when $\Delta(l^*) \equiv \Delta_R = \Lambda(l^*)$, and hence the RG breaks down. The energy scale corresponding to this is $l^* = \log \omega_c/\Delta_R$. Plugging this into Eq. (B.4) gives Eq. (3.2),

$$\Delta_R = \frac{\Delta}{1 + 2\alpha \log(\omega_c/\Delta_R)}. \tag{B.5}$$

This differs from the result presented in Refs. [232, 233] in that we kept the Δ_R on the right-hand-side (whereas these references approximated it by Δ) as it agrees better with the numerical results.

As we show later in Appendix B.4, we also reproduce exactly this equation by applying the Callan-Symanzik equation to the bare Green's function of the spin.

B.2 Numerical methods

In this section, we describe the numerical methods we use to compute the single photon transport properties.

We first write the Hamiltonian (Eq. (3.1)) in terms of bosonic creation and annihilation operators, as follows,

$$\hat{\mathcal{H}} = -\Delta \frac{\hat{\sigma}_z}{2} + \sum_{i=x,y} \left[\int_{-k_{max}}^{k_{max}} \omega(k) \hat{a}^\dagger_{i,k} \hat{a}^\dagger_{i,k} dk + \frac{\hat{\sigma}_i}{2} \int_{-k_{max}}^{k_{max}} g(k) (\hat{a}^\dagger_{i,k} + \hat{a}^\dagger_{i,k}) dk \right] \tag{B.6}$$

with $\left[\hat{a}^\dagger_{i,k}, \hat{a}^\dagger_{j,k'}\right] = \delta_{ij}\delta(k - k')$. We make the transformation

$$\begin{aligned}\hat{a}_{i,k} =& \frac{\hat{A}_{i,k} + \hat{B}_{i,k}}{\sqrt{2}}, \quad k > 0, \\ \hat{a}_{i,-k} =& \frac{\hat{A}_{i,k} - \hat{B}_{i,k}}{\sqrt{2}}, \quad k > 0,\end{aligned} \tag{B.7}$$

which transforms the Hamiltonian into two commuting parts

$$\begin{aligned}\hat{\mathcal{H}} &= \hat{\mathcal{H}}_{XYSB} + \hat{\mathcal{H}}_{free}, \\ \hat{\mathcal{H}}_{XYSB} &= -\Delta\frac{\hat{\sigma}_z}{2} + \sum_{i=x,y}\left[\int_0^{k_{max}} \omega(k)\hat{A}^\dagger_{i,k}\hat{A}^\dagger_{i,k} + \frac{\hat{\sigma}_i}{2}\int_0^{k_{max}} \tilde{g}_i(k)(\hat{A}^\dagger_{i,k} + \hat{A}^\dagger_{i,k})\right], \\ \hat{\mathcal{H}}_{free} &= \sum_{i=x,y}\left[\int_0^{k_{max}} \omega(k)\hat{B}^\dagger_{i,k}\hat{B}^\dagger_{i,k}\right],\end{aligned} \tag{B.8}$$

where $\tilde{g}(k) = \sqrt{2}g(k)$. It is enough therefore to only simulate the dynamics of the $\hat{\mathcal{H}}_{XYSB}$ Hamiltonian.

Explicitly, to determine the single-particle scattering properties, we perform the following procedure. We create a single-particle Gaussian wavepacket on top of the ground state, with amplitude $c_k = \mathcal{N}e^{-\frac{(k-k_0)^2}{2\sigma^2}+ikx_0}$, where $\mathcal{N}$ is a normalization so that $\int_0^{k_{max}} dk|c_k|^2 = 1$. Without loss of generality, we choose this excitation to be of the x type (since for $\alpha_x = \alpha_y$ the Hamiltonian is invariant under $x \leftrightarrow y$ exchange.). We then evolve this state in time, which leads to the scattering of the wavepacket off the spin. At long times after the scattering, we can extract several observables such as the elastic scattering amplitudes and number of elastic and inelastic photons in the final state.

Denoting the ground state of the full Hamiltonian $\hat{\mathcal{H}}$ by $|GS\rangle = \left|GS^{XYSB}\right\rangle \otimes \left|0^{free}\right\rangle$, the initial state is

$$\begin{aligned}|\psi(0)\rangle &= \int_0^{k_{max}} dk c_k \hat{a}^\dagger_{x,k}|GS\rangle \\ &= \frac{1}{\sqrt{2}}\int_0^{k_{max}} dk c_k \hat{A}^\dagger_{x,k}\left|GS^{XYSB}\right\rangle \otimes \left|0^{free}\right\rangle + \left|GS^{XYSB}\right\rangle \otimes \frac{1}{\sqrt{2}}\int_0^{k_{max}} dk c_k \hat{B}^\dagger_{x,k}\left|0^{free}\right\rangle.\end{aligned} \tag{B.9}$$

The time-evolved state is

$$|\psi(t)\rangle = \frac{1}{\sqrt{2}}|\psi_{XYSB}(t)\rangle \otimes \left|0^{free}\right\rangle + e^{-iE_{GS}t}\left|GS^{XYSB}\right\rangle \otimes \frac{1}{\sqrt{2}}\int_0^{k_{max}} dk c_k e^{-i\omega_k t}\hat{B}^\dagger_{x,k}\left|0^{free}\right\rangle, \tag{B.10}$$

where $|\psi_{XYSB}(t)\rangle \equiv e^{-i\hat{\mathcal{H}}_{XYSB}t}\int_0^{k_{max}} c_k \hat{A}^\dagger_{x,k}\left|GS^{XYSB}\right\rangle$ and E_{GS} is the ground state energy.

From this state, we can extract the elastic scattering amplitudes as follows [242] (with $t = t_\infty$ sufficiently long so that the scattering event has finished):

$$t_{xx} = \frac{\langle GS|\,\hat{a}_{x,k}\,|\psi(t_\infty)\rangle}{c_k} = \frac{1}{2}\left\langle GS^{XYSB}\right|\hat{A}_{x,k}\,|\psi_{XYSB}(t_\infty)\rangle + \frac{1}{2}c_k e^{-i(E_{GS}+\omega_k)t_\infty}, \tag{B.11}$$

$$r_{xx} = \frac{\langle GS|\,\hat{a}_{i,-k}\,|\psi(t_\infty)\rangle}{c_k} = \frac{1}{2}\left\langle GS^{XYSB}\right|\hat{A}_{x,k}\,|\psi_{XYSB}(t_\infty)\rangle - \frac{1}{2}c_k e^{-i(E_{GS}+\omega_k)t_\infty}, \tag{B.12}$$

$$t_{xy} = \frac{\langle GS|\,\hat{a}_{y,k}\,|\psi(t_\infty)\rangle}{c_k} = \frac{1}{2}\left\langle GS^{XYSB}\right|\hat{A}_{y,k}\,|\psi_{XYSB}(t_\infty)\rangle\,. \tag{B.13}$$

The number of elastic photons generated by a given wavepacket can be found from the above amplitudes by squaring and integrating over all k. This gives (for $i = x, y$)

$$\begin{aligned}\bar{n}_{i,elastic} &= \int_0^{k_{max}} dk\left(|\langle GS|\,\hat{a}_{i,k}\,|\psi(t_\infty)\rangle|^2 + |\langle GS|\,\hat{a}_{i,-k}\,|\psi(t_\infty)\rangle|^2\right)\\ &= \int_0^{k_{max}} dk\left[\frac{1}{2}\left|\left\langle GS^{XYSB}\right|\hat{A}_{i,k}\,|\psi_{XYSB}(t_\infty)\rangle\right|^2 + \frac{1}{2}|c_k|^2\delta_{x,i}\right].\end{aligned} \tag{B.14}$$

The number of inelastic photons is

$$\begin{aligned}\bar{n}_{i,inelastic} = &\int_0^{k_{max}} dk\frac{1}{2}\langle\psi_{XYSB}(t_\infty)|\,\hat{A}^\dagger_{i,k}\hat{A}_{i,k}\,|\psi_{XYSB}(t_\infty)\rangle\\ &- \int_0^{k_{max}} dk\frac{1}{2}\left\langle GS^{XYSB}\right|\hat{A}^\dagger_{i,k}\hat{A}_{i,k}\left|GS^{XYSB}\right\rangle\\ &- \int_0^{k_{max}} dk\frac{1}{2}\left|\left\langle GS^{XYSB}\right|\hat{A}_{i,k}\,|\psi_{XYSB}(t_\infty)\rangle\right|^2.\end{aligned} \tag{B.15}$$

Thus we see that all quantities of interest can be obtained from correlation functions and matrix elements of the states $\left|GS^{XYSB}\right\rangle$ and $|\psi_{XYSB}(t_\infty)\rangle$.

B.2.1 Orthogonal polynomial mapping

The Hamiltonian $\hat{\mathcal{H}}_{XYSB}$ from Eq. (B.8) describes a system with very nonlocal interactions. In order to efficiently simulate it with matrix-product-states, we use the orthogonal polynomial mapping introduced in [240, 241], which maps the Hamiltonian into a tight-binding model with only nearest-neighbor interactions.

Here we summarize the main steps of the mapping. For more details, see Refs. [240, 241]. We work with the Hamiltonian from Eq. (B.8), reproduced here

$$\hat{\mathcal{H}}_{XYSB} = -\Delta\frac{\hat{\sigma}_z}{2} + \sum_{i=x,y}\left[\int_0^{k_{max}} \omega(k)\hat{A}^\dagger_{i,k}\hat{A}_{i,k} + \frac{\hat{\sigma}_i}{2}\int_0^{k_{max}} \tilde{g}_i(k)(\hat{A}_{i,k} + \hat{A}^\dagger_{i,k})\right], \quad \text{(B.16)}$$

where $\omega(k) = \omega_c k$, $k_{max} = 1$, and $\tilde{g}_i(k) = \sqrt{2\alpha_i\omega_c k}$. The resulting spectral functions are

$$J_i(\omega) = \pi\sum_k \bar{g}_i(k)^2\delta(\omega - \omega(k)) = 2\pi\alpha_i\omega\theta(\omega_c - \omega). \quad \text{(B.17)}$$

We introduce the unitary transformation

$$U_{i,n}(k) = \tilde{g}_i(k)p_{i,n}(k), \quad n = 0, 1, \cdots, \quad \text{(B.18)}$$

where $p_{i,n}(k)$ are orthonormal polynomials with respect to the measure $d\mu_i(k) = \tilde{g}_i^2(k)dk$ [i.e. $\langle p_{i,n}, p_{j,m}\rangle \equiv \int_0^{k_{max}} d\mu_i(k)p_{i,n}(k)p_{j,m}(k) = \delta_{nm}\delta_{ij}$], and a set of new discrete bosonic modes

$$\hat{b}^\dagger_{i,n} = \int_0^{k_{max}} dk U_{i,n}(k)A^\dagger_{i,k}, \quad \text{(B.19)}$$

that satisfy $\left[\hat{b}_{i,n}, \hat{b}^\dagger_{j,m}\right] = \delta_{ij}\delta_{n,m}$.

Using the recurrence relations of orthogonal polynomials, one can show that the Hamiltonian in Eq. (B.16) can be written as

$$\begin{aligned}\hat{\mathcal{H}}_{XYSB} = &-\Delta\frac{\hat{\sigma}_z}{2} + \sum_{i=x,y}\frac{\hat{\sigma}_i}{2}\sqrt{\alpha_i\omega_c}(\hat{b}^\dagger_{i,0} + \hat{b}_{i,0}) + \omega_c\sum_{i=x,y}\sum_{n=0}^{\infty}\nu_n\hat{b}^\dagger_{i,n}\hat{b}_{i,n} \\ &+ \omega_c\sum_{i=x,y}\sum_{n=0}^{\infty}\left[\beta_{n+1}\hat{b}^\dagger_{i,n}\hat{b}_{i,n+1} + H.c\right],\end{aligned} \quad \text{(B.20)}$$

which describes two semi-infinite tight-binding bosonic chains that are both coupled to the spin via their first site. For the Ohmic spectral function, the $p_{i,n}$ polynomials are the Jacobi polynomials, and the on-site energies and hopping coefficients are given by

$$\begin{aligned} \nu_n &= \frac{1}{2}\left(1 + \frac{1}{(1+2n)(3+2n)}\right), \\ \beta_{n+1} &= \frac{1+n}{1+n+2n}\sqrt{\frac{1+n}{2+n}}. \end{aligned} \tag{B.21}$$

Using the inverse transformation

$$\hat{A}^\dagger_{i,k} = \sum_n U_{i,n}(k)\hat{b}^\dagger_{i,n}, \tag{B.22}$$

we can convert measurements in the $\hat{b}$ basis to observables in frequency space. For example, the frequency-mode occupation is (for $k = k'$)

$$\left\langle \hat{A}^\dagger_{i,k}\hat{A}_{i,k'} \right\rangle = \sum_{n,m=0}^{\infty} U_{i,n}(k)U_{i,m}(k') \left\langle \hat{b}^\dagger_{i,n}\hat{b}_{i,m} \right\rangle. \tag{B.23}$$

Note that this is an exact mapping, provided the length of the chains is infinite. In practice, the length of the chains is truncated to a finite value L, and the dimension of each bosonic Hilbert space is truncated to a finite value d. We varied these parameters and found that $L = 250$, $d = 5$, and bond dimension of $\chi = 30$ are adequate to obtain converging results for the scattering for most values of α.

B.3 Elastic S-matrix in terms of spin susceptibilities

In this section, we derive the relation between the elastic scattering coefficients and the spin susceptibilities, given in Eqs. (3.3) and (3.4).

Let us write the Hamiltonian as

$$\hat{\mathcal{H}} = \hat{\mathcal{H}}_0 + \hat{V}, \tag{B.24}$$

$$\hat{\mathcal{H}}_0 = \sum_k \omega_k \hat{a}^\dagger_{x,k} \hat{a}_{x,k} + \sum_k \omega_k \hat{a}^\dagger_{y,k} \hat{a}_{y,k}, \tag{B.25}$$

$$\hat{V} = -\frac{\Delta}{2}\hat{\sigma}_z + \frac{\hat{\sigma}_x}{2}\sum_k g_{x,k}(\hat{a}^\dagger_{x,k} + \hat{a}_{x,k}) + \frac{\hat{\sigma}_y}{2}\sum_k g_{x,k}(\hat{a}^\dagger_{y,k} + \hat{a}_{y,k}). \tag{B.26}$$

We are interested in the S-matrix between a particle with momentum k in bath i and a particle with momentum k' in bath j:

$$S_{jk',ik} = \langle \psi^-_{jk'} | \psi^+_{ik} \rangle , \tag{B.27}$$

where $|\psi^\pm_{ik}\rangle$ are the exact incoming and outgoing scattering eigenstates. Following Ref. [450], we can write these eigenstates as follows:

$$|\psi^\pm_{ik}\rangle = \hat{a}^\dagger_{i,k} |\psi_0\rangle + |\chi^\pm_i\rangle , \tag{B.28}$$

where $|\psi_0\rangle$ is the ground state of the full $\hat{\mathcal{H}}$ with energy E_0, and $|\chi^\pm_i\rangle$ are the states of the scattered particles. Since $|\psi^\pm_{ik}\rangle$ are eigenstates of $\hat{\mathcal{H}}$ with energy $E_0 + \omega_k$, Schrodinger's equation implies

$$(\hat{\mathcal{H}} - \omega_k - E_0)\Big(\hat{a}^\dagger_{i,k} |\psi_0\rangle + |\chi_i\rangle\Big) = 0. \tag{B.29}$$

Furthermore,

$$\hat{\mathcal{H}}\hat{a}^\dagger_{i,k} |\psi_0\rangle = \Big(\hat{a}^\dagger_{i,k}\hat{\mathcal{H}} - \Big[\hat{a}^\dagger_{i,k}, \hat{\mathcal{H}}\Big]\Big) |\psi_0\rangle = (E_0 + \omega_k)\hat{a}^\dagger_{i,k} |\psi_0\rangle + \frac{\hat{\sigma}_i}{2} g_{i,k} |\psi_0\rangle . \tag{B.30}$$

Substituting this into Eq. (B.29) gives

$$(E_0 + \omega_k - \hat{\mathcal{H}}) |\chi_i\rangle = \frac{\hat{\sigma}_i}{2} g_{i,k} |\psi_0\rangle \rightarrow |\chi^\pm_i\rangle = \frac{1}{E_0 + \omega_k - \hat{\mathcal{H}} \pm i\epsilon} \frac{\hat{\sigma}_i}{2} g_{i,k} |\psi_0\rangle , \tag{B.31}$$

with $\epsilon > 0$ taken to zero at the very end. From this we find

$$|\psi^+_{ik}\rangle - |\psi^-_{ik}\rangle = -2\pi i \delta(E_0 - \omega_k - \hat{\mathcal{H}}) \frac{\hat{\sigma}_i}{2} g_{i,k} |\psi_0\rangle . \tag{B.32}$$

Plugging this back into the S-matrix Eq. (B.27) gives

$$S_{jk',ik} = \delta_{kk'}\delta_{ij} - 2\pi i\delta(\omega_{k'} - \omega_k) g_{ik} \langle \psi^-_{jk'}| \frac{\hat{\sigma}_i}{2} |\psi_0\rangle \equiv \delta_{kk'}\delta_{ij} - 2\pi i\delta(\omega_{k'} - \omega_k) T_{jk',ik}, \tag{B.33}$$

where we defined the T-matrix

$$\begin{aligned} T_{jk',ik} &= g_{ik} \langle \psi^-_{jk'}| \frac{\hat{\sigma}_i}{2} |\psi_0\rangle \\ &= g_{ik} \langle \psi_0| \hat{a}_{jk'} \frac{\hat{\sigma}_i}{2} |\psi_0\rangle + g_{ik} g_{jk'} \langle \psi_0| \frac{\hat{\sigma}_j}{2} \frac{1}{E_0 + \omega_k - \hat{\mathcal{H}} + i\epsilon} \frac{\hat{\sigma}_i}{2} |\psi_0\rangle . \end{aligned} \tag{B.34}$$

To evaluate the first term, we perform a similar manipulation as in Eq. (B.30):

$$\hat{\mathcal{H}}\hat{a}_{j,k'} |\psi_0\rangle = \left(\hat{a}_{j,k'}\hat{\mathcal{H}} - \left[\hat{a}_{j,k'}, \hat{\mathcal{H}}\right]\right) |\psi_0\rangle = (E_0 - \omega_{k'})\hat{a}_{j,k'} |\psi_0\rangle - \frac{\hat{\sigma}_j}{2} g_{j,k'} |\psi_0\rangle \tag{B.35}$$

$$\rightarrow \hat{a}_{j,k'} |\psi_0\rangle = \frac{1}{E_0 - \omega_{k'} - \hat{\mathcal{H}} - i\epsilon} \frac{\hat{\sigma}_j}{2} g_{j,k'} |\psi_0\rangle . \tag{B.36}$$

Inserting this into Eq. (B.34) yields

$$T_{jk',ik} = g_{ik} g_{jk'} \left[\langle \psi_0| \frac{\hat{\sigma}_j}{2} \frac{1}{E_0 + \omega_k - \hat{\mathcal{H}} + i\epsilon} \frac{\hat{\sigma}_i}{2} |\psi_0\rangle + \langle \psi_0| \frac{\hat{\sigma}_i}{2} \frac{1}{E_0 - \omega_{k'} - \hat{\mathcal{H}} - i\epsilon} \frac{\hat{\sigma}_j}{2} |\psi_0\rangle \right], \tag{B.37}$$

which, when $\omega_k = \omega_{k'}$, we recognize as the Fourier transform of the retarded Green's function

$$T_{jk',ik} = g_{ik} g_{jk'} G^R_{ji}(\omega + i\epsilon) \tag{B.38}$$

with

$$G^R_{ji}(\omega + i\epsilon) = -\frac{i}{4} \int_0^\infty dt\, e^{i(\omega + i\epsilon)t} \langle [\hat{\sigma}_j(t), \hat{\sigma}_i] \rangle , \tag{B.39}$$

which we equivalently refer to as the spin susceptibility in Chapter 3.

B.4 Derivation of the spin susceptibilities

In this section, we explicitly compute the spin susceptibility, Eq. (B.39). We will do so by first computing the imaginary-time Matsubara Green's function,

$$\mathcal{G}_{ji}(i\Omega) = \int_0^\beta d\tau\, e^{i\Omega_n \tau} \left\langle \mathcal{T}_\tau \hat{\sigma}_j(\tau) \hat{\sigma}_i(0) \right\rangle . \tag{B.40}$$

Here, the imaginary-time dependence of operators is $\hat{\sigma}_j(\tau) = e^{H\tau}\hat{\sigma}_j e^{-H\tau}$, and $\mathcal{T}_\tau$ is the imaginary-time ordering operator. This function may be computed using the usual diagrammatic perturbation theory if we can use Wick's theorem, after which we may obtain the spin susceptibility by analytic continuation [451]:

$$G^R_{ji}(\omega + i\epsilon) = -\frac{1}{4}\mathcal{G}_{ji}(i\Omega \to \omega + i\epsilon). \tag{B.41}$$

However, the Pauli matrices do not satisfy Wick's theorem. We can get around this by using an Abrikosov pseudo-fermion representation of the spins. We introduce a two-component set of fermions, $\{\chi_a, \chi_b^\dagger\} = \delta_{ab}$, $a, b = 1, 2$, related to the spin operators by

$$\begin{aligned}
\hat{\sigma}_x &= \chi_1^\dagger \chi_2 + \chi_2^\dagger \chi_1, \\
\hat{\sigma}_y &= -i\left(\chi_1^\dagger \chi_2 - \chi_2^\dagger \chi_1\right), \\
\hat{\sigma}_z &= \chi_1^\dagger \chi_1 - \chi_2^\dagger \chi_2.
\end{aligned} \tag{B.42}$$

This is only a faithful representation of the spin operators in the subspace $\chi_1^\dagger\chi_1 + \chi_2^\dagger\chi_2 = 1$. However, we can project to this subspace using the Popov-Fedotov trick of using an imaginary chemical potential $\mu = -i\pi/2\beta$, which results in a cancellation between the unphysical subspaces [451]. This method requires us to work at finite temperature during intermediate calculations, but below we will always take the $\beta \to \infty$ limit as early as possible.

We may now express the system as a coherent-state path integral. We introduce the bosonic

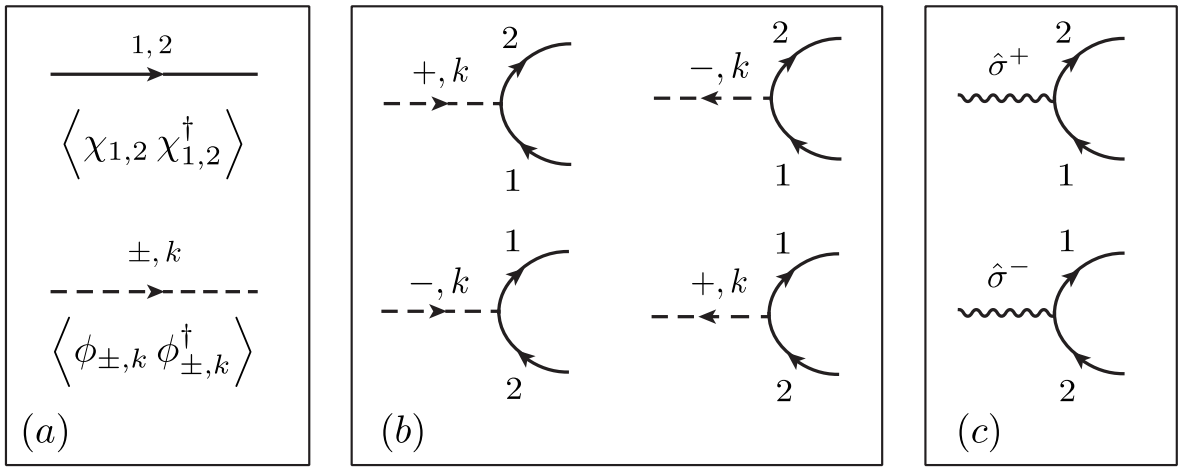

Figure B.1: The Feynman rules, which follow from Eq. (B.43). (a) The fermionic (top) and bosonic (bottom) propagators, which are given in Eqs. (B.44)-(B.47). (b) The interaction vertices for our theory. Each vertex contributes a factor of $\sum_k g_k/\sqrt{2}$. The dependence of diagrams on the spectral function comes from internal bosonic propagators connecting two such vertices. (c) Diagrammatic representation of the insertion of external spin operators, which are composite when written in terms of the fermionic χ_a fields.

fields $\phi_{\pm,k} = (a_{x,k} \pm i a_{y,k})/\sqrt{2}$, after which our model may be described by the Lagrangian

$$\begin{aligned} L &= \sum_{i=\pm} \sum_k \phi^\dagger_{i,k} \left(\partial_\tau + \omega_k\right) \phi_{i,k} + \sum_{a,b=1}^{2} \chi^\dagger_a \left[\left(\partial_\tau - \mu\right) \delta_{ab} - \frac{\Delta}{2} \sigma^z_{ab} \right] \chi_b \\ &\quad + \frac{1}{\sqrt{2}} \chi^\dagger_1 \chi_2 \sum_k g_k \left(\phi_{-,k} + \phi^\dagger_{+,k} \right) + \frac{1}{\sqrt{2}} \chi^\dagger_2 \chi_1 \sum_k g_k \left(\phi_{+,k} + \phi^\dagger_{-,k} \right). \end{aligned} \tag{B.43}$$

In this form, it is straightforward to treat the interactions g_k perturbatively using a Feynman-diagram expansion and the Matsubara formalism. We have the bare fermionic Green's functions

$$\delta_{ab} \Pi_a(\tau) = \langle \mathcal{T}_\tau \chi_a(\tau) \chi^\dagger_b(0) \rangle, \qquad \Pi_a(i\alpha_n) = \int_0^\beta d\tau\, e^{i\alpha_n \tau} \Pi_a(\tau), \tag{B.44}$$

with

$$\Pi_1(i\alpha_n) = -\frac{1}{i\alpha_n + \mu + \Delta/2}, \qquad \Pi_2(i\alpha_n) = -\frac{1}{i\alpha_n + \mu - \Delta/2}, \tag{B.45}$$

where $\alpha_n = \pi(2n+1)/\beta$, $n \in \mathbb{Z}$. Similarly, the bosonic propagators are

$$\delta_{ij} \delta_{kk'} D_k(\tau) = \langle \mathcal{T}_\tau \phi_{i,k}(\tau) \phi^\dagger_{j,k'}(0) \rangle, \qquad D_k(i\Omega_n) = \int_0^\beta d\tau\, e^{i\Omega_n \tau} D_k(\tau), \tag{B.46}$$

with

$$D_k(i\Omega_n) = \frac{1}{-i\Omega_n + \omega_k} \tag{B.47}$$

and $\Omega_n = 2\pi n/\beta$, $n \in \mathbb{Z}$. The interaction terms in Eq. (B.43) result in four interaction vertices, which contribute dependence on g_k. Since we are interested in correlation functions of the spin operators, we also introduce a diagrammatic notation representing the composite operators $\hat{\sigma}^+ = \chi_1^\dagger \chi_2$ and $\hat{\sigma}^- = \chi_2^\dagger \chi_1$. The Feynman rules for this theory are displayed in Fig. B.1.

As a demonstration of this formalism, we obtain the spin susceptibility in the non-interacting ($\alpha = 0$) limit by computing the diagrams with a single fermion loop and no bosonic propagators,

$$\begin{aligned}
\mathcal{G}_{+-}(i\Omega_n) &= \int_0^\beta d\tau e^{i\Omega_n \tau} \langle \mathcal{T} \chi_1^\dagger(\tau) \chi_2(\tau) \chi_2^\dagger(0) \chi_1(0) \rangle \\
&= -\frac{1}{\beta} \sum_{i\alpha_n} \frac{1}{(i\alpha_n + \mu + \Delta/2)(i\alpha_n + i\Omega_n + \mu - \Delta/2)} \\
&= \frac{\tanh(\beta\Delta/2)}{\Delta - i\Omega_n}.
\end{aligned} \tag{B.48}$$

We also have $\mathcal{G}_{-+}(i\Omega_n) = \mathcal{G}_{+-}(-i\Omega_n)$ and $\mathcal{G}_{++} = \mathcal{G}_{--} = 0$. Going back to the xy basis, taking $\beta = \infty$, and analytically continuing, we obtain the expected form for the spin susceptibilities for $\alpha = 0$:

$$\begin{aligned}
G^R_{xx}(\omega + i\epsilon) &= G^R_{yy}(\omega + i\epsilon) = \frac{\Delta/2}{(\omega + i\epsilon)^2 - \Delta^2}, \\
G^R_{xy}(\omega + i\epsilon) &= -G^R_{yx}(\omega + i\epsilon) = \frac{i\omega/2}{(\omega + i\epsilon)^2 - \Delta^2}.
\end{aligned} \tag{B.49}$$

These expressions could be simply obtained through a direct computation at zero temperature with the spin operators, but the diagrammatic approach is useful for including interactions.

We note that the susceptibilities in Eq. (B.49) have a simple pole located at the bare spin

frequency, and such a pole can never be shifted or broadened by computing a finite number of diagrams. Therefore, we will use both the Callan-Symanzik equations and a Dyson equation to sum an infinite number of diagrams, which will result in a change in the analytic structures of the susceptibilities.

As discussed in Sec. B.1, if we perform an RG transformation on our system, redefining the cutoff from $\omega_c \equiv \Lambda(0)$ to some lower cutoff $\Lambda(l)$, we obtain the flow equations

$$\Lambda \frac{\mathrm{d}\alpha}{\mathrm{d}\Lambda} = 2\alpha^2, \tag{B.50}$$

$$\Lambda \frac{\mathrm{d}h}{\mathrm{d}\Lambda} = -(1-2\alpha)h, \tag{B.51}$$

where $h \equiv \Delta/\Lambda$. In addition to coupling renormalization, it turns out that one also needs to renormalize the spin operators under an RG transformation, and one may show that, perturbatively,

$$\sigma_i(l) \approx (1 - \alpha \log \omega_c/\Lambda)\sigma_i(0), \qquad (i = x, y), \tag{B.52}$$

implying a flow for the operators,

$$\Lambda \frac{\mathrm{d}\sigma_i}{\mathrm{d}\Lambda} = \alpha\, \sigma_i, \qquad (i = x, y). \tag{B.53}$$

These flow equations, first obtained in Ref. [233] using a Wilsonian momentum-shell RG scheme, may also be obtained by treating Eq. (B.43) using the conventional methods of quantum field theory. We now use the fact that the susceptibilities should be independent of an RG transformation, $dG^R_{ji}/d\Lambda = 0$. Taking into account any explicit and implicit dependence on the cutoff, this implies the Callan-Symanzik equation,

$$\left[\Lambda \frac{\partial}{\partial \Lambda} - h(1-2\alpha)\frac{\partial}{\partial h} + 4\alpha^2 \frac{\partial}{\partial \alpha} + 2\alpha\right] G^R_{ji} = 0. \tag{B.54}$$

The general solution to this partial differential equation is

$$G^R_{ji} = \frac{f_{ji}(\bar{h}(\Lambda), \bar{\alpha}(\Lambda))}{\omega + 2\alpha\omega \log \Lambda/\omega}, \tag{B.55}$$

where the f_{ji} are arbitrary functions of the "running couplings," defined as

$$\bar{h}(\Lambda) = \frac{h\Lambda}{\omega + 2\alpha\omega \log \Lambda/\omega}, \qquad \bar{\alpha}(\Lambda) = \frac{\alpha}{1 + 2\alpha \log \Lambda/\omega}. \tag{B.56}$$

Comparing this general solution to the leading-order expressions of Eq. (B.49), we may read off the $\alpha = 0$ limit of the functions f_{ji}, and then use the α-dependence implied by the solution of the differential equation to find

$$\begin{aligned} G^R_{xx} &= \frac{\Delta/2}{\omega^2(1 + 2\alpha \log \omega_c/\omega)^2 - \Delta^2}, \\ G^R_{xy} &= \frac{i\omega(1 + 2\alpha \log \omega_c/\omega)/2}{\omega^2(1 + 2\alpha \log \omega_c/\omega)^2 - \Delta^2}, \end{aligned} \tag{B.57}$$

where we have plugged in $\Lambda(l = 0) = \omega_c$ to give expressions in terms of the initial cutoff and the bare quantities, and ω has a small positive imaginary part. We see that both expressions no longer diverge at $\omega = \Delta$, but instead they have poles at $\omega = \Delta_R$, where Δ_R satisfies

$$\Delta_R = \frac{\Delta}{1 + 2\alpha \log(\omega_c/\Delta_R)}. \tag{B.58}$$

From Eq. (B.57), we see that the effect of solving the Callan-Symanzik equation was to sum the "leading logarithms," which are terms of the form $\alpha^n \log^n \omega_c/\omega$ at nth order in perturbation theory.

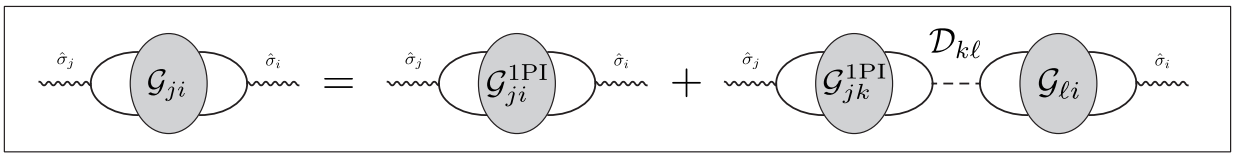

Figure B.2: Diagrammatic representation of the Dyson equation, Eq. (B.59).

Although we have succeeded in capturing the renormalization of the spin frequency using the Callan-Symanzik equations, they still predict a sharp behavior at $\omega = \Delta_R$, whereas we expect in-

teractions to broaden the peak near the renormalized spin frequency. We rectify this by computing an additional infinite set of diagrams using Dyson's equation. We first consider the one-particle irreducible Green's functions, $\mathcal{G}^{1\mathrm{PI}}_{ji}$, which are defined to be the complete set of diagrams that cannot be split in two by cutting a single propagator. By the structure of the interactions, the only possible propagators which can be cut to disconnect a susceptibility diagram is a bosonic propagator. As a result, we have the exact relation (in matrix notation)

$$\mathcal{G} = \mathcal{G}^{1\mathrm{PI}} + \mathcal{G}^{1\mathrm{PI}}\mathcal{D}\mathcal{G}. \tag{B.59}$$

See Fig. B.2 for a diagrammatic representation of this Dyson equation. Here, $\mathcal{D}$ is the result from computing the diagrams. We find the simple structure, $\mathcal{D}^{++} = \mathcal{D}^{--} = 0$ and $\mathcal{D}^{+-} = \mathcal{D}^{-+}$. An explicit calculation gives

$$\mathcal{D}^{+-} = -\pi\alpha|\Omega_n|. \tag{B.60}$$

Then the full Matsubara Green's function satisfies

$$\mathcal{G} = \left[\mathbb{I} - \mathcal{G}^{1\mathrm{PI}}\mathcal{D}\right]^{-1}\mathcal{G}^{1\mathrm{PI}}. \tag{B.61}$$

We now approximate the full Green's function by just using the leading-order result, Eq. (B.48), for $\mathcal{G}^{1\mathrm{PI}}$. This corresponds to summing all possible "bubble diagrams" which contribute to the susceptibility, which is reminiscent of the RPA approximation in the dense electron gas. In this approximation, we obtain the susceptibilities as

$$\begin{aligned} G^R_{xx}(\omega) &= \frac{(\Delta - i\pi\alpha\omega)/2}{(1+\pi^2\alpha^2)\,\omega^2 + i2\pi\alpha\Delta\omega - \Delta^2}, \\ G^R_{xy}(\omega) &= \frac{i\omega/2}{(1+\pi^2\alpha^2)\,\omega^2 + i2\pi\alpha\Delta\omega - \Delta^2}. \end{aligned} \tag{B.62}$$

We see that the inclusion of these diagrams has resulted in a finite imaginary part in the denominator, which removes the pole on the real-ω axis. We may now furthermore use the Callan-Symanzik

equation to sum the leading logarithms. After matching Eq. (B.55) to Eq. (B.62), we obtain the spin susceptibilities given in Eqs. (3.5) and (3.6).

As noted in Chapter 3, to this order, we have found that the above expressions do not lead to any contribution to inelastic scattering ($\gamma(\omega)$ in Chapter 3). We have checked that including all $O(\alpha)$ contributions to $\mathcal{G}^{\rm 1PI}$ still does not lead to inelastic scattering. We believe that including $O(\alpha^2)$ contributions to $\mathcal{G}^{\rm 1PI}$ will lead to inelastic contributions, which is consistent with Appendix B.5, where we show that inelastic contributions to the S-matrix appear at $O(\alpha^2)$.

B.5 Inelastic scattering

In this section, we will consider the leading contributions to inelastic scattering in perturbation theory using the diagrammatic approach developed in Appendix B.4. To proceed, we need a relation between time-ordered expectation values and S matrix elements. Such a relation is called the LSZ reduction formula in relativistic quantum field theory [452], but we can follow the derivation for our present system and derive a non-relativistic analogue of the reduction formula. If we consider the scattering of n photons with momenta k_1, k_2, ..., k_n into a state with n' photons with momenta $k_{1'}$, $k_{2'}$, ..., $k_{n'}$, the S matrix element is given by

$$\begin{aligned} S &= i^{n+n'} \int dt_{1'}\, e^{i\omega_{k_{1'}} t_{1'}} \left(-i\partial_{t_{1'}} + \omega_{k_{1'}}\right) \cdots \\ &\qquad dt_1\, e^{-i\omega_{k_1} t_1} \left(i\partial_{t_1} + \omega_{k_1}\right) \cdots \\ &\qquad \times \left\langle \mathcal{T}_t \left\{ \phi_{k_{1'}}(t_{1'}) \cdots \phi^\dagger_{k_1}(t_1) \cdots \right\} \right\rangle . \end{aligned} \tag{B.63}$$

Here, $\omega_k = |k|$ is the energy of the photon. Note that the real time-ordered correlation function appears in this expression, which is related to the Matsubara correlation functions in Appendix B.4

by a Wick rotation. This expression greatly simplifies after Fourier transforming to frequency space. When we evaluate diagrams using Wick's theorem, we will come across the following bosonic contractions from the external legs of Feynman diagrams,

$$\left\langle \mathcal{T}_t \left\{ \phi_k(t_1) \phi_k^\dagger(t) \right\} \right\rangle = -i \int \frac{d\omega}{2\pi} \frac{e^{-i\omega(t_1 - t)}}{\omega_k - (\omega + i\epsilon)}. \tag{B.64}$$

These will set the external legs of the Feynman diagrams to their on-shell values, $\omega = \omega_k$, and additionally cancel out the contribution of the external propagators. Then the S matrix elements simply become

$$S = \left\langle \mathcal{T}_t \left\{ \phi_{k_{1'}}(\omega_{k_{1'}}) \cdots \phi_{k_1}^\dagger(\omega_{k_1}) \cdots \right\} \right\rangle_{\text{amp.}}. \tag{B.65}$$

That is, we evaluate the diagram in momentum space with on-shell external legs and omit the external propagators (i.e. we "amputate" the legs).

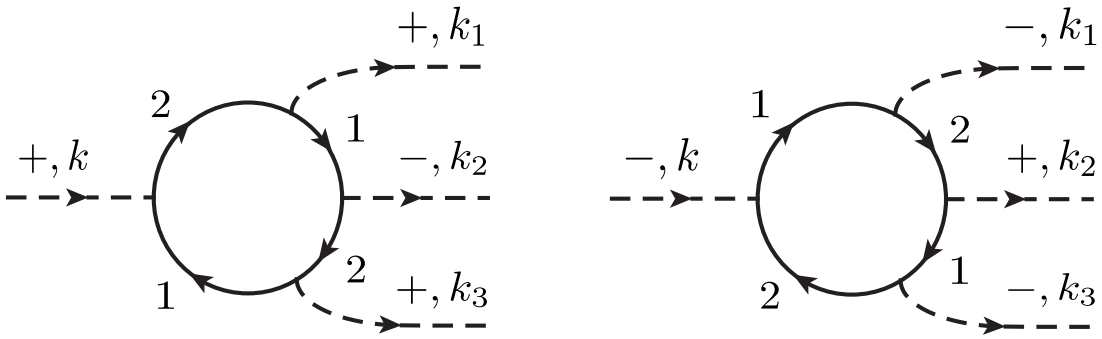

Figure B.3: The nonzero diagrams contributing to the scattering of one photon into three photons.

The symmetry of the model greatly reduces the number of diagrams we need to consider. In particular, the Hamiltonian has a U(1) symmetry [453], and the conserved charge [which is more easily apparent in terms of the $\pm$ photons $\hat{a}_\pm = \frac{1}{2}(\hat{a}_x \pm i\hat{a}_y)$] is

$$Q = \frac{\hat{\sigma}_z + 1}{2} + \sum_k (\hat{a}_{-,k}^\dagger \hat{a}_{-,k} - \hat{a}_{+,k}^\dagger \hat{a}_{+,k}). \tag{B.66}$$

Since the scattering cannot change the spin (as this would require the existence of bound spin-photon eigenstates), it follows that the quantity $\sum_k(\hat{a}^\dagger_{-,k}\hat{a}_{-,k} - \hat{a}^\dagger_{+,k}\hat{a}_{+,k})$ must be conserved in any scattering process.

We now consider the simplest case, where one photon scatters into three photons. The discussion above means that there are only two nonzero diagrams, pictured in Fig. B.3. An explicit calculation finds that to lowest order we have

$$\langle 0|\,\hat{a}_{+,k_1}\hat{a}_{-,k_2}\hat{a}_{+,k_3}S\hat{a}^\dagger_{+,k}\,|0\rangle = \frac{\alpha^2\omega_c^2}{4}\sqrt{\omega\omega_1\omega_2\omega_3}\frac{2\Delta-\omega_1-\omega_3}{(\omega-\Delta)(\omega_1-\Delta)(\omega_3-\Delta)(\omega_2+\Delta)}, \tag{B.67}$$

$$\langle 0|\,\hat{a}_{-,k_1}\hat{a}_{+,k_2}\hat{a}_{-,k_3}S\hat{a}^\dagger_{-,k}\,|0\rangle = \frac{\alpha^2\omega_c^2}{4}\sqrt{\omega\omega_1\omega_2\omega_3}\frac{2\Delta+\omega_1+\omega_3}{(\omega+\Delta)(\omega_1+\Delta)(\omega_3+\Delta)(\omega_2-\Delta)}, \tag{B.68}$$

together with the energy conservation condition $\omega = \omega_1 + \omega_2 + \omega_3$ (enforced by a delta function, which has been omitted in these expressions). Denoting Eq. (B.67) by a function $f(\omega_1, \omega_2, \omega_3; \omega)$, we see that Eq. (B.68) is simply $f(-\omega_1, -\omega_2, -\omega_3; -\omega)$. Alternatively, each amplitude can be found from the other by substituting $\Delta \to -\Delta$ (up to an overall minus sign). This is because the two diagrams in Fig. B.3 are related to each other by replacing $+$ photons with $-$ photons and $-$ photons by $+$ photons. From Appendix B.4 we see that this requires flipping the sign of Δ.

Converting Eqs. (B.67) and (B.68) to the xy basis, we find the four amplitudes

$$\begin{aligned} 4\,\langle 0|\,\hat{a}_{x,k_1}\hat{a}_{x,k_2}\hat{a}_{x,k_3}S\hat{a}^\dagger_{x,k}\,|0\rangle = {} & f(\omega_1,\omega_3,\omega_2;\omega) + f(\omega_1,\omega_2,\omega_3;\omega) \\ & + f(\omega_2,\omega_1,\omega_3;\omega) + f(-\omega_2,-\omega_1,-\omega_3;-\omega) \\ & + f(-\omega_1,-\omega_2,-\omega_3;-\omega) + f(-\omega_1,-\omega_3,-\omega_2;-\omega), \end{aligned} \tag{B.69}$$

$$\begin{aligned} i^3 4\,\langle 0|\,\hat{a}_{y,k_1}\hat{a}_{y,k_2}\hat{a}_{y,k_3}S\hat{a}^\dagger_{x,k}\,|0\rangle = {} & -f(\omega_1,\omega_3,\omega_2;\omega) - f(\omega_1,\omega_2,\omega_3;\omega) \\ & - f(\omega_2,\omega_1,\omega_3;\omega) + f(-\omega_2,-\omega_1,-\omega_3;-\omega) \\ & + f(-\omega_1,-\omega_2,-\omega_3;-\omega) + f(-\omega_1,-\omega_3,-\omega_2;-\omega), \end{aligned} \tag{B.70}$$

$$\begin{aligned} i^2 4\,\langle 0|\,\hat{a}_{x,k_1}\hat{a}_{y,k_2}\hat{a}_{y,k_3}S\hat{a}^\dagger_{x,k}\,|0\rangle = {} & -f(\omega_1,\omega_3,\omega_2;\omega) - f(\omega_1,\omega_2,\omega_3;\omega) \\ & + f(\omega_2,\omega_1,\omega_3;\omega) + f(-\omega_2,-\omega_1,-\omega_3;-\omega) \\ & - f(-\omega_1,-\omega_2,-\omega_3;-\omega) - f(-\omega_1,-\omega_3,-\omega_2;-\omega), \end{aligned} \tag{B.71}$$

$$
\begin{aligned}
i4\,\langle 0|\,\hat{a}_{x,k_1}\hat{a}_{x,k_2}\hat{a}_{y,k_3}S\hat{a}^{\dagger}_{x,k}\,|0\rangle = &-f(\omega_1,\omega_3,\omega_2;\omega)+f(\omega_1,\omega_2,\omega_3;\omega)\\
&+f(\omega_2,\omega_1,\omega_3;\omega)-f(-\omega_2,-\omega_1,-\omega_3;-\omega)\\
&-f(-\omega_1,-\omega_2,-\omega_3;-\omega)+f(-\omega_1,-\omega_3,-\omega_2;-\omega).
\end{aligned}
\tag{B.72}
$$

The resulting probabilities are: for $x \to xxx$

$$
\begin{aligned}
\gamma_{xxx}(\omega_1,\omega_2,\omega_3;\omega) = &\frac{\alpha^4\omega_c^4}{16}\omega_1\omega_2\omega_3\omega|\Delta|^2\\
&\times\left|\frac{3\Delta^4-\Delta^2\left(\omega^2-\omega_1\omega_2-\omega_2\omega_3-\omega_1\omega_2\right)-\omega\omega_1\omega_2\omega_3}{(\omega-\Delta)(\Delta+\omega)(\Delta-\omega_1)(\Delta+\omega_1)(\Delta-\omega_3)(\Delta+\omega_3)(\Delta+\omega_2)(\Delta-\omega_2)}\right|^2.
\end{aligned}
\tag{B.73}
$$

This expression is equivalent to the leading-order result given in Ref. [209] for the spin-boson model. This can be understood from the fact that, at leading order, the $x \to xxx$ process does not involve any y photons. Computing the other scattering probabilities, we find that the processes $x \to \{yyy, xxy\}$ have a simple relation to the above process, given by

$$
\gamma_{yyy}(\omega_1,\omega_2,\omega_3;\omega) = \gamma_{xxx}(\omega_1,\omega_2,\omega_3;\omega)\frac{\omega^2}{|\Delta|^2},
\tag{B.74}
$$

$$
\gamma_{xxy}(\omega_1,\omega_2,\omega_3;\omega) = \gamma_{xxx}(\omega_1,\omega_2,\omega_3;\omega)\frac{\omega_3^2}{|\Delta|^2}.
\tag{B.75}
$$

The remaining process, $x \to xyy$, does not have a simple relation to the above expressions. It is explicitly given by

$$
\begin{aligned}
\gamma_{xyy}(\omega_1,\omega_2,\omega_3;\omega) = &\frac{\alpha^4\omega_c^4}{16}\omega_1\omega_2\omega_3\omega|\Delta|^2\\
\times&\left|\frac{\Delta^4+\Delta^2\left(\omega^2-\omega(\omega_2+\omega_3)-\omega_2^2-3\omega_2\omega_3-\omega_3^2\right)+\omega_2\omega_3(\omega_2+\omega_3)^2-\omega\omega_1(\omega_2^2-\omega_2\omega_3+\omega_3^2)}{(\omega-\Delta)(\Delta+\omega)(\Delta-\omega_1)(\Delta+\omega_1)(\Delta-\omega_3)(\Delta+\omega_3)(\Delta+\omega_2)(\Delta-\omega_2)}\right|^2.
\end{aligned}
\tag{B.76}
$$

As with the elastic probabilities, the leading-order calculation leads to poles in the scattering probabilities at the bare spin frequency Δ. We may apply procedures like those in Appendix B.4 to obtain an analytic dependence, which better resembles that of the fully-interacting problem. For

example, by applying the Callan-Symanzik equation to the amplitudes in Eq. (B.67)-(B.68), we will find that the instances of Δ will be corrected to the renormalized value Δ_R. Similarly, if we developed a Dyson equation for this amplitude, we expect that the poles will be softened to broad peaks with a similar width to the peaks seen in the elastic probabilities given in Chapter 3.

From Eq. (B.74), we see that scattering processes involving a photon from one waveguide into three photons in the other waveguide will dominate over scattering entirely within the same waveguide if $\omega \gg \Delta_R$. In this same limit, we do not expect a large region of phase space with very large final ω_3, so γ_{xxy} is expected to be much smaller than γ_{yyy}. We have verified by numerically integrating the above expressions over the possible final frequencies that, when $\omega \gg \Delta_R$, the total cross section for the processes $x \to \{xyy, xxy\}$ are of the same order of magnitude, and they are both much smaller than $x \to yyy$. We also found that the cross section for $x \to xxx$ is much smaller than the three other processes in the same limit. This is consistent with our numerical results, where we found that the inelastic scattering for $\omega \gg \Delta_R$ is dominated by scattering from one photon flavor to the other.

B.6 Comparison with a model without frustration

In this section, we compare the results of Chapter 3 to the more common situation in waveguide QED, without frustration. We assume the same geometry as in Chapter 3 [shown in Fig. B.4], with the spin coupling to two waveguides, but the coupling is via the same operator $\hat{\sigma}_x$. The coupling constant to each waveguide is given by $\alpha_1 = \alpha_2 = \alpha_T/2$.

We obtain the elastic scattering probabilities shown in Fig. B.5 by the same method as described in the Chapter 3 and in Appendices B.2 and B.4 above. For the analytical calculation, the only

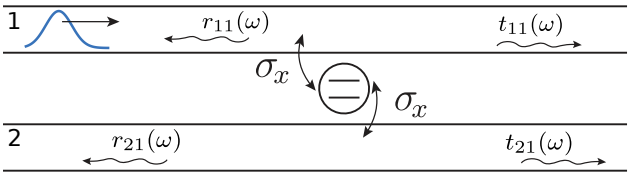

Figure B.4: Schematic of the same model as in Chapter 3 but without frustration. Here the spin-1/2 is coupled locally to two independent waveguides with the same operator $\hat{\sigma}_x$.

major difference is that the ϕ_+ and ϕ_- bosons are now equivalent, so the bottom two vertices in Fig. B.1(b) are equivalent to the top two. The elastic scattering coefficients shown in Fig. B.4 take the form

$$r_{11}(\omega) = r_{21}(\omega) = t_{21}(\omega) = -i\pi\alpha_T\omega\chi_{xx}(\omega), \tag{B.77}$$
$$t_{11}(\omega) = 1 + r_{11}(\omega), \tag{B.78}$$

and the susceptibility computed using the methods of Sec. B.4 is given by

$$\chi_{xx}(\omega) = \frac{-(\omega/\omega_c)^{\alpha_T}\Delta/2}{\Delta^2(\omega/\omega_c)^{2\alpha_T} - \omega^2 - i\pi\alpha_T\Delta\omega(\omega/\omega_c)^{\alpha_T}}. \tag{B.79}$$

Figure B.5 shows that the elastic response has a resonance that is in excellent agreement with the well-known result from the spin-boson [223] or Kondo literature:

$$\Delta_R = \Delta\left(\frac{\Delta}{\omega_c}\right)^{\alpha_T/(1-\alpha_T)}. \tag{B.80}$$

However, we see that, in contrast to the frustrated case, the transmission away from the resonance is very high, whereas the reflection is only nonzero around the Δ_R resonance. Note that $\mathrm{Im}(\chi_{xx}(\omega))$ in Eq. (B.79), describing the spectral weight of the spin, shows a sharp peak at Δ_R. Moreover, the large ω limit of Eq. (B.79) is $\mathrm{Re}(\chi_{xx}(\omega)) \sim \omega^{\alpha_T-2}$ and $\mathrm{Im}(\chi_{xx}(\omega)) \sim \omega^{2\alpha_T-3}$, both of which decay to zero much faster than in the frustrated case. These results are consistent with previous studies [207–210, 212], in other one-dimensional realizations of the spin-boson model. In all of these cases, the system is well described in terms of the polaron or dressed-spin picture. Even

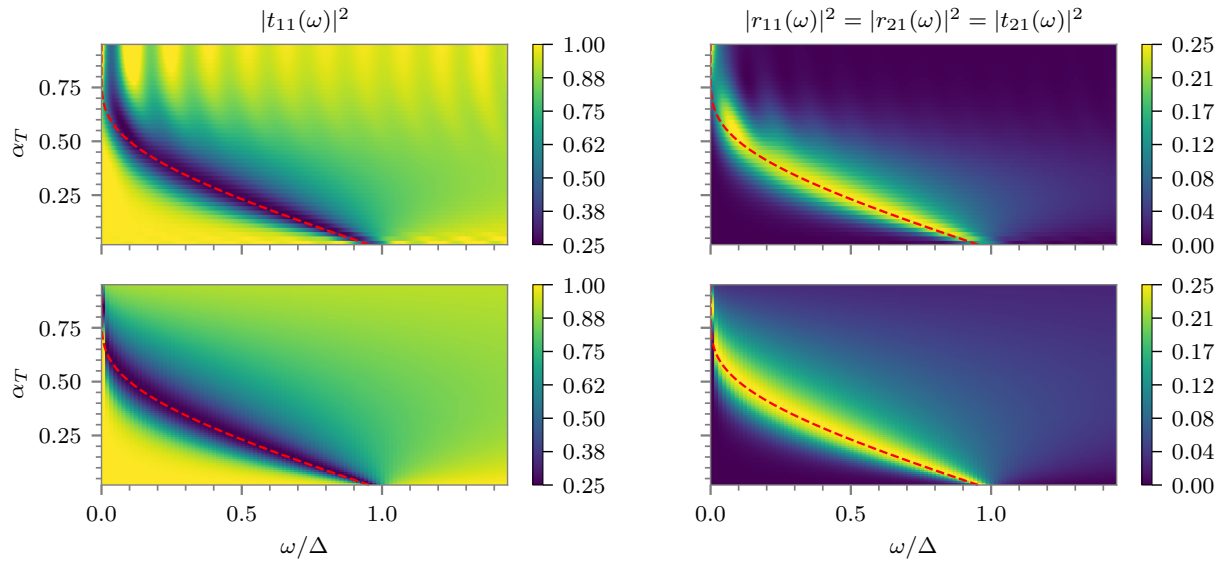

Figure B.5: Numerical (top row) and analytical (bottom row) elastic scattering coefficients for Fig. B.5, as a function of the incoming frequency ω and coupling constant α_T. The red dashed line corresponds to Δ_R from Eq. (B.80). The cutoff is given by $\omega_c = 10\Delta$. The large oscillations at the top of the numerical $|t(\omega)|^2$ are finite time/size effects due to the fact that the scattering takes a very long time at those large couplings.

at very large couplings, where $\Delta_R \to 0$ and the resonance is disappearing, the photons show almost no trace of the coupling to the spin, being almost fully transmitted. This should be contrasted to the frustrated case discussed in Chapter 3, where we have the complete opposite scenario, where the spin becomes extremely widespread over the entire energy spectrum, leading to strong elastic response in the whole range $\omega > \Delta_R$.

Next, we look at the inelastic scattering, employing the same numerical procedure as we used in Chapter 3. We scatter narrow wavepackets and record the resulting number of elastic and inelastic particles, shown in Fig. B.6. Note that because the coupling to both waveguides is the same, the number of inelastic photon emitted in each of the two waveguides is also the same. Hence, we present only the total number of elastic and inelastic photons. We see that the number of elastic photons is always near 1, never going below ~ 0.9 for the wavepackets considered. In fact, since

$\Delta_R/\Delta \approx 0.5$ for $\alpha_T = 0.25$ (see Fig. B.5), most of Fig. B.6 is in the regime $\omega \gg \Delta_R$. The number of inelastic particles does not exceed ~ 0.36, which occurs for the lowest-energy wavepacket $\bar{\omega}_{in} = 0.5\Delta$. In fact, as shown also in Ref. [209], for a given α_T, the inelastic scattering rate peaks at an energy close to Δ_R. For example, for $\alpha_T = 0.5$ (the Toulouse point), the peak occurs at $2\Delta_R$ [209]. This should be contrasted again to the situation with frustration, described in Chapter 3, where we found that the inelastic rate remained *saturated* close to its maximum allowed value 0.5 even for energies above the bar spin gap Δ.

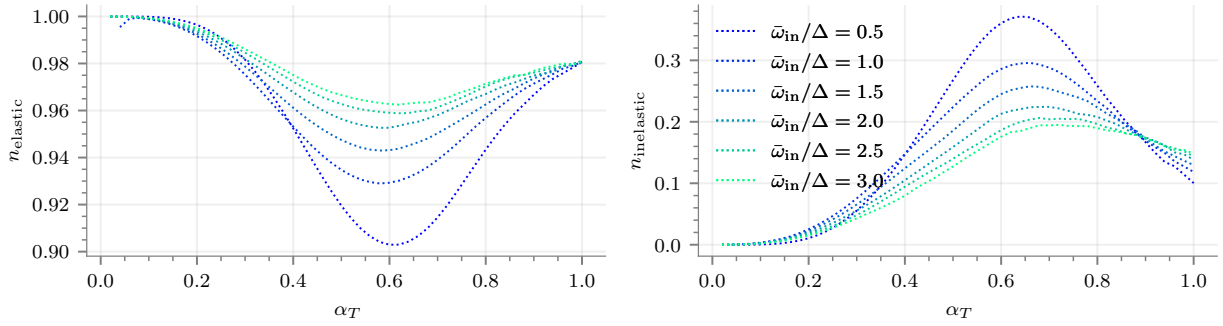

Figure B.6: Numerically computed total number of elastic (left) and inelastic (right) particles as a function of α_T for six different incoming wavepackets, for Fig. B.5. The incoming single-particle wavepackets are Gaussians centered at $\bar{\omega}_{in}$ with a standard deviation of 0.2Δ. The cutoff is $\omega_c = 10\Delta$.

Finally, from Fig. B.5 we also observe that the analytics are in much greater agreement with the numerics, even at very large α. This is consistent with our assertion in Chapter 3, that the disagreement in the frustrated case is due to the fact that inelastic processes are missing from the susceptibility calculation. In the frustrated case, these inelastic processes can be extremely important, accounting for half of the scattering, whereas in the present case with no frustration they are insignificant.

Appendix C: Supplemental Material for Chapter 4

C.1 Experimental setup

C.1.1 Device Design and Fabrication

The photonic crystal is experimentally implemented using 26 lumped-element microwave resonators, capacitively connected in a chain as shown in Fig. 4.1c in Chapter 4. The lumped element resonator geometry was optimized using commercial software. The capacitive elements are implemented as interdigitated structures where the values for both the ground and coupling capacitances are calibrated using ANSYS Maxwell (electrostatic solver). The resonator inductors are implemented as meandered microstrip wires with a 4μm width.The inductance values are inferred from calibrating the resonance frequency of the resonator site using ANSYS HFSS (eigenmode solver) and AWR Microwave Office (AXIEM solver). The inductance of the resonator site coupled to the fluxonium is intentionally made smaller to accommodate the inductive contribution from the fluxonium coupling inductor. The photonic crystal circuit is fabricated using a 200 nm-thick Nb film sputtered on a 525 μm-thick high-purity C-plane sapphire substrate. The components are defined using optical lithography and reactive ion etching, with an attainable minimum feature size of 1μm. The wafer was diced into individual 7x7 mm^2 chips.

The fluxonium artificial atom is composed of a small Josephson junction (100 nm $\times$ 220 nm)

inductively shunted by an array of 38 larger Josephson junctions (190 nm $\times$ 1500 nm) and a tunable inductor, implemented as a chain of four asymmetric SQuIDs. The junctions and superconducting loop were defined via electron-beam lithography using a bi-layer resist MMA(methyl methacrylate)-PMMA(poly methyl methacrylate). The junctions were fabricated via double-angle electron-beam evaporation using a Dolan bridge technique. Aluminum films, with a thickness of 30 nm and 60 nm respectively, were deposited at different angles. The junction electrodes were separated by an AlO_x oxide grown at ambient temperature for 10 minutes in 200 mbar static pressure of a Ar:O_2 (85 %:15 %) gas mixture. After the evaporation of the second aluminum layer, a final oxide was grown using the same gas mixture for 20 minutes at 40 mbar, in order to passivate the surface. After evaporation, the remaining resist was lifted off by leaving the sample in N-Methyl-2-Pyrrolidone (NMP) at 80 °C for 3 hours. The fluxonium is inductively coupled to the edge resonator on the input port of the device. The contact pads for the galvanic connection between the resonator inductor and the fluxonium loop is intentionally made larger (20×50 μm^2) than the inductor width to ensure a small contact resistance.

The fluxonium loop and tunable inductor are magnetically biased using an on-chip flux line where we apply a DC current. The magnetic field induced by the DC current is modelled using the Biot-Savart law, and integrating the field integrated over the area of the loops gives an estimate for the applied magnetic flux. The area of the fluxonium and SQuID loops, as well as their distance with respect to the flux bias line, are designed to achieve a desired ratio of applied flux. Specifically, for a given applied current bias, we want the magnetic flux enclosing the fluxonium loop to be at least an order of magnitude larger than the magnetic flux in each SQuID loop. This large asymmetry allows the flexibility of biasing the qubit to have the same energy spectrum, while sampling various coupling regimes. Taking into consideration screening currents due to the Meissner

effect is not critical for this analysis since we are interested in the ratio of applied flux instead of the absolute values.

The parameters of the circuit are summarized in Table C.1 using the circuit notation outlined in Chapter 4 and in Appendix C.2. The parameter values are inferred from fitting the experimental data.

C.1.2 Cryogenic Setup and Control Instrumentation

The device was mounted to the base stage of a dilution refrigerator, as shown in Fig. C.1. Device shielding consists of a can with two μ-metal layers and an inner aluminum can covered with Stycast. The cryogenic setup, including attenuation and filtering, is shown schematically in Fig. C.1. The resonator chain is connected to two coax cables, an input line used for voltage driving, and an output line used for measuring the transmitted field through the waveguide. The flux bias current is sent through a separate control line with a bandwidth of 12 kHz. The transmitted signal passes through two cryogenic isolators, thermalized at the base stage, and is amplified using a high-electron-mobility transistor (HEMT) amplifier, anchored at the 4 K stage.

The elastic transmission experiments were performed using a Network Analyzer (Keysight N5241A PNA-X) and the inelastic emission experiments were performed using the pulsed setup

Fluxonium	
$E_J/\hbar$	8.17 GHz
$E_L/\hbar$	5.55 GHz
$E_C/\hbar$	3.30 GHz
Resonator chain	
L_r	2.80 nH
L_r' (edge)	$\sim$ 0.1nH
L_c	(4 to 14) nH
C_g	249.15 fF
C_c	202.70 fF

Table C.1: Parameters for the joint qubit and photonic crystal circuit.

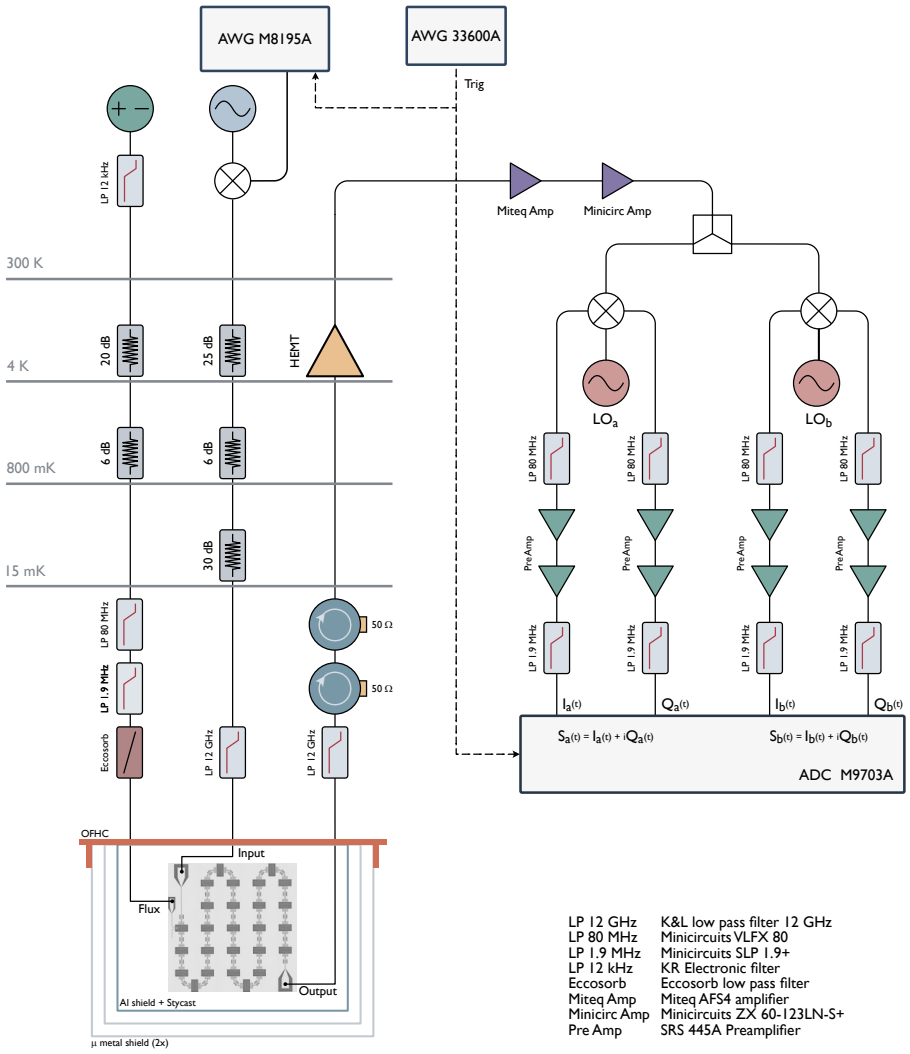

Figure C.1: Experimental setup. Schematic diagram of the cryogenic and instrumentation setup.

shown in Fig. C.1. The microwave pulses used for driving the photonic crystal waveguide are generated using a vector signal generators (Keysight E8267D), with internal wide-band IQ mixing functionality. The base-band and marker pulses are generated with an arbitrary waveform generator (AWG Keysight M8195A). The flux bias current is provided by a low-noise current source (YOKOGAWA GS200). The signal coming out of the fridge is amplified by low-noise room temperature amplifiers. The quadrature components of the output inelastic signal are measured with a

standard two-channel homodyne setup, using an IQ mixer (Marki IQ4509LXP) and local oscillator set in the frequency range of the eigenmode band. After filtering and amplifying the homodyne signal, we digitize it using a fast analog-to-digital converter (ADC) card (Keysight M9703A). For the multi-mode correlations, we split the output signal into two homodyne measurement branches, with separate local oscillators set to the desired eigenmode frequencies. The homodyne voltages in the two branches, $\{I_a(t), Q_a(t)\}$ and $\{I_b(t), Q_b(t)\}$, are extracted simultaneously using the four channels of the ADC card. The complex field amplitudes $S_{a,b}(t) = I_{a,b}(t) + iQ_{a,b}(t)$ are used for evaluating the second order moments $\langle S_a^* S_a \rangle, \langle S_b^* S_b \rangle, \langle S_a S_b \rangle$.

C.2 Physical model of the circuit

C.2.1 Photonic metamaterial

In this section we describe the lumped-element circuit model for the photonic crystal using various methods that involve characterizing the waveguide eigenmodes and mapping the circuit to a tight-binding lattice model.

C.2.1.1 Chain of coupled cavities

In this section we describe the eigenmodes of the cavity array in terms of its Lagrangian, using the well established circuit quantization formalism [454]. The circuit diagram of the bare (qubit-less) resonator chain is shown in Fig. C.2. The chain consists of N lumped-element resonators, composed of inductors of inductance L and capacitors of capacitance C_g, and their voltages are coupled through a series capacitor of capacitance C_c. This circuit has $2N$ degrees of freedom, equal to the number of nodes, and as it will be made clear later in this section, half of these

degrees of freedom are relevant for this experimental study. In the realistic experimental scenario, the resonator array is capacitively coupled to waveguides at the input and output ports, which we model as impedance terminations Z_{in} and Z_{out}, respectfully. The useful variables to describe the Lagrangian are the flux Φ_n and electric voltages $\dot{\Phi}_n$ at each node $n \in [1, 2N]$. The drawback of this formalism is not being able to take into account the impedance at the input and output ports, except for the limits when they tend to zero or infinity. The Lagrangian of the cavity chain for the boundary conditions Z_{in}, $Z_{\text{out}} \to 0$ is given by

$$\mathcal{L}_{\text{cca}} = \sum_{n=1}^{N} \left[\frac{C_\Sigma}{2} \left(\dot{\Phi}_{2n-1}^2 + \dot{\Phi}_{2n}^2 \right) - C_c \dot{\Phi}_{2n} \dot{\Phi}_{2n+1} - \frac{1}{2L} \left(\Phi_{2n} - \Phi_{2n-1} \right)^2 \right], \tag{C.1}$$

where the summation is performed over every resonator unit cell, and we define $C_\Sigma \triangleq C_g + C_c$. Since the chain contains only linear elements, the Lagrangian is quadratic in the coordinate variables. This allows the Lagrangian to be written in a compact matrix form

$$\mathcal{L}_{\text{cca}} = \frac{1}{2} |\Phi\dot{\vec{\rangle}}\langle\Phi|^{\text{t}} |C\hat{\rangle}\langle C| \, |\Phi\dot{\vec{\rangle}}\langle\Phi| - \frac{1}{2} |\Phi\vec{\rangle}\langle\Phi|^{\text{t}} |L\hat{\rangle}\langle L|^{-1} |\Phi\vec{\rangle}\langle\Phi| \tag{C.2}$$

where we define the flux and voltage coordinate vectors as

$$|\Phi\vec{\rangle}\langle\Phi| = \begin{pmatrix} \Phi_1 \\ \Phi_2 \\ \vdots \\ \Phi_{2N} \end{pmatrix} \qquad |\Phi\dot{\vec{\rangle}}\langle\Phi| = \begin{pmatrix} \dot{\Phi}_1 \\ \dot{\Phi}_2 \\ \vdots \\ \dot{\Phi}_{2N} \end{pmatrix} \tag{C.3}$$

and we used the following capacitance $|C\hat{\rangle}\langle C|$ and inductance $|L\hat{\rangle}\langle L|$ matrices

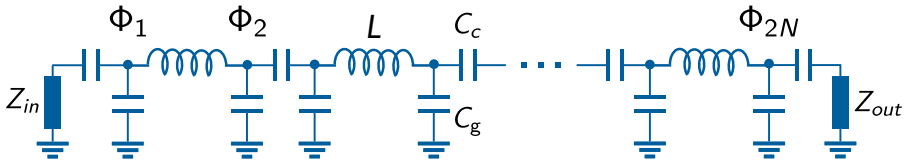

Figure C.2: Circuit diagram for a discretized photonic crystal. Schematic diagram of a one-dimensional chain of capacitively coupled microwave resonators.

$$|C\hat{\rangle}C| = \begin{pmatrix} C_\Sigma & & & & & & \\ & C_\Sigma & -C_c & & & & \\ & -C_c & C_\Sigma & & & & \\ & & \ddots & \ddots & \ddots & & \\ & & & & C_\Sigma & -C_c & \\ & & & & -C_c & C_\Sigma & \\ & & & & & & C_\Sigma \end{pmatrix} \qquad |L\hat{\rangle}L|^{-1} = \frac{1}{L}\begin{pmatrix} 1 & -1 & & & & & \\ -1 & 1 & & & & & \\ & & 1 & -1 & & & \\ & & -1 & 1 & & & \\ & & & & \ddots & \ddots & \ddots \\ & & & & & 1 & -1 \\ & & & & & -1 & 1 \end{pmatrix}. \tag{C.4}$$

If we focus on a single unit cell, we can characterize the resonator in terms of the voltage $\dot{\Phi}_{2n} - \dot{\Phi}_{2n-1}$ across the series ground capacitor and current $\Phi_{2n} - \Phi_{2n-1}$ flowing through the inductor. This argument will also become clear when visiting the treatment for galvanically coupling the fluxonium to a unit cell. It becomes more intuitive to describe the resonator chain in a different coordinate basis $\Phi_n^\pm \triangleq \Phi_{2n} \pm \Phi_{2n-1}$, defined by *differential* Φ_n^- and *center of mass* (COM) Φ_n^+ degrees of freedom for $n \in [0, N]$. The corresponding Lagrangian in this basis becomes

$$\mathcal{L}_{\text{cca}}^\pm = \sum_{n=1}^{N}\left[\frac{C_\Sigma}{4}\left(\dot{\Phi}_n^{-2} + \dot{\Phi}_n^{+2}\right) - \frac{C_c}{4}\left(\dot{\Phi}_n^+ + \dot{\Phi}_n^-\right)\left(\dot{\Phi}_{n+1}^+ + \dot{\Phi}_{n+1}^-\right) - \frac{1}{2L}\Phi_n^{-2}\right]. \tag{C.5}$$

We can also write it in a similar compact matrix form

$$\mathcal{L}_{\text{cca}}^\pm = \frac{1}{2}\,|\dot{\Phi}\hat{\rangle}\vec{\Phi}|_\pm^{\text{t}}|C\hat{\rangle}C|_\pm\,|\dot{\Phi}\hat{\rangle}\vec{\Phi}|_\pm - \frac{1}{2}|\Phi\hat{\rangle}\vec{\Phi}|_\pm^{\text{t}}|L\hat{\rangle}L|_\pm^{-1}|\Phi\hat{\rangle}\vec{\Phi}|_\pm \tag{C.6}$$

with basis vectors in the differential/COM coordinates

$$|\Phi\vec{\rangle\langle}\Phi|_{\pm} = \begin{pmatrix} \Phi_1^{\pm} \\ \Phi_2^{\pm} \\ \vdots \\ \Phi_{2N}^{\pm} \end{pmatrix} \qquad |\Phi\dot{\vec{\rangle\langle}}\Phi|_{\pm} = \begin{pmatrix} \dot{\Phi}_1^{\pm} \\ \dot{\Phi}_2^{\pm} \\ \vdots \\ \dot{\Phi}_N^{\pm} \end{pmatrix}, \tag{C.7}$$

and with different capacitance and inductance matrices

$$|C\hat{\rangle\langle}C|_{\pm} = \begin{pmatrix} C_\alpha & & C_\beta & -C_\beta & & & & & & \\ & C_\alpha & C_\beta & -C_\beta & & & & & & \\ C_\beta & C_\beta & C_\alpha & & C_\beta & C_\beta & & & & \\ -C_\beta & -C_\beta & & C_\alpha & -C_\beta & -C_\beta & & & & \\ & & C_\beta & -C_\beta & C_\alpha & & & & & \\ & & C_\beta & -C_\beta & & C_\alpha & & & & \\ & & & & & & \ddots & & C_\beta & -C_\beta \\ & & & & & & & & C_\beta & -C_\beta \\ & & & & & & C_\beta & C_\beta & C_\alpha & \\ & & & & & & -C_\beta & -C_\beta & & C_\alpha \end{pmatrix} \tag{C.8}$$

$$|L\hat{\rangle\langle}L|_{\pm}^{-1} = \frac{1}{L} \begin{pmatrix} 1 & 0 & & & & \\ & 1 & 0 & & & \\ & & & \ddots & & \\ & & & & 1 & 0 \end{pmatrix}, \tag{C.9}$$

where for abbreviation purposes we defined $C_\alpha = C_\Sigma/2$ and $C_\beta = C_c/4$.

The Euler-Lagrange equation of motion takes the form of a wave equation

$$|\Phi\ddot{\vec{\rangle\langle}}\Phi|_{\pm} + |C\hat{\rangle\langle}C|_{\pm}^{-1}|L\hat{\rangle\langle}L|_{\pm}^{-1}|\Phi\vec{\rangle\langle}\Phi|_{\pm} = 0, \tag{C.10}$$

where the normal mode resonance frequencies of the chain ω_{k} are the positive square roots of the eigenvalues of the matrix $|C\hat{\rangle\langle}C|_{\pm}^{-1}|L\hat{\rangle\langle}L|_{\pm}^{-1}$. The matrices $|C\hat{\rangle\langle}C|^{-1}|L\hat{\rangle\langle}L|^{-1}$ and $|C\hat{\rangle\langle}C|_{\pm}^{-1}|L\hat{\rangle\langle}L|_{\pm}^{-1}$ are connected through a basis transformation $|\Phi\vec{\rangle\langle}\Phi|_{\pm} = \mathbf{U}_{\pm}|\Phi\vec{\rangle\langle}\Phi|$ and therefore have the same eigenfrequencies. Inspecting the eigenvalue spectrum, N of these eigenvalues have zero-frequency while the other N modes have the desired cosine dispersion expected for a tight-binding chain. These zero-frequency eigenvalues correspond to the static COM variables Φ_n^+, while the dispersive band centered around the bare resonator frequency corresponds to the dynamics of the coupled

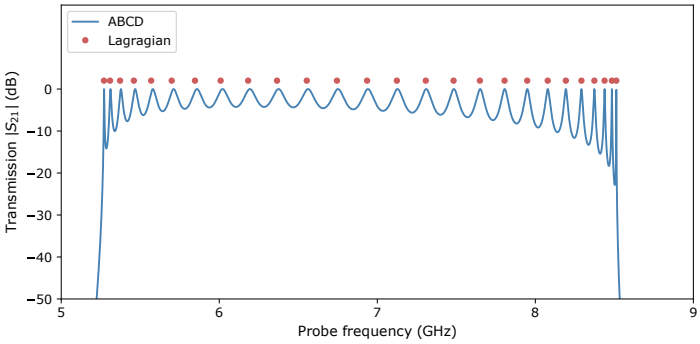

Figure C.3: Calculated transmission in a resonator chain using ABCD matrices. Solid line (blue) corresponds to the magnitude of the transmission coefficient using the ABCD matrix approach. Data points (red) correspond to the eigenmode frequencies of the circuit Lagrangian. .

differential variables Φ_n^-. This transformation $\mathbf{U}_\pm$ becomes convenient for rewriting the eigenvectors in a different basis that allows us to differentiate static degrees of freedom from the oscillator degrees of freedom. Although, from Eq. C.6, the differential and COM variables are coupled to each other through their voltages, the effect on the tight-binding model for the differential degrees of freedom is a minimal, small renormalization of the hopping parameters. For the remainder of this theoretical treatment, we will not consider these zero frequency eigenvalues and focus only on the differential normal modes of the chain.

C.2.1.2 ABCD matrix calculation

Here we apply the ABCD matrix formalism, used extensively for calculating the scattering parameters of a circuit with an arbitrary configuration, probed at any given frequency. Circuits with multiple ports can be conveniently analyzed by decomposing them into two-port modules connected in series. Any two-port circuit can be described in terms of a 2×2 matrix which relates the voltage V_j and current I_j between each port as

$$\begin{pmatrix} V_1 \\ I_1 \end{pmatrix} = \begin{pmatrix} A & B \\ C & D \end{pmatrix} \begin{pmatrix} V_2 \\ I_2 \end{pmatrix}. \tag{C.11}$$

The convenience lies in the fact that the ABCD matrix of several two-port networks connected in series is given by the product of the ABCD matrices of each network.

For the case of our photonic crystal circuit, the ABCD matrix of a single lumped-element resonator can be extracted from the individual matrices for the series inductor and parallel capacitor to ground

$$\begin{aligned} \mathbf{M}_{\mathrm{uc}}(\omega) &= \mathbf{M}_{\mathrm{C_g}} \mathbf{M}_{\mathrm{L}} \mathbf{M}_{\mathrm{C_g}} \\ &= \begin{pmatrix} 1 & 0 \\ \mathrm{j}\omega C_g & 1 \end{pmatrix} \cdot \begin{pmatrix} 1 & \mathrm{j}\omega L \\ 0 & 1 \end{pmatrix} \cdot \begin{pmatrix} 1 & 0 \\ \mathrm{j}\omega C_g & 1 \end{pmatrix}. \end{aligned} \tag{C.12}$$

The unit cells are connected in series through a coupling capacitor, and the edge unit cells are capacitvely coupled to a section L of a coplanar waveguide with a characteristic impedance $Z_0 = 50\,\Omega$ and phase velocity v_p. The matrix terms for these additional components are given by

$$\mathbf{M}_{\mathrm{C_c}} = \begin{pmatrix} 1 & \mathrm{j}/\omega C_c \\ 0 & 1 \end{pmatrix} \qquad \mathbf{M}_{\mathrm{cpw}} = \begin{pmatrix} \cos(\omega L/v_p) & \mathrm{j}Z_0 \sin(\omega L/v_p) \\ \mathrm{j}\sin(\omega L/v_p)/Z_0 & \cos(\omega L/v_p) \end{pmatrix}. \tag{C.13}$$

From the periodicity of the circuit, the ABCD matrix of the entire resonator chain becomes

$$\mathbf{M}_{\mathrm{cca}}(\omega) = \mathbf{M}_{\mathrm{cpw}}\, \mathbf{M}_{\mathrm{C_c}}\, \left[\mathbf{M}_{\mathrm{uc}} \mathbf{M}_{\mathrm{C_c}}\right]^N\, \mathbf{M}_{\mathrm{cpw}}. \tag{C.14}$$

Since we are interested in the transmission coefficient through the device, we can easily calculate the scattering parameter S_{21} using the ABCD matrix of the chain

$$S_{21}(\omega) = \frac{2}{A + B/Z_0 + CZ_0 + D}, \tag{C.15}$$

where A, B, C, and D are functions of the probe frequency ω.

The advantage of this method over the Lagrangian approach is the capability of finding the eigenmodes of the circuit for arbitrary boundary conditions set by input and output port impedances Z_{in} and Z_{out}, which are set to $50\,\Omega$ for this experiment. The eigenmode frequencies correspond to the resonances found in transmission. In the Lagrangian case, as mentioned in the previous section, these impedances can only be set to zero or infinity. The small disadvantage of this method is that the precision of eigenmode values is set by the resolution of the frequency grid in which you are evaluating the ABCD matrices, whereas diagonalizing a $2N \times 2N$ matrix can be more efficient. We combine both methods for determining the circuit parameters of the device.

For completeness, we compare these two methods as shown in Fig. C.3. The eigenfrequencies of the differential modes, inferred from the eigenvalues of the $|C\hat{\rangle}\langle C|_{\pm}^{-1}|L\hat{\rangle}\langle L|_{\pm}^{-1}$ matrix, are overlayed on top of the magnitude of the transmission coefficient $|S_{21}|$ evaluated over a frequency range that captures the dispersive single-photon band. The eigenfrequencies align with the resonance frequencies found as Lorentzian peaks in transmission, with small discrepancies ranging between 1 MHz to 10 MHz. Both calculations are performed with the circuit parameters used in the experiment, displayed in Table C.1, which yield similar eigenmode frequencies.

C.2.1.3 Tight-binding model

In this section the circuit Lagrangian is translated into a tight-binding model, which is a more familiar approach for describing lattices in condensed matter. The first step is to move to the Hamiltonian picture, described using the flux Φ_n and charge Q_n at each node. The charge variables are conjugate momenta of the node fluxes, and are found from $|Q\vec{\rangle}\langle Q| = \partial\mathcal{L}_{\text{cca}}/\partial\,|\dot{\Phi}\vec{\rangle}\langle\Phi| = \hat{\mathbf{C}}\,|\dot{\Phi}\vec{\rangle}\langle\Phi|$, where $|Q\vec{\rangle}\langle Q|$ represents the basis vector for all the node charges $(Q_1, Q_2, \ldots Q_{2N})^{\text{t}}$. A similar

relationship holds in the differential/COM basis $|Q\vec{\rangle\langle}Q|_{\pm} = \hat{\mathbf{C}}_{\pm}\,|\Phi\dot{\vec{\rangle\langle}}\Phi|_{\pm}$. Using the Lagrangian in Eq. C.6, we can obtain the Hamiltonian for the resonator chain from a Legendre transformation

$$\mathbf{H}^{\pm}_{\text{cca}} = \frac{1}{2}|Q\vec{\rangle\langle}Q|^{\text{t}}_{\pm}|C\hat{\rangle\langle}C|^{-1}_{\pm}|Q\vec{\rangle\langle}Q|_{\pm} + \frac{1}{2}|\Phi\vec{\rangle\langle}\Phi|^{\text{t}}_{\pm}|L\hat{\rangle\langle}L|^{-1}_{\pm}|\Phi\vec{\rangle\langle}\Phi|_{\pm} \tag{C.16}$$

Following the discussion from section C.2.1.1, we can expand the Hamiltonian in terms of differential variables, and purposefully write it in this form

$$\mathbf{H}^{\pm}_{\text{cca}} = \sum_{j}\left(\frac{1}{2}\left[|C\hat{\rangle\langle}C|^{-1}_{\pm}\right]_{j,j}Q_j^{-2} + \frac{1}{2}\left[|L\hat{\rangle\langle}L|^{-1}_{\pm}\right]_{j,j}\Phi_j^{-2}\right) + \sum_{\langle i,j\rangle}\left[|C\hat{\rangle\langle}C|^{-1}_{\pm}\right]_{i,j}Q_i^{-}Q_j^{-}, \tag{C.17}$$

where we decouple harmonic oscillator terms containing quadratic charge and flux variables with the same resonator coordinate, from terms which couple the charge degrees of freedom of different resonators.

Moving to the quantum picture, the flux Φ and charge Q variables are promoted to quantum variables, $\mathbf{\Phi}$ and $\mathbf{Q}$, which obey the canonical commutation relation for bosonic operators $[\mathbf{\Phi}_n, \mathbf{Q}_m] = \mathrm{i}\hbar\delta_{n,m}$. As we do for the case of a single harmonic oscillator, we can express the charge and flux operators in terms of bosonic ladder operators

$$\mathbf{Q}_j^{-} = \mathrm{i}\sqrt{\frac{\hbar}{2}}\,Z_j^{-\frac{1}{2}}\,\left(|a\rangle\langle a|_j^{\dagger} - |a\rangle\langle a|_j\right) \qquad \mathbf{\Phi}_j^{-} = \sqrt{\frac{\hbar}{2}}\,Z_j^{\frac{1}{2}}\,\left(|a\rangle\langle a|_j^{\dagger} + |a\rangle\langle a|_j\right),$$

where $|a\rangle\langle a|_j^{\dagger}$ ($|a\rangle\langle a|_j$) create (annihilate) photons in the j^{th} resonator, and the resonator's characteristic impedance which enters in the zero point fluctuation amplitudes is given by $Z_j \triangleq \left[|C\hat{\rangle\langle}C|^{-1}_{\pm}\right]^{\frac{1}{2}}_{j,j} / \left[|L\hat{\rangle\langle}L|^{-1}_{\pm}\right]^{\frac{1}{2}}_{j,j}$. Inserting the quantum operators into the Hamiltonian in Eq. C.16 gives the following tight-binding model for describing the photonic lattice

$$\mathbf{H}_{\text{tb}}/\hbar = \sum_j \omega_j \left(|a\rangle\langle a|_j^\dagger \, |a\rangle\langle a|_j + \frac{1}{2} \right) + \sum_{\langle i,j \rangle} t_{i,j} \left(|a\rangle\langle a|_i^\dagger - |a\rangle\langle a|_i \right) \left(|a\rangle\langle a|_j^\dagger - |a\rangle\langle a|_j \right), \quad \text{(C.18)}$$

where the first summation takes into account the on-site energy given by the resonator frequency ω_j, and the second summation accounts for the tunneling of microwave excitations between nearest neighbor oscillators with a tunneling rate $t_{i,j}$. These terms can be easily extracted from the capacitance and inductance matrices in the circuit model

$$\omega_j \triangleq \left[|L\hat{\rangle}\langle L|_{\pm}^{-1} \right]_{j,j}^{\frac{1}{2}} \left[|C\hat{\rangle}\langle C|_{\pm}^{-1} \right]_{j,j}^{\frac{1}{2}} \qquad t_{i,j} \triangleq -\frac{1}{2} \left(Z_i Z_j \right)^{-\frac{1}{2}} \left[|C\hat{\rangle}\langle C|_{\pm}^{-1} \right]_{i,j}. \quad \text{(C.19)}$$

Describing the photonic crystal in this tight-binding model provides a more intuitive representation which we will adopt for modeling transport through the lattice doped with an impurity.

C.2.2 Galvanically coupled impurity

In this section we analyze and derive the microscopic model for a fluxonium circuit, which plays the role of a highly nonlinear impurity, embedded in the photonic crystal. At first we will thoroughly formulate the coupling to a single unit cell, a resonator, and extend that to the full oscillator chain.

C.2.2.1 Coupling to a single unit cell

The circuit diagram for a fluxonium qubit galvanically coupled to a single lumped-element resonator is shown in Fig. C.4. The independent resonator circuit has a total inductance of L_r and a capacitance to ground C_r at both resonator nodes. The fluxonium circuit consists of a Josephson junction, with a characteristic critical current I_c and energy E_J, shunted by its self-capacitance

C_q and by an inductor implemented using a linear array of larger Josephson junctions. The total inductance consists of two sections: one section of total inductance L_q independent from the resonator circuit, and a smaller section of inductance L_c shared between the resonator and fluxonium which leads to their currents being coupled. This mutual inductive coupling will lead to a magnetic dipole interaction between the resonator field and the qubit phase difference across the Josephson junction. A static magnetic flux Φ_{ext} is externally applied to the fluxonium loop.

The equations of motion for the node fluxes are given by Kirchoff's law of current conservation at each node

$$\begin{aligned}
\frac{2}{L_r}\left(\Phi_R-\Phi_b\right)+C_r\ddot{\Phi}_R&=0 \qquad \text{(node R)}\\
\frac{2}{L_r}\left(\Phi_L-\Phi_a\right)+C_r\ddot{\Phi}_L&=0 \qquad \text{(node L)}\\
\frac{2}{L_q}\left(\Phi_2-\Phi_b\right)+I_c\sin\frac{2\pi}{\Phi_0}\left(\Phi_2-\Phi_1-\Phi_{\text{ext}}\right)+C_q\left(\ddot{\Phi}_2-\ddot{\Phi}_1\right)&=0 \qquad \text{(node 1)}\\
\frac{2}{L_q}\left(\Phi_1-\Phi_a\right)-I_c\sin\frac{2\pi}{\Phi_0}\left(\Phi_2-\Phi_1-\Phi_{\text{ext}}\right)-C_q\left(\ddot{\Phi}_2-\ddot{\Phi}_1\right)&=0 \qquad \text{(node 2)}\\
\frac{2}{L_r}\left(\Phi_R-\Phi_b\right)-\frac{1}{L_c}\left(\Phi_b-\Phi_a\right)-\frac{2}{L_q}\left(\Phi_b-\Phi_2\right)&=0 \qquad \text{(node a)}\\
\frac{2}{L_r}\left(\Phi_L-\Phi_a\right)+\frac{1}{L_c}\left(\Phi_b-\Phi_a\right)-\frac{2}{L_q}\left(\Phi_a-\Phi_1\right)&=0 \qquad \text{(node b).}
\end{aligned} \tag{C.20}$$

Similar to the analysis for the resonator chain, we define the new variables $\Phi_r^{\pm}\triangleq\Phi_R\pm\Phi_L$, $\Phi_q^{\pm}\triangleq\Phi_2\pm\Phi_1$, $\Phi_s^{\pm}\triangleq\Phi_b\pm\Phi_a$. Combining the above equations, we arrive at the equations of motion for the differential variables

$$\begin{aligned}
\frac{2}{L_r}\left(\Phi_r^-\right)+C_r\ddot{\Phi}_r^-&=0\\
\frac{2}{L_q}\left(\Phi_q^-\right)+2I_c\sin\frac{2\pi}{\Phi_0}\left(\Phi_q^-\right)+2C_q\ddot{\Phi}_q^-&=0\\
\frac{2}{L_r}\left(\Phi_r^-\right)-\frac{2}{L_c}\Phi_s^-&=0.
\end{aligned} \tag{C.21}$$

From the last equation we can express the shunt differential variable Φ_s^- in terms of the resonator

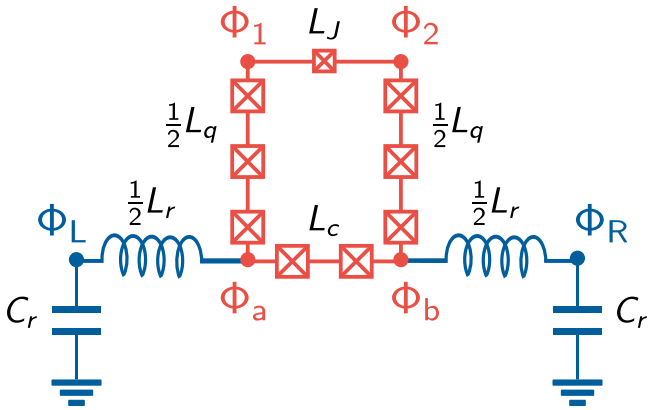

Figure C.4: Circuit diagram for a galvanically coupled fluxonium. Schematic diagram for a fluxonium artificial atom current-coupled to a single microwave resonator, through a mutually shared inductor.

Φ_r^- and fluxonium Φ_q^- differential variables

$$\Phi_s^- = \frac{L_q L_c}{L_\Sigma^2}\Phi_r^- + \frac{L_r L_c}{L_\Sigma^2}\Phi_q^-, \tag{C.22}$$

where for brevity we define $L_\Sigma^2 \triangleq L_r L_q + L_q L_c + L_c L_r$.

In combining Eqs. C.20 we find that the fluxonium and resonator have the same center of mass $\Phi_q^+ = \Phi_r^+ = \Phi_s^+$, as expected from the symmetry of the circuit. Additionally, the COM variables are not coupled to the differential ones, in particular the phase difference across the qubit junction Φ_q^- which captures the internal fluxonium states. For the remainder of the analysis we consider only the differential variables. Replacing the shunt variable (Eq. C.22) in Eq. C.21 gives a set of equations just for the resonator and fluxonium

$$\begin{aligned} \frac{L_q + L_c}{L_\Sigma^2}\Phi_r^- + \frac{C_r}{2}\ddot{\Phi}_r^- - \frac{L_c}{L_\Sigma^2}\Phi_q^- &= 0 \\ \frac{L_r + L_c}{L_\Sigma^2}\Phi_q^- + I_c \sin\frac{2\pi}{\Phi_0}\left(\Phi_q^- - \Phi_{\text{ext}}\right) + C_q\ddot{\Phi}_q^- - \frac{L_c}{L_\Sigma^2}\Phi_r^- &= 0. \end{aligned} \tag{C.23}$$

The Euler-Lagrange equations of motion can be directly derived from the following Lagrangian

$$\begin{aligned}\mathcal{L} = &\frac{1}{2}\left(\frac{C_r}{2}\right)\dot{\Phi}_r^{-2} - \frac{1}{2}\frac{L_q + L_c}{L_\Sigma^2}\Phi_r^{-2} + \frac{L_c}{L_\Sigma^2}\Phi_r^-\Phi_q^- \\ &+ \frac{1}{2}C_q\dot{\Phi}_q^{-2} - \frac{1}{2}\frac{L_r + L_c}{L_\Sigma^2}\Phi_q^{-2} + E_J\cos\frac{2\pi}{\Phi_0}\left(\Phi_q^- - \Phi_{\text{ext}}\right).\end{aligned} \tag{C.24}$$

The canonical conjugate momenta, corresponding to the charge variables, are given by $Q_r^- = \partial\mathcal{L}/\partial\dot{\Phi}_r^- = (C_r/2)\dot{\Phi}_r^-$ for the resonator and $Q_q^- = \partial\mathcal{L}/\partial\dot{\Phi}_q^- = C_q\dot{\Phi}_q^-$ for the fluxonium. Following the Legendre transformation we obtain the circuit Hamiltonian

$$\begin{aligned}\mathrm{H} &= Q_r^-\dot{\Phi}_r^- + Q_q^-\dot{\Phi}_q^- - \mathcal{L} \\ &= \frac{1}{C_r}Q_r^{-2} + \frac{1}{2L_r'}\Phi_r^{-2} + \frac{L_c}{L_\Sigma^2}\Phi_r^-\Phi_q^- \\ &+ \frac{1}{2C_q}Q_q^{-2} + \frac{1}{2L_r'}\Phi_q^{-2} - E_J\cos\frac{2\pi}{\Phi_0}\left(\Phi_q^- - \Phi_{\text{ext}}\right)\end{aligned} \tag{C.25}$$

Moving to the quantum picture, the flux and charge variables are promoted to quantum variables, $|\Phi\rangle\langle\Phi|_n$ and $|Q\rangle\langle Q|_n$, which obey the canonical commutation relation for bosonic operators $[|\Phi\rangle\langle\Phi|_n, |Q\rangle\langle Q|_m] = \mathrm{i}\hbar\delta_{n,m}$. For brevity, the minus superscript is removed since all variables are differential. The total Hamiltonian can be decomposed as $\mathbf{H} = \mathbf{H}_\mathrm{r} + \mathbf{H}_\mathrm{q} + \mathbf{H}_\mathrm{int}$ with separate terms corresponding to the resonator, fluxonium and fluxonium-resonator dipole interaction, respectively.

The resonator Hamiltonian can be written in a second quantized form as

$$\mathbf{H}_\mathrm{r} = \frac{1}{C_r}|Q\rangle\langle Q|_r^{\,2} + \frac{1}{2L_r'}|\Phi\rangle\langle\Phi|_r^2 = \hbar\omega_r\left(|a\rangle\langle a|^\dagger\,|a\rangle\langle a| + \frac{1}{2}\right), \tag{C.26}$$

writing the charge and flux operators in terms of raising (lowering) operators $|a\rangle\langle a|^\dagger$ ($|a\rangle\langle a|$), $|\Phi\rangle\langle\Phi|_r = \sqrt{\hbar Z_r/2}\left(|a\rangle\langle a|^\dagger + |a\rangle\langle a|\right)$ and $|Q\rangle\langle Q|_r = \mathrm{i}\sqrt{\hbar/2Z_r}\left(|a\rangle\langle a|^\dagger - |a\rangle\langle a|\right)$. The cavity resonance frequency and impedance is given by $\omega_r = \sqrt{2/L_r'C_r}$ and $Z_r = \sqrt{2L_r'/C_r}$. Due to the galvanic coupling with the fluxonium circuit, the renormalised resonator inductance becomes $L_r' = L_\Sigma^2/(L_q + L_c) = L_r + (L_q \parallel L_c)$, which effectively translates to an inductive contribution

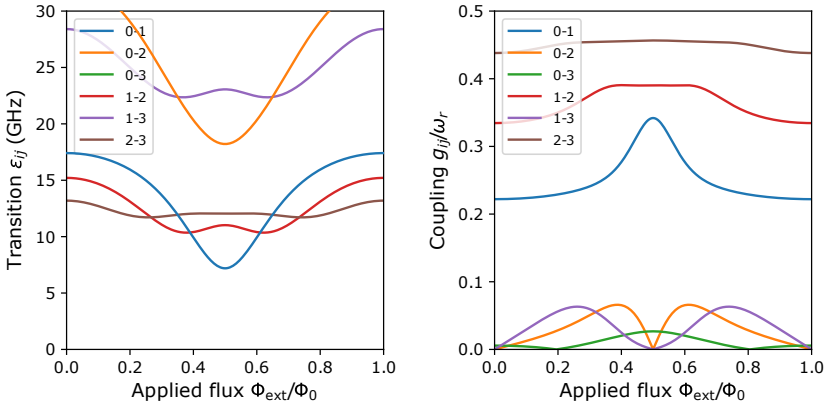

Figure C.5: Fluxonium-resonator coupling strength. (left) Transition frequencies between the ground state and first three excited states of the fluxonium circuit and (right) their normalized coupling strengths with the edge-resonator as a function of applied flux.

from the parallel combination of the bare fluxonium inductance and coupling inductance.

Moving to the fluxonium Hamiltonian, we can write it in the familiar form [276]

$$\mathbf{H}_{\mathrm{q}} = 4E_C|n\rangle\langle n|_q^2 + \frac{1}{2}E_L|\varphi\rangle\langle\varphi|_q^2 - E_J\cos\left(|\varphi\rangle\langle\varphi|_q - \varphi_{\mathrm{ext}}\right) = \sum_l \varepsilon_l|l\rangle\langle l|, \tag{C.27}$$

using the charge number $|n\rangle\langle n|_q = |Q\rangle\langle Q|_q/2e$ and phase $|\varphi\rangle\langle\varphi|_q = 2\pi|\Phi\rangle\langle\Phi|_q/\Phi_0$ operators. The charging and inductive energies are defined as $E_C = e^2/2C_q$ and $E_L = (\Phi_0/2\pi)^2/L'_q$, and the flux bias phase is defined as $\varphi_{\mathrm{ext}} = 2\pi\Phi_{\mathrm{ext}}/\Phi_0$. Similarly due to the galvanic coupling, the renormalized fluxonium inductance becomes $L'_q = L_\Sigma^2/(L_r + L_c) = L_q + (L_r \parallel L_c)$, which effectively translates to an inductive contribution from the parallel combination of the bare resonator inductance and coupling inductance. To calculate the fluxonium eigenspectrum, the phase difference across the junction is discretized in a 1D grid and the operators are expressed in matrix form in this grid basis. The eigenvalues ε_l and eigenstates $|l\rangle$ are then obtained from diagonalizing the fluxonium Hamiltonian in the grid basis.

The magnetic dipole coupling is given by the inductive term

$$
\begin{aligned}
\mathbf{H}_{\text{int}} &= \frac{L_c}{L_\Sigma^2} |\Phi\rangle\langle\Phi|_r \cdot |\Phi\rangle\langle\Phi|_q \\
&= \frac{\omega_r}{Z_r} \frac{L_c}{L_c + L_q} \sqrt{\frac{\hbar Z_r}{2}} \left(|a\rangle\langle a|^\dagger + |a\rangle\langle a| \right) \cdot \frac{\Phi_0}{2\pi} \sum_{l,l'} \langle l||\varphi\rangle\langle\varphi|_q |l'\rangle |l\rangle\langle l'| \\
&= \sum_{l,l'} \hbar g_{l,l'} \, |\sigma\rangle\langle\sigma|_{l,l'} \left(|a\rangle\langle a|^\dagger + |a\rangle\langle a| \right),
\end{aligned}
\tag{C.28}
$$

where we expanded the qubit flux operator in terms of all possible transitions between fluxonium eigenstates $l \rightarrow l'$ coupled to the cavity field through the dipole matrix elements $\langle l||\varphi\rangle\langle\varphi|_q|l'\rangle$. These matrix elements dictate the selection rules for the fluxonium circuit which, unlike the transmon, allow non-trivial dipole transitions between eigenstates differing by more than one quanta. The coupling amplitude between the oscillator current and the fluxonium dipole, normalized by the oscillator resonance frequency, can be rewritten as

$$
\frac{g_{l,l'}}{\omega_r} = \frac{\Phi_0}{2\pi} \frac{L_c}{L_c + L_q} \left(2\hbar Z_r\right)^{-\frac{1}{2}} \; \langle l||\varphi\rangle\langle\varphi|_q|l'\rangle. \tag{C.29}
$$

This form emphasizes how the normalized coupling strength depends on the resonator impedance, fluxonium matrix element, and the inductive participation which sets the fraction of the qubit phase bias $|\varphi\rangle\langle\varphi|_q$ interacting with the resonator. The range of parameters for the full circuit are chosen to reach the USC regime $g_{0,1}/\omega_r \approx 1$ (see Fig. C.5).

C.2.2.2 Tunable coupling

Following the expression in Eq. C.29, the normalized fluxonium-resonator coupling can be varied by tuning the coupling inductor L_c. Operating in the parameter regime $L_q > L_c \gg L_r$, the effective fluxonium shunting inductance $L_q' = L_q + (L_r \parallel L_c) \approx L_q$, and with that E_L, does not significantly depend on L_c. Given that the other parameters E_J and E_C remain fixed, this approach is suitable for maintaining the same fluxonium energy spectrum while varying the light-matter coupling.

The coupling inductor is implemented as a chain of flux-tunable asymmetric SQuIDs as shown in the diagram in Fig. 4.1b. Each SQuID is defined as a ring interrupted by two junctions with different energies, E_{J1} and E_{J2}, with a relative asymmetry defined as $d = (E_{J2} - E_{J1})/(E_{J2} + E_{J1})$. The Hamiltonian for a single SQuID is given by $\mathbf{H}_J = -E_{J1}\cos|\varphi\rangle\langle\varphi|_1 - E_{J2}\cos|\varphi\rangle\langle\varphi|_2$, where $|\varphi\rangle\langle\varphi|_1, |\varphi\rangle\langle\varphi|_2$ denote the phase difference across each junction. For an externally applied magnetic flux Φ_{ext}, these phase differences satisfy the fluxoid quantization condition in the loop $|\varphi\rangle\langle\varphi|_2 - |\varphi\rangle\langle\varphi|_1 + 2\pi\Phi_{\text{ext}}/\Phi_0 = 2\pi m$, where $m \in \mathbb{Z}$. Defining the phase difference across the SQuID as $|\varphi\rangle\langle\varphi| = (|\varphi\rangle\langle\varphi|_2 + |\varphi\rangle\langle\varphi|_1)/2$, the Hamiltonian can be rewritten as a single cosine potential with a tunable junction energy [455]

$$\begin{aligned}\mathbf{H}_J &= -(E_{J1}+E_{J2})\cos\left(\pi\frac{\Phi_{\text{ext}}}{\Phi_0}\right)\sqrt{1+d^2\tan^2\left(\pi\frac{\Phi_{\text{ext}}}{\Phi_0}\right)}\cos\Big(|\varphi\rangle\hat{\langle}\varphi| - \varphi_0\Big) \\ &\triangleq -E'_J(\Phi_{\text{ext}})\cos\Big(|\varphi\rangle\hat{\langle}\varphi| - \varphi_0\Big),\end{aligned} \tag{C.30}$$

where the phase shift in the potential $\varphi_0 = \tan^{-1}[d\tan(\pi\Phi_{\text{ext}}/\Phi_0)]$ can be safely disregarded by a change of variables. The SQuID can be regarded as a flux-tunable inductor $L'_J = (\Phi_0/2\pi)^2/E'_J$. The coupling element is implemented as $M = 4$ SQuIDs connected in series, and has an inductance $L_c = ML'_J$. Since we are using junctions of similar size as the fluxonium inductance, we can treat the SQuID array as a tunable linear inductor and neglect the nonlinearities originating from the cosine potential.

C.2.2.3 Coupling to a resonator chain

After describing the linear resonator chain in Eq. C.18 and the inductive coupling between a resonator and a qubit in Eq. C.28, it becomes straightforward to combine these to describe the full Hamiltonian where the fluxonium is coupled to the multi-mode metamaterial

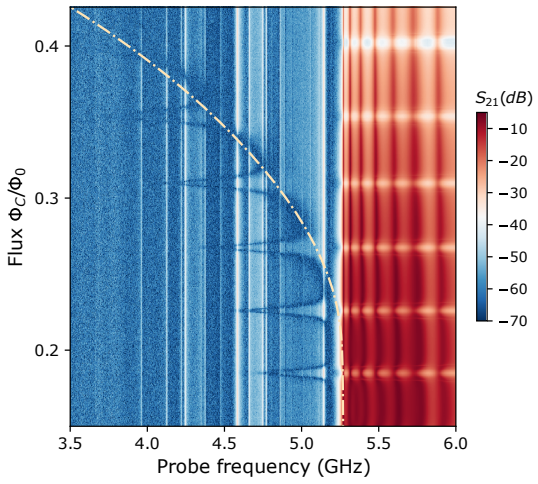

Figure C.6: Coupling inductor calibration. Transmission spectrum near the lower band edge. The frequency shift of the lowest lattice mode is fitted (dotted line) to estimate the values of the SQuID coupling inductors.

$$\begin{aligned}\mathbf{H}/\hbar = &\sum_j \omega_j \left|a\right\rangle\!\left\langle a\right|_j^\dagger \left|a\right\rangle\!\left\langle a\right|_j + \sum_l \varepsilon_l |l\rangle\langle l| \\ &- \sum_{\langle i,j\rangle} t_{ij} \left(\left|a\right\rangle\!\left\langle a\right|_i^\dagger \left|a\right\rangle\!\left\langle a\right|_j + \left|a\right\rangle\!\left\langle a\right|_j^\dagger \left|a\right\rangle\!\left\langle a\right|_i^\dagger \right) + \sum_{l,l'} g_{ll'} \left|\sigma\right\rangle\!\left\langle\sigma\right|_{ll'} \left(\left|a\right\rangle\!\left\langle a\right|_0^\dagger + \left|a\right\rangle\!\left\langle a\right|_0 \right),\end{aligned} \tag{C.31}$$

where the fluxonium is coupled to the edge resonator (site 0) in the tight-binding chain. The expression for the on-site cavity resonances ω_j and photon hopping rates t_{ij} follow the relations in Eq. C.19, with modifications from the inductive coupling element at the edge and finite size of the chain. It is assumed that the fluxonium circuit and the SQuID coupler do not modify the capacitance matrix $|C\hat{\rangle\langle}C|$ for the resonator chain .

The resonator sites in the bulk have the same resonance frequency and impedance, given by $\omega_r = L_r^{-\frac{1}{2}} \left[|C\hat{\rangle\langle}C|_{\pm}^{-1} \right]_{jj}^{\frac{1}{2}}$ and $Z_r = L_r^{\frac{1}{2}} \left[|C\hat{\rangle\langle}C|_{\pm}^{-1} \right]_{jj}^{\frac{1}{2}}$. This makes the hopping rate between the bulk sites $t = t_{ij} = -\frac{1}{2} Z_r \left[|C\hat{\rangle\langle}C|_{\pm}^{-1} \right]_{i,j}$. For the edge site not coupled to the qubit ($j = N$), the diagonal and off-diagonal capacitance matrix elements are different from the bulk since the the edge

is coupled on side to another resonator and on the other to the $50\,\Omega$ waveguide. This difference in the capacitive loading leads to a very small change in the on-site resonance $\omega_N \simeq \omega_r$ and hopping rate $t_{N,N-1} \simeq t$, which is nevertheless taken into consideration in the numerical analysis. In addition to a capacitive perturbation, the edge site coupled to the qubit ($j = 0$) has also an inductive perturbation. The edge resonator inductance has contributions from both the coupler and qubit $L'_r = L_r + (L_q \parallel L_c)$, which is mostly given by the coupler inductance for the choice of device parameters. This leads to modified expressions for the resonance frequency $\omega'_r = L_r'^{\frac{1}{2}} \left[|C\hat{\rangle}\langle C|_{\pm}^{-1}\right]_{1,1}^{\frac{1}{2}}$, impedance $Z'_r = L_r'^{\frac{1}{2}} \left[|C\hat{\rangle}\langle C|_{\pm}^{-1}\right]_{1,1}^{\frac{1}{2}}$ and hopping $t' = -\frac{1}{2}\sqrt{Z_r Z'_r}\left[|C\hat{\rangle}\langle C|_{\pm}^{-1}\right]_{1,2}$. This inductive perturbation leads to a lattice mode being shifted outside the single-particle band. We reduce the bare inductance of this edge resonator such that this perturbation in the resonance frequency does not decouple the edge resonator from the rest of the lattice. Additionally, the frequency shift in the lowest eigenmode is used to extract the SQuID inductor values (see Fig. C.6).

C.2.3 Qubit Stark shift calculation

We attribute the qubit frequency shift in Fig. 4.4b to an ac-Stark shift induced by driving the lowest lattice mode, having a resonant frequency $\omega_{k=0}$ and linewidth κ, and populating it with an average number of photons $\bar{n} = P_d/\hbar\omega_{k=0}\kappa$. The line attenuation in the experimental setup has been calibrated to provide an estimate for the input drive power P_d at the device. The Stark shift is given by $\chi_{k=0,l=1}\bar{n}$, where $\chi_{k,l}$ corresponds to the dispersive shift between the lattice mode k and $|l\rangle$ state of the fluxonium. This dispersive shift was calculated following the procedure outlined in [456] $\chi_{k,l} = \sum_{l'}(\chi_{k,ll'} - \chi_{k,l'l})$. The partial dispersive shifts between mode k and the $l \to l'$ transitions are given by $\chi_{k,ll'} = |g_{k,ll'}|^2/(\varepsilon_{ll'} - \omega_k)$, with the dipole coupling $g_{k,ll'} = u_{k,0}g_{ll'}$ being rescaled by

the eigenmode participation $u_{k,0}$ at the $j = 0$ edge lattice site.

C.3 Elastic scattering

In this section, we present the theoretical modeling of the elastic scattering. We model the device by an infinite tight-binding model, which is locally coupled to a fluxonium, described by the Hamiltonian

$$\begin{aligned}\mathbf{H}/\hbar = \omega_0 \sum_{j=-\infty}^{\infty} |a\rangle\langle a|_j^\dagger \, |a\rangle\langle a|_j - \delta \, |a\rangle\langle a|_0^\dagger \, |a\rangle\langle a|_0 + \sum_l \varepsilon_l |l\rangle\langle l| \\ -t \sum_i \left(|a\rangle\langle a|_i^\dagger \, |a\rangle\langle a|_{i+1} + \text{H.c} \right) + \sum_{l,l'} g_{ll'} \, |\sigma\rangle\langle\sigma|_{ll'} \left(|a\rangle\langle a|_0^\dagger + |a\rangle\langle a|_0 \right),\end{aligned} \tag{C.32}$$

where the fluxonium is coupled to the zeroth cavity, and we take into account the multi-level structure of the Fluxonium, as well as the detuning, δ, of the zeroth cavity frequency due to the coupling inductor.

C.3.1 Scattering coefficients for a two-level system within the rotating-wave approximation

Truncating the fluxonium to the two lowest energy states and performing the rotating-wave approximation (RWA), we can derive simple analytical expressions for the scattering coefficients of a single photon. Writing a single-particle eigenstate as

$$|\psi_k\rangle = \left[\sum_x u_k(x) \, |a\rangle\langle a|_x^\dagger + c_1 \, |\sigma\rangle\langle\sigma|_+ \right] |0, 0_{\mathbf{k}}\rangle, \quad u_k(x) = \begin{cases} e^{ikx} + R_k e^{-ikx}, & x < 0, \\ T_k e^{i\mathbf{k}x}, & 0 < x, \end{cases} \tag{C.33}$$

where $|0, 0_{\mathbf{k}}\rangle$ corresponds to the ground state of the fluxonium and the vacuum of all the photonic

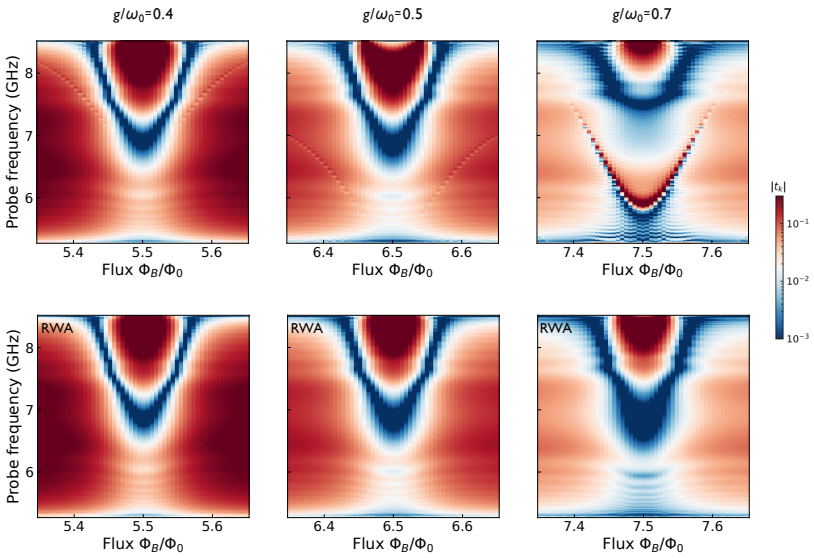

Figure C.7: MPS simulations. Normalized elastic scattering coefficient using MPS, for the coupling strengths g/ω_0 probed in the experiment (see top labels). Upper plots represent the full model, while the lower plots represent the RWA model without the counter-rotating terms.

modes. We can solve for the scattering coefficients R, T, giving

$$\begin{aligned} T_k =& \frac{2t\sin(k)}{-\delta + G(k) - 2ti\sin(k)}, \\ R_k =& -\frac{\delta + G(k)}{-\delta + G(k) - 2ti\sin(k)}, \end{aligned} \tag{C.34}$$

where $G(k) = g^2/(\omega_k - \Delta)$ and $\omega_k = \omega_0 - 2t\cos(k)$. We have also defined $\Delta = \varepsilon_1$ and $g = g_{10}$ for simplicity.

Equation (C.34) admits two resonance-like behaviors. First, when $\Delta = \omega_k$, i.e., the incoming photon is resonant with the qubit transition, we have that $T \to 0, R \to 1$, as expected and as was predicted for a uniform cavity array [457]. Second, when $G(k) - \delta = 0$, i.e., $\omega_k = \Delta + g^2/\delta$, we have $R \to 0, T \to 1$. Thus, we see that the detuned cavity (with detuning δ) acts as an impurity, giving rise to a non-zero reflection even in the absence of the fluxonium.

C.3.2 Matrix-product-states

To go beyond the RWA and the two-level truncation of the fluxonium, we employ matrix-product-states (MPS), using the methods of Refs. [242, 284]. We describe the system in real space, using 200 cavities on each side of the fluxonium. This allows us to simulate the scattering of a single photon free of boundary effects. The on-site bosonic Hilbert space is truncated to 5 Fock states, and all results were found to have converged at this value. To obtain the elastic scattering coefficients we perform the procedure from [242]. We first find the ground state $|GS\rangle$ of the Hamiltonian in Eq. (C.32) using the density-matrix-renormalization-group method. We then create a single-photon Gaussian wavepacket on top of the ground state, i.e., we create the state $|\psi(t=0)\rangle = \sum_x c_x \left|a\right\rangle\!\left\langle a\right|_x^\dagger |GS\rangle$, where $c_x = \mathcal{N} e^{-\frac{(x-x_0)^2}{2\sigma^2}+ik_0x}$, and $\mathcal{N}$ is a normalization so that $\sum_x |c_x|^2 = 1$. We choose the wavepacket parameters so that it spans the whole frequency band, and so that it starts localized on one side of the spin. We then evolve this state for a sufficiently long time t_∞, until the scattering process has ended. From the resulting state, $|\psi(t_\infty)\rangle$, we extract the overlaps $\langle GS|\left|a\right\rangle\!\left\langle a\right|_x |\psi(t_\infty)\rangle$ for all x. Fourier transforming this quantity, and dividing by c_k (the Fourier transform of the wavepacket c_x) gives us the normalized elastic scattering coefficients, shown in Fig. 4.3c and reproduced here in the top row of Fig. C.7. In the bottom row of Fig. C.7 we show the same simulations under the RWA, i.e we consider Eq. (C.32) but with the counter-rotating terms ($\sum_{l>l'}(\left|\sigma\right\rangle\!\left\langle\sigma\right|_{ll'} \left|a\right\rangle\!\left\langle a\right|^\dagger + \text{h.c.})$) removed. This is not equivalent to Appendix C.3.1 since here we include higher levels of the fluxonium and their coupling to the cavity. In particular, g_{02}, g_{12} couple the $N = 1, 2, 3$ number of excitations sectors, even in the absence of the counter-rotating terms. Nevertheless, for our device parameters, $g_{02} \ll g_{01}, \varepsilon_1$, and as a result, the Fano resonances that are visible in the top row of Fig. C.7 are essentially invisible in the RWA model in the bottom

row of Fig. C.7. The theory curves in Fig. 4.3 are calculated from diagnolizing the tight-binding Hamiltonian in Eq. (C.31) with flux-tunable parameters. Given the large Hilbert space of the joint system, the Hamiltonian was truncated to a maximum number of excitations. The discrepancy between the calculated energy levels for the two- and three-photon bound states and the MPS resonances is likely caused by this truncation restriction.

C.4 Multimode correlations and entanglement

For characterizing the inelastically emitted microwave fields we adopt the formalism in Refs. [281, 458] for probing the quantum state of propagating microwave photons and their correlations using linear amplifiers and quadrature amplitude detectors. In the case of a single mode, the output field $|a\rangle\langle a|$ goes through a phase insensitive amplifier of gain G which introduces an additional noise mode $|h\rangle\langle h|$. The amplified field is then down-converted in a microwave mixer using a local oscillator (LO), in order to detect the in-phase and quadrature components $|I\rangle\langle I|$ and $|Q\rangle\langle Q|$. These quantities are related through the complex amplitude operator defined as $|S\rangle\langle S| = \sqrt{G}(|a\rangle\langle a| + |h\rangle\langle h|^{\dagger}) = |I\rangle\langle I| + i\,|Q\rangle\langle Q|$.

For probing correlations in the emitted microwave fields, the device output is split at room temperature into two separate homodyne branches, as shown in Fig. C.1. Each branch has a separate local oscillator set to the desired mode frequencies ω_α and ω_β, respectively. The time domain traces of the complex field amplitudes $|S\rangle\langle S|_{\alpha,\beta}$ on each branch are recorded simultaneously, and the gain prefactors are accounted from calibrated values at the mode frequencies $G_\alpha = G(\omega_\alpha)$ and $G_\beta = G(\omega_\beta)$, respectively. If the noise added by the detection chain is uncorrelated with the generated signal, then the field moments can be decomposed into products of signal and noise

moments:

$$\langle(|S\rangle\langle S|_{\alpha}^{\dagger})^{n}\,|S\rangle\langle S|_{\beta}^{m}\rangle = G_{\alpha}^{\frac{n}{2}}G_{\beta}^{\frac{m}{2}}\sum_{i,j=0}^{n,m}\binom{n}{i}\binom{m}{j}\langle(|a\rangle\langle a|_{\alpha}^{\dagger})^{i}\,|a\rangle\langle a|_{\beta}^{j}\rangle\langle(|h\rangle\langle h|_{\alpha}^{n-i}\,(|h\rangle\langle h|_{\beta}^{\dagger})^{m-j}\rangle. \tag{C.35}$$

For the measured inelastic multi-mode emission presented in Chapter 4, the power spectrum $\langle|a\rangle\langle a|_{\omega}^{\dagger}\,|a\rangle\langle a|_{\omega}\rangle$ is extracted from the measured moments of the signal $|S\rangle\langle S|_{\omega}$ and noise $|h\rangle\langle h|_{\omega}$, at a single homodyne branch, by sweeping the local oscillator frequency around the single-photon band. Processing the time domain traces such that the noise amplitude has zero mean $\langle|h\rangle\langle h|^{\dagger}\rangle = 0$ yields the simplified relationship between signal and noise power terms:

$$\langle|S\rangle\langle S|_{\omega}^{\dagger}\,|S\rangle\langle S|_{\omega}\rangle = G(\omega)\left(\langle|a\rangle\langle a|_{\omega}^{\dagger}\,|a\rangle\langle a|_{\omega}\rangle + \langle|h\rangle\langle h|_{\omega}\,|h\rangle\langle h|_{\omega}^{\dagger}\rangle\right). \tag{C.36}$$

Therefore, the power spectrum is measured from the signal power subtracted by the noise power. The noise power term is extracted from the output noise of the detection chain when the waveguide is not driven by the pump tone.

C.4.1 Hillery-Zubairy criteria

To characterize the entanglement properties of the generated multimode state we rely on the Hillery-Zubairy criterion for two-mode states [282]. For two harmonic modes with annihilation operators $|a\rangle\langle a|_{A}$ and $|a\rangle\langle a|_{B}$, respectively, the following Cauchy-Schwarz inequality holds for pure product states

$$|\langle|a\rangle\langle a|_{A}\,|a\rangle\langle a|_{B}\rangle|^{2} = |\langle|a\rangle\langle a|_{A}\rangle|^{2}|\langle|a\rangle\langle a|_{B}\rangle|^{2} \leq \langle|a\rangle\langle a|_{A}^{\dagger}\,|a\rangle\langle a|_{A}\rangle\langle|a\rangle\langle a|_{B}^{\dagger}\,|a\rangle\langle a|_{B}\rangle. \tag{C.37}$$

Furthermore, Hillery and Zubairy have shown that this inequality holds for any separable state, generalized as a mixture of pure product states $\rho^{AB} = \sum p_{n}|\Psi_{n}^{AB}\rangle\langle\Psi_{n}^{AB}|$. A violation of this

inequality implies that the two-mode state is entangled, which is a necessary but not sufficient condition since there exist two-mode entangled states that satisfy this inequality.

This entanglement criterion justifies our choice of two-mode correlators

$$\mathcal{C}_{ij} = |\langle |a\rangle\langle a|_i \, |a\rangle\langle a|_j \rangle|^2 / \langle |a\rangle\langle a|_i^\dagger \, |a\rangle\langle a|_i \rangle \langle |a\rangle\langle a|_j^\dagger \, |a\rangle\langle a|_j \rangle,$$

measured for every pair of waveguide modes. The photon intensity $\langle |a\rangle\langle a|_i^\dagger \, |a\rangle\langle a|_i \rangle$ is measured from the power spectrum, while the squeezing correlators $\langle |a\rangle\langle a|_i \, |a\rangle\langle a|_j \rangle$ are extracted from the dual homodyne measurement of the second order moments.

$$\langle |S\rangle\langle S|_i \, |S\rangle\langle S|_j \rangle = \sqrt{G_i G_j} \left(\langle |a\rangle\langle a|_i \, |a\rangle\langle a|_j \rangle + \langle |h\rangle\langle h|_i^\dagger \, |h\rangle\langle h|_j^\dagger \rangle \right). \tag{C.38}$$

The map of squeezing correlators for every pair of waveguide modes, and its dependence on the pump amplitude, is displayed in Fig. C.8.

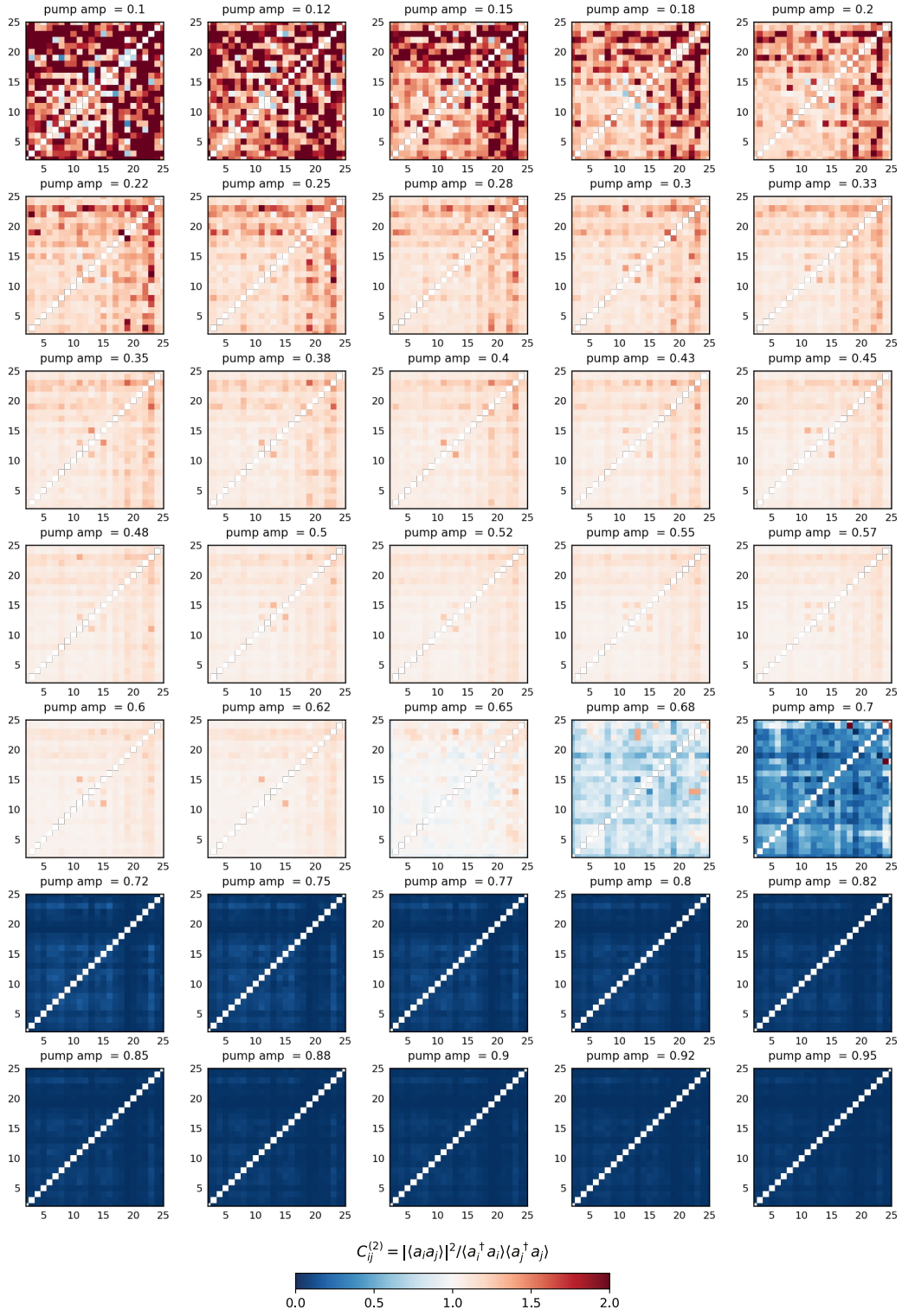

Figure C.8: Hillery-Zubairy criterion. Two-mode squeezing correlators C_{ij} as a function of the pump amplitude. The diagonal elements $i = j$ are not a relevant measure of entanglement and have been removed.

Appendix D: Supplemental Material for Chapter 5

In this Supplemental Material we present additional details concerning the random circuit of Section 5.2. In Appendix D.1, we derive the general transition rate matrix W, given in Eq. (5.5). In Appendix D.2 we specialize it to the case of an initial single-site operator, deriving Eqs. (5.7) and (5.8). In Appendix D.3, we present the continuum approximation for small g, deriving the Fokker-Planck equation, Eqs. (5.9) to (5.11). In Appendix D.4, we derive the relation between the average squared commutator and the mean operator weight. In Appendix D.5, we provide additional details on the dynamics and steady-state of the probability weight distribution. In Appendix D.6, we derive an analytical expression for the probability weight distribution after one step of the random circuit and show that if the interactions are strong enough, the scrambling time is $O(1)$.

D.1 Derivation of the stochastic matrix W

To be slightly more general, we consider a system of N sites, each of local dimension q. As discussed in Section 5.2, we are interested in the time evolution of a simple initial operator $\mathcal{O}(t) = U^\dagger(t)\mathcal{O}U(t)$

$$\mathcal{O}(t) = \sum_{\mathcal{S}} a_{\mathcal{S}}(t)\mathcal{S}, \tag{D.1}$$

where the strings $\mathcal{S}$ form a basis for $SU(q^N)$, normalized as $\mathrm{tr}(\mathcal{S}) = q^N\delta_{\mathcal{S},1}, \mathrm{tr}(\mathcal{S}\mathcal{S}') = q^N\delta_{\mathcal{S}\mathcal{S}'}$.

We take $U(t) = \prod_{i=1}^{t} U_i$ where $U_i = U_{\mathrm{I}} U_{\mathrm{II}} U_{\mathrm{I}}$ and U_{I} is a product of single site Haar random unitaries while U_{II} is the global interaction. Note that the two U_{I} appearing on either side of the U_{II} are different, i.e the random unitaries are random in both space in time. Here we inserted an additional layer of the Haar unitaries, as compared to Chapter 5. This is completely equivalent, as this extra layer can always be absorbed into the Haar layer of either the step before or the step after, but it simplifies calculations.

Using $a_{\mathcal{S}}(t) = q^{-N} \operatorname{tr}(\mathcal{O}(t)\mathcal{S})$, we can write $a_{\mathcal{S}}^2(t)$ in terms of the coefficients at the previous time step

$$a_{\mathcal{S}}^2(t) = q^{-2N} \sum_{\mathcal{S}',\mathcal{S}''} a_{\mathcal{S}'}(t-1) a_{\mathcal{S}''}(t-1) \operatorname{tr}\left(U^\dagger \mathcal{S}' U \mathcal{S}\right) \operatorname{tr}\left(U^\dagger \mathcal{S}'' U \mathcal{S}\right). \tag{D.2}$$

Thus, we want to evaluate the quantity

$$\left\langle \operatorname{tr}\left(U^\dagger \mathcal{S}' U \mathcal{S}\right) \operatorname{tr}\left(U^\dagger \mathcal{S}'' U \mathcal{S}\right) \right\rangle, \tag{D.3}$$

where $\langle ... \rangle$ denotes Haar average over the random unitaries.

Using properties of trace, we can write

$$\left\langle \operatorname{tr}\left(U^\dagger \mathcal{S}' U \mathcal{S}\right) \operatorname{tr}\left(U^\dagger \mathcal{S}'' U \mathcal{S}\right) \right\rangle = \left\langle \operatorname{tr}\left(U^\dagger \mathcal{S}' U \mathcal{S} \otimes U^\dagger \mathcal{S}'' U \mathcal{S}\right) \right\rangle. \tag{D.4}$$

In doing so, we now have a trace over two copies of the system, which could still be thought as a N-site system, where every site is now of dimension q^2 instead of q. In the following, we will denote operators acting on the right system by an overbar. For example $Z_i \bar{Z}_i$ corresponds to the Pauli Z operator acting on site i of both copies, i.e $Z_i \otimes Z_i$.

For our choice of U, Eq. (D.4) becomes

$$\begin{aligned} &\left\langle \operatorname{tr}\left(U^\dagger \mathcal{S}' U \mathcal{S}\right) \operatorname{tr}\left(U^\dagger \mathcal{S}'' U \mathcal{S}\right) \right\rangle \\ &= \operatorname{tr}\Big(\Big\langle (U_{\mathrm{I}} \otimes U_{\mathrm{I}})(U_{\mathrm{II}} \otimes U_{\mathrm{II}}) \left\langle U_{\mathrm{I}} \mathcal{S}' U_{\mathrm{I}}^\dagger \otimes U_{\mathrm{I}} \mathcal{S}'' U_{\mathrm{I}}^\dagger \right\rangle (U_{\mathrm{II}} \otimes U_{\mathrm{II}})^\dagger (U_{\mathrm{I}} \otimes U_{\mathrm{I}})^\dagger \Big\rangle (\mathcal{S} \otimes \mathcal{S}) \Big). \end{aligned} \tag{D.5}$$

We will calculate the above in several steps, working from inside out

$$\mathcal{I}_1 = \left\langle U_{\rm I}\mathcal{S}'U_{\rm I}^\dagger \otimes U_{\rm I}\mathcal{S}''U_{\rm I}^\dagger \right\rangle, \tag{D.6}$$

$$\mathcal{I}_2 = (U_{\rm II}\otimes U_{\rm II})\mathcal{I}_1(U_{\rm II}\otimes U_{\rm II})^\dagger, \tag{D.7}$$

$$\mathcal{I}_3 = \left\langle (U_{\rm I}\otimes U_{\rm I})\mathcal{I}_2(U_{\rm I}\otimes U_{\rm I})^\dagger \right\rangle, \tag{D.8}$$

with $\mathrm{tr}(\mathcal{I}_3(\mathcal{S}\otimes\mathcal{S}))$ being our quantity of interest.

Before proceeding, let us introduce an important formula for calculating the Haar averages. Consider a $d^2\times d^2$ matrix A, and a $d\times d$ Haar random unitary matrix U. Then, we have the following formula [318, 459]

$$\begin{aligned}\left\langle (U\otimes U)A(U\otimes U)^\dagger\right\rangle &\equiv \int_{U(d)} (U\otimes U)A(U\otimes U)^\dagger d\mu(U)\\ &= \left(\frac{\mathrm{tr}(A)}{d^2-1}-\frac{\mathrm{tr}(AF)}{d(d^2-1)}\right)\mathbb{1}_{d^2}-\left(\frac{\mathrm{tr}(A)}{d(d^2-1)}-\frac{\mathrm{tr}(AF)}{d^2-1}\right)F,\end{aligned} \tag{D.9}$$

where $F=\sum_{ij}|ij\rangle\langle ji|$ is the swap operator.

From this, it follows that

$$\mathcal{I}_1 = \prod_r \left\langle U_r^\dagger \mathcal{S}_r' U_r \otimes U_r^\dagger \mathcal{S}_r'' U_r\right\rangle = \delta_{\mathcal{S}',\mathcal{S}''}\prod_r\left(\frac{q^2\delta_{\mathcal{S}_r',1}-1}{q^2-1}\mathbb{1}_{q^2}+\frac{q-q\delta_{\mathcal{S}_r',1}}{q^2-1}F_r\right) \tag{D.10}$$

where we used $\mathrm{tr}(\mathcal{S}_r)=q\delta_{\mathcal{S}_r,1}$ and $\mathrm{tr}(\mathcal{S}_r\mathcal{S}_r')=q\delta_{\mathcal{S}_r,\mathcal{S}_r'}$. Here F_r swaps site r of the left system with the corresponding site r of the right system.

The overall delta function $\delta_{\mathcal{S}',\mathcal{S}''}$ immediately implies that the Haar average of Eq. (D.2) may be written as

$$\left\langle a_{\mathcal{S}}^2(t+1)\right\rangle = \sum_{\mathcal{S}'} W_{\mathcal{S},\mathcal{S}'}\left\langle a_{\mathcal{S}'}^2(t)\right\rangle, \tag{D.11}$$

where $W_{\mathcal{S},\mathcal{S}'}=q^{-2N}\,\mathrm{tr}(\mathcal{I}_3(\mathcal{S}\otimes\mathcal{S}))$.

To proceed, we specialize to qubits, i.e. $q=2$, in which case the swap operator can be written as $F_r=\frac{1}{2}(\mathbb{1}_r\otimes\bar{\mathbb{1}}_r+\boldsymbol{\sigma}_r\cdot\bar{\boldsymbol{\sigma}}_r)=\frac{1}{2}(\mathbb{1}_r\bar{\mathbb{1}}_r+X_r\bar{X}_r+Y_r\bar{Y}_r+Z_r\bar{Z}_r)$ where bar denotes operators acting on the second system. We can combine all the $\mathbb{1}$s together, giving

$$\begin{aligned}\mathcal{I}_1 &= \delta_{\mathcal{S}',\mathcal{S}''}\prod_i\left(\delta_{\mathcal{S}'_i,1}\mathbb{1}_{2^2}+\frac{1-\delta_{\mathcal{S}'_i,1}}{3}\boldsymbol{\sigma}_i\cdot\bar{\boldsymbol{\sigma}}_i\right)\\ &= \delta_{\mathcal{S}',\mathcal{S}''}\sum_{\Omega_{\mathcal{S}'}\subset\{1,2,\cdots,N\}}\prod_{i\in\{1,2,\cdots,N\}/\Omega_{\mathcal{S}'}}\delta_{\mathcal{S}'_i,1}\mathbb{1}_4\prod_{j\in\Omega_{\mathcal{S}'}}\frac{1-\delta_{\mathcal{S}'_j,1}}{3}\boldsymbol{\sigma}_j\cdot\bar{\boldsymbol{\sigma}}_j,\end{aligned} \tag{D.12}$$

where in the second equality the sum is over the powerset of $\{1,2,\cdots,N\}$, i.e, all the (2^N) subsets of $\{1,2,\cdots,N\}$. The sum above essentially contains every possible string of the form $\mathcal{S}\otimes\mathcal{S}$, i.e the same operator appears on both copies of the system. Note that for a given string $\mathcal{S}'$, there is only one nonzero term in the sum. For each site i, we either put an $\mathbb{1}_4$ if $\mathcal{S}'_i=\mathbb{1}$ or we place $\frac{1}{3}\boldsymbol{\sigma}_i\cdot\bar{\boldsymbol{\sigma}}_i$, if $\mathcal{S}'_i$ is any other generator. The set $\Omega_{\mathcal{S}'}$ therefore represents the support of the string $\mathcal{S}'$.

Before proceeding, let us summarize the high-level idea behind the derivation that follows. Our tasks consist of the following:

1. First, we need to apply the global interaction $U_{\mathrm{II}}\otimes U_{\mathrm{II}}$ on Eq. (D.12), giving us $\mathcal{I}_2$.

2. Then, we need to apply the layer of single-site Haar unitaries $U_{\mathrm{I}}\otimes U_{\mathrm{I}}$, and average over the Haar distribution on each site, giving us $\mathcal{I}_3$.

3. Finally, we need to multiply the result by $\mathcal{S}\otimes\mathcal{S}$ and take the trace, giving us $W_{\mathcal{S},\mathcal{S}'}$.

Recall that

$$U_{\mathrm{II}}=e^{-i\frac{g'}{2}\sum_{i<j}Z_iZ_j}, \tag{D.13}$$

where in Chapter 5 we have assumed $g'=\frac{g}{\sqrt{N}}$. To perform the first step, we will make use of the formulas

$$U_{\mathrm{II}} X_r U_{\mathrm{II}}^\dagger = X_r \cos\left(g' \sum_{i\neq r} Z_i\right) + Y_r \sin\left(g' \sum_{i\neq r} Z_i\right), \tag{D.14}$$

$$U_{\mathrm{II}} Y_r U_{\mathrm{II}}^\dagger = Y_r \cos\left(g' \sum_{i\neq r} Z_i\right) - X_r \sin\left(g' \sum_{i\neq r} Z_i\right). \tag{D.15}$$

Now, note that each term in the sum in Eq. (D.12) is a product of single-site operators. By performing our first task, using Eqs. (D.14) and (D.15), we will obtain complicated operators, like those appearing on the right-hand-side of Eqs. (D.14) and (D.15), that are supported on a large number of sites. In order to perform the second step, we can make use of Eq. (D.9). However, to use Eq. (D.9), we need A to be a single-site operator. Thus, we will have to break down complicated operators, like those appearing on the right-hand-side of Eqs. (D.14) and (D.15), into sums of simple terms consisting of products of single-site operators. This will allow us to use Eq. (D.9), after which we can easily perform the last step, 3, since this will only require taking traces of single-site operators.

The result of step 1 and 2 can be simplified by noting that Eq. (D.12) contains all possible strings of the form $\mathcal{S} \otimes \mathcal{S}$. Hence, it is instructive to first consider the result of applying $U_{\mathrm{II}} \otimes U_{\mathrm{II}}$ and $U_{\mathrm{I}} \otimes U_{\mathrm{I}}$ to a single string of this form. Note that the result of applying $U_{\mathrm{II}} \otimes U_{\mathrm{II}}$, $U_{\mathrm{I}} \otimes U_{\mathrm{I}}$, and averaging over the Haar unitaries is invariant if we replace any number of Xs in the string by Ys or vice-versa. To see this, we use the fact that we can change a X into a Y (or vice-versa) by applying a rotation about the Z axis, i.e $e^{-i\frac{\pi}{4}Z} X e^{i\frac{\pi}{4}Z} = Y$. This rotation clearly commutes with U_{II} and can be absorbed into U_{I}, since by definition, the Haar measure is invariant under multiplication by any unitary.

This means that we may calculate the result for a single representative string from each group

and multiply by the degeneracy. Let us denote $\Omega_{\mathcal{S}}$ the support of some string $\mathcal{S}$. We can further divide $\Omega_{\mathcal{S}}$ based on the number and location of Zs in the string. Define the subset $\Sigma \subseteq \Omega$ as the set of all sites with Z in them, and the remaining sites (with either Xs or Ys) by $\Lambda = \Omega \setminus \Sigma$. For strings that are supported on k sites (i.e $|\Omega_{\mathcal{S}}| = k$), with fixed number and position of Zs, the degeneracy is $2^{|\Lambda|}$.

Without loss of generality, we can therefore consider strings composed of either Xs or Zs. Consider the string $\prod_{i\in\Lambda} X_i \bar{X}_i \prod_{j\in\Sigma} Z_j \bar{Z}_j$. To apply U_{II}, we can use the fact that $[X_i X_j, Z_i Z_j] = 0$. We get

$$\begin{aligned}
&(U_{\mathrm{II}} \otimes U_{\mathrm{II}})(\prod_{i\in\Lambda} X_i \bar{X}_i \prod_{j\in\Sigma} Z_j \bar{Z}_j)(U_{\mathrm{II}} \otimes U_{\mathrm{II}})^\dagger \\
&= \prod_{i\in\Lambda} \left[(X_i \cos(Q_\Lambda) + Y_i \sin(Q_\Lambda))\big(\bar{X}_i \cos\big(\bar{Q}_\Lambda\big) + \bar{Y}_i \sin\big(\bar{Q}_\Lambda\big)\big)\right] \prod_{j\in\Sigma} Z_j \bar{Z}_j
\end{aligned} \tag{D.16}$$

where we used Eq. (D.14). Here, Q_Λ acts on all sites except those in Λ, i.e $Q_\Lambda \equiv g' \sum_{l\notin\Lambda} Z_l$.

We see that we can safely apply the Haar unitaries and perform the Haar average on sites inside of Λ, since all the cosines and sines and the $Z\bar{Z}$ act on sites outside of Λ. With slight abuse of notation, let us denote $\left\langle (U_{\mathrm{I}} \otimes U_{\mathrm{I}}) A (U_{\mathrm{I}} \otimes U_{\mathrm{I}})^\dagger \right\rangle$ by simply $\langle A \rangle$ where it is understood that the Haar unitaries act only on the support of A.

From Eq. (D.9), one can easily check that $\left\langle X_i \bar{Y}_i \right\rangle = 0$, so the cross terms in the above expression will vanish. Only $\left\langle X_i \bar{X}_i \right\rangle = \left\langle Y_i \bar{Y}_i \right\rangle \equiv V_i$ will remain. Here the single site operator V_i is defined as $V_j = -\frac{1}{3}\mathbb{1}_4 + \frac{2}{3}F$. Explicitly, we find

$$\left\langle (U_{\mathrm{II}} \otimes U_{\mathrm{II}})(\prod_{i\in\Lambda} X_i \bar{X}_i \prod_{j\in\Sigma} Z_j \bar{Z}_j)(U_{\mathrm{II}} \otimes U_{\mathrm{II}})^\dagger \right\rangle = \prod_{i\in\Lambda} V_i \left\langle \cos^{|\Lambda|}(R_\Lambda) \prod_{j\in\Sigma} Z_j \bar{Z}_j \right\rangle \tag{D.17}$$

where $R_\Lambda = \bar{Q}_\Lambda - Q_\Lambda$.

Combining this with the discussion above, we find that $\mathcal{I}_3$ may be written as

$$\mathcal{I}_3 = \delta_{\mathcal{S}',\mathcal{S}''} \sum_{\Omega_{\mathcal{S}'} \subset \{1,2,\cdots,N\}} \left(\prod_{j \notin \Omega_{\mathcal{S}'}} \delta_{\mathcal{S}'_j,1} \right) \left(\prod_{i \in \Omega_{\mathcal{S}'}} \frac{1 - \delta_{\mathcal{S}'_i,1}}{3} \right) \times \sum_{\Lambda \subset \Omega_{\mathcal{S}'}} 2^{|\Lambda|} \left(\prod_{m \in \Lambda} V_m \right) \left\langle \cos^{|\Lambda|}(R_\Lambda) \prod_{n \in \Omega_{\mathcal{S}'} \setminus \Lambda} Z_n \bar{Z}_n \right\rangle . \quad \text{(D.18)}$$

It remains to compute $\left\langle \cos^{|\Lambda|}(R_\Lambda) \prod_{n \in \Omega_{\mathcal{S}'} \setminus \Lambda} Z_n \bar{Z}_n \right\rangle$. To do so we expand the cosine as follows $\cos^k(x) = \frac{1}{2^k} \sum_{n=0}^k \binom{k}{n} \cos[(2n-k)x]$,

$$\left\langle \cos^{|\Lambda|}(R_\Lambda) \prod_{n \in \Omega_{\mathcal{S}'} \setminus \Lambda} Z_n \bar{Z}_n \right\rangle = \frac{1}{2^{|\Lambda|}} \sum_{l=0}^{|\Lambda|} \binom{|\Lambda|}{l} \left\langle \cos((2l - |\Lambda|) R_\Lambda) \prod_{n \in \Omega_{\mathcal{S}'} \setminus \Lambda} Z_n \bar{Z}_n \right\rangle . \quad \text{(D.19)}$$

To proceed we can pull a single-site operator out of R_Λ. Since $R_\Lambda = \sum_{k \notin \Lambda} D_k$ where $D_k = g'(\bar{Z}_k - Z_k)$, we can pull out a $D_j, \quad j \in \Omega_{\mathcal{S}'} \setminus \Lambda$ so that $R_\Lambda = R_{\Lambda \cup \{j\}} + D_j$. We then use the trig identity

$$\begin{aligned} \cos((2l - |\Lambda|) R_\Lambda) = &\cos\big((2l - |\Lambda|) R_{\Lambda \cup \{j\}}\big) \cos((2l - |\Lambda|) D_j) \\ &- \sin\big((2l - |\Lambda|) R_{\Lambda \cup \{j\}}\big) \sin((2l - |\Lambda|) D_j). \end{aligned} \quad \text{(D.20)}$$

This allows us to perform the Haar average over site j. The sine term will not contribute, since $\left\langle \sin((2l - |\Lambda|) D_j) Z_j \bar{Z}_j \right\rangle = 0$. Repeating this procedure recursively for all sites in $\Omega_{\mathcal{S}'} \setminus \Lambda$, we get

$$\left\langle \cos((2l - |\Lambda|) R_\Lambda) \prod_{n \in \Omega_{\mathcal{S}'} \setminus \Lambda} Z_n \bar{Z}_n \right\rangle = \left\langle \cos\big((2l - |\Lambda|) R_{\Omega_{\mathcal{S}'}}\big) \right\rangle \prod_{n \in \Omega_{\mathcal{S}'} \setminus \Lambda} \left\langle \cos((2l - |\Lambda|) D_n) Z_n \bar{Z}_n \right\rangle . \quad \text{(D.21)}$$

Continuing the procedure for the $\left\langle \cos\big((2l - |\Lambda|) R_{\Omega_{\mathcal{S}'}}\big) \right\rangle$ term, we have

$$\begin{aligned} &\left\langle \cos((2n - |\Lambda|) R_\Lambda) \prod_{n \in \Omega_{\mathcal{S}'} \setminus \Lambda} Z_n \bar{Z}_n \right\rangle \\ &= \prod_{t \notin \Omega_{\mathcal{S}'}} \langle \cos((2l - |\Lambda|) D_t) \rangle \prod_{n \in \Omega_{\mathcal{S}'} \setminus \Lambda} \left\langle \cos((2l - |\Lambda|) D_n) Z_n \bar{Z}_n \right\rangle . \end{aligned} \quad \text{(D.22)}$$

Using $\cos((2l-|\Lambda|)D) = \cos^2((2l-|\Lambda|)g') + Z\bar{Z}\sin^2((2l-|\Lambda|)g')$ gives

$$\left\langle \cos((2n-|\Lambda|)R_\Lambda) \prod_{n\in\Omega_{\mathcal{S}'}\setminus\Lambda} Z_n\bar{Z}_n \right\rangle = \prod_{t\notin\Omega_{\mathcal{S}'}} \left(\cos^2((2l-|\Lambda|)g') + V_t\sin^2((2l-|\Lambda|)g')\right) \times \prod_{n\in\Omega_{\mathcal{S}'}\setminus\Lambda} \left(\cos^2((2l-|\Lambda|)g')V_n + \sin^2((2l-|\Lambda|)g')\right). \tag{D.23}$$

Putting things together, we find that Eq. (D.19) is

$$\left\langle \cos^{|\Lambda|}(R_\Lambda) \prod_{n\in\Omega_{\mathcal{S}'}\setminus\Lambda} Z_n\bar{Z}_n \right\rangle = \frac{1}{2^{|\Lambda|}} \sum_{l=0}^{|\Lambda|} \binom{|\Lambda|}{l} \prod_{t\notin\Omega_{\mathcal{S}'}} \left(\cos^2((2l-|\Lambda|)g') + V_t\sin^2((2l-|\Lambda|)g')\right) \times \prod_{n\in\Omega_{\mathcal{S}'}\setminus\Lambda} \left(\cos^2((2l-|\Lambda|)g')V_n + \sin^2((2l-|\Lambda|)g')\right), \tag{D.24}$$

and finally, $\mathcal{I}_3$ is given by

$$\mathcal{I}_3 = \delta_{\mathcal{S}',\mathcal{S}''} \sum_{\Omega_{\mathcal{S}'}\subset\{1,2,\cdots,N\}} \left(\prod_{j\notin\Omega_{\mathcal{S}'}} \delta_{\mathcal{S}'_j,1}\right) \left(\prod_{i\in\Omega_{\mathcal{S}'}} \frac{1-\delta_{\mathcal{S}'_i,1}}{3}\right) \sum_{\Lambda\subset\Omega_{\mathcal{S}'}} \left(\prod_{m\in\Lambda} V_m\right) \sum_{l=0}^{|\Lambda|} \binom{|\Lambda|}{l} \times \prod_{t\notin\Omega_{\mathcal{S}'}} \left(\cos^2((2l-|\Lambda|)g') + V_t\sin^2((2l-|\Lambda|)g')\right) \times \prod_{n\in\Omega_{\mathcal{S}'}\setminus\Lambda} \left(\cos^2((2l-|\Lambda|)g')V_n + \sin^2((2l-|\Lambda|)g')\right). \tag{D.25}$$

To compute the $W_{\mathcal{S},\mathcal{S}'}$-matrix from Eq. (D.11), it remains to take the trace of Eq. (D.25) with $\mathcal{S}\otimes\mathcal{S}$ and divide by 2^{2N}, i.e

$$W_{\mathcal{S},\mathcal{S}'} = \frac{1}{2^{2N}}\operatorname{tr}(\mathcal{I}_3(\mathcal{S}\otimes\mathcal{S})). \tag{D.26}$$

Using Eq. (D.25) together with $\operatorname{tr}(V_i(\mathcal{S}_i\otimes\mathcal{S}_i)) = \frac{4}{3}(1-\delta_{\mathcal{S}_i,1})$, gives

$$W_{\mathcal{S},\mathcal{S}'} = \frac{1}{2^{2N}} \sum_{\Omega_{\mathcal{S}'} \subset \{1,2,\cdots,N\}} \left(\prod_{j \notin \Omega_{\mathcal{S}'}} \delta_{\mathcal{S}'_j,1} \right) \left(\prod_{i \in \Omega_{\mathcal{S}'}} \frac{1-\delta_{\mathcal{S}'_i,1}}{3} \right) \sum_{\Lambda \subset \Omega_{\mathcal{S}'}} \left(\prod_{m \in \Lambda} \frac{4}{3}(1-\delta_{\mathcal{S}_m,1}) \right)$$
$$\times \sum_{l=0}^{|\Lambda|} \binom{|\Lambda|}{l} \prod_{t \notin \Omega_{\mathcal{S}'}} \left(\cos^2((2l-|\Lambda|)g') 4\delta_{\mathcal{S}_t,1} + \frac{4}{3}(1-\delta_{\mathcal{S}_t,1}) \sin^2((2l-|\Lambda|)g') \right)$$
$$\times \prod_{n \in \Omega_{\mathcal{S}'} \setminus \Lambda} \left(\cos^2((2l-|\Lambda|)g') \frac{4}{3}(1-\delta_{\mathcal{S}_n,1}) + 4\delta_{\mathcal{S}_n,1} \sin^2((2l-|\Lambda|)g') \right). \quad \text{(D.27)}$$

Note that because of $\prod_{m \in \Lambda} \frac{4}{3}(1-\delta_{\mathcal{S}_m,1})$ in Eq. (D.27), Λ is constrained to be in $\Omega_{\mathcal{S}} \cap \Omega_{\mathcal{S}'}$. The matrix elements of W are

$$W = \frac{1}{2^{2N}} \left(\frac{1}{3}\right)^{|\Omega_{\mathcal{S}'}|} \sum_{\Lambda \subset \Omega_{\mathcal{S}} \cap \Omega_{\mathcal{S}'}} \left(\frac{4}{3}\right)^{|\Lambda|} \Bigg[\sum_{l=0, 2l \neq |\Lambda|}^{|\Lambda|} \binom{|\Lambda|}{l} \left(4\cos^2((2l-|\Lambda|)g')\right)^{N-|\Omega_{\mathcal{S}} \cup \Omega_{\mathcal{S}'}|}$$
$$\times \left(\frac{4}{3}\sin^2((2l-|\Lambda|)g')\right)^{|\Omega_{\mathcal{S}} \setminus \Omega_{\mathcal{S}'}|} \times \left(\frac{4}{3}\cos^2((2l-|\Lambda|)g')\right)^{|\Omega_{\mathcal{S}} \cap \Omega_{\mathcal{S}'}|-|\Lambda|} \times \left(4\sin^2((2l-|\Lambda|)g')\right)^{|\Omega_{\mathcal{S}'} \setminus \Omega_{\mathcal{S}}|}$$
$$+ \delta_{2l,|\Lambda|} \binom{|\Lambda|}{|\Lambda|/2} \prod_{t \notin \Omega_{\mathcal{S}'}} (4\delta_{\mathcal{S}_t,1}) \prod_{n \in \Omega_{\mathcal{S}'} \setminus \Lambda} \left(\frac{4}{3}(1-\delta_{\mathcal{S}_n,1})\right) \Bigg]. \quad \text{(D.28)}$$

Note that the last term is only nonzero when both $2l = |\Lambda|$ and $\Omega_{\mathcal{S}} = \Omega_{\mathcal{S}'}$. The last condition is equivalent to $|\Omega_{\mathcal{S}}| + |\Omega_{\mathcal{S}'}| - 2|\Omega_{\mathcal{S}} \cap \Omega_{\mathcal{S}'}| = 0$.

We can combine all constant factors (with the same result holding for the $2l = |\Lambda|$ term)

$$\frac{1}{2^{2N}} \left(\frac{1}{3}\right)^{|\Omega_{\mathcal{S}'}|} \left(\frac{4}{3}\right)^{|\Lambda|} 4^{N-|\Omega_{\mathcal{S}} \cup \Omega_{\mathcal{S}'}|} \left(\frac{4}{3}\right)^{|\Omega_{\mathcal{S}} \setminus \Omega_{\mathcal{S}'}|} \left(\frac{4}{3}\right)^{|\Omega_{\mathcal{S}} \cap \Omega_{\mathcal{S}'}|-|\Lambda|} 4^{|\Omega_{\mathcal{S}'} \setminus \Omega_{\mathcal{S}}|} = \left(\frac{1}{3}\right)^{|\Omega_{\mathcal{S}'}|+|\Omega_{\mathcal{S}}|}. \quad \text{(D.29)}$$

Now, note that Λ only appears in Eq. (D.28) as $|\Lambda|$. Thus, we can replace the sum over subsets of $\Omega_{\mathcal{S}} \cap \Omega_{\mathcal{S}'}$ as $\sum_{\Lambda \subset \Omega_{\mathcal{S}} \cap \Omega_{\mathcal{S}'}} = \sum_{k=0}^{|\Omega_{\mathcal{S}} \cap \Omega_{\mathcal{S}'}|} \binom{|\Omega_{\mathcal{S}} \cap \Omega_{\mathcal{S}'}|}{k}$. Thus, the W matrix can be written as

$$W_{\mathcal{S},\mathcal{S}'} = W(|\Omega_{\mathcal{S}}|, |\Omega_{\mathcal{S}'}|, |\Omega_{\mathcal{S}} \cap \Omega_{\mathcal{S}'}|) \tag{D.30}$$
$$= \left(\frac{1}{3}\right)^{|\Omega_{\mathcal{S}'}|+|\Omega_{\mathcal{S}}|} \sum_{k=0}^{|\Omega_{\mathcal{S}}\cap\Omega_{\mathcal{S}'}|} \binom{|\Omega_{\mathcal{S}} \cap \Omega_{\mathcal{S}'}|}{k} \Bigg[\sum_{l=0,2l\neq k}^{k} \binom{k}{l} \left[\cos^2((2l-k)g')\right]^{N-k-(|\Omega_{\mathcal{S}}|+|\Omega_{\mathcal{S}'}|-2|\Omega_{\mathcal{S}}\cap\Omega_{\mathcal{S}'}|)}$$
$$\times \left[\sin^2((2l-k)g')\right]^{|\Omega_{\mathcal{S}}|+|\Omega_{\mathcal{S}'}|-2|\Omega_{\mathcal{S}}\cap\Omega_{\mathcal{S}'}|} + \delta_{2l,k}\delta_{|\Omega_{\mathcal{S}}|+|\Omega_{\mathcal{S}'}|-2|\Omega_{\mathcal{S}}\cap\Omega_{\mathcal{S}'}|,0}\binom{k}{k/2}\Bigg],$$

which is what appears in Eq. (5.5), with the identification $w = |\Omega_{\mathcal{S}}|, w' = |\Omega_{\mathcal{S}'}|, v = |\Omega_{\mathcal{S}} \cap \Omega_{\mathcal{S}'}|$. In Section 5.2, we also dropped the $\delta_{2l,k}\delta_{|\Omega_{\mathcal{S}}|+|\Omega_{\mathcal{S}'}|-2|\Omega_{\mathcal{S}}\cap\Omega_{\mathcal{S}'}|,0}$ term and the $2l \neq k$ restriction in the sum which requires one to be careful to identify 0^0 as 1. From this expression it is clear that W is a real symmetric ($W_{\mathcal{S},\mathcal{S}'} = W_{\mathcal{S}',\mathcal{S}}$) matrix with all positive matrix elements.

D.2 Master equation for simple initial operator

Let us now assume that the initial operator $\mathcal{O}$ starts as a single-site operator on site 1 without loss of generality. We may further assume that we start with X_1, i.e $a_{\mathcal{S}} = \delta_{\mathcal{S},X_1}$. Since the circuit will involve random Haar unitaries, let us consider the result of applying a Haar random unitary on X_1, which, after averaging over the Haar unitary, will be $\frac{1}{3}(X_1 + Y_1 + Z_1)$, which already does not contain any information about the specific generator we picked. Let us therefore pick this as the initial conditions at $t = 0$ for the master equation, Eq. (D.11),

$$\left\langle a_{\mathcal{S}}^2(t=0)\right\rangle = \begin{cases} \frac{1}{3} & \text{if} \quad \mathcal{S} = X_1, Y_1, Z_1, \\ 0 & \text{otherwise} \quad . \end{cases} \tag{D.31}$$

We now claim that for these initial conditions, the probabilities $\langle a_{\mathcal{S}}^2(t)\rangle$ only depend on the string weight $w \equiv |\Omega_{\mathcal{S}}|$ and the weight on site 1, $w_1 \equiv |\Omega_{\mathcal{S}} \cap \{1\}|$. Note that w_1 takes values either 0 or 1. In light of this, it is convenient to account for the number of string configurations with constant w and w_1 by defining the operator weight probability h_t,

$$h_t(w, w_1) = \left\langle a_{\mathcal{S}}^2(t) \right\rangle D(w, w_1), \tag{D.32}$$

where $D(w, w_1)$ is the number of string configurations for a given w and w_1. Since $\sum_{\mathcal{S}'} = \sum_{w_1=0,1} \sum_{w=w_1}^{N-1+w_1} 3^k \binom{N-1}{w-w_1}$, we have

$$D(w, w_1) = 3^w \binom{N-1}{w-w_1}. \tag{D.33}$$

Note that $h_t(w, w_1)$ is a valid (normalized) probability distribution since $\sum_{w_1=0,1} \sum_{w=w_1}^{N-1+w_1} h_t(w, w_1) = \sum_{w_1=0,1} \sum_{w=w_1}^{N-1+w_1} \langle a_{\mathcal{S}}^2(t) \rangle D(w, w_1) = \sum_{\mathcal{S}} \langle a_{\mathcal{S}}^2(t) \rangle = 1$, using the fact that $a_{\mathcal{S}}^2$ are probabilities that sum to 1. Thus, $h_t(w, w_1)$ gives the probability of $\mathcal{O}(t)$ being a string of total weight w with a weight of w_1 on the initial site 1.

The claim above can be proved by induction. The base case is trivial to see, by multiplying the initial conditions Eq. (D.31) by the transition matrix W from Eq. (D.30) (see also Appendix D.6). The inductive step proceeds as follows. First, we decompose the sum over strings $\mathcal{S}'$ as $\sum_{\mathcal{S}'} = \sum_{\Omega_{\mathcal{S}'} \subset \{1,\cdots,N\}} 3^{|\Omega_{\mathcal{S}'}|}$, which yields

$$\left\langle a_{\mathcal{S}}^2(t+1) \right\rangle = \sum_{\Omega_{\mathcal{S}'} \subset \{1,\cdots,N\}} \frac{1}{D(|\Omega_{\mathcal{S}'}|, |\Omega_{\mathcal{S}'} \cap 1|)} 3^{|\Omega_{\mathcal{S}'}|} W(|\Omega_{\mathcal{S}}|, |\Omega_{\mathcal{S}'}|, |\Omega_{\mathcal{S}} \cap \Omega_{\mathcal{S}'}|) h_t(|\Omega_{\mathcal{S}'}|, |\Omega_{\mathcal{S}'} \cap 1|). \tag{D.34}$$

We then split the sum over terms where $|\Omega_{\mathcal{S}'} \cap \{1\}| = 0$ or $|\Omega_{\mathcal{S}'} \cap \{1\}| = 1$. For each of these terms, we further decompose the sum over terms with equal $|\Omega_{\mathcal{S}'}|$. The remaining sum can be written as a sum over different values of the overlap $|\Omega_{\mathcal{S}} \cap \Omega_{\mathcal{S}'}|$. The final result is

$$\left\langle a_{\mathcal{S}}^2(t+1)\right\rangle = \sum_{k=0}^{N-1} 3^k \Bigg[\sum_{m=0}^{\min\{|\Omega_{\mathcal{S}}|-|\Omega_{\mathcal{S}}\cap\{1\}|,k\}} \binom{|\Omega_{\mathcal{S}}| - |\Omega_{\mathcal{S}}\cap\{1\}|}{m} \times \binom{N-1-|\Omega_{\mathcal{S}}|+|\Omega_{\mathcal{S}}\cap\{1\}|}{k-m} W(|\Omega_{\mathcal{S}}|,k,m)\Bigg] \frac{h_t(k,0)}{D(k,0)} + \sum_{k=1}^{N} 3^k \Bigg[\sum_{m=|\Omega_{\mathcal{S}}\cap\{1\}|}^{\min\{|\Omega_{\mathcal{S}}|,k-1+|\Omega_{\mathcal{S}}\cap\{1\}|\}} \binom{|\Omega_{\mathcal{S}}| - |\Omega_{\mathcal{S}}\cap\{1\}|}{m-|\Omega_{\mathcal{S}}\cap\{1\}|} \times \binom{N-1+|\Omega_{\mathcal{S}}\cap\{1\}|-|\Omega_{\mathcal{S}}|}{k-m-1+|\Omega_{\mathcal{S}}\cap\{1\}|} W(|\Omega_{\mathcal{S}}|,k,m)\Bigg] \frac{h_t(k,1)}{D(k,1)}. \quad \text{(D.35)}$$

Here, the first binomial in each bracket counts the number of ways one can choose the part of $\Omega_{\mathcal{S}'}$ that is overlapping with $\Omega_{\mathcal{S}}$ and the second binomial counts the number of ways to choose the non-overlapping part of $\Omega_{\mathcal{S}'}$. It is clear at this point that the right-hand-side is a function of $w = |\Omega_{\mathcal{S}}|$ and $w_1 = |\Omega_{\mathcal{S}} \cap 1|$. Thus, replacing $\langle a_{\mathcal{S}}^2(t+1)\rangle$ by Eq. (D.32) and simplifying gives

$$h_{t+1}(w,w_1) = \sum_{w_1'=0,1} \sum_{w'=w_1'}^{N-1+w_1'} \mathcal{R}(w,w_1,w',w_1') h_t(w',w_1') \quad \text{(D.36)}$$

where the $2N \times 2N$ matrix $\mathcal{R}$ is

$$\mathcal{R}(w,w_1,w',w_1') = 3^w \sum_{m=\max\{0,w+w'-N+1-w_1-w_1'\}}^{\min\{w-w_1,w'-w_1'\}} \binom{w'-w_1'}{m} \times \binom{N-1-w'+w_1'}{w-w_1-m} W(w,w',m+w_1w_1'), \quad \text{(D.37)}$$

where $w_1, w_1' \in \{0,1\}$, $w \in [w_1, N-1+w_1]$, $w' \in [w_1', N-1+w_1']$, and for completeness

$$W(w,w',v) = \left(\frac{1}{3}\right)^{w+w'} \sum_{k=0}^{v} \binom{v}{k} \Bigg[\sum_{l=0,2l\neq k}^{k} \binom{k}{l} \left[\cos^2((2l-k)g')\right]^{N-k-(w+w'-2v)} \times \left[\sin^2((2l-k)g')\right]^{w+w'-2v} + \delta_{2l,k}\delta_{w+w'-2v,0} \binom{k}{k/2} \Bigg]. \quad \text{(D.38)}$$

One may verify that $\sum_i \mathcal{R}_{i,j} = 1$ where $i = (w,w_1)$ and $j = (w',w_1')$. This means that if we start

with normalized h_0, we will have a valid (normalized) probability distribution at later times.

The initial conditions become

$$h_0(w, w_1) = \begin{cases} 1 & \text{if} \quad w = w_1 = 1, \\ 0 & \text{otherwise} \quad . \end{cases} \tag{D.39}$$

To get the probability of having a specific weight, we can sum over w_1,

$$h(w) = \begin{cases} h(0,0) & \text{if} \quad w = 0, \\ h(N,1) & \text{if} \quad w = N, \\ h(w,0) + h(w,1) & \text{otherwise} \quad . \end{cases} \tag{D.40}$$

Note that $h(0,0)$ does not actually participate in the dynamics since $\mathcal{R}(0,0,w',w_1') = W(0,w',0) = \delta_{w',0}$.

D.3 Continuum approximation

We assume here the normalization $g' = \frac{g}{\sqrt{N}}$. The first step is to approximate $W(w,w',v)$ for small g. We consider the two cases $w + w' - 2v = 0, 1$ which amount to a change of the string weight by $0, \pm 1$ and give rise to terms up to g^2.

Taylor expanding the factors of cosine and sine appearing in Eq. (D.38), up to g^2, gives

$$\begin{aligned} &\left[\cos^2\left((2l-k)\frac{g}{\sqrt{N}}\right)\right]^{N-k-(w+w'-2v)} \left[\sin^2\left((2l-k)\frac{g}{\sqrt{N}}\right)\right]^{w+w'-2v} \\ &\approx \begin{cases} \frac{g^2(k-2l)^2(k-N)}{N} + 1 & \text{if} \quad w + w' - 2v = 0, \\ \frac{g^2(k-2l)^2}{N} & \text{if} \quad w + w' - 2v = 1. \end{cases} \end{aligned} \tag{D.41}$$

In general, the $w + w' - 2v = n$, $n \in \mathbb{N}_{>0}$ case will scale as $O(g^{2n})$. We can now perform the sums over l and k appearing in Eq. (D.38). We find

$$W(w,w',v) \approx \left(\frac{1}{3}\right)^{w+w'-v} \begin{cases} 1 + g^2 \frac{2v}{3^2 N}(1 - 3N + 2v) & \text{if} \quad w + w' - 2v = 0, \\ g^2 \frac{2v}{3N} & \text{if} \quad w + w' - 2v = 1. \end{cases} \tag{D.42}$$

The higher order terms will scale at most like $O(g^4 N^2/N^2) = O(g^4)$ and so for small g, the above expression for $W(w,w',v)$ is an excellent approximation. In the general case of $g' = \frac{g}{N^a}$, $a \geq 0$,

the above Taylor expansion yields a series expression for $W(w, w', v)$ where the nth term scales at most as $O(g^{2n}N^n/N^{2na})$. Thus, for $a < \frac{1}{2}$, the series is not convergent, and Eq. (D.42) does not constitute a good approximation. Below, we assume $a = \frac{1}{2}$, but all results and expressions in this section are applicable for $a \geq \frac{1}{2}$ as well, with the appropriate replacement of g. For some discussion of the $a = 0$ case, see Appendix D.6.

Let us now consider the $\mathcal{R}$ matrix. The $w + w' - 2v = 0, 1$ cases contribute to the diagonal as well as super- and sub-diagonals of each block of $\mathcal{R}$. These matrix elements are

$$\begin{aligned}
\mathcal{R}(w,0,w',0) &= \delta_{w,w'}3^w W(w,w',w') + \delta_{w,w'+1}3^w(N-w'-1)W(w,w',w') \\
&\quad + \delta_{w,w'-1}3^w w' W(w,w',w'-1) + O(g^4), \qquad \text{(D.43)}\\
\mathcal{R}(w,1,w',0) &= \delta_{w,w'+1}3^w W(w,w',w') + O(g^4), \qquad \text{(D.44)}\\
\mathcal{R}(w,0,w',1) &= \delta_{w,w'-1}3^w W(w,w',w'-1) + O(g^4), \qquad \text{(D.45)}\\
\mathcal{R}(w,1,w',1) &= \delta_{w,w'}3^w W(w,w',w') + \delta_{w,w'+1}3^w(N-w')W(w,w',w') \\
&\quad + \delta_{w,w'-1}3^w(w'-1)W(w,w',w'-1) + O(g^4). \qquad \text{(D.46)}
\end{aligned}$$

Writing out the master equation, Eq. (D.36), within the g^2 approximation, we have two coupled equations for the two ($w_1 = 0, 1$) blocks:

$$\begin{aligned}
\frac{h_{t+1}(w,0) - h_t(w,0)}{g^2} =& \frac{2w}{9N}h_t(w+1,1) + \frac{2w}{9N}(1-3N+2w)h_t(w,0) \qquad \text{(D.47)}\\
&+ \frac{2(N-w)}{3N}(w-1)h_t(w-1,0) + \frac{2w(w+1)}{9N}h_t(w+1,0),\\
\frac{h_{t+1}(w,1) - h_t(w,1)}{g^2} =& \frac{2(w-1)}{3N}h_t(w-1,0) + \frac{2w}{9N}(1-3N+2w)h_t(w,1) \qquad \text{(D.48)}\\
&+ \frac{2(w-1)}{3N}(N-w+1)h_t(w-1,1) + \frac{2w^2}{9N}h_t(w+1,1).
\end{aligned}$$

Note that the coupling between the two w_1 sectors scales as w/N. Since the initial conditions are constrained to the $w_1 = 1$ sector [see Eq. (D.39)], the early time dynamics will remain approximately in $h_t(w, 1)$ (i.e $h_t(w, 0) \approx 0$ at early times) until w reaches $O(N)$.

By adding Eqs. (D.47) and (D.48), we get a closed equation for the total operator weight

probability $h_t(w) \equiv h_t(w,0) + h_t(w,1)$

$$\begin{aligned}\frac{h_{t+1}(w) - h_t(w)}{g^2} = &\frac{2w(w+1)}{9N} h_t(w+1) + \frac{2w}{9N}(1 - 3N + 2w) h_t(w) \\ &+ \frac{N - w + 1}{3N} 2(w-1) h_t(w-1).\end{aligned} \tag{D.49}$$

Up to now, the only approximation we made was the expansion up to g^2. We now assume that $h(w,t)$ varies slowly with respect to $g^2 t$ and w, and replace finite differences by derivatives which yields a Fokker-Planck equation

$$\partial_\tau h(w,\tau) = -\partial_w (D_1(w) h(w,\tau)) + \partial_w^2 (D_2(w) h(w,\tau)), \tag{D.50}$$

where we introduced a rescaled time $\tau = g^2 t$. Note that Eqs. (D.47) and (D.48) individually are not in the form of a Fokker-Planck equation, but their sum is. The drift and diffusion coefficients are

$$D_1(w) = \frac{2(4 + w + 3Nw - 4w^2)}{9N}, \tag{D.51}$$

$$D_2(w) = \frac{-3 + 3N(w-1) + 7w - 2w^2}{9N}. \tag{D.52}$$

In terms of the scaled weight $\phi \equiv w/N$, the Fokker-Planck equation takes the form

$$\partial_\tau h(\phi,\tau) = -\partial_\phi \left(\frac{2}{3} \left(\phi - \frac{4}{3}\phi^2 \right) h(\phi,\tau) \right) + \partial_\phi^2 \left(\left(\frac{\phi}{3N} - \frac{2}{9}\frac{\phi^2}{N} \right) h(\phi,\tau) \right), \tag{D.53}$$

where we dropped all the $O(1/N)$ terms from the drift coefficient and all the $O(1/N^2)$ terms from the diffusion.

D.4 Relation between the average of the squared commutator and the mean operator weight

In this section, we derive the relation between the average of the squared commutator, defined in Eq. (5.1), and the operator weight probability $h_t(w, w_1)$.

Let us start with Eq. (5.1), and, without loss of generality, pick the two operators to be X_1 at position 1 and Y_r at position $r > 1$

$$\mathcal{C}(r,t) = -\frac{1}{2}\operatorname{tr}\big(\rho_\infty [X_1(t), Y_r]^2\big), \tag{D.54}$$

where ρ_∞ is the infinite-temperature Gibbs state, and $X_1(t)$ is the Heisenberg evolved operator. Using Eq. (D.1), the commutator in Eq. (D.54) can be written as

$$[X_1(t), Y_r]^2 = \left(\sum_{\mathcal{S}} a_{\mathcal{S}}(t)[\mathcal{S}, Y_r]\right)^2 = \left(2\sum_{\mathcal{S}:\mathcal{S}_r=X,Z} a_{\mathcal{S}}(t)\mathcal{S}Y_r\right)^2, \tag{D.55}$$

which gives

$$\begin{aligned}\mathcal{C}(r,t) =& -2\sum_{\mathcal{S}:\mathcal{S}_r=X,Z}\sum_{\mathcal{S}':\mathcal{S}'_r=X,Z} a_{\mathcal{S}}(t)a_{\mathcal{S}'}(t)\operatorname{tr}(\rho_\infty \mathcal{S}Y_r\mathcal{S}'Y_r) &\text{(D.56)}\\ =& 2\sum_{\mathcal{S}:\mathcal{S}_r=X,Z} a_{\mathcal{S}}(t)^2, &\text{(D.57)}\end{aligned}$$

where we used $\operatorname{tr}(\rho_\infty \mathcal{S}\mathcal{S}') = \delta_{\mathcal{S}\mathcal{S}'}$ and the fact that different Pauli matrices anti-commute. Here the sum is constrained to be over all strings that have an X or a Z on site r.

The average of Eq. (D.56) over many realizations of the random circuit is therefore given by

$$\langle \mathcal{C}(r,t)\rangle = 2\sum_{\mathcal{S}:\mathcal{S}_r=X,Z}\left\langle a_{\mathcal{S}}(t)^2\right\rangle, \tag{D.58}$$

where the evolution of $\langle a_{\mathcal{S}}^2(t)\rangle$ is what we calculated in the previous sections.

Since we have assumed in this section that we start from a single site operator, as we did in

Appendix D.2, we have that the average probabilities $\langle a_{\mathcal{S}}^2(t)\rangle$ only depend on the total weight w and weight w_1 on site 1, as explained in Appendix D.2. Thus, we may rewrite Eq. (D.58) in terms of $h_t(w, w_1)$, using Eq. (D.32). A similar calculation to the one leading to Eq. (D.36) yields

$$\langle \mathcal{C}(r,t)\rangle = 4 \sum_{\substack{\Omega_{\mathcal{S}}\subset\{1,\cdots,N\} \\ r\in\Omega_{\mathcal{S}}}} 3^{|\Omega_{\mathcal{S}}|-1} \frac{h_t(|\Omega_{\mathcal{S}}|, |\Omega_{\mathcal{S}}\cap\{1\}|)}{3^{|\Omega_{\mathcal{S}}|}\binom{N-1}{|\Omega_{\mathcal{S}}|-|\Omega_{\mathcal{S}}\cap\{1\}|}} \tag{D.59}$$

$$= \frac{4}{3}\left[\sum_{w=1}^{N-1}\binom{N-2}{w-1}\frac{h_t(w,0)}{\binom{N-1}{w}} + \sum_{w=2}^{N}\binom{N-2}{w-2}\frac{h_t(w,1)}{\binom{N-1}{w-1}}\right] \tag{D.60}$$

$$= \frac{4}{3(N-1)}\sum_{w=1}^{N}[(w-1)h_t(w) + h_t(w,0)], \tag{D.61}$$

where $h_t(w) \equiv h_t(w,0) + h_t(w,1)$, as defined in Section 5.2 and in Appendix D.3 [Eq. (D.40)].

Using the fact that $h_t(w)$ is normalized (i.e. $\sum_w h_t(w) = 1$) and defining the mean weight $\langle w(t)\rangle = \sum_w w h_t(w)$, we get

$$\langle \mathcal{C}(r,t)\rangle = \frac{4}{3}\frac{\langle w(t)\rangle - 1}{N-1} + \frac{4}{3(N-1)}\sum_{w=1}^{N} h_t(w,0). \tag{D.62}$$

By the normalization of the probability distribution, we further know that $\sum_{w=1}^{N} h_t(w,0) < 1$. Hence, the second term in the equation above scales as $O(1/N)$ and is therefore negligible for large N. Thus, in the limit of large N we have

$$\langle \mathcal{C}(r,t)\rangle = \frac{4}{3}\frac{\langle w(t)\rangle}{N} + O(1/N). \tag{D.63}$$

D.5 Additional details on the time-evolution of $h(w, w_1)$

In this section, we provide additional numerical and analytical details regarding the probability weight distribution.

In Fig. D.1, we plot snapshots of $h(w)$ and $h(w, w_1 = 0, 1)$, at different times, computed

numerically using the exact master equation. The initial distribution starts in the $w_1 = 1$ sector and quickly (exponentially) expands. At early times, during the exponential growth, the distribution is supported almost exclusively on the $w_1 = 1$ sector. At later times, when $h(w)$ is very broad in weight space and has large support on weights $w \sim O(N)$, the coupling between the two $w_1 = 0, 1$ sectors turns on and $h(w, 0)$ starts to get populated. Finally, $h(w)$ reaches the steady-state, which, as we show below, is, to a good approximation, a Gaussian centered at $w = 3N/4$ with a width $\sim \Delta w/N \propto 1/\sqrt{N}$. The steady-state corresponds to all strings being equally likely, and hence the Gaussian peak in $h(w, 1)$ is three times as large as the one in $h(w, 0)$.

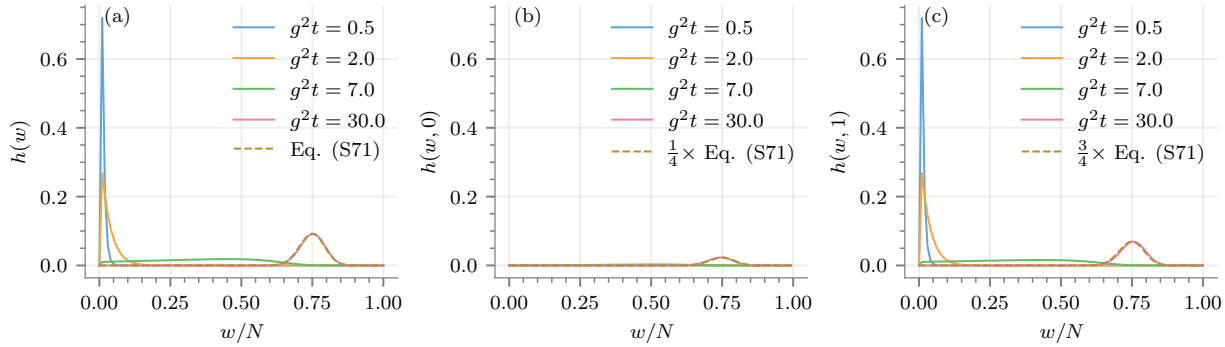

Figure D.1: (a) Snapshots of the numerically computed total probability weight distribution $h(w) = h(w, 0) + h(w, 1)$ for $g = 0.1$ and $N = 100$, together with the analytical expression of the steady-state from Eq. (D.71), which essentially agrees with the $g^2t = 30$ numerics. (b) The same plot for $h(w, w_1 = 0)$. While $h(w, 0) \approx 0$ for early and intermediate times, the numerics for $g^2t = 30$ essentially agree with the analytical prediction for the steady state. (c) The same plot for $h(w, w_1 = 1)$.

D.5.1 Stationary solution for $h(w)$

At large t the distribution $h(t, \phi = w/N)$ approaches a stationary solution that obeys following equation

$$-\partial_\phi \left[D_1(\phi)h(\phi)\right] + \partial_\phi^2 \left[D_2(\phi)h(\phi)\right] = 0, \tag{D.64}$$

where

$$D_1(\phi) = \frac{2}{3}\phi\left(1 - \frac{4\phi}{3}\right), \qquad D_2(\phi) = \frac{\phi}{3N}\left(1 - \frac{2\phi}{3}\right). \tag{D.65}$$

Integrating out Eq. D.64 we obtain

$$-D_1(\phi)h(\phi) + \partial_\phi\left[D_2(\phi)h(\phi)\right] = C. \tag{D.66}$$

Equation (D.66) can be rewritten as

$$\partial_\phi h(\phi) = \left(\frac{D_1(\phi) - \partial_\phi D_2(\phi)}{D_2(\phi)}\right)h(\phi) + \frac{C}{D_2(\phi)}. \tag{D.67}$$

Solution of (D.67) is straightforward:

$$\begin{aligned} h(\phi) &= \text{const} \times e^{J(\phi)} \int_0^\phi \frac{d\phi' e^{-J(\phi')}}{D_2(\phi')}, \\ J(\phi) &= \int d\phi \frac{D_1 - \partial_\phi D_2}{D_2} = 4N\phi - \log\phi + (3N-1)\log(3-2\phi). \end{aligned} \tag{D.68}$$

As a result we obtain solution for $h(\phi)$ in the form:

$$h(\phi) = \text{const} \times \frac{e^{NS(\phi)}}{(3-2\phi)\phi}\int_0^\phi d\phi'\ e^{-NS(\phi')}, \tag{D.69}$$

where

$$S(\phi) = 4\phi + 3\log(3-2\phi). \tag{D.70}$$

In the limit $N \to \infty$ the main contribution in the integral (D.69) comes from the vicinity of the boundary point $\phi = 0$. Expanding $S(\phi)$ in Taylor series in powers ϕ: $S(\phi) \approx S(0) + 2\phi$ and substituting it inside of the integrand in Eq. (D.69) results in

$$h(\phi) \sim \frac{e^{NS(\phi)}}{(3-2\phi)\phi}\left[1 - e^{-2N\phi}\right]. \tag{D.71}$$

Expression Eq. (D.71) can be further simplified since $e^{NS(\phi)}$ is strongly peaked in the vicinity of $\phi_0 = 3/4$ which is the extremum of $S(\phi)$: $S(\phi) \approx S(\phi_0) + \frac{S''(\phi_0)}{2}(\phi - \phi_0)^2 + ...$, that gives

$$h(\phi) \sim \frac{e^{-\frac{8N}{3}(\phi-3/4)^2}}{\phi(3-2\phi)}\left[1-e^{-2N\phi}\right]. \tag{D.72}$$

D.6 Mean-weight after one step and scrambling in O(1)

In this section, we derive a simple expression for the mean-weight after a single step of the random circuit. Here, a single step is defined as in Appendix D.1, i.e $U = U_{\rm I}U_{\rm II}U_{\rm I}$. In doing so, we show that if the global interactions are sufficiently strong (i.e if g' is independent of N) then a single step of the circuit is sufficient to achieve scrambling.

Starting from the initial conditions defined in Eq. (D.39), and using the master equation in Eq. (D.36), we find after a single step

$$h_{t=1}(w, w_1) = \mathcal{R}(w, w_1, 1, 1). \tag{D.73}$$

Using Eqs. (D.37) and (D.38), we can further simplify

$$\begin{aligned} h_{t=1}(w, w_1) &= 3^w \binom{N-1}{w-w_1} W(w, 1, w_1) \\ &= \begin{cases} 0 \quad \text{if} \quad w_1 = 0, \\ \frac{1}{3}\binom{N-1}{w-1}\left(\delta_{w,1} + 2[\cos^2(g')]^{2(N-w)}\left[\sin^2(g')\right]^{2(w-1)}\right) \quad \text{if} \quad w_1 = 1. \end{cases} \end{aligned} \tag{D.74}$$

The above describes the probability weight distribution after a single step, valid for arbitrary g'.

The mean of the above distribution can be computed exactly,

$$\langle w \rangle = \sum_{w=1}^{N} w h_{t=1}(w, w_1 = 1) = \frac{1}{3} + \frac{2}{3}\cos^2(g') + \frac{2}{3}N\sin^2(g'). \tag{D.75}$$

Thus, if g' is independent of N, then $\langle w \rangle$ is $O(N)$ and $\langle \mathcal{C} \rangle$ (see Appendix D.4) is $O(1)$ after just a single step.

Appendix E: Supplemental Material for Chapter 6

E.1 Experimental Details

The experimental setup and basic parameters are described in detail in the supplement of Ref. [460]. The procedure for calibrating the spatial light modulator is described in the supplement of Ref [392]. The $231\,\mathrm{nm}$ UV laser system for Rydberg excitation is described in the supplement of Ref. [387].

Power stabilization of the Rydberg dressing light

The UV light used for Rydberg dressing is generated using a $923\,\mathrm{nm}$ amplified diode laser system followed by two second harmonic generation cavities in series. The fractional power stability of the UV light after the second cavity is about 10% which was sufficient for our previous work with direct excitation to Rydberg states [387]. However, in the case of dressing, power stability is more critical due to the interaction strength having a quartic dependence on the Rabi frequency ($V \propto \Omega^4$). Furthermore, the stability of the power during the spin-echo sequence used in the Ramsey interferometry is important to cancel the phases accumulated due to the single-particle light shift. We improved the power stability to much better than 1 % by adding a noise-eater. The noise-eater consists of an electro-optic polarization modulator (QuBig PCx2B-UV) and an

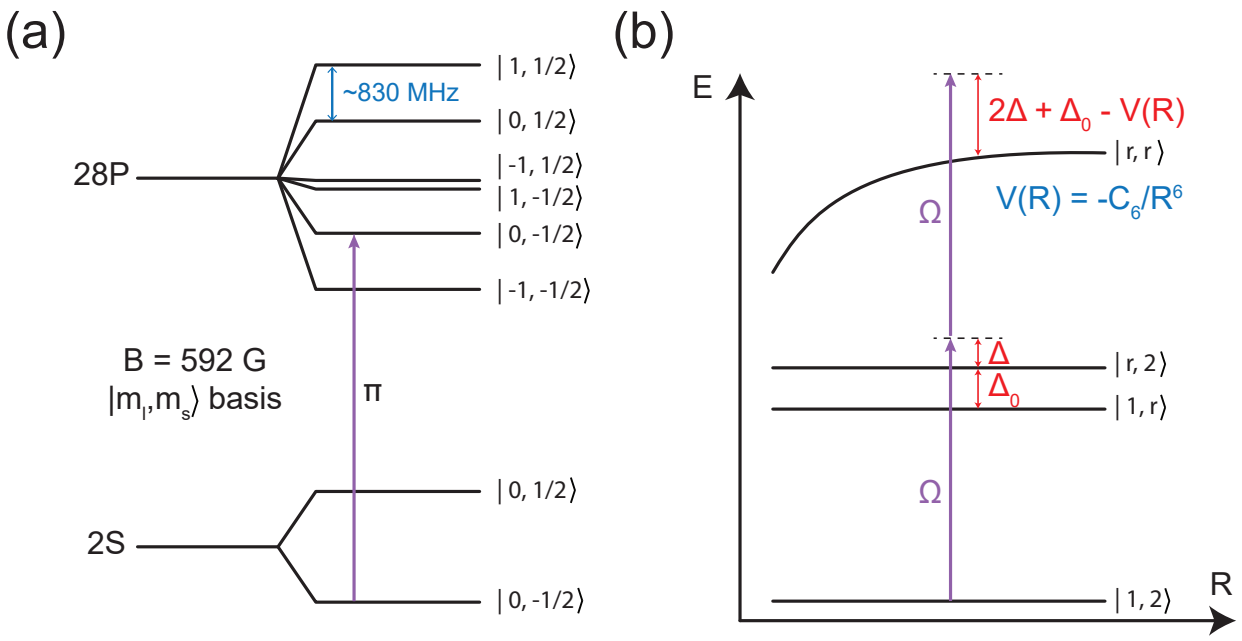

Figure E.1: Rydberg dressing of ^{6}Li. (a) Level diagram showing the hyperfine ground states of ^{6}Li directly coupled to the $28P$ Rydberg state using linearly (π) polarized light at a field of $592\,\mathrm{G}$. The basis used is $|m_l, m_s\rangle$. (b) Rydberg dressing scheme for two atoms in different hyperfine ground states $|1\rangle$ and $|2\rangle$ coupled to the Rydberg state $|r\rangle$. Ω is the Rabi coupling of the laser, Δ is the detuning from the resonant transition between $|1\rangle$ and $|r\rangle$, Δ_0 is the hyperfine splitting between $|1\rangle$ and $|2\rangle$ and $V(R) = -C_6/R^6$ is the van der Waals interaction potential between two Rydberg states $|r\rangle$.

α-BBO Glan-Taylor polarizer (EKSMA 441-2108). By measuring the laser power using a pick-off before the last acousto-optic modulator ([387]) and feeding back on the noise-eater, we suppressed intensity noise for frequencies up to $1\,\mathrm{MHz}$ and eliminated shot-to-shot drifts in the dressing light intensity that limited our previous experiments.

Ground and Rydberg states used in the experiments

We work at a magnetic field of $592\,\mathrm{G}$ pointing in the direction perpendicular to the 2D lattice plane. At this field, both the ground and Rydberg states are in the Paschen-Back regime such that we can approximately label them using the $|nl, m_l, m_s, m_I\rangle$ basis (Fig. E.1a). As explained in the text, the hyperfine ground states we use are $|1\rangle$, $|2\rangle$ and $|3\rangle$ numbered from lowest to highest in

energy and having $m_I = 1, 0, -1$ respectively. For the Rydberg states, the nuclear spin splitting is negligible so states with different m_I can be considered degenerate. This approximation means that two atoms in different hyperfine ground states will couple to Rydberg states at the same energy (both labeled as $|r\rangle$) and interact with each other via a van der Waals potential (Fig. E.1b).

In our quenches and lifetime measurements, we always start with a spin-polarized gas of either state $|1\rangle$ or $|3\rangle$ atoms (both states are essentially equivalent and we happen to have take some of our data in this Chapter using one or the other). However, for the interferometry measurements, we need to take into account the dressed interaction potential between two atoms in different hyperfine ground states which couple to $|r\rangle$.

E.2 Interaction potential for two Rydberg dressed atoms in different ground states

To obtain the dressed potential for two atoms in different ground states, we start by writing down the single-particle Hamiltonians for each atom in the $\{|i\rangle, |r\rangle\}$ basis in the rotating frame (where $i \in \{1, 2\}$ labels the ground states):

$$\hat{H}_1 = \begin{pmatrix} 0 & \Omega/2 \\ \Omega/2 & -\Delta \end{pmatrix} \quad \text{and} \quad \hat{H}_2 = \begin{pmatrix} 0 & \Omega/2 \\ \Omega/2 & -(\Delta + \Delta_0) \end{pmatrix} \tag{E.1}$$

Using these and the interaction potential between two atoms in the Rydberg state separated by a distance R, $V(R) = -C_6/R^6$, we write down the two-particle dressing Hamiltonian as

$$\hat{H}_{\text{dr}}(R) = \hat{H}_1 \otimes \hat{\mathbb{I}} + \hat{\mathbb{I}} \otimes \hat{H}_2 + V(R)(|r\rangle \langle r| \otimes |r\rangle \langle r|). \tag{E.2}$$

We calculate the dressed potential by solving for the eigenenergy of the eigenstate with maximum

overlap with the bare ground state $|1,2\rangle$. This can be done numerically, or using perturbation theory up to 4th order in Ω assuming $\Omega \ll \Delta$. In this limit, we find that the relevant eigenergy has the form

$$E(R) = -\frac{\Omega^4(2\Delta+\Delta_0)}{16\Delta^2(\Delta+\Delta_0)^2}\left(\frac{1}{1+\frac{(2\Delta+\Delta_0)R^6}{|C_6|}}\right) + \delta(\Omega,\Delta) + \delta(\Omega,\Delta+\Delta_0), \tag{E.3}$$

where $\delta(\Omega,\Delta) = (-\Delta+\sqrt{\Delta^2+\Omega^2})/2$ is the single-particle light shift and the first term is the desired interaction potential.

E.3 Many-body Ramsey interferometry

We use the same many-body Ramsey interferometry technique as Ref. [364] to characterize the interaction potentials of the Rydberg dressed atoms. However, because the splitting between the ground states we use in the Ramsey interferometry is only $75.806(3)\,\mathrm{MHz}$ and the detunings we use are between $30\,\mathrm{MHz}$ and $100\,\mathrm{MHz}$, we need to take into account the dressing of both states. Since the experiments are performed in the frozen-gas regime, we rewrite the dressing Hamiltonian as a spin Hamiltonian. For our interferometer, we use hyperfine ground states $|1\rangle \equiv |\uparrow\rangle$ and $|2\rangle \equiv |\downarrow\rangle$. The many-body dressing Hamiltonian is

$$\begin{aligned}\hat{H}_{\mathrm{dr}} = &\sum_i \left(\delta_i^{\uparrow}\hat{\sigma}_{\uparrow\uparrow}^{(i)} + \delta_i^{\downarrow}\hat{\sigma}_{\downarrow\downarrow}^{(i)}\right) \\ &+ \frac{1}{2}\sum_{i\neq j}\Big(V_{ij}^{\uparrow\uparrow}\hat{\sigma}_{\uparrow\uparrow}^{(i)}\hat{\sigma}_{\uparrow\uparrow}^{(j)} + V_{ij}^{\downarrow\downarrow}\hat{\sigma}_{\downarrow\downarrow}^{(i)}\hat{\sigma}_{\downarrow\downarrow}^{(j)} \\ &+ V_{ij}^{\uparrow\downarrow}\hat{\sigma}_{\uparrow\uparrow}^{(i)}\hat{\sigma}_{\downarrow\downarrow}^{(j)} + V_{ij}^{\downarrow\uparrow}\hat{\sigma}_{\downarrow\downarrow}^{(i)}\hat{\sigma}_{\uparrow\uparrow}^{(j)}\Big),\end{aligned} \tag{E.4}$$

where δ_i^{α} is the single-particle light shift for spin α at site i, $V_{ij}^{\alpha\beta}$ is the Rydberg dressed potential

between spins α and β at sites i and j, and $V_{ij}^{\uparrow\downarrow} = V_{ij}^{\downarrow\uparrow}$. Using the relations $\hat{\sigma}_{\uparrow\uparrow}^{(i)} = \frac{1}{2}\left(\hat{\mathbb{I}} + \hat{\sigma}_z^{(i)}\right)$ and $\hat{\sigma}_{\downarrow\downarrow}^{(i)} = \frac{1}{2}\left(\hat{\mathbb{I}} - \hat{\sigma}_z^{(i)}\right)$, we can rewrite the Hamiltonian as

$$\begin{aligned}\hat{H}_{\text{dr}} = H_0 &\\ &+ \frac{1}{2}\sum_i \left(\delta_i^{\uparrow} - \delta_i^{\downarrow} + \frac{1}{2}\sum_{j\neq i}\left(V_{ij}^{\uparrow\uparrow} - V_{ij}^{\downarrow\downarrow}\right)\right)\hat{\sigma}_z^{(i)} \\ &+ \frac{1}{8}\sum_{i\neq j}\left(V_{ij}^{\uparrow\uparrow} + V_{ij}^{\downarrow\downarrow} - 2V_{ij}^{\uparrow\downarrow}\right)\hat{\sigma}_z^{(i)}\hat{\sigma}_z^{(j)} \qquad \text{(E.5)}\\ \hat{H}_{\text{dr}} = H_0 + \frac{1}{2}\sum_i \delta_i^* \hat{\sigma}_z^{(i)} &+ \frac{1}{8}\sum_{i\neq j} V_{ij}^* \hat{\sigma}_z^{(i)}\hat{\sigma}_z^{(j)}, \qquad \text{(E.6)}\end{aligned}$$

where H_0 is an energy offset, the second term is a longitudinal field of strength δ_i^* dominated by the single-particle light shifts, and the third term is an effective interaction term with strength V_{ij}^*. Similar to what is done in the supplement of Ref. [364], we can calculate various observables for different pulse sequences in terms of the accumulated phases $\phi_i = \int_0^\tau \delta_i^*(t)\mathrm{dt}$ and $\Phi_{ij} = \int_0^\tau V_{ij}^*(t)\mathrm{dt}$ over the length τ of the dressing pulse.

For a $\pi/2 - \tau - \pi/2$ pulse sequence, the observable is the expected single-component density $\hat{\sigma}_{\uparrow\uparrow}^i = |\uparrow\rangle\langle\uparrow|$ which can be calculated to be:

$$\left\langle \hat{\sigma}_{\uparrow\uparrow}^i \right\rangle = \frac{1}{2} - \frac{1}{2}\cos(\phi_i)\prod_{j\neq i}\cos\left(\frac{\Phi_{ij}}{2}\right). \qquad \text{(E.7)}$$

For a spin echo $\pi/2 - \tau - \pi - \tau - \pi/2$ pulse sequence, the observable is the single-component density correlation which can be calculated to be:

$$\begin{aligned}\left\langle \hat{\sigma}_{\uparrow\uparrow}^i \hat{\sigma}_{\uparrow\uparrow}^j \right\rangle_C =& \frac{1}{8}\left(\prod_{k\neq i,j}\cos\Phi_{k,ij}^{(+)} + \prod_{k\neq i,j}\cos\Phi_{k,ij}^{(-)}\right) \\ &- \frac{1}{4}\cos\Phi_{ij}^2 \prod_{k\neq i,j}\cos\Phi_{ik}\cos\Phi_{jk}, \qquad \text{(E.8)}\end{aligned}$$

where $\Phi_{k,ij}^{(\pm)} = \Phi_{ik} \pm \Phi_{jk}$ and $\Phi_{ii} = 0$.

E.4 Dependence of lifetime on atom number at fixed density

In our search for a suitable Rydberg state to use for our dressing experiments, we explored many different principal quantum numbers. We eventually chose $28P$ because it gave us a good ratio between the measured collective lifetime and the theoretical single-particle lifetime, while also having a large enough C_6 to achieve strong nearest-neighbor interactions in the lattice. We explored larger principal quantum numbers but found much shorter lifetimes than the expected values. One possible reason is the coupling to neighboring pair-potentials that have non-zero overlaps with the target state at close distances (Fig. 6.1). However, the general behavior of the many-body lifetimes with atom number and geometry of the cloud remained the same over significantly different principal quantum numbers. In particular, the lifetime showed no strong dependence on the atom number at fixed density over the range we could explore in the experiment. Fig. E.2 shows the initial lifetime vs. the initial atom number for 2D systems $4\,\mathrm{a_{latt}}$ wide and of variable length along the direction parallel to the dressing beam for the $31P$ and $40P$ Rydberg states.

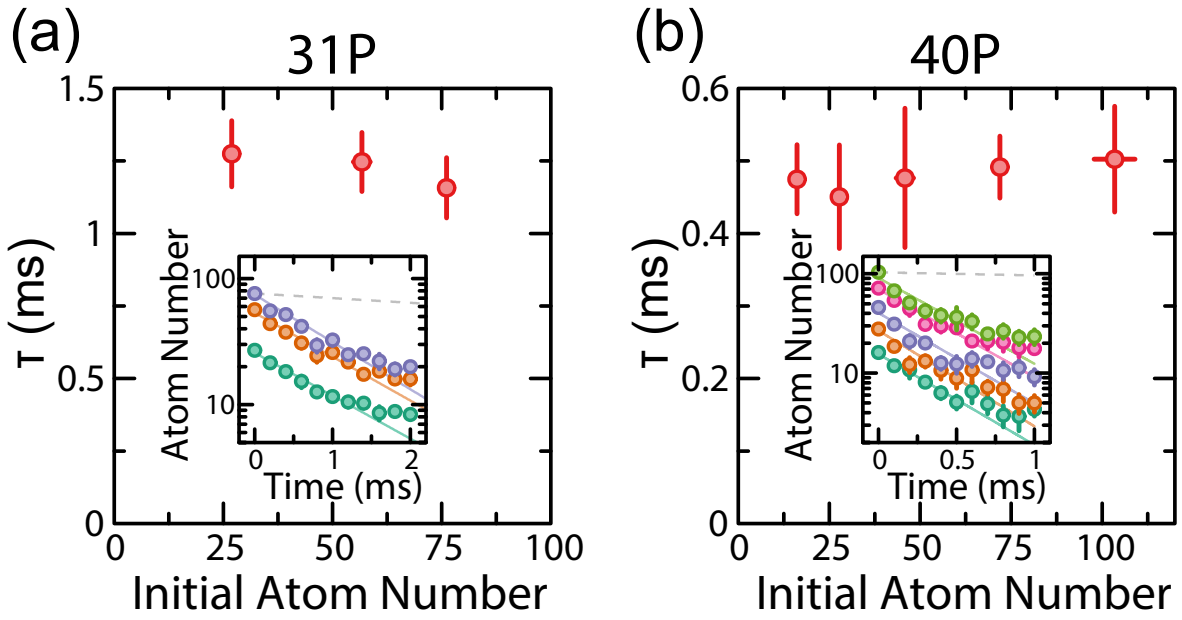

Figure E.2: Dependence of lifetime on atom number at fixed density. (a) Initial lifetime for 2D systems with different initial atom number dressed to $31P$. Measurements are made in a 2D rectangular system of small width $\sim 4\,\mathrm{a_{latt}}$ and variable length along the dressing beam direction. We observe no strong dependence on the atom number. The Rabi frequency is approximately constant over the entire system. For this data, $\Omega = 2\pi \times 7.02(5)\,\mathrm{MHz}$, $\Delta = 2\pi \times 60\,\mathrm{MHz}$ and $n = 0.8$. (b) Same as in (a) but for systems dressed to $40P$. For this data, $\Omega = 2\pi \times 5.6(2)\,\mathrm{MHz}$, $\Delta = 2\pi \times 40\,\mathrm{MHz}$ and $n = 0.55$. (insets) Raw data with exponential fits to extract the initial decay rate. Experimental error bars correspond to standard error of the mean.

E.5 Atom loss during charge density wave dynamics

We observe an atom loss of $\sim 30\%$ for the longest evolution times for the dataset with the maximum initial density and interaction strength. For the dataset where interaction was varied by changing the dressing laser intensity, the lifetime gets longer for smaller interactions due to the reduction of the Rydberg dressing parameter $\beta = \frac{\Omega}{2\Delta}$. For the dataset where the initial density was varied at fixed interaction strength, the lifetime increased for lower initial densities (Fig. E.3). These measurements are in accordance with our observed density dependent lifetime measurements shown in Fig. 6.3.

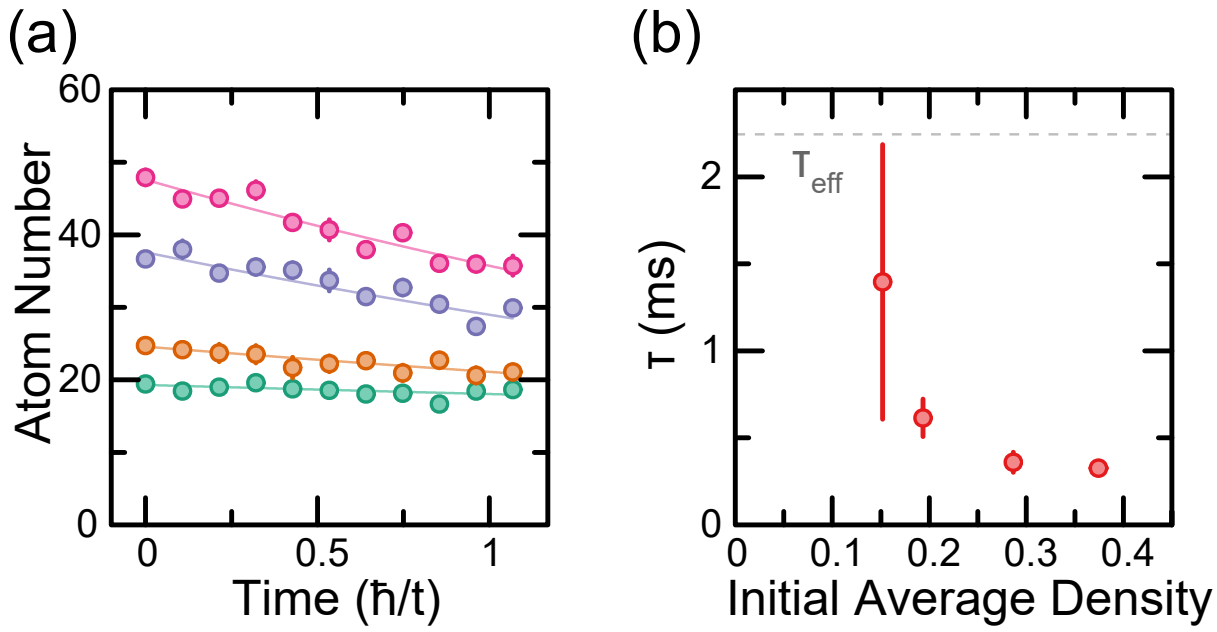

Figure E.3: Atom loss during charge density wave dynamics. (a) Atom number decay over the quenches shown in Fig. 6.5. Each color represents a set with a different initial density. Circles are measured data with error bars and lines are simple exponential decay fits. The dressing parameters were $\Omega = 2\pi \times 6.99(8)\,\mathrm{MHz}$ and $\Delta = 2\pi \times 30\,\mathrm{MHz}$. (b) Lifetime vs. the initial average density of the charge density wave as extracted from the data in (a). This behavior is in agreement with our observations shown in Fig. 6.3. Experimental error bars correspond to standard error of the mean.

Appendix F: Supplemental Material for Chapter 7

This supplemental material is organized as follows: in Appendix F.1, we derive the Hamiltonian for the van-der-Waals interactions between the Zeeman sublevels of two atoms in either $S_{1/2}+S_{1/2}$, $S_{1/2}+P_{1/2}$, or $P_{1/2}+P_{1/2}$. In Appendix F.2, we derive the Hamiltonian for the phonon interactions between two atoms and discuss how to implement the phonon-swap for up to two trap components. We also comment on the validity of the Taylor approximation. Then, in Appendix F.3, we present the adiabatic protocol for the phonon-swap and discuss how to perform 3D cooling by swapping all three trap components. In Appendix F.4, we generalize the phonon-swap for a 1D chain of data and auxiliary atoms and derive the time-dependence of the average phonon number in each species. Finally, in Appendix F.5, we give an example of the spin-1/2 states and the choice of the laser polarizations for a ^{87}Rb atom.

F.1 vdW interactions

In this section, we derive the van-der-Waals interactions (Eqs. (7.4), (7.5) and (7.8)) between the Zeeman sublevels of two atoms. In second order perturbation theory, this can be written as [68]

$$\hat{\mathcal{H}}_{\text{vdW}} = \hat{P} \sum_{\alpha,\beta} \frac{\hat{V}_{dd} \hat{Q}_{\alpha,\beta} \hat{V}_{dd}}{\delta_{\alpha\beta}} \hat{P}, \tag{F.1}$$

where $\hat{Q}_{\alpha,\beta} = |\alpha,\beta\rangle\langle\alpha,\beta|$ and $\hat{P} = \sum_{k,l} |k,l\rangle\langle k,l|$ are projectors onto the intermediate and initial states, respectively. The dipole-dipole operator, $\hat{V}_{dd}$, is given by

	$S_{1/2}+S_{1/2}$	$S_{1/2}+P_{1/2}$	$P_{1/2}+P_{1/2}$
(a)	$S_{1/2}+S_{1/2}\to P_{1/2}+P_{1/2}$	$S_{1/2}+P_{1/2}\to P_{1/2}+S_{1/2}$	$P_{1/2}+P_{1/2}\to S_{1/2}+S_{1/2}$
(b)	$S_{1/2}+S_{1/2}\to P_{3/2}+P_{3/2}$	$S_{1/2}+P_{1/2}\to P_{3/2}+D_{3/2}$	$P_{1/2}+P_{1/2}\to D_{3/2}+D_{3/2}$
(c)	$S_{1/2}+S_{1/2}\to P_{3/2}+P_{1/2}$	$S_{1/2}+P_{1/2}\to P_{3/2}+S_{1/2}$	$P_{1/2}+P_{1/2}\to S_{1/2}+D_{3/2}$
(d)	$S_{1/2}+S_{1/2}\to P_{1/2}+P_{3/2}$	$S_{1/2}+P_{1/2}\to P_{1/2}+D_{3/2}$	$P_{1/2}+P_{1/2}\to D_{3/2}+S_{1/2}$

Table F.1: The four channels describing the dipole-allowed virtual processes $(L_1,J_1)+(L_2,J_2)\to(L_1',J_1')+(L_2',J_2')$ that lead to vdW interactions, in the case of both atoms in $S_{1/2}$ states (left), one atom in $S_{1/2}$ and the other in $P_{1/2}$ (middle), both atoms in $P_{1/2}$ states (right).

$$\hat{V}_{dd}=-\sqrt{\frac{24\pi}{5}}\frac{1}{r^3}\sum_{\mu,\nu}C^{1,1;2}_{\mu,\nu;\mu+\nu}Y_2^{\mu+\nu}(\theta,\phi)^*\hat{d}^{(1)}_\mu\hat{d}^{(2)}_\nu, \tag{F.2}$$

where $C^{J_1,J_2;J}_{m_1,m_2;M}$ is a Clebsch-Gordan coefficient and Y_l^m spherical harmonics. $\hat{d}^{(1)}_\mu$ and $\hat{d}^{(2)}_\nu$ are the spherical components of the dipole operators for the two atoms ($\mu,\nu\in\{-1,0,1\}$), whose matrix elements are

$$\langle n_a,L_a,J_a,m_a|\,\hat{d}_q\,|n_c,L_c,J_c,m_c\rangle\equiv\mathcal{R}_{n_a,L_a,J_a,n_c,L_c,J_c}J^q_{L_a,J_a,m_a,L_c,J_c,m_c}, \tag{F.3}$$

where

$$\mathcal{R}_{n_a,L_a,J_a,n_c,L_c,J_c}=\int R_{n_a,L_a,J_c}(r)R_{n_c,L_c,J_c}(r)r^3dr, \tag{F.4}$$

is the overlap of the radial wavefunctions $R_{n,L,J}(r)$ and

$$\begin{aligned}J^q_{L_a,J_a,m_a,L_c,J_c,m_c}=(-1)^{2J_c+1/2+m_a}&\sqrt{(2J_a+1)(2J_c+1)(2L_a+1)(2L_c+1)}\\&\begin{pmatrix}J_c&1&J_a\\m_c&q&-m_a\end{pmatrix}\begin{pmatrix}L_a&1&L_c\\0&0&0\end{pmatrix}\begin{Bmatrix}J_a&1&J_c\\L_c&1/2&L_a\end{Bmatrix}.\end{aligned} \tag{F.5}$$

We can write the sum over the intermediate states α,β in Eq. (F.1) as follows

$$\sum_{\alpha,\beta}=\sum_{\text{channels}}\sum_{n_\alpha,n_\beta}\sum_{m_\alpha,m_\beta}, \tag{F.6}$$

where the channels for $S_{1/2}+S_{1/2}$, $S_{1/2}+P_{1/2}$ and $P_{1/2}+P_{1/2}$ are given in Table F.1.

Note that specifying the channel specifies both the L and J quantum numbers. We first consider the diagonal interactions, where the initial and final principal quantum numbers n_1,n_2 of the atoms

are the same. Note that for $n_1S_{1/2}+n_2S_{1/2}$ and $n_1P_{1/2}+n_2P_{1/2}$ with $n_1 \neq n_2$ there are additional flip-flop interactions that swap the principal quantum numbers of the two atoms. We describe these at the end of this section.

Using Eqs. (F.2), (F.3) and (F.6), we can rewrite the diagonal interactions part of Eq. (F.1) in the following form

$$\begin{aligned}\hat{\mathcal{H}}_{\text{vdW}} =& \frac{1}{r^6}\sum_{\text{channels}}\left(\sum_{n_\alpha,n_\beta}\frac{(\mathcal{R}_{\alpha,1})^2(\mathcal{R}_{\beta,2})^2}{\delta_{\alpha\beta}}\right)\times \\ &\sum_{\substack{m_k,m_l\\ m_k',m_l'}}\left[\frac{24\pi}{5}\sum_{m_\alpha,m_\beta}\left(\sum_{\substack{\mu,\nu\\ \mu',\nu'}} C^{1,1;2}_{\mu,\nu;\mu+\nu}Y_2^{\mu+\nu\,*}J^{\mu}_{1_k,\alpha}J^{\nu}_{2_l,\beta}C^{1,1;2}_{\mu',\nu';\mu'+\nu'}Y_2^{\mu'+\nu'\,*}J^{\mu'}_{\alpha,1_{k'}}J^{\nu'}_{\beta,2_{l'}}\right)\right. \\ &\left.\times\left|m_k,m_l\right\rangle\left\langle m_{k'},m_{l'}\right|\right].\end{aligned} \tag{F.7}$$

In Eq. (F.7), each term in the parentheses on the first line only depends on the intermediate n_α, n_β values, for a given channel. The label α in $\mathcal{R}_{\alpha,1}$ is short for $n_\alpha, L_\alpha, J_\alpha$ where L_α, J_α are specified by the channel. Similarly, the label 1 (2) is specifying the n, L, J values of the first (second) term in the channel.

The quantity in the second line of Eq. (F.7) is a 4×4 matrix in the subspace of the magnetic sublevels $\left|{+}{+}\right\rangle, \left|{+}{-}\right\rangle, \left|{-}{+}\right\rangle, \left|{-}{-}\right\rangle$. For a given channel, the matrix elements are found by summing over the m_α, m_β values and are independent of n.

Thus, for a given channel, p, we can define a $C_6^{(p)}$ coefficient and a matrix $\mathcal{D}^{(p)}$

$$\begin{aligned}C_6^{(p)} =& \sum_{n_\alpha,n_\beta}\frac{(\mathcal{R}_{\alpha,1})^2(\mathcal{R}_{\beta,2})^2}{\delta_{\alpha\beta}}, \\ \mathcal{D}^{(p)}_{kl,k'l'} =& \frac{24\pi}{5}\sum_{m_\alpha,m_\beta}\left(\sum_{\substack{\mu,\nu\\ \mu',\nu'}} C^{1,1;2}_{\mu,\nu;\mu+\nu}Y_2^{\mu+\nu\,*}J^{\mu}_{1_k,\alpha}J^{\nu}_{2_l,\beta}C^{1,1;2}_{\mu',\nu';\mu'+\nu'}Y_2^{\mu'+\nu'\,*}J^{\mu'}_{\alpha,1_{k'}}J^{\nu'}_{\beta,2_{l'}}\right).\end{aligned} \tag{F.8}$$

With these, Eq. (F.7) takes the simple form

$$\hat{\mathcal{H}}_{\rm vdW} = \frac{1}{r^6}\sum_p C_6^{(p)}\mathcal{D}^{(p)}. \tag{F.9}$$

For the channels in Table F.1 (same results for all three cases) we find (different definition than in [68])

$$\begin{aligned}
\mathcal{D}^{(a)} &= \frac{2}{27}\mathbb{1} - \mathcal{D}_0,\\
\mathcal{D}^{(b)} &= \frac{8}{27}\mathbb{1} - \mathcal{D}_0,\\
\mathcal{D}^{(c)} &= \frac{4}{27}\mathbb{1} + \mathcal{D}_0,\\
\mathcal{D}^{(d)} &= \frac{4}{27}\mathbb{1} + \mathcal{D}_0,
\end{aligned} \tag{F.10}$$

where

$$\mathcal{D}_0(\theta,\phi) = \begin{pmatrix}
\frac{1}{81}(3\cos(2\theta)-1) & \frac{1}{27}e^{-i\phi}\sin(2\theta) & \frac{1}{27}e^{-i\phi}\sin(2\theta) & \frac{2}{27}e^{-2i\phi}\sin^2(\theta)\\
\frac{1}{27}e^{i\phi}\sin(2\theta) & \frac{1}{81}(1-3\cos(2\theta)) & \frac{1}{81}(-3\cos(2\theta)-5) & -\frac{1}{27}e^{-i\phi}\sin(2\theta)\\
\frac{1}{27}e^{i\phi}\sin(2\theta) & \frac{1}{81}(-3\cos(2\theta)-5) & \frac{1}{81}(1-3\cos(2\theta)) & -\frac{1}{27}e^{-i\phi}\sin(2\theta)\\
\frac{2}{27}e^{2i\phi}\sin^2(\theta) & -\frac{1}{27}e^{i\phi}\sin(2\theta) & -\frac{1}{27}e^{i\phi}\sin(2\theta) & \frac{1}{81}(3\cos(2\theta)-1)
\end{pmatrix}, \tag{F.11}$$

is a traceless matrix. Writing Eq. (F.9) in terms of $\mathbb{1}$ and $\mathcal{D}_0$ gives Eq. (7.4).

We now discuss the flip-flop interactions that are present for $n_1S_{1/2} + n_2S_{1/2}$ and $n_1P_{1/2} + n_2P_{1/2}$ with $n_1 \neq n_2$ (for $n_1S + n_2P$ they are forbidden by selection rules). These take a very similar form to the above. In particular, the full vdW Hamiltonian can be written in a block form as follows

$$\hat{\mathcal{H}}_{\rm vdW} = \begin{pmatrix} \hat{\mathcal{H}}^{\rm diag}_{\rm vdW} & \hat{\mathcal{H}}^{\rm flip-flop}_{\rm vdW} \\ \hat{\mathcal{H}}^{\rm flip-flop}_{\rm vdW} & \hat{\mathcal{H}}^{\rm diag}_{\rm vdW} \end{pmatrix}, \tag{F.12}$$

where the diagonals $\hat{\mathcal{H}}^{\rm diag}_{\rm vdW}$ are given by Eq. (F.9). In the diagonal terms ($\hat{\mathcal{H}}^{\rm diag}_{\rm vdW}$), the atoms undergo virtual transitions to nearby states and then back, i.e. $n_1 \to n_\alpha \to n_1$ and $n_2 \to n_\beta \to n_2$. For the flip-flop terms ($\hat{\mathcal{H}}^{\rm flip-flop}_{\rm vdW}$), the atoms jump all the way between n_1 and n_2, i.e $n_1 \to n_\alpha \to n_2$ and

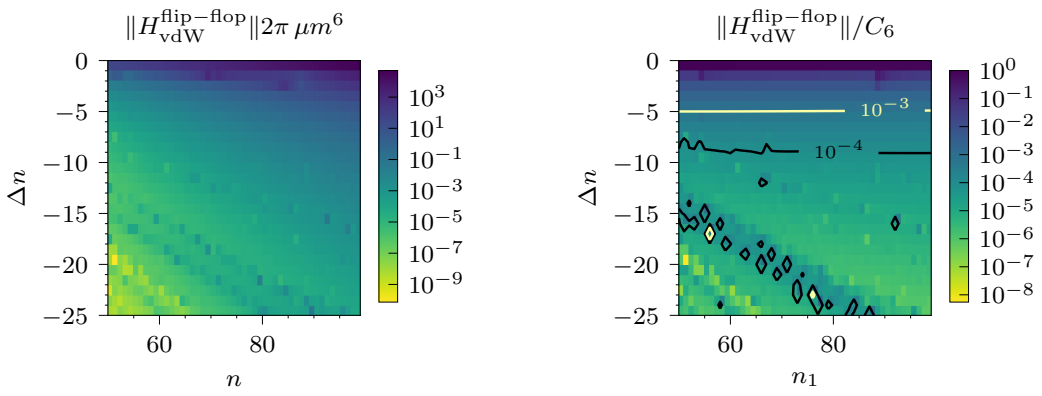

(a) (b)

Figure F.1: Flip-flop vdW interactions for $n_1S + n_2S$ as a function of n_1 and $\Delta n = n_2 - n_1$. (a) Norm of the off-diagonal vdW block. (b) Ratio of the off-diagonal vdW interactions to the diagonal identity interactions.

$n_2 \to n_\beta \to n_1$. The flip-flop terms, $\hat{\mathcal{H}}_{\text{vdW}}^{\text{flip-flop}}$, have a similar matrix structure to $\hat{\mathcal{H}}_{\text{vdW}}^{\text{diag}}$, with the only difference being the C_6 coefficients, i.e.,

$$\hat{\mathcal{H}}_{\text{vdW}}^{\text{flip-flop}} = \frac{1}{r^6} \sum_p \tilde{C}_6^{(p)} \mathcal{D}^{(p)}, \tag{F.13}$$

where the $\mathcal{D}^{(p)}$ are identical to Eq. (F.10) but the $\tilde{C}_6^{(p)}$ coefficients are given by

$$\tilde{C}_6^{(p)} = \sum_{n_\alpha, n_\beta} \frac{\mathcal{R}_{1,\alpha}\mathcal{R}_{\alpha,2}\mathcal{R}_{2,\beta}\mathcal{R}_{\beta,1}}{\delta_{\alpha\beta}}. \tag{F.14}$$

The radial matrix element $\mathcal{R}_{nn'}$ is only significant for $n - n' \approx 0$, hence we expect the flip-flop vdW terms to decay rapidly as $\Delta n = n_1 - n_2$ is increased. Figure F.1(a) shows the strength of these flip-flop vdW interactions for $n_1S + n_2S$ and Fig. F.1(b) shows the ratio of the flip-flop interactions to the desired identity C_6 interactions. We see that already for $\Delta n > 5$, the off-diagonal interactions are 10^3 times smaller than the identity interactions. Moreover, the deviation of Eq. (F.12) from an identity is dominated by the off-diagonal $\mathcal{D}_0$ term appearing in $\hat{\mathcal{H}}_{\text{vdW}}^{\text{diag}}$ for $\Delta n > 1$. Already at $\Delta n = 2$, the deviation from identity due to the latter [shown in Fig. 7.3(b) of Chapter 7] is an order of magnitude larger than the corresponding error due to $\hat{\mathcal{H}}_{\text{vdW}}^{\text{flip-flop}}$.

F.2 Phonon interactions

In this section, we derive the effective phonon interactions (Eq. (7.1)) between two atoms in harmonic traps, separated by a macroscopic distance r. We assume that the interactions are independent of the internal state and are given by

$$\hat{\mathcal{H}}_{\text{int}}(r) = \frac{\mathcal{A}}{r^6 + R_c^6}, \tag{F.15}$$

where R_c is a blockade radius and $\mathcal{A}$ depends on the vdW interaction strength. We further assume that the position of each atom can be decomposed into quantum fluctuations on top of a coherent (classical) part: $\mathbf{r_i} \to \mathbf{r_i} + \hat{\mathbf{r}}_\mathbf{i}$. Without loss of generality, we assume that the macroscopic separation $r_0 = |\mathbf{r}_1 - \mathbf{r}_2|$ is along the y direction. In this case, to second order in the small quantum fluctuations we get

$$\hat{\mathcal{H}}_{\text{int}} \approx \hat{\mathcal{H}}_x + \hat{\mathcal{H}}_y + \hat{\mathcal{H}}_z + \text{Constants}, \tag{F.16}$$

where

$$\begin{aligned}
\hat{\mathcal{H}}_x &= -3\mathcal{A}\frac{(\hat{x}_1 - \hat{x}_2)^2}{r_0^8[1 + (R_c/r_0)^6]^2}, \\
\hat{\mathcal{H}}_y &= -6\mathcal{A}\frac{(\hat{y}_1 - \hat{y}_2)}{r_0^7[1 + (R_c/r_0)^6]^2} + 3\mathcal{A}\frac{(\hat{y}_1 - \hat{y}_2)^2[7 - 5(R_c/r_0)^6]}{r_0^8[1 + (R_c/r_0)^6]^3}, \\
\hat{\mathcal{H}}_z &= -3\mathcal{A}\frac{(\hat{z}_1 - \hat{z}_2)^2}{r_0^8[1 + (R_c/r_0)^6]^2}.
\end{aligned} \tag{F.17}$$

The full Hamiltonian of the motional degrees of freedom is

$$\hat{\mathcal{H}} = \sum_{\alpha=x,y,z}\left[\sum_{i=1,2}\left(\frac{\hat{P}_{i,\alpha}^2}{2M} + \frac{1}{2}M\omega_\alpha^2\hat{\alpha}_i^2\right) + \hat{\mathcal{H}}_\alpha\right]. \tag{F.18}$$

The full Hamiltonian is therefore a sum of three independent, commuting Hamiltonians for the three directions, which means we can analyze each direction separately. Note that $\hat{\mathcal{H}}_x$ and $\hat{\mathcal{H}}_z$ have the same form while $\hat{\mathcal{H}}_y$ contains a linear term. This linear term, which represents the force

between the two atoms, is inherently larger than the quadratic term which gives rise to the phonon-swap terms. This fact prevents an efficient cooling of the y direction. In Appendix F.3 we show how one can overcome this and nevertheless cool all three directions using an adiabatic protocol. Here we assume that the confinement along y is sufficiently strong and hence focus on the x and z directions.

The Hamiltonian for the z direction in terms of bosonic creation and annihilation operators $\hat{z}_1 = \frac{1}{\sqrt{2M\omega_z}}(\hat{a}_z + \hat{a}_z^\dagger)$, $\hat{P}_{1,z} = -i\frac{\sqrt{M\omega_z}}{2}(\hat{a}_z - \hat{a}_z^\dagger)$ and $\hat{z}_2 = \frac{1}{\sqrt{2M\omega_z}}(\hat{d}_z + \hat{d}_z^\dagger)$, $\hat{P}_{2,z} = -i\frac{\sqrt{M\omega_z}}{2}(\hat{d}_z - \hat{d}_z^\dagger)$ is given by (the Hamiltonian for x is the same with $z \to x$)

$$\hat{\mathcal{H}}_{\text{ph},z} = \omega_z(\hat{d}_z^\dagger \hat{d}_z + \hat{a}_z^\dagger \hat{a}_z) - \frac{G_z}{2}\left[(\hat{d}_z + \hat{d}_z^\dagger)^2 + (\hat{a}_z + \hat{a}_z^\dagger)^2\right] + G_z(\hat{d}_z + \hat{d}_z^\dagger)(\hat{a}_z + \hat{a}_z^\dagger), \quad \text{(F.19)}$$

where the phonon-coupling G_z is

$$G_z = \frac{3\mathcal{A}}{M\omega_z r_0^8}\frac{1}{[1 + (R_c/r_0)^6]^2}. \quad \text{(F.20)}$$

which is given under Eq. (7.1) in Chapter 7, where we dropped the z label. Assuming that $\omega_z \gg G_z$ and making the rotating wave approximation we have

$$\hat{\mathcal{H}}_{\text{ph},z} \approx \omega_z(\hat{d}_z^\dagger \hat{d}_z + \hat{a}_z^\dagger \hat{a}_z) + G_z(\hat{d}_z \hat{a}_z^\dagger + \hat{d}_z^\dagger \hat{a}_z), \quad \text{(F.21)}$$

or in the rotating frame simply $G_z(\hat{d}_z \hat{a}_z^\dagger + \hat{d}_z^\dagger \hat{a}_z)$.

This Hamiltonian effectuates a state-transfer between the two modes $\hat{a}_z, \hat{d}_z$, which can be seen from the solution to the Heisenberg equations of motion ($\dot{\hat{d}}_z(t) = i\left[G_z(\hat{d}_z \hat{a}_z^\dagger + \hat{d}_z^\dagger \hat{a}_z), \hat{d}_z\right]$, $\dot{\hat{a}}_z(t) = i\left[G_z(\hat{d}_z \hat{a}_z^\dagger + \hat{d}_z^\dagger \hat{a}_z), \hat{a}_z\right]$)

$$\begin{aligned} \hat{a}_z(t) &= \cos(G_z t)\hat{a}_z(0) - i\sin(G_z t)\hat{d}_z(0), \\ \hat{d}_z(t) &= -i\sin(G_z t)\hat{a}_z(0) + \cos(G_z t)\hat{d}_z(0). \end{aligned} \quad \text{(F.22)}$$

After a time of $t_s = \frac{\pi}{2G_z}$, the states of the two modes, and hence the phonon occupations, are swapped. If, in addition, we have that $\omega_z = \omega_x$ (and accordingly $G_z = G_x$) then the same swap

process would cool both the x and z directions.

Finally, let us comment on the higher-order terms that we neglect in the Taylor expansion. Each term in the expansion of Eq. (F.15) is smaller than the precedent by the dimensionless factor $\sim \frac{1}{r_0}\sqrt{\frac{1}{M\omega_\alpha}}\,(\alpha = x, y, z)$. For Rubidium atoms separated by $3\,\mu\mathrm{m}$ in $\omega_z/2\pi = 15\,\mathrm{kHz}$ traps (assuming $\omega_z < \omega_{x,y}$) this factor is ~ 0.03. Moreover, if we work in the regime where the rotating-wave approximation is valid, i.e $\omega_z \gg G_z$, all the terms that do not conserve the total number of excitations, and in particular all the odd powers in the expansion, can be neglected. Thus, in that regime, the leading order correction to Eq. (F.19) is smaller by the factor $\sim \left(\frac{1}{r_0}\sqrt{\frac{1}{M\omega_z}}\right)^2 \sim 9 \times 10^{-4}$.

F.3 Adiabatic phonon-swap

In this section, we present an adiabatic protocol for performing the phonon-swap. As we have discussed in the previous section, the repulsive force between a pair of atoms prevents the simple phonon-swap from taking place for the trap component parallel to the inter-atomic axis. This manifests itself in the presence of the linear term in the y component of Eq. (F.17). We show here how this can be mitigated by implementing a smooth, slowly varying $\pi/2$ pulse.

This adiabatic protocol can be intuitively understood as follows: we imagine slowly turning on and off the interactions [$\mathcal{A} \to \mathcal{A}(t)$] such that the atoms adiabatically follow the new equilibrium positions, determined by the total potential, which is the sum of the trap potentials and the interactions. During this time, the phonon-swap can take place, swapping the phonon excitations while the displacements slowly change.

We assume the same setup as in the previous section, where the two atoms, data and auxiliary,

are initially (at time $t = 0$) separated by some distance $r_0 \equiv r(0) = y_2^{eq}(0) - y_1^{eq}(0)$ (determined by the trap separation). As we slowly increase $\mathcal{A}(t)$, the equilibrium positions (which at $t = 0$ are $y_1^{eq}(0) = 0, y_2^{eq}(0) = r_0$) slowly change as well. These equilibrium positions are found by minimizing the full potential at each time t, and are given by the solutions to the following equations

$$\begin{aligned} M\omega_y^2 y_1^{eq}(t) - \frac{6\mathcal{A}(t)[y_1^{eq}(t) - y_2^{eq}(t)]^5}{[R_c^6 + (y_1^{eq}(t) - y_2^{eq}(t))^6]^2} = 0, \\ \frac{6\mathcal{A}(t)[y_1^{eq}(t) - y_2^{eq}(t)]^5}{[R_c^6 + (y_1^{eq}(t) - y_2^{eq}(t))^6]^2} + M\omega_y^2(y_2^{eq}(t) - r_0) = 0. \end{aligned} \tag{F.23}$$

Taylor expanding the potential about those equilibrium positions gives (up to constants)

$$\begin{aligned} \hat{\mathcal{H}}_{\text{ph},y} = \frac{\hat{P}_{1,y}^2 + \hat{P}_{2,y}^2}{2M} + \frac{1}{2}M\omega_y^2(\hat{y}_1 - y_1^{eq}(t))^2 + \frac{1}{2}M\omega_y^2(\hat{y}_2 - y_2^{eq}(t))^2 \\ - M\omega_y G_y(t)[\hat{y}_1 - y_1^{eq}(t) - (\hat{y}_2 - y_2^{eq}(t))]^2, \end{aligned} \tag{F.24}$$

where

$$G_y(t) = -\frac{3\mathcal{A}(t)}{M\omega_y}\frac{7 - 5(R_b/r(t))^6}{r(t)^8[1 + (R_b/r(t))^6]^3}, \quad r(t) = y_2^{eq}(t) - y_1^{eq}(t). \tag{F.25}$$

The x and z Hamiltonians are still given by Eq. (F.17) and Eq. (F.19) with the only difference being that G_z, G_x are now time-dependent. In the following we therefore first focus on the y component. Note that by expanding about the equilibrium positions, we have implicitly assumed that the process is adiabatic. This assumption can be justified self-consistently, as we show later in this section.

We now transform to the bosonic creation and annihilation operators $\hat{y}_1 = \frac{1}{\sqrt{2M\omega_y}}(\hat{a}_y + \hat{a}_y^\dagger)$, $\hat{y}_2 = \frac{1}{\sqrt{2M\omega_y}}(\hat{d}_y + \hat{d}_y^\dagger)$, $\hat{P}_{1,y} = i\sqrt{\frac{M\omega_y}{2}}(\hat{a}_y^\dagger - \hat{a}_y)$, $\hat{P}_{2,y} = i\sqrt{\frac{M\omega_y}{2}}(\hat{d}_y^\dagger - \hat{d}_y)$ which gives

$$\begin{aligned} \hat{\mathcal{H}}_{\text{ph},y} = \omega_y(\hat{a}_y^\dagger\hat{a}_y + \hat{d}_y^\dagger\hat{d}_y) - \omega_y\alpha_1(t)(\hat{a}_y + \hat{a}_y^\dagger) - \omega_y\alpha_2(t)(\hat{d}_y + \hat{d}_y^\dagger) \\ - \frac{G_y(t)}{2}[\hat{a}_y + \hat{a}_y^\dagger - 2\alpha_1(t) - (\hat{d}_y + \hat{d}_y^\dagger - 2\alpha_2(t))]^2, \end{aligned} \tag{F.26}$$

where $\alpha_i(t) = \sqrt{\frac{M\omega_y}{2}} y_i^{eq}(t)$. Moving to the adiabatic frame with the displacement operator $\hat{D}(t) = \exp\Big[-\alpha_1(t)(\hat{a}_y^\dagger - \hat{a}_y) - \alpha_2(t)(\hat{d}_y^\dagger - \hat{d}_y)\Big]$ yields

$$\begin{aligned}\hat{\mathcal{H}}_{\text{ph,y,ad}} &= \hat{D}(t)\hat{\mathcal{H}}_{\text{ph},y}\hat{D}^\dagger(t) + i\dot{D}(t)D^\dagger(t) \\ &= \omega_y(\hat{a}_y^\dagger\hat{a}_y + \hat{d}_y^\dagger\hat{d}_y) - \frac{G_y(t)}{2}\Big[(\hat{a}_y^\dagger + \hat{a}_y)^2 + (\hat{d}_y^\dagger + \hat{d}_y)^2\Big] \\ &\quad + G_y(t)(\hat{a}_y^\dagger + \hat{a}_y)(\hat{d}_y^\dagger + \hat{d}_y) + i\dot{\alpha}_1(\hat{a}_y - \hat{a}_y^\dagger) + i\dot{\alpha}_2(\hat{d}_y - \hat{d}_y^\dagger).\end{aligned} \tag{F.27}$$

From Eq. (F.27) we can see that the adiabatic Hamiltonian for the y component has a similar structure as the x and z Hamiltonians in the previous section in Eq. (F.19), with additional non-adiabatic corrections proportional to $\dot{\alpha}_1$ and $\dot{\alpha}_2$. The adiabaticity condition is therefore $\omega_y \gg \dot{\alpha}_1, \dot{\alpha}_2$, which together with the condition $\omega_y \gg G_y$ allows us to make the rotating wave approximation, giving

$$\hat{\mathcal{H}}_{\text{ph,y,ad}} \approx \omega_y(\hat{a}_y^\dagger\hat{a}_y + \hat{d}_y^\dagger\hat{d}_y) + G_y(t)(\hat{a}_y^\dagger\hat{d}_y + \hat{a}_y\hat{d}_y^\dagger). \tag{F.28}$$

If $\omega_y \gg \dot{\alpha}_1, \dot{\alpha}_2$, then the atoms follow adiabatically the equilibria of the total potential. This is in fact the justification for the self-consistent assumption mentioned at the beginning of this section.

Equation (F.28) effectuates a state-transfer between the two modes, exactly as the time-independent version in the previous section [see Eq. (F.21)]. The solution of the Heisenberg equations (in the rotating frame) are in this case (with equivalent expressions for the x, z components)

$$\begin{aligned}\hat{a}_y(t) &= \cos\left(\int G_y(t)dt\right)\hat{a}_y(0) - i\sin\left(\int G_y(t)dt\right)\hat{d}_y(0), \\ \hat{d}_y(t) &= -i\sin\left(\int G_y(t)dt\right)\hat{a}_y(0) + \cos\left(\int G_y(t)dt\right)\hat{d}_y(0).\end{aligned} \tag{F.29}$$

For a full phonon-swap of the y phonons to take place we require $\int G_y(t)dt = \frac{\pi}{2}$. However, since the phonon interaction strength for the y direction is different than for the x and z directions [i.e., $G_y(t) \neq G_{x,z}(t)$ as one can see in Fig. F.2(a)] a $\pi/2$ pulse for y is not necessarily a $\pi/2$ pulse for the other two directions. Nevertheless, in typical scenarios the traps are not isotropic, and one can

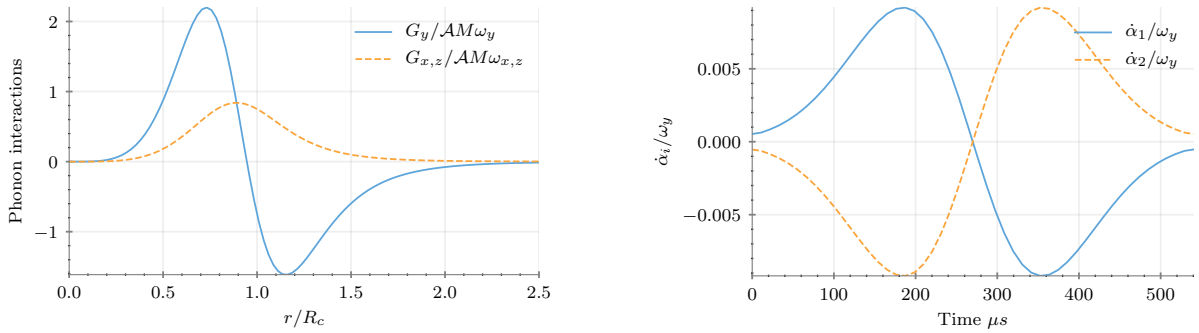

Figure F.2: (a) Normalized phonon interactions as a function of distance. (b) Non-adiabatic corrections normalized to the trap frequency $\omega_y/2\pi = 50\,\mathrm{kHz}$ as a function of time for a Gaussian pulse with $\mathcal{A}_{max}/2\pi = 34.4\,\mathrm{MHz}\,\mu\mathrm{m}^6$, $\sigma = 6.7\,\mu\mathrm{s}$, $t_0 = 215.9\,\mu\mathrm{s}$ for a trap separation of $r_0 = 1.93\,\mu\mathrm{m}$.

utilize this fact together with the different interaction curves to compensate and optimize a pulse that is as close as possible to $\pi/2$ for all three directions.

As a simple example, we take a Gaussian pulse for $\mathcal{A}(t) = \mathcal{A}_{max}\left[\exp\left(-\frac{(t-t_0)^2}{2\sigma^2}\right) - c\right]$ where c is a constant chosen such that $\mathcal{A}(0) = 0$. Using similar parameters as in Chapter 7 (see caption of Fig. F.2), assuming $\omega_x/2\pi = \omega_z/2\pi = 15\,\mathrm{kHz}$ and $\omega_y/2\pi = 50\,\mathrm{kHz}$ we can find pulse parameters that yield $\int G_y(t)dt/(\pi/2) \approx \int G_{x,z}(t)dt/(\pi/2) \approx 1$. Furthermore, even if for a given parameter regime it is not possible to perform the 3D phonon-swap with a single pulse, one can always perform the cooling in three steps: one can first apply a $\pi/2$ pulse to swap the phonons in the x and z components. This would only partially swap the y phonons. One then has to cool the auxiliary atoms before applying another $\pi/2$ pulse, this time designed to fully swap the y phonons.

Finally, in Fig. F.2(b) we show the ratios of $\dot{\alpha}_{1,2}$ to the trap frequency ω_y for the Gaussian pulse described above. As one can see, the adiabaticity constraint is satisfied well at all times.

F.4 Phonon-swap for 1D chain

Here we generalize the results of the previous sections to the more realistic case of an atomic register consisting of many atoms. We derive Eq. (7.3).

For concreteness we consider the setup in Fig. 7.1(a) of Chapter 7 where a 1D chain of N auxiliary atoms (lattice constant x_0) is brought to a distance of y_0 from an identical 1D chain of N data atoms. For simplicity we only consider a single trap direction (z) and the time-independent swap protocol. The generalizations to two or three directions and the adiabatic swap are straightforward. The Hamiltonian for the vibrational modes in the z direction is (we drop the z labels from here on)

$$\hat{\mathcal{H}} = \sum_{i=1}^{N} \omega_z (\hat{a}_i^\dagger \hat{a}_i + \hat{d}_i^\dagger \hat{d}_i) - \frac{1}{2} \sum_{i=1,j=1,i\neq j}^{N} G_{ij} \left[(\hat{z}_i^a - \hat{z}_j^a)^2 + (\hat{z}_i^d - \hat{z}_j^d)^2 \right] - \sum_{i=1,j=1}^{N} F_{ij} (\hat{z}_i^a - \hat{z}_j^d)^2, \tag{F.30}$$

where by $\hat{a}_i$ ($\hat{d}_i$) we denote the phonon-annihilation operator for an auxiliary (data) atom i and by $z_i^a = \frac{1}{\sqrt{2}}(\hat{a} + \hat{a}^\dagger)$ ($z_i^d = \frac{1}{\sqrt{2}}(\hat{d} + \hat{d}^\dagger)$) the z coordinate of an auxiliary (data) atom (we have absorbed $M\omega_z$ into the definition of G_{ij} and F_{ij}). The $\frac{1}{2}$ is to avoid double-counting and the coefficients are given by

$$\begin{aligned} G_{ij} &= \frac{G}{\eta^8 |i-j|^8}, \\ F_{ij} &= \frac{G}{\left[\eta^2 (i-j)^2 + 1\right]^4}, \end{aligned} \tag{F.31}$$

where G is defined in Eq. (F.20) with $r = y_0$ and $\eta \equiv \frac{x_0}{y_0}$. To be consistent with the two-atom case, we have defined G with the nearest neighbor separation between data-auxiliary atoms (y_0). We have also assumed that pairs of atoms that are farther apart than the nearest-neighbor separation (i.e next nearest-neighbors and so on) experience power-law interactions. In other words, we assumed that the separation between next-nearest neighbors is significantly larger than the blockade radius.

In terms of bosonic operators Eq. (F.30) is

$$\begin{aligned}\hat{\mathcal{H}} = &\sum_{i=1}^{N}\left[\tilde{\omega}_{z,i}(\hat{a}_i^\dagger\hat{a}_i + \hat{d}_i^\dagger\hat{d}_i) - \frac{1}{2}(\tilde{G}_i + \tilde{F}_i)(\hat{a}_i^2 + \hat{d}_i^2 + \text{H.c.})\right] \\ &+ \frac{1}{2}\sum_{i\neq j} G_{ij}(\hat{a}_i\hat{a}_j + \hat{a}_i^\dagger\hat{a}_j + \hat{d}_i\hat{d}_j + \hat{d}_i^\dagger\hat{d}_j + \text{H.c.}) + \sum_{ij} F_{ij}(\hat{a}_i\hat{d}_j + \hat{a}_i\hat{d}_j^\dagger + \text{H.c.}),\end{aligned} \tag{F.32}$$

where

$$\begin{aligned}\tilde{\omega}_{z,i} &= \omega_z + \tilde{G}_i + \tilde{F}_i, \\ \tilde{G}_i &= \sum_{j\neq i} G_{ij}, \\ \tilde{F}_i &= \sum_j F_{ij}.\end{aligned} \tag{F.33}$$

We now assume that the system is translationally invariant, i.e, $\tilde{\omega}_{z,i} \approx \tilde{\omega}_z, \tilde{G}_i \approx \tilde{G}, \tilde{F}_i \approx \tilde{F}$ for all i. This is a good approximation for the "bulk" of the atoms, away from the edges, in the limit where $N \to \infty$, or for a system with periodic boundary conditions. We also assume that $\tilde{\omega}_z \gg \tilde{G}, \tilde{F}$ which allows us to drop terms that do not conserve the total number of excitations. With these assumptions, the Hamiltonian in the rotating frame is given by

$$\hat{\mathcal{H}} = \sum_{i\neq j} G_{ij}(\hat{a}_i^\dagger\hat{a}_j + \hat{d}_i^\dagger\hat{d}_j) + \sum_{ij} F_{ij}(\hat{a}_i\hat{d}_j^\dagger + \hat{a}_i^\dagger\hat{d}_j). \tag{F.34}$$

Taking the Fourier transform with

$$\hat{a}_n = \frac{1}{\sqrt{N}}\sum_k \hat{a}_k e^{iknx_0}, \qquad \hat{a}_k = \frac{1}{\sqrt{N}}\sum_n \hat{a}_n e^{-iknx_0}, \tag{F.35}$$

and using the fact that G_{ij} and F_{ij} are transitionally invariant, i.e depend on $|i-j|$, we get

$$\hat{\mathcal{H}} = \sum_k \Big[G_k(\hat{a}_k^\dagger\hat{a}_k + \hat{d}_k^\dagger\hat{d}_k) + F_k(\hat{a}_k\hat{d}_k^\dagger + \hat{a}_k^\dagger\hat{d}_k)\Big], \tag{F.36}$$

where we used $\sum_n e^{i(k-k')nx_0} = N\delta_{k,k'}$ and the following definitions

$$G_k = \sum_{n=-N, n\neq 0}^{N} G_n e^{-iknx_0} = 2\sum_{n=1}^{N} G_n \cos(knx_0),$$
$$F_k = \sum_{n=-N}^{N} G_n e^{-iknx_0} = F_{n=0} + 2\sum_{n=1}^{N} F_n \cos(knx_0). \tag{F.37}$$

Equation (F.36) can be diagonalized with the transformation

$$\hat{c}_k = \frac{\hat{a}_k + \hat{d}_k}{\sqrt{2}}, \qquad \hat{b}_k = \frac{\hat{a}_k - \hat{d}_k}{\sqrt{2}}, \tag{F.38}$$

which gives

$$\hat{\mathcal{H}} = \sum_k \left[(G_k + F_k)\hat{c}_k^\dagger \hat{c}_k + (G_k - F_k)\hat{b}_k^\dagger \hat{b}_k \right]. \tag{F.39}$$

Using this, we can now compute the average excitation number in the auxiliary and data atoms, given by

$$\bar{n}_a(t) = \frac{1}{N}\sum_n \left\langle \hat{a}_n^\dagger(t)\hat{a}_n(t) \right\rangle,$$
$$\bar{n}_d(t) = \frac{1}{N}\sum_n \left\langle \hat{d}_n^\dagger(t)\hat{d}_n(t) \right\rangle. \tag{F.40}$$

Below, we first compute $\bar{n}_a(t)$:

$$\bar{n}_a(t) = \frac{1}{N}\sum_n \left\langle \hat{a}_n^\dagger(t)\hat{a}_n(t) \right\rangle \tag{F.41}$$
$$= \frac{1}{4N^2}\sum_k \sum_{nm} e^{ikx_0(n-m)} \left\langle 4\cos^2(F_k t)\hat{a}_n^\dagger \hat{a}_m + 4\sin^2(F_k t)\hat{d}_n^\dagger \hat{d}_m + 2i\sin(2F_k t)\hat{a}_n^\dagger \hat{d}_m - 2i\sin(2F_k t)\hat{d}_n^\dagger \hat{a}_m \right\rangle.$$

For simplicity, we now assume that the initial state is a product state and also that $\langle \hat{a}_i \rangle = \langle \hat{a}_i^2 \rangle = \langle \hat{d}_i \rangle = \langle \hat{d}_i^2 \rangle = 0$ for all i. This would be the case, for example, if every atom starts at a pure Fock state or a thermal state. With this assumption, only the diagonal terms in Eq. (F.41) contribute, yielding

$$\bar{n}_a(t) = \frac{1}{N}\left[\sum_k \cos^2(F_k t)\right]\bar{n}_a(0) + \frac{1}{N}\left[\sum_k \sin^2(F_k t)\right]\bar{n}_d(0). \tag{F.42}$$

Taking the continuum limit $\frac{1}{N}\sum_k \to \frac{x_0}{2\pi}\int_{-\pi/x_0}^{\pi/x_0} dk$ and changing variables $kx_0 \to k$ gives

$$\bar{n}_a(t) = \bar{n}_a(0)\int_{-\pi}^{\pi}\frac{dk}{2\pi}\cos^2(F_k t) + \bar{n}_d(0)\int_{-\pi}^{\pi}\frac{dk}{2\pi}\sin^2(F_k t). \tag{F.43}$$

To obtain a closed form expression, we approximate the sum in F_k by the first term $n = 1$ which corresponds to only keeping up to next nearest-neighbors interactions between auxiliary and data atoms. This gives rise to

$$\begin{aligned}\bar{n}_a(t) &= \frac{\bar{n}_a(0)+\bar{n}_d(0)}{2} + \frac{\bar{n}_a(0)-\bar{n}_d(0)}{2}J_0\left[\frac{4Gt}{(1+\eta^2)^4}\right]\cos(2Gt),\\ \bar{n}_d(t) &= \frac{\bar{n}_a(0)+\bar{n}_d(0)}{2} - \frac{\bar{n}_a(0)-\bar{n}_d(0)}{2}J_0\left[\frac{4Gt}{(1+\eta^2)^4}\right]\cos(2Gt),\end{aligned} \tag{F.44}$$

where $J_0(z)$ is a Bessel function of the first kind.

F.5 Laser excitation from ground states

In this section we give an example level structure and laser polarization choice for ^{87}Rb atoms for some of the schemes we presented in Chapter 7. One choice for the spin-1/2 states of the data atoms are the following two hyperfine ground states

$$\begin{aligned}|g_-\rangle &\equiv |5^2S_{1/2}, F=1, m_F=1\rangle,\\ |g_+\rangle &\equiv |5^2S_{1/2}, F=2, m_F=2\rangle.\end{aligned} \tag{F.45}$$

To excite to $S_{1/2}$ states, we need to use an intermediate P state. Using σ_+, σ_-, and σ_0 polarized light, one can for example use the following ladder scheme

$$\begin{aligned}|g_-\rangle &\xrightarrow{\sigma_0} \left|5P_{3/2}, F=1, m_F=1\right\rangle \xrightarrow{\sigma_+} \left|nS_{1/2}, m_J=+\tfrac{1}{2}\right\rangle,\\ |g_+\rangle &\xrightarrow{\sigma_0} \left|5P_{3/2}, F=2, m_F=2\right\rangle \xrightarrow{\sigma_-} \left|nS_{1/2}, m_J=-\tfrac{1}{2}\right\rangle.\end{aligned} \tag{F.46}$$

For the auxiliary atoms, a single state out of the two is sufficient. For exciting to $P_{1/2}$ states, one choice is the following

$$
\begin{aligned}
|g_-\rangle &\xrightarrow{\sigma_+} |nP_{1/2}, m_J = +\tfrac{1}{2}\rangle, \\
|g_+\rangle &\xrightarrow{\sigma_-} |nP_{1/2}, m_J = -\tfrac{1}{2}\rangle.
\end{aligned}
\tag{F.47}
$$

Bibliography

[1] A. G. J. MacFarlane, J. P. Dowling, and G. J. Milburn, Quantum technology: The second quantum revolution, Philos. Trans. R. Soc. Lond. Ser. Math. Phys. Eng. Sci. **361**, 1655–1674 (2003).

[2] Z. Hu and H. J. Kimble, Observation of a single atom in a magneto-optical trap, Opt. Lett., OL **19**, 1888–1890 (1994).

[3] D. Haubrich, H. Schadwinkel, F. Strauch, B. Ueberholz, R. Wynands, and D. Meschede, Observation of individual neutral atoms in magnetic and magneto-optical traps, EPL **34**, 663 (1996).

[4] D. J. Wineland, Atomic-Ion Coulomb Clusters in an Ion Trap, Phys. Rev. Lett. **59**, 2935–2938 (1987).

[5] M. Brune, Quantum Rabi Oscillation: A Direct Test of Field Quantization in a Cavity, Phys. Rev. Lett. **76**, 1800–1803 (1996).

[6] G. S. Buller and R. J. Collins, Single-photon generation and detection, Meas. Sci. Technol. **21**, 012002 (2009).

[7] B. Lounis and M. Orrit, Single-photon sources, Rep. Prog. Phys. **68**, 1129 (2005).

[8] G. Rempe, Observation of quantum collapse and revival in a one-atom maser, Phys. Rev. Lett. **58**, 353–356 (1987).

[9] R. J. Thompson, Observation of normal-mode splitting for an atom in an optical cavity, Phys. Rev. Lett. **68**, 1132–1135 (1992).

[10] R. Hanson, Spins in few-electron quantum dots, Rev. Mod. Phys. **79**, 1217–1265 (2007).

[11] J. Wrachtrup and F. Jelezko, Processing quantum information in diamond, J. Phys.: Condens. Matter **18**, S807 (2006).

[12] J. M. Martinis, Energy-Level Quantization in the Zero-Voltage State of a Current-Biased Josephson Junction, Phys. Rev. Lett. **55**, 1543–1546 (1985).

[13] M. H. Devoret, Measurements of Macroscopic Quantum Tunneling out of the Zero-Voltage State of a Current-Biased Josephson Junction, Phys. Rev. Lett. **55**, 1908–1911 (1985).

[14] N. Gisin, G. Ribordy, W. Tittel, and H. Zbinden, Quantum cryptography, Rev. Mod. Phys. **74**, 145–195 (2002).

[15] D. Bouwmeester, A. Ekert, and A. Zeilinger, eds., *The Physics of Quantum Information* (Springer Berlin Heidelberg, Berlin, Heidelberg, 2000).

[16] C. L. Degen, F. Reinhard, and P. Cappellaro, Quantum sensing, Rev. Mod. Phys. **89**, 035002 (2017).

[17] J. I. Cirac and P. Zoller, Goals and opportunities in quantum simulation, Nat. Phys. **8**, 264–266 (2012).

[18] I. M. Georgescu, S. Ashhab, and F. Nori, Quantum simulation, Rev. Mod. Phys. **86**, 153–185 (2014).

[19] M. A. Nielsen and I. L. Chuang, *Quantum Computation and Quantum Information*, 10th ed. (Cambridge University Press, Cambridge ; New York, 2010).

[20] A. Montanaro, Quantum algorithms: An overview, npj Quantum Inf **2**, 1–8 (2016).

[21] C. Gross and I. Bloch, Quantum simulations with ultracold atoms in optical lattices, Science **357**, 995–1001 (2017).

[22] A. Browaeys and T. Lahaye, Many-body physics with individually controlled Rydberg atoms, Nat. Phys. **16**, 132–142 (2020).

[23] M. Saffman, T. G. Walker, and K. Mølmer, Quantum information with Rydberg atoms, Rev. Mod. Phys. **82**, 2313–2363 (2010).

[24] H. Häffner, C. F. Roos, and R. Blatt, Quantum computing with trapped ions, Physics Reports **469**, 155–203 (2008).

[25] R. Blatt and C. F. Roos, Quantum simulations with trapped ions, Nat. Phys. **8**, 277–284 (2012).

[26] A. Blais, A. L. Grimsmo, S. M. Girvin, and A. Wallraff, Circuit Quantum Electrodynamics, Rev. Mod. Phys. **93**, 025005 (2021).

[27] G. Wendin, Quantum information processing with superconducting circuits: A review, Rep. Prog. Phys. **80**, 106001 (2017).

[28] M. H. Devoret and R. J. Schoelkopf, Superconducting Circuits for Quantum Information: An Outlook, Science **339**, 1169–1174 (2013).

[29] M. Serbyn, D. A. Abanin, and Z. Papić, Quantum many-body scars and weak breaking of ergodicity, Nat. Phys. **17**, 675–685 (2021).

[30] A. Polkovnikov, K. Sengupta, A. Silva, and M. Vengalattore, Colloquium: Nonequilibrium dynamics of closed interacting quantum systems, Rev. Mod. Phys. **83**, 863–883 (2011).

[31] A. Mitra, Quantum Quench Dynamics, Annu. Rev. Condens. Matter Phys. **9**, 245–259 (2018).

[32] M. P. Fisher, V. Khemani, A. Nahum, and S. Vijay, Random Quantum Circuits, Annu. Rev. Condens. Matter Phys. **14**, 335–379 (2023).

[33] N. Defenu, T. Donner, T. Macrì, G. Pagano, S. Ruffo, and A. Trombettoni, Long-range interacting quantum systems 10.48550/ARXIV.2109.01063 (2021).

[34] L. M. Sieberer, M. Buchhold, and S. Diehl, Keldysh field theory for driven open quantum systems, Rep. Prog. Phys. **79**, 096001 (2016).

[35] H. Weimer, A. Kshetrimayum, and R. Orús, Simulation methods for open quantum many-body systems, Rev. Mod. Phys. **93**, 015008 (2021).

[36] A. J. Daley, Quantum trajectories and open many-body quantum systems, Adv. Phys. **63**, 77–149 (2014).

[37] A. C. Potter and R. Vasseur, Entanglement Dynamics in Hybrid Quantum Circuits, in *Entanglement in Spin Chains: From Theory to Quantum Technology Applications*, Quantum Science and Technology, edited by A. Bayat, S. Bose, and H. Johannesson (Springer International Publishing, Cham, 2022) pp. 211–249.

[38] R. J. Lewis-Swan, A. Safavi-Naini, A. M. Kaufman, and A. M. Rey, Dynamics of quantum information, Nat. Rev. Phys. Phys **1**, 627–634 (2019).

[39] A. J. Daley, I. Bloch, C. Kokail, S. Flannigan, N. Pearson, M. Troyer, and P. Zoller, Practical quantum advantage in quantum simulation, Nature **607**, 667–676 (2022).

[40] E. Altman, K. R. Brown, G. Carleo, L. D. Carr, E. Demler, C. Chin, B. DeMarco, S. E. Economou, M. A. Eriksson, K.-M. C. Fu, M. Greiner, K. R. Hazzard, R. G. Hulet, A. J. Kollár, B. L. Lev, *et al.*, Quantum Simulators: Architectures and Opportunities, PRX Quantum **2**, 017003 (2021).

[41] R. P. Feynman, Simulating physics with computers, Int J Theor Phys **21**, 467–488 (1982).

[42] Y. Manin, *Computable and Uncomputable* (Sovetskoye Radio, 1980).

[43] P. Benioff, The computer as a physical system: A microscopic quantum mechanical Hamiltonian model of computers as represented by Turing machines, J Stat Phys **22**, 563–591 (1980).

[44] S. Lloyd, Universal Quantum Simulators, Science **273**, 1073–1078 (1996).

[45] J. Preskill, Quantum Computing in the NISQ era and beyond, Quantum **2**, 79 (2018).

[46] B. Ulmann, *Analog Computing* (Oldenbourg, München, 2013).

[47] M. H. Devoret, *Quantum Fluctuations in Electrical Circuits* (1997) p. 351.

[48] J. J. García Ripoll, *Quantum Information and Quantum Optics with Superconducting Circuits* (Cambridge University Press, New York, 2022).

[49] S. E. Rasmussen, K. S. Christensen, S. P. Pedersen, L. B. Kristensen, T. Baekkegaard, N. J. S. Loft, and N. T. Zinner, Superconducting Circuit Companion-an Introduction with Worked Examples, Phys. Rev. Appl. **10**, 40204 (2021).

[50] M. Kjaergaard, M. E. Schwartz, J. Braumüller, P. Krantz, J. I.-J. Wang, S. Gustavsson, and W. D. Oliver, Superconducting Qubits: Current State of Play, Annu. Rev. Condens. Matter Phys. **11**, 369–395 (2020).

[51] P. Krantz, M. Kjaergaard, F. Yan, T. P. Orlando, S. Gustavsson, and W. D. Oliver, A quantum engineer's guide to superconducting qubits, Applied Physics Reviews **6**, 021318 (2019).

[52] M. Devoret, S. Girvin, and R. Schoelkopf, Circuit-QED: How strong can the coupling between a Josephson junction atom and a transmission line resonator be?*, Ann. Phys. **519**, 767–779 (2007).

[53] P. Forn-Díaz, L. Lamata, E. Rico, J. Kono, and E. Solano, Ultrastrong coupling regimes of light-matter interaction, Rev. Mod. Phys **91**, 25005 (2019).

[54] A. Frisk Kockum, A. Miranowicz, S. De Liberato, S. Savasta, and F. Nori, Ultrastrong coupling between light and matter, Nat. Rev. Phys. **1**, 19–40 (2019).

[55] F. Schäfer, T. Fukuhara, S. Sugawa, Y. Takasu, and Y. Takahashi, Tools for quantum simulation with ultracold atoms in optical lattices, Nat. Rev. Phys. Phys **2**, 411–425 (2020).

[56] I. Bloch, Ultracold quantum gases in optical lattices, Nature Phys **1**, 23–30 (2005).

[57] D. Barredo, V. Lienhard, S. de Léséleuc, T. Lahaye, and A. Browaeys, Synthetic three-dimensional atomic structures assembled atom by atom, Nature **561**, 79–82 (2018).

[58] M. Endres, H. Bernien, A. Keesling, H. Levine, E. R. Anschuetz, A. Krajenbrink, C. Senko, V. Vuletic, M. Greiner, and M. D. Lukin, Atom-by-atom assembly of defect-free one-dimensional cold atom arrays., Science **354**, 1024–1027 (2016).

[59] H. Kim, W. Lee, H.-g. Lee, H. Jo, Y. Song, and J. Ahn, In situ single-atom array synthesis using dynamic holographic optical tweezers, Nat. Commun. **7**, 13317 (2016).

[60] Y. Wang, M. Um, J. Zhang, S. An, M. Lyu, J.-N. Zhang, L.-M. Duan, D. Yum, and K. Kim, Single-qubit quantum memory exceeding ten-minute coherence time, Nature Photon **11**, 646–650 (2017).

[61] J. Yang, X. He, R. Guo, P. Xu, K. Wang, C. Sheng, M. Liu, J. Wang, A. Derevianko, and M. Zhan, Coherence Preservation of a Single Neutral Atom Qubit Transferred between Magic-Intensity Optical Traps, Phys. Rev. Lett. **117**, 123201 (2016).

[62] C. Monroe, W. C. Campbell, L.-M. Duan, Z.-X. Gong, A. V. Gorshkov, P. W. Hess, R. Islam, K. Kim, N. M. Linke, G. Pagano, P. Richerme, C. Senko, and N. Y. Yao, Programmable quantum simulations of spin systems with trapped ions, Rev. Mod. Phys. **93**, 025001 (2021).

[63] B. C. Sawyer, J. W. Britton, A. C. Keith, C.-C. J. Wang, J. K. Freericks, H. Uys, M. J. Biercuk, and J. J. Bollinger, Spectroscopy and Thermometry of Drumhead Modes in a Mesoscopic Trapped-Ion Crystal Using Entanglement, Phys. Rev. Lett. **108**, 213003 (2012).

[64] J. W. Britton, B. C. Sawyer, A. C. Keith, C.-C. J. Wang, J. K. Freericks, H. Uys, M. J. Biercuk, and J. J. Bollinger, Engineered two-dimensional Ising interactions in a trapped-ion quantum simulator with hundreds of spins, Nature **484**, 489–492 (2012).

[65] C.-C. J. Wang, A. C. Keith, and J. K. Freericks, Phonon-mediated quantum spin simulator employing a planar ionic crystal in a Penning trap, Phys. Rev. A **87**, 013422 (2013).

[66] J. G. Bohnet, B. C. Sawyer, J. W. Britton, M. L. Wall, A. M. Rey, M. Foss-Feig, and J. J. Bollinger, Quantum spin dynamics and entanglement generation with hundreds of trapped ions, Science **352**, 1297–1301 (2016).

[67] S. Korenblit, D. Kafri, W. C. Campbell, R. Islam, E. E. Edwards, Z.-X. Gong, G.-D. Lin, L.-M. Duan, J. Kim, K. Kim, and C. Monroe, Quantum simulation of spin models on an arbitrary lattice with trapped ions, New J. Phys. **14**, 095024 (2012).

[68] A. W. Glaetzle, M. Dalmonte, R. Nath, C. Gross, I. Bloch, and P. Zoller, Designing frustrated quantum magnets with laser-dressed Rydberg atoms, Phys. Rev. Lett. **114**, 173002 (2015).

[69] R. M. W. van Bijnen and T. Pohl, Quantum Magnetism and Topological Ordering via Rydberg Dressing near Förster Resonances, Phys. Rev. Lett. **114**, 243002 (2015).

[70] J. T. Young, P. Bienias, R. Belyansky, A. M. Kaufman, and A. V. Gorshkov, Asymmetric blockade and multi-qubit gates via dipole-dipole interactions, arXiv:2006.02486 (2020).

[71] K. Hammerer, A. S. Sørensen, and E. S. Polzik, Quantum interface between light and atomic ensembles, Rev. Mod. Phys. **82**, 1041–1093 (2010).

[72] H. Ritsch, P. Domokos, F. Brennecke, and T. Esslinger, Cold atoms in cavity-generated dynamical optical potentials, Rev. Mod. Phys. **85**, 553–601 (2013).

[73] F. Mivehvar, F. Piazza, T. Donner, and H. Ritsch, Cavity QED with quantum gases: New paradigms in many-body physics, Adv. Phys. **70**, 1–153 (2021).

[74] A. S. Sørensen and K. Mølmer, Entangling atoms in bad cavities, Phys. Rev. A **66**, 022314 (2002).

[75] I. D. Leroux, M. H. Schleier-Smith, and V. Vuletić, Implementation of Cavity Squeezing of a Collective Atomic Spin, Phys. Rev. Lett. **104**, 073602 (2010).

[76] M. H. Schleier-Smith, I. D. Leroux, and V. Vuletić, Squeezing the collective spin of a dilute atomic ensemble by cavity feedback, Phys. Rev. A **81**, 021804 (2010).

[77] V. D. Vaidya, Y. Guo, R. M. Kroeze, K. E. Ballantine, A. J. Kollár, J. Keeling, and B. L. Lev, Tunable-range, photon-mediated atomic interactions in multimode cavity QED, Phys. Rev. X **8**, 011002 (2018).

[78] A. André, L.-M. Duan, and M. D. Lukin, Coherent atom interactions mediated by dark-state polaritons, Phys. Rev. Lett. **88**, 243602 (2002).

[79] J. Gelhausen, M. Buchhold, A. Rosch, and P. Strack, Quantum-optical magnets with competing short- and long-range interactions: Rydberg-dressed spin lattice in an optical cavity, SciPost Phys. **1**, 004 (2016).

[80] W. Florkowski, *Phenomenology of Ultra-Relativistic Heavy-Ion Collisions* (WORLD SCIENTIFIC, 2010).

[81] A. Lovato, T. Dore, R. D. Pisarski, B. Schenke, K. Chatziioannou, J. S. Read, P. Landry, P. Danielewicz, D. Lee, S. Pratt, F. Rennecke, H. Elfner, V. Dexheimer, R. Kumar, M. Strickland, *et al.*, Long Range Plan: Dense matter theory for heavy-ion collisions and neutron stars, arXiv:2211.02224 .

[82] A. Accardi, J. L. Albacete, M. Anselmino, N. Armesto, E. C. Aschenauer, A. Bacchetta, D. Boer, W. K. Brooks, T. Burton, N. B. Chang, W. T. Deng, A. Deshpande, M. Diehl, A. Dumitru, R. Dupré, *et al.*, Electron-Ion Collider: The next QCD frontier: Understanding the glue that binds us all, Eur. Phys. J. A **52**, 268 (2016).

[83] P. Achenbach, D. Adhikari, A. Afanasev, F. Afzal, C. A. Aidala, A. Al-bataineh, D. K. Almaalol, M. Amaryan, D. Androić, W. R. Armstrong, M. Arratia, J. Arrington, A. Asaturyan, E. C. Aschenauer, H. Atac, *et al.*, The Present and Future of QCD, arXiv:2303.02579 .

[84] H. Gallagher, G. Garvey, and GP. Zeller, Neutrino-nucleus interactions, Annu. Rev. Nucl. Part. Sci. **61**, 355–378 (2011).

[85] L. Alvarez-Ruso, M. S. Athar, M. Barbaro, D. Cherdack, M. Christy, P. Coloma, T. Donnelly, S. Dytman, A. de Gouvêa, R. Hill, P. Huber, N. Jachowicz, T. Katori, A. Kronfeld, K. Mahn, *et al.*, NuSTEC White Paper: Status and challenges of neutrino–nucleus scattering, Prog. Part. Nucl. Phys. **100**, 1–68 (2018).

[86] A. S. Kronfeld, D. G. Richards, W. Detmold, R. Gupta, H.-W. Lin, K.-F. Liu, A. S. Meyer, R. Sufian, and S. Syritsyn, Lattice QCD and neutrino-nucleus scattering, Eur. Phys. J. A **55**, 1–18 (2019).

[87] L. A. Ruso, A. M. Ankowski, S. Bacca, A. B. Balantekin, J. Carlson, S. Gardiner, R. Gonzalez-Jimenez, R. Gupta, T. J. Hobbs, M. Hoferichter, J. Isaacson, N. Jachowicz, W. I. Jay, T. Katori, F. Kling, *et al.*, Theoretical tools for neutrino scattering: Interplay between lattice QCD, EFTs, nuclear physics, phenomenology, and neutrino event generators, arXiv:2203.09030 .

[88] A. Sorensen, K. Agarwal, K. W. Brown, Z. Chajecki, P. Danielewicz, C. Drischler, S. Gandolfi, J. W. Holt, M. Kaminski, C.-M. Ko, R. Kumar, B.-A. Li, W. G. Lynch, A. B. McIntosh, W. G. Newton, *et al.*, Dense Nuclear Matter Equation of State from Heavy-Ion Collisions, arXiv:2301.13253 .

[89] S. A. Bass, M. Gyulassy, H. Stoecker, and W. Greiner, Signatures of quark-gluon plasma formation in high energy heavy-ion collisions: A critical review, J. Phys. G Nucl. Part. Phys. **25**, R1 (1999).

[90] E. V. Shuryak, Quantum chromodynamics and the theory of superdense matter, Phys. Rept. **61**, 71–158 (1980).

[91] R. Baier, A. H. Mueller, D. Schiff, and D. T. Son, "Bottom-up" thermalization in heavy ion collisions, Phys. Lett. B **502**, 51–58 (2001).

[92] J. Berges, M. P. Heller, A. Mazeliauskas, and R. Venugopalan, QCD thermalization: Ab initio approaches and interdisciplinary connections, Rev. Mod. Phys. **93**, 035003 (2021).

[93] B. Andersson, G. Gustafson, G. Ingelman, and T. Sjostrand, Parton fragmentation and string dynamics, Phys. Rept. **97**, 31–145 (1983).

[94] B. R. Webber, A QCD model for jet fragmentation including soft gluon interference, Nucl. Phys. B **238**, 492–528 (1984).

[95] SA. Bass and A. Dumitru, Dynamics of hot bulk QCD matter: From the quark-gluon plasma to hadronic freeze-out, Phys. Rev. C **61**, 064909 (2000).

[96] A. Andronic, P. Braun-Munzinger, K. Redlich, and J. Stachel, Decoding the phase structure of QCD via particle production at high energy, Nature **561**, 321–330 (2018).

[97] J. D. Bjorken, Asymptotic sum rules at infinite momentum, Phys. Rev. **179**, 1547 (1969).

[98] D. J. Gross and F. Wilczek, Ultraviolet behavior of non-abelian gauge theories, Phys. Rev. Lett. **30**, 1343 (1973).

[99] J. C. Collins, D. E. Soper, and G. Sterman, Factorization of hard processes in QCD, in *Perturbative QCD* (World Scientific, 1989) pp. 1–91.

[100] J. Blümlein, The theory of deeply inelastic scattering, Prog. Part. Nucl. Phys. **69**, 28–84 (2013).

[101] A. S. Kronfeld, T. Bhattacharya, T. Blum, N. H. Christ, C. DeTar, W. Detmold, R. Edwards, A. Hasenfratz, H.-W. Lin, S. Mukherjee, K. Orginos, R. Brower, V. Cirigliano, Z. Davoudi, B. Jóo, *et al.*, Lattice QCD and Particle Physics, arXiv:2207.07641 .

[102] Z. Davoudi, E. T. Neil, C. W. Bauer, T. Bhattacharya, T. Blum, P. Boyle, R. C. Brower, S. Catterall, N. H. Christ, V. Cirigliano, G. Colangelo, C. DeTar, W. Detmold, R. G. Edwards, A. X. El-Khadra, *et al.*, Report of the Snowmass 2021 Topical Group on Lattice Gauge Theory, arXiv:2209.10758 .

[103] SR. Beane, W. Detmold, K. Orginos, and MJ. Savage, Nuclear physics from lattice QCD, Prog. Part. Nucl. Phys. **66**, 1–40 (2011).

[104] Z. Davoudi, W. Detmold, P. Shanahan, K. Orginos, A. Parreno, M. J. Savage, and M. L. Wagman, Nuclear matrix elements from lattice QCD for electroweak and beyond-Standard-Model processes, Phys. Rep. **900**, 1–74 (2021).

[105] C. Drischler, W. Haxton, K. McElvain, E. Mereghetti, A. Nicholson, P. Vranas, and A. Walker-Loud, Towards grounding nuclear physics in QCD, Prog. Part. Nucl. Phys. **121**, 103888 (2021).

[106] H.-T. Ding, F. Karsch, and S. Mukherjee, Thermodynamics of strong-interaction matter from Lattice QCD, Int. J. Mod. Phys. E **24**, 1530007 (2015).

[107] C. Ratti, Lattice QCD and heavy ion collisions: A review of recent progress, Rep. Prog. Phys. **81**, 084301 (2018).

[108] A. Bazavov, F. Karsch, S. Mukherjee, and P. Petreczky, Hot-dense lattice QCD, Eur. Phys. J. A **55**, 1–11 (2019).

[109] J. N. Guenther, Overview of the QCD phase diagram: Recent progress from the lattice, Eur. Phys. J. A **57**, 136 (2021).

[110] S. P. Jordan, K. S. M. Lee, and J. Preskill, Quantum Computation of Scattering in Scalar Quantum Field Theories, arXiv:1112.4833 .

[111] S. P. Jordan, K. S. Lee, and J. Preskill, Quantum algorithms for quantum field theories, Science **336**, 1130–1133 (2012).

[112] S. P. Jordan, H. Krovi, K. S. Lee, and J. Preskill, BQP-completeness of scattering in scalar quantum field theory, Quantum **2**, 44 (2018).

[113] A. Roggero, A. C. Li, J. Carlson, R. Gupta, and G. N. Perdue, Quantum computing for neutrino-nucleus scattering, Phys. Rev. D **101**, 074038 (2020).

[114] N. Mueller, A. Tarasov, and R. Venugopalan, Deeply inelastic scattering structure functions on a hybrid quantum computer, Phys. Rev. D **102**, 016007 (2020).

[115] J. Barata, N. Mueller, A. Tarasov, and R. Venugopalan, Single-particle digitization strategy for quantum computation of a ϕ^4 scalar field theory, Phys. Rev. A **103**, 042410 (2021).

[116] R. C. Farrell, I. A. Chernyshev, S. J. M. Powell, N. A. Zemlevskiy, M. Illa, and M. J. Savage, Preparations for quantum simulations of quantum chromodynamics in 1 + 1 dimensions. II. Single-baryon β -decay in real time, Phys. Rev. D **107**, 054513 (2023).

[117] F. M. Surace and A. Lerose, Scattering of mesons in quantum simulators, New J. Phys. **23**, 062001 (2021).

[118] C. W. Bauer, Z. Davoudi, A. B. Balantekin, T. Bhattacharya, M. Carena, W. A. De Jong, P. Draper, A. El-Khadra, N. Gemelke, M. Hanada, D. Kharzeev, H. Lamm, Y.-Y. Li, J. Liu, M. Lukin, *et al.*, Quantum Simulation for High-Energy Physics, PRX Quantum **4**, 027001 (2023).

[119] D. Beck, J. Carlson, Z. Davoudi, J. Formaggio, S. Quaglioni, M. Savage, J. Barata, T. Bhattacharya, M. Bishof, I. Cloet, A. Delgado, M. DeMarco, C. Fink, A. Florio, M. Francois, *et al.*, Quantum Information Science and Technology for Nuclear Physics. Input into U.S. Long-Range Planning, 2023, arXiv:2303.00113 .

[120] N. Klco, A. Roggero, and M. J. Savage, Standard model physics and the digital quantum revolution: Thoughts about the interface, Rep. Prog. Phys. **85**, 064301 (2022).

[121] C. W. Bauer, Z. Davoudi, N. Klco, and M. J. Savage, Quantum simulation of fundamental particles and forces, Nat. Rev. Phys. **5**, 420–432 (2023).

[122] U. Schollwöck, The density-matrix renormalization group in the age of matrix product states, Ann. Phys. **326**, 96–192 (2011).

[123] S. Paeckel, T. Köhler, A. Swoboda, S. R. Manmana, U. Schollwöck, and C. Hubig, Time-evolution methods for matrix-product states, Ann. Phys. **411**, 167998 (2019).

[124] T. Pichler, M. Dalmonte, E. Rico, P. Zoller, and S. Montangero, Real-time Dynamics in U(1) Lattice Gauge Theories with Tensor Networks, Phys. Rev. X **6**, 011023 (2016).

[125] M. Rigobello, S. Notarnicola, G. Magnifico, and S. Montangero, Entanglement generation in $(1+1)D$ QED scattering processes, Phys. Rev. D **104**, 114501 (2021).

[126] M. Van Damme, L. Vanderstraeten, J. De Nardis, J. Haegeman, and F. Verstraete, Real-time scattering of interacting quasiparticles in quantum spin chains, Phys. Rev. Res. **3**, 013078 (2021).

[127] A. Milsted, J. Liu, J. Preskill, and G. Vidal, Collisions of False-Vacuum Bubble Walls in a Quantum Spin Chain, PRX Quantum **3**, 020316 (2022).

[128] B. Buyens, J. Haegeman, K. Van Acoleyen, H. Verschelde, and F. Verstraete, Matrix Product States for Gauge Field Theories, Phys. Rev. Lett. **113**, 091601 (2014).

[129] B. Buyens, J. Haegeman, H. Verschelde, F. Verstraete, and K. Van Acoleyen, Confinement and String Breaking for QED 2 in the Hamiltonian Picture, Phys. Rev. X **6**, 041040 (2016).

[130] B. Buyens, J. Haegeman, F. Hebenstreit, F. Verstraete, and K. Van Acoleyen, Real-time simulation of the Schwinger effect with matrix product states, Phys. Rev. D **96**, 114501 (2017).

[131] T. M. R. Byrnes, P. Sriganesh, R. J. Bursill, and C. J. Hamer, Density matrix renormalization group approach to the massive Schwinger model, Phys. Rev. D **66**, 013002 (2002).

[132] M. Bañuls, K. Cichy, J. Cirac, and K. Jansen, The mass spectrum of the Schwinger model with matrix product states, J. High Energ. Phys. **2013** (11), 158.

[133] E. Rico, T. Pichler, M. Dalmonte, P. Zoller, and S. Montangero, Tensor Networks for Lattice Gauge Theories and Atomic Quantum Simulation, Phys. Rev. Lett. **112**, 201601 (2014).

[134] M. C. Bañuls, K. Cichy, J. I. Cirac, K. Jansen, and H. Saito, Thermal evolution of the Schwinger model with matrix product operators, Phys. Rev. D **92**, 034519 (2015).

[135] K. Zapp and R. Orús, Tensor network simulation of QED on infinite lattices: Learning from (1+1) d, and prospects for (2+1) d, Phys. Rev. D **95**, 114508 (2017).

[136] L. Funcke, K. Jansen, and S. Kühn, Topological vacuum structure of the Schwinger model with matrix product states, Phys. Rev. D **101**, 054507 (2020).

[137] N. Butt, S. Catterall, Y. Meurice, R. Sakai, and J. Unmuth-Yockey, Tensor network formulation of the massless Schwinger model with staggered fermions, Phys. Rev. D **101**, 094509 (2020).

[138] M. C. Bañuls and K. Cichy, Review on novel methods for lattice gauge theories, Rep. Prog. Phys. **83**, 024401 (2020).

[139] Y. Meurice, R. Sakai, and J. Unmuth-Yockey, Tensor lattice field theory for renormalization and quantum computing, Rev. Mod. Phys. **94**, 025005 (2022).

[140] E. A. Martinez, C. A. Muschik, P. Schindler, D. Nigg, A. Erhard, M. Heyl, P. Hauke, M. Dalmonte, T. Monz, P. Zoller, and R. Blatt, Real-time dynamics of lattice gauge theories with a few-qubit quantum computer, Nature **534**, 516–519 (2016).

[141] N. Klco, E. F. Dumitrescu, A. J. McCaskey, T. D. Morris, R. C. Pooser, M. Sanz, E. Solano, P. Lougovski, and M. J. Savage, Quantum-classical computation of Schwinger model dynamics using quantum computers, Phys. Rev. A **98**, 032331 (2018).

[142] N. H. Nguyen, M. C. Tran, Y. Zhu, A. M. Green, C. H. Alderete, Z. Davoudi, and N. M. Linke, Digital Quantum Simulation of the Schwinger Model and Symmetry Protection with Trapped Ions, PRX Quantum **3**, 020324 (2022).

[143] N. Mueller, J. A. Carolan, A. Connelly, Z. Davoudi, E. F. Dumitrescu, and K. Yeter-Aydeniz, Quantum computation of dynamical quantum phase transitions and entanglement tomography in a lattice gauge theory, arXiv:2210.03089 .

[144] B. Chakraborty, M. Honda, T. Izubuchi, Y. Kikuchi, and A. Tomiya, Classically emulated digital quantum simulation of the Schwinger model with a topological term via adiabatic state preparation, Phys. Rev. D **105**, 094503 (2022).

[145] W. A. de Jong, K. Lee, J. Mulligan, M. Płoskoń, F. Ringer, and X. Yao, Quantum simulation of nonequilibrium dynamics and thermalization in the Schwinger model, Phys. Rev. D **106**, 054508 (2022).

[146] A. F. Shaw, P. Lougovski, J. R. Stryker, and N. Wiebe, Quantum Algorithms for Simulating the Lattice Schwinger Model, Quantum **4**, 306 (2020).

[147] A. Kan and Y. Nam, Lattice Quantum Chromodynamics and Electrodynamics on a Universal Quantum Computer, arXiv:2107.12769 .

[148] Z.-Y. Zhou, G.-X. Su, J. C. Halimeh, R. Ott, H. Sun, P. Hauke, B. Yang, Z.-S. Yuan, J. Berges, and J.-W. Pan, Thermalization dynamics of a gauge theory on a quantum simulator, Science **377**, 311–314 (2022).

[149] B. Yang, H. Sun, R. Ott, H.-Y. Wang, T. V. Zache, J. C. Halimeh, Z.-S. Yuan, P. Hauke, and J.-W. Pan, Observation of gauge invariance in a 71-site Bose–Hubbard quantum simulator, Nature **587**, 392–396 (2020).

[150] A. Mil, T. V. Zache, A. Hegde, A. Xia, R. P. Bhatt, M. K. Oberthaler, P. Hauke, J. Berges, and F. Jendrzejewski, A scalable realization of local U(1) gauge invariance in cold atomic mixtures, Science **367**, 1128–1130 (2020).

[151] D. Banerjee, M. Dalmonte, M. Müller, E. Rico, P. Stebler, U.-J. Wiese, and P. Zoller, Atomic Quantum Simulation of Dynamical Gauge Fields Coupled to Fermionic Matter: From String Breaking to Evolution after a Quench, Phys. Rev. Lett. **109**, 175302 (2012).

[152] P. Hauke, D. Marcos, M. Dalmonte, and P. Zoller, Quantum Simulation of a Lattice Schwinger Model in a Chain of Trapped Ions, Phys. Rev. X **3**, 041018 (2013).

[153] U.-J. Wiese, Ultracold quantum gases and lattice systems: Quantum simulation of lattice gauge theories, Ann. Phys. **525**, 777–796 (2013).

[154] E. Zohar, J. I. Cirac, and B. Reznik, Quantum simulations of lattice gauge theories using ultracold atoms in optical lattices, Rep. Prog. Phys. **79**, 014401 (2015).

[155] D. Yang, G. S. Giri, M. Johanning, C. Wunderlich, P. Zoller, and P. Hauke, Analog quantum simulation of (1 + 1) -dimensional lattice QED with trapped ions, Phys. Rev. A **94**, 052321 (2016).

[156] Z. Davoudi, M. Hafezi, C. Monroe, G. Pagano, A. Seif, and A. Shaw, Towards analog quantum simulations of lattice gauge theories with trapped ions, Phys. Rev. Research **2**, 023015 (2020).

[157] D. Luo, J. Shen, M. Highman, B. K. Clark, B. DeMarco, A. X. El-Khadra, and B. Gadway, Framework for simulating gauge theories with dipolar spin systems, Phys. Rev. A **102**, 032617 (2020).

[158] S. Notarnicola, M. Collura, and S. Montangero, Real-time-dynamics quantum simulation of (1 + 1) -dimensional lattice QED with Rydberg atoms, Phys. Rev. Research **2**, 013288 (2020).

[159] F. M. Surace, P. P. Mazza, G. Giudici, A. Lerose, A. Gambassi, and M. Dalmonte, Lattice Gauge Theories and String Dynamics in Rydberg Atom Quantum Simulators, Phys. Rev. X **10**, 021041 (2020).

[160] Z. Davoudi, N. M. Linke, and G. Pagano, Toward simulating quantum field theories with controlled phonon-ion dynamics: A hybrid analog-digital approach, Phys. Rev. Research **3**, 043072 (2021).

[161] B. Andrade, Z. Davoudi, T. Graß, M. Hafezi, G. Pagano, and A. Seif, Engineering an effective three-spin Hamiltonian in trapped-ion systems for applications in quantum simulation, Quantum Sci. Technol. **7**, 034001 (2022).

[162] D. Marcos, P. Rabl, E. Rico, and P. Zoller, Superconducting Circuits for Quantum Simulation of Dynamical Gauge Fields, Phys. Rev. Lett. **111**, 110504 (2013).

[163] J. C. Halimeh, I. P. McCulloch, B. Yang, and P. Hauke, Tuning the Topological θ-Angle in Cold-Atom Quantum Simulators of Gauge Theories, PRX Quantum **3**, 040316 (2022).

[164] J. Osborne, B. Yang, I. P. McCulloch, P. Hauke, and J. C. Halimeh, Spin-S $\mathrm{U}(1)$ Quantum Link Models with Dynamical Matter on a Quantum Simulator, arXiv:2305.06368 .

[165] A. Kruckenhauser, R. van Bijnen, T. V. Zache, M. Di Liberto, and P. Zoller, High-dimensional SO(4)-symmetric Rydberg manifolds for quantum simulation, arXiv:2206.01108 .

[166] L. Vanderstraeten, J. Haegeman, and F. Verstraete, Tangent-space methods for uniform matrix product states, SciPost Phys. Lect. Notes , 7 (2019).

[167] J. Berges, S. Floerchinger, and R. Venugopalan, Thermal excitation spectrum from entanglement in an expanding quantum string, Phys. Lett. B **778**, 442–446 (2018).

[168] J. Berges, S. Floerchinger, and R. Venugopalan, Dynamics of entanglement in expanding quantum fields, J. High Energy Phys. **04** (4), 145.

[169] D. E. Kharzeev and E. M. Levin, Deep inelastic scattering as a probe of entanglement, Phys. Rev. D **95**, 114008 (2017).

[170] Y. Hagiwara, Y. Hatta, B.-W. Xiao, and F. Yuan, Classical and quantum entropy of parton distributions, Phys. Rev. D **97**, 094029 (2018).

[171] A. Kovner, M. Lublinsky, and M. Serino, Entanglement entropy, entropy production and time evolution in high energy QCD, Phys. Lett. B **792**, 4–15 (2019).

[172] S. R. Beane, D. B. Kaplan, N. Klco, and M. J. Savage, Entanglement suppression and emergent symmetries of strong interactions, Phys. Rev. Lett. **122**, 102001 (2019).

[173] S. R. Beane and P. J. Ehlers, Chiral symmetry breaking, entanglement, and the nucleon spin decomposition, Mod. Phys. Lett. A **35**, 2050048 (2020).

[174] S. R. Beane and R. C. Farrell, Geometry and entanglement in the scattering matrix, Ann. Phys. **433**, 168581 (2021).

[175] S. Coleman, R. Jackiw, and L. Susskind, Charge shielding and quark confinement in the massive schwinger model, Ann. Phys. **93**, 267–275 (1975).

[176] S. Coleman, More about the massive Schwinger model, Ann. Phys. **101**, 239–267 (1976).

[177] A. B. Özgüler, V. E. Manucharyan, and M. G. Vavilov, Excitation dynamics in inductively coupled fluxonium circuits, arXiv:2104.03300 .

[178] J. Fröhlich and E. Seiler, The massive Thirring-Schwinger model (QED_2) : Convergence of perturbation theory and particle structure, Helvetica Phys. Acta **49**, 889–924 (1976).

[179] X. Zhang, E. Kim, D. K. Mark, S. Choi, and O. Painter, A superconducting quantum simulator based on a photonic-bandgap metamaterial, Science **379**, 278–283 (2023).

[180] P. Forn-Díaz, J. J. García-Ripoll, B. Peropadre, J.-L. Orgiazzi, M. A. Yurtalan, R. Belyansky, C. M. Wilson, and A. Lupascu, Ultrastrong coupling of a single artificial atom to an electromagnetic continuum in the nonperturbative regime, Nature Phys **13**, 39–43 (2017).

[181] A. Vrajitoarea, R. Belyansky, R. Lundgren, S. Whitsitt, A. V. Gorshkov, and A. A. Houck, Ultrastrong light-matter interaction in a photonic crystal, arXiv:2209.14972 .

[182] T. V. Zache, M. Van Damme, J. C. Halimeh, P. Hauke, and D. Banerjee, Toward the continuum limit of a $(1+1)$D quantum link Schwinger model, Phys. Rev. D **106**, L091502 (2022).

[183] R. Shankar and G. Murthy, Deconfinement in d = 1 : Asymptotic and half-asymptotic particles, Phys. Rev. B **72**, 224414 (2005).

[184] V. Zauner-Stauber, L. Vanderstraeten, M. T. Fishman, F. Verstraete, and J. Haegeman, Variational optimization algorithms for uniform matrix product states, Phys. Rev. B **97**, 045145 (2018).

[185] J. Haegeman, B. Pirvu, D. J. Weir, J. I. Cirac, T. J. Osborne, H. Verschelde, and F. Verstraete, Variational matrix product ansatz for dispersion relations, Phys. Rev. B **85**, 100408 (2012).

[186] J. Haegeman, S. Michalakis, B. Nachtergaele, T. J. Osborne, N. Schuch, and F. Verstraete, Elementary Excitations in Gapped Quantum Spin Systems, Phys. Rev. Lett. **111**, 080401 (2013).

[187] A. Milsted, J. Haegeman, T. J. Osborne, and F. Verstraete, Variational matrix product ansatz for nonuniform dynamics in the thermodynamic limit, Phys. Rev. B **88**, 155116 (2013).

[188] H. N. Phien, G. Vidal, and I. P. McCulloch, Dynamical windows for real-time evolution with matrix product states, Phys. Rev. B **88**, 035103 (2013).

[189] V. Zauner, M. Ganahl, H. G. Evertz, and T. Nishino, Time Evolution within a Comoving Window: Scaling of signal fronts and magnetization plateaus after a local quench in quantum spin chains, J. Phys.: Condens. Matter **27**, 425602 (2015).

[190] H. J. Rothe, K. D. Rothe, and J. A. Swieca, Screening versus confinement, Phys. Rev. D **19**, 3020–3023 (1979).

[191] S. Coleman, Fate of the false vacuum: Semiclassical theory, Phys. Rev. D **15**, 2929–2936 (1977).

[192] C. G. Callan and S. Coleman, Fate of the false vacuum. II. First quantum corrections, Phys. Rev. D **16**, 1762–1768 (1977).

[193] F. Hebenstreit, J. Berges, and D. Gelfand, Real-Time Dynamics of String Breaking, Phys. Rev. Lett. **111**, 201601 (2013).

[194] L. Vanderstraeten, J. Haegeman, T. J. Osborne, and F. Verstraete, S Matrix from Matrix Product States, Phys. Rev. Lett. **112**, 257202 (2014).

[195] R. Verdel, G.-Y. Zhu, and M. Heyl, Dynamical localization transition of string breaking in quantum spin chains, arXiv:2304.12957 .

[196] T. V. Zache, N. Mueller, J. T. Schneider, F. Jendrzejewski, J. Berges, and P. Hauke, Dynamical Topological Transitions in the Massive Schwinger Model with a θ Term, Phys. Rev. Lett. **122**, 050403 (2019).

[197] Z. Tian, J. Jing, and A. Dragan, Analog cosmological particle generation in a superconducting circuit, Phys. Rev. D **95**, 125003 (2017).

[198] L. García-Álvarez, J. Casanova, A. Mezzacapo, I. L. Egusquiza, L. Lamata, G. Romero, and E. Solano, Fermion-Fermion Scattering in Quantum Field Theory with Superconducting Circuits, Phys. Rev. Lett. **114**, 070502 (2015).

[199] A. Roy, D. Schuricht, J. Hauschild, F. Pollmann, and H. Saleur, The quantum sine-Gordon model with quantum circuits, Nuclear Physics B **968**, 115445 (2021).

[200] A. Roy and S. Lukyanov, Soliton Confinement in a Quantum Circuit, arXiv:2302.06289 .

[201] M. C. Bañuls, K. Cichy, J. I. Cirac, K. Jansen, and S. Kühn, Density Induced Phase Transitions in the Schwinger Model: A Study with Matrix Product States, Phys. Rev. Lett. **118**, 071601 (2017).

[202] D. Roy, C. M. Wilson, and O. Firstenberg, Colloquium : Strongly interacting photons in one-dimensional continuum, Rev. Mod. Phys. **89**, 021001 (2017).

[203] J.-T. Shen and S. Fan, Coherent Single Photon Transport in a One-Dimensional Waveguide Coupled with Superconducting Quantum Bits, Phys. Rev. Lett. **95**, 213001 (2005).

[204] J.-T. Shen and S. Fan, Strongly correlated multiparticle transport in one dimension through a quantum impurity, Phys. Rev. A **76**, 062709 (2007).

[205] D. E. Chang, A. S. Sørensen, E. A. Demler, and M. D. Lukin, A single-photon transistor using nanoscale surface plasmons, Nat. Phys. **3**, 807–812 (2007).

[206] O. Astafiev, A. M. Zagoskin, A. A. Abdumalikov, Y. A. Pashkin, T. Yamamoto, K. Inomata, Y. Nakamura, and J. S. Tsai, Resonance fluorescence of a single artificial atom, Science **327**, 840–843 (2010).

[207] K. Le Hur, Kondo resonance of a microwave photon, Phys. Rev. B **85**, 140506 (2012).

[208] B. Peropadre, D. Zueco, D. Porras, and J. J. García-Ripoll, Nonequilibrium and Nonperturbative Dynamics of Ultrastrong Coupling in Open Lines, Phys. Rev. Lett. **111**, 243602 (2013).

[209] M. Goldstein, M. H. Devoret, M. Houzet, and L. I. Glazman, Inelastic Microwave Photon Scattering off a Quantum Impurity in a Josephson-Junction Array, Phys. Rev. Lett. **110**, 017002 (2013).

[210] S. Bera, H. U. Baranger, and S. Florens, Dynamics of a qubit in a high-impedance transmission line from a bath perspective, Phys. Rev. A **93**, 33847 (2016).

[211] N. Gheeraert, X. H. H. Zhang, T. Sépulcre, S. Bera, N. Roch, H. U. Baranger, and S. Florens, Particle production in ultrastrong-coupling waveguide QED, Phys. Rev. A **98**, 043816 (2018).

[212] T. Shi, Y. Chang, and J. J. García-Ripoll, Ultrastrong Coupling Few-Photon Scattering Theory, Phys. Rev. Lett. **120**, 153602 (2018).

[213] X. Gu, A. F. Kockum, A. Miranowicz, Y.-x. Liu, and F. Nori, Microwave photonics with superconducting quantum circuits, Phys. Rep. **718–719**, 1–102 (2017).

[214] A. Le Boité, Theoretical Methods for Ultrastrong Light–Matter Interactions, Adv. Quantum Technol. **3**, 1900140 (2020).

[215] L. Magazzù, P. Forn-Díaz, R. Belyansky, J. L. Orgiazzi, M. A. Yurtalan, M. R. Otto, A. Lupascu, C. M. Wilson, and M. Grifoni, Probing the strongly driven spin-boson model in a superconducting quantum circuit, Nat. Commun. **9**, 1403 (2018).

[216] J. Puertas Martínez, S. Léger, N. Gheeraert, R. Dassonneville, L. Planat, F. Foroughi, Y. Krupko, O. Buisson, C. Naud, W. Hasch-Guichard, S. Florens, I. Snyman, and N. Roch, A tunable Josephson platform to explore many-body quantum optics in circuit-QED, Npj Quantum Inf. **5**, 19 (2019).

[217] R. Kuzmin, N. Mehta, N. Grabon, R. Mencia, and V. E. Manucharyan, Superstrong coupling in circuit quantum electrodynamics, npj Quantum Information **5**, 20 (2019).

[218] S. Léger, J. Puertas-Martínez, K. Bharadwaj, R. Dassonneville, J. Delaforce, F. Foroughi, V. Milchakov, L. Planat, O. Buisson, C. Naud, W. Hasch-Guichard, S. Florens, I. Snyman, and N. Roch, Observation of quantum many-body effects due to zero point fluctuations in superconducting circuits, Nat. Commun. **10**, 5259 (2019).

[219] M. Vojta, Impurity quantum phase transitions, Philos. Mag. **86**, 1807–1846 (2006).

[220] V. J. Emery and A. Luther, Ground-State Properties in the Kondo Problem, Phys. Rev. Lett. **26**, 1547–1549 (1971).

[221] R. Silbey and R. A. Harris, Variational calculation of the dynamics of a two level system interacting with a bath, J. Chem. Phys. **80**, 2615–2617 (1984).

[222] R. A. Harris and R. Silbey, Variational calculation of the tunneling system interacting with a heat bath. II. Dynamics of an asymmetric tunneling system, J. Chem. Phys. **83**, 1069–1074 (1985).

[223] A. J. Leggett, S. Chakravarty, A. T. Dorsey, M. P. A. Fisher, A. Garg, and W. Zwerger, Dynamics of the dissipative two-state system, Rev. Mod. Phys. **59**, 1–85 (1987).

[224] A. Nazir, D. P. S. McCutcheon, and A. W. Chin, Ground state and dynamics of the biased dissipative two-state system: Beyond variational polaron theory, Phys. Rev. B **85**, 224301 (2012).

[225] A. W. Chin, J. Prior, S. F. Huelga, and M. B. Plenio, Generalized polaron ansatz for the ground state of the sub-Ohmic spin-boson model: An analytic theory of the localization transition, Phys. Rev. Lett. **107**, 160601 (2011).

[226] G. Díaz-Camacho, A. Bermudez, and J. J. García-Ripoll, Dynamical polaron Ansatz: A theoretical tool for the ultrastrong-coupling regime of circuit QED, Phys. Rev. A **93**, 43843 (2016).

[227] S. He, L. Duan, and Q. H. Chen, Improved Silbey-Harris polaron ansatz for the spin-boson model, Phys. Rev. B **97**, 115157 (2018).

[228] E. Sánchez-Burillo, L. Martín-Moreno, J. J. García-Ripoll, and D. Zueco, Single photons by quenching the vacuum, Phys. Rev. Lett. **123**, 013601 (2019).

[229] V. Paulisch, T. Shi, and J. J. Garcia-Ripoll, Two-Photon Scattering in USC regime, (2018).

[230] S. Bera, A. Nazir, A. W. Chin, H. U. Baranger, and S. Florens, Generalized multipolaron expansion for the spin-boson model: Environmental entanglement and the biased two-state system, Phys. Rev. B **90**, 075110 (2014).

[231] J. Román-Roche, E. Sánchez-Burillo, and D. Zueco, Bound states in ultrastrong waveguide qed, Phys. Rev. A **102**, 023702 (2020).

[232] A. H. Castro Neto, E. Novais, L. Borda, G. Zaránd, and I. Affleck, Quantum Magnetic Impurities in Magnetically Ordered Systems, Phys. Rev. Lett. **91**, 096401 (2003).

[233] E. Novais, A. H. Castro Neto, L. Borda, I. Affleck, and G. Zarand, Frustration of decoherence in open quantum systems, Phys. Rev. B **72**, 014417 (2005).

[234] A. M. Sengupta, Spin in a fluctuating field: The Bose(+Fermi) Kondo models, Phys. Rev. B **61**, 4041–4043 (2000).

[235] L. Zhu and Q. Si, Critical local-moment fluctuations in the Bose-Fermi Kondo model, Phys. Rev. B **66**, 024426 (2002).

[236] G. Zaránd and E. Demler, Quantum phase transitions in the Bose-Fermi Kondo model, Phys. Rev. B **66**, 024427 (2002).

[237] D. V. Khveshchenko, Quantum impurity models of noisy qubits, Phys. Rev. B **69**, 153311 (2004).

[238] A. Baksic and C. Ciuti, Controlling discrete and continuous symmetries in "superradiant" phase transitions with circuit qed systems, Phys. Rev. Lett. **112**, 173601 (2014).

[239] S. Mahmoodian, Chiral Light-Matter Interaction beyond the Rotating-Wave Approximation, Phys. Rev. Lett. **123**, 133603 (2019).

[240] J. Prior, A. W. Chin, S. F. Huelga, and M. B. Plenio, Efficient simulation of strong system-environment interactions, Phys. Rev. Lett. **105**, 050404 (2010).

[241] A. W. Chin, Á. Rivas, S. F. Huelga, and M. B. Plenio, Exact mapping between system-reservoir quantum models and semi-infinite discrete chains using orthogonal polynomials, J. Math. Phys. **51**, 092109 (2010).

[242] E. Sanchez-Burillo, D. Zueco, J. J. Garcia-Ripoll, and L. Martin-Moreno, Scattering in the ultrastrong regime: Nonlinear optics with one photon, Phys. Rev. Lett. **113**, 263604 (2014), 1406.5779 .

[243] D. C. Langreth, Friedel Sum Rule for Anderson's Model of Localized Impurity States, Phys. Rev. **150**, 516–518 (1966).

[244] G. Zaránd, L. Borda, J. von Delft, and N. Andrei, Theory of Inelastic Scattering from Magnetic Impurities, Phys. Rev. Lett. **93**, 107204 (2004).

[245] L. Fritz, S. Florens, and M. Vojta, Universal crossovers and critical dynamics of quantum phase transitions: A renormalization group study of the pseudogap Kondo problem, Phys. Rev. B **74**, 144410 (2006).

[246] L. Borda, L. Fritz, N. Andrei, and G. Zaránd, Theory of inelastic scattering from quantum impurities, Phys. Rev. B **75**, 235112 (2007).

[247] H. Bruus and K. Flensberg, *Many-body quantum theory in condensed matter physics: an introduction* (Oxford university press, 2004).

[248] V. J. Emery and A. Luther, Low- temperature properties of the Kondo Hamiltonian, Phys. Rev. B **9**, 215–226 (1974).

[249] P. Nozières, A "fermi-liquid" description of the Kondo problem at low temperatures, J. Low Temp. Phys. **17**, 31–42 (1974).

[250] Y. Yao, N. Zhou, J. Prior, and Y. Zhao, Competition between diagonal and off-diagonal coupling gives rise to charge-transfer states in polymeric solar cells, Sci. Rep. **5**, 14555 (2015).

[251] C. Duan, C.-Y. Hsieh, J. Liu, J. Wu, and J. Cao, Unusual Transport Properties with Noncommutative System–Bath Coupling Operators, J. Phys. Chem. Lett. **11**, 4080–4085 (2020).

[252] I. Bloch, J. Dalibard, and S. Nascimbene, Quantum simulations with ultracold quantum gases, Nat. Phys. **8**, 267–276 (2012).

[253] D. E. Chang, J. S. Douglas, A. González-Tudela, C.-L. Hung, and H. J. Kimble, Colloquium: Quantum matter built from nanoscopic lattices of atoms and photons, Rev. Mod. Phys. **90**, 031002 (2018).

[254] I. Carusotto, A. A. Houck, A. J. Kollár, P. Roushan, D. I. Schuster, and J. Simon, Photonic materials in circuit quantum electrodynamics, Nat. Phys. **16**, 268–279 (2020).

[255] S. John and J. Wang, Quantum electrodynamics near a photonic band gap: Photon bound states and dressed atoms, Phys. Rev. Lett. **64**, 2418–2421 (1990).

[256] Y. Liu and A. A. Houck, Quantum electrodynamics near a photonic bandgap, Nat. Phys. **13**, 48–52 (2017).

[257] V. I. Rupasov and M. Singh, Quantum gap solitons and many-polariton–atom bound states in dispersive medium and photonic band gap, Phys. Rev. Lett. **77**, 338–341 (1996).

[258] S. John and V. I. Rupasov, Multiphoton localization and propagating quantum gap solitons in a frequency gap medium, Phys. Rev. Lett. **79**, 821–824 (1997).

[259] G. Calajó, F. Ciccarello, D. Chang, and P. Rabl, Atom-field dressed states in slow-light waveguide qed, Phys. Rev. A **93**, 033833 (2016).

[260] T. Shi, Y.-H. Wu, A. González-Tudela, and J. I. Cirac, Bound states in boson impurity models, Phys. Rev. X **6**, 021027 (2016).

[261] T. Kraemer, M. Mark, P. Waldburger, J. G. Danzl, C. Chin, B. Engeser, A. D. Lange, K. Pilch, A. Jaakkola, H.-C. Nägerl, and R. Grimm, Evidence for efimov quantum states in an ultracold gas of caesium atoms, Nature **440**, 315–318 (2006).

[262] R. Coldea, D. A. Tennant, E. M. Wheeler, E. Wawrzynska, D. Prabhakaran, M. Telling, K. Habicht, P. Smeibidl, and K. Kiefer, Quantum criticality in an ising chain: Experimental evidence for emergent e_8 symmetry, Science **327**, 177–180 (2010).

[263] T. Fukuhara, P. Schauß, M. Endres, S. Hild, M. Cheneau, I. Bloch, and C. Gross, Microscopic observation of magnon bound states and their dynamics, Nature **502**, 76–79 (2013).

[264] J. S. Douglas, H. Habibian, C.-L. Hung, A. V. Gorshkov, H. J. Kimble, and D. E. Chang, Quantum many-body models with cold atoms coupled to photonic crystals, Nature Photonics **9**, 326–331 (2015).

[265] M. Bello, G. Platero, and A. González-Tudela, Spin many-body phases in standard- and topological-waveguide qed simulators, PRX Quantum **3**, 010336 (2022).

[266] J. D. Hood, A. Goban, A. Asenjo-Garcia, M. Lu, S.-P. Yu, D. E. Chang, and H. J. Kimble, Atom-atom interactions around the band edge of a photonic crystal waveguide, PNAS **113**, 10507–10512 (2016).

[267] N. M. Sundaresan, R. Lundgren, G. Zhu, A. V. Gorshkov, and A. A. Houck, Interacting qubit-photon bound states with superconducting circuits, Phys. Rev. X **9**, 011021 (2019).

[268] E. Kim, X. Zhang, V. S. Ferreira, J. Banker, J. K. Iverson, A. Sipahigil, M. Bello, A. González-Tudela, M. Mirhosseini, and O. Painter, Quantum electrodynamics in a topological waveguide, Phys. Rev. X **11**, 011015 (2021).

[269] M. Scigliuzzo, G. Calajò, F. Ciccarello, D. Perez Lozano, A. Bengtsson, P. Scarlino, A. Wallraff, D. Chang, P. Delsing, and S. Gasparinetti, Controlling atom-photon bound states in an array of josephson-junction resonators, Phys. Rev. X **12**, 031036 (2022).

[270] C. Ciuti, G. Bastard, and I. Carusotto, Quantum vacuum properties of the intersubband cavity polariton field, Phys. Rev. B **72**, 115303 (2005).

[271] T. Niemczyk, F. Deppe, H. Huebl, E. P. Menzel, F. Hocke, M. J. Schwarz, J. J. Garcia-Ripoll, D. Zueco, T. Hümmer, E. Solano, A. Marx, and R. Gross, Circuit quantum electrodynamics in the ultrastrong-coupling regime, Nat. Phys. **6**, 772–776 (2010).

[272] P. Forn-Díaz, J. Lisenfeld, D. Marcos, J. J. García-Ripoll, E. Solano, C. J. P. M. Harmans, and J. E. Mooij, Observation of the bloch-siegert shift in a qubit-oscillator system in the ultrastrong coupling regime, Phys. Rev. Lett. **105**, 237001 (2010).

[273] F. Yoshihara, T. Fuse, S. Ashhab, K. Kakuyanagi, S. Saito, and K. Semba, Superconducting qubit–oscillator circuit beyond the ultrastrong-coupling regime, Nat. Phys. **13**, 44–47 (2017).

[274] R. Kuzmin, N. Grabon, N. Mehta, A. Burshtein, M. Goldstein, M. Houzet, L. I. Glazman, and V. E. Manucharyan, Inelastic scattering of a photon by a quantum phase slip, Phys. Rev. Lett. **126**, 197701 (2021).

[275] N. Mehta, R. Kuzmin, C. Ciuti, and V. E. Manucharyan, Down-conversion of a single photon as a probe of many-body localization, Nature **613**, 650–655 (2023).

[276] V. E. Manucharyan, J. Koch, L. I. Glazman, and M. H. Devoret, Fluxonium: Single cooper-pair circuit free of charge offsets, Science **326**, 113–116 (2009).

[277] V. E. Manucharyan, A. Baksic, and C. Ciuti, Resilience of the quantum rabi model in circuit QED, J. Phys. A Math. **50**, 294001 (2017).

[278] B. Peropadre, J. Lindkvist, I.-C. Hoi, C. M. Wilson, J. J. Garcia-Ripoll, P. Delsing, and G. Johansson, Scattering of coherent states on a single artificial atom, NPJ **15**, 035009 (2013).

[279] D. Meiser and P. Meystre, Superstrong coupling regime of cavity quantum electrodynamics, Phys. Rev. A **74**, 065801 (2006).

[280] N. M. Sundaresan, Y. Liu, D. Sadri, L. J. Szőcs, D. L. Underwood, M. Malekakhlagh, H. E. Türeci, and A. A. Houck, Beyond strong coupling in a multimode cavity, Phys. Rev. X **5**, 021035 (2015).

[281] C. Eichler, D. Bozyigit, C. Lang, L. Steffen, J. Fink, and A. Wallraff, Experimental state tomography of itinerant single microwave photons, Phys. Rev. Lett. **106**, 220503 (2011).

[282] M. Hillery and M. S. Zubairy, Entanglement conditions for two-mode states, Phys. Rev. Lett. **96**, 050503 (2006).

[283] A. F. Kockum, A. Miranowicz, V. Macrì, S. Savasta, and F. Nori, Deterministic quantum nonlinear optics with single atoms and virtual photons, Phys. Rev. A **95**, 063849 (2017).

[284] R. Belyansky, S. Whitsitt, R. Lundgren, Y. Wang, A. Vrajitoarea, A. A. Houck, and A. V. Gorshkov, Frustration-induced anomalous transport and strong photon decay in waveguide qed, Phys. Rev. Research **3**, L032058 (2021).

[285] A. Vrajitoarea, , Z. Huang, P. Groszkowski, J. Koch, and A. A. Houck, Quantum control of an oscillator using a stimulated josephson nonlinearity, Nat. Phys. **16**, 211–217 (2020).

[286] M. Fitzpatrick, N. M. Sundaresan, A. C. Y. Li, J. Koch, and A. A. Houck, Observation of a dissipative phase transition in a one-dimensional circuit qed lattice, Phys. Rev. X **7**, 011016 (2017).

[287] B. Kraus and J. I. Cirac, Discrete entanglement distribution with squeezed light, Phys. Rev. Lett. **92**, 013602 (2004).

[288] J. Agustí, Y. Minoguchi, J. M. Fink, and P. Rabl, Long-distance distribution of qubit-qubit entanglement using gaussian-correlated photonic beams, arXiv:2204.02993 (2022).

[289] A. Deshpande, A. Mehta, T. Vincent, N. Quesada, M. Hinsche, M. Ioannou, L. Madsen, J. Lavoie, H. Qi, J. Eisert, D. Hangleiter, B. Fefferman, and I. Dhand, Quantum computational advantage via high-dimensional gaussian boson sampling, Science Advances **8**, eabi7894 (2022).

[290] J. M. Deutsch, Quantum statistical mechanics in a closed system, Phys. Rev. A **43**, 2046–2049 (1991).

[291] M. Srednicki, Chaos and quantum thermalization, Phys. Rev. E **50**, 888–901 (1994).

[292] M. Rigol, V. Dunjko, and M. Olshanii, Thermalization and its mechanism for generic isolated quantum systems, Nature **452**, 854–858 (2008).

[293] P. Hayden and J. Preskill, Black holes as mirrors: quantum information in random subsystems, J. High Energy Phys. **2007** (09), 120–120.

[294] N. Lashkari, D. Stanford, M. Hastings, T. Osborne, and P. Hayden, Towards the fast scrambling conjecture, J. High Energy Phys. **2013** (4), 22.

[295] S. H. Shenker and D. Stanford, Black holes and the butterfly effect, J. High Energy Phys. **2014** (3), 67.

[296] J. Maldacena, S. H. Shenker, and D. Stanford, A bound on chaos, J. High Energy Phys. **2016** (8), 106.

[297] A. A. Patel, D. Chowdhury, S. Sachdev, and B. Swingle, Quantum Butterfly Effect in Weakly Interacting Diffusive Metals, Phys. Rev. X **7**, 031047 (2017).

[298] S. Xu and B. Swingle, Locality, Quantum Fluctuations, and Scrambling, Phys. Rev. X **9**, 031048 (2019).

[299] S. Xu and B. Swingle, Accessing scrambling using matrix product operators, Nat. Phys. **16**, 199–204 (2020).

[300] Y. Sekino and L. Susskind, Fast scramblers, J. High Energy Phys. **2008** (10), 065–065.

[301] S. Sachdev and J. Ye, Gapless spin-fluid ground state in a random quantum Heisenberg magnet, Phys. Rev. Lett. **70**, 3339–3342 (1993).

[302] A. Kitaev, A simple model of quantum holography (2015), in KITP Program: Entanglement in Strongly-Correlated Quantum Matter.

[303] I. Danshita, M. Hanada, and M. Tezuka, Creating and probing the Sachdev–Ye–Kitaev model with ultracold gases: Towards experimental studies of quantum gravity, Prog. Theor. Exp. Phys. **2017**, 83–84 (2017).

[304] A. Chen, R. Ilan, F. de Juan, D. I. Pikulin, and M. Franz, Quantum Holography in a Graphene Flake with an Irregular Boundary, Phys. Rev. Lett. **121**, 036403 (2018).

[305] A. Chew, A. Essin, and J. Alicea, Approximating the Sachdev-Ye-Kitaev model with Majorana wires, Phys. Rev. B **96**, 121119 (2017).

[306] Y. Gu, X.-L. Qi, and D. Stanford, Local criticality, diffusion and chaos in generalized Sachdev-Ye-Kitaev models, J. High Energy Phys. **2017** (5), 125.

[307] J. Li, R. Fan, H. Wang, B. Ye, B. Zeng, H. Zhai, X. Peng, and J. Du, Measuring Out-of-Time-Order Correlators on a Nuclear Magnetic Resonance Quantum Simulator, Phys. Rev. X **7**, 031011 (2017).

[308] M. Gärttner, J. G. Bohnet, A. Safavi-Naini, M. L. Wall, J. J. Bollinger, and A. M. Rey, Measuring out-of-time-order correlations and multiple quantum spectra in a trapped-ion quantum magnet, Nat. Phys. **13**, 781–786 (2017).

[309] K. X. Wei, C. Ramanathan, and P. Cappellaro, Exploring Localization in Nuclear Spin Chains, Phys. Rev. Lett. **120**, 070501 (2018).

[310] K. A. Landsman, C. Figgatt, T. Schuster, N. M. Linke, B. Yoshida, N. Y. Yao, and C. Monroe, Verified quantum information scrambling, Nature **567**, 61–65 (2019).

[311] M. K. Joshi, A. Elben, B. Vermersch, T. Brydges, C. Maier, P. Zoller, R. Blatt, and C. F. Roos, Quantum information scrambling in a trapped-ion quantum simulator with tunable range interactions, arXiv:2001.02176 (2020).

[312] M. S. Blok, V. V. Ramasesh, T. Schuster, K. O'Brien, J. M. Kreikebaum, D. Dahlen, A. Morvan, B. Yoshida, N. Y. Yao, and I. Siddiqi, Quantum Information Scrambling in a Superconducting Qutrit Processor, arXiv:2003.03307 (2020).

[313] B. Swingle, G. Bentsen, M. Schleier-Smith, and P. Hayden, Measuring the scrambling of quantum information, Phys. Rev. A **94**, 040302 (2016).

[314] J. Marino and A. M. Rey, Cavity-QED simulator of slow and fast scrambling, Phys. Rev. A **99**, 051803 (2019).

[315] G. Bentsen, T. Hashizume, A. S. Buyskikh, E. J. Davis, A. J. Daley, S. S. Gubser, and M. Schleier-Smith, Treelike Interactions and Fast Scrambling with Cold Atoms, Phys. Rev. Lett. **123**, 130601 (2019).

[316] S. Chaudhury, S. Merkel, T. Herr, A. Silberfarb, I. H. Deutsch, and P. S. Jessen, Quantum Control of the Hyperfine Spin of a Cs Atom Ensemble, Phys. Rev. Lett. **99**, 163002 (2007).

[317] T. Fernholz, H. Krauter, K. Jensen, J. F. Sherson, A. S. Sørensen, and E. S. Polzik, Spin squeezing of atomic ensembles via nuclear-electronic spin entanglement, Phys. Rev. Lett. **101**, 073601 (2008).

[318] A. Nahum, S. Vijay, and J. Haah, Operator Spreading in Random Unitary Circuits, Phys. Rev. X **8**, 021014 (2018).

[319] C. W. von Keyserlingk, T. Rakovszky, F. Pollmann, and S. L. Sondhi, Operator Hydrodynamics, OTOCs, and Entanglement Growth in Systems without Conservation Laws, Phys. Rev. X **8**, 021013 (2018).

[320] O. C. O. Dahlsten, R. Oliveira, and M. B. Plenio, The emergence of typical entanglement in two-party random processes, J. Phys. A Math. Theor. **40**, 8081–8108 (2007).

[321] M. Žnidarič, Exact convergence times for generation of random bipartite entanglement, Phys. Rev. A **78**, 032324 (2008).

[322] T. Zhou and X. Chen, Operator dynamics in a Brownian quantum circuit, Phys. Rev. E **99**, 052212 (2019).

[323] E. B. Rozenbaum, S. Ganeshan, and V. Galitski, Lyapunov exponent and out-of-time-ordered correlator's growth rate in a chaotic system, Phys. Rev. Lett. **118**, 086801 (2017).

[324] T. Bilitewski, S. Bhattacharjee, and R. Moessner, Temperature dependence of the butterfly effect in a classical many-body system, Phys. Rev. Lett. **121**, 250602 (2018).

[325] J. Chávez-Carlos, B. López-del Carpio, M. A. Bastarrachea-Magnani, P. Stránský, S. Lerma-Hernández, L. F. Santos, and J. G. Hirsch, Quantum and classical lyapunov exponents in atom-field interaction systems, Phys. Rev. Lett. **122**, 024101 (2019).

[326] R. A. Jalabert, I. García-Mata, and D. A. Wisniacki, Semiclassical theory of out-of-time-order correlators for low-dimensional classically chaotic systems, Phys. Rev. E **98**, 062218 (2018).

[327] B. Yan, L. Cincio, and W. H. Zurek, Information Scrambling and Loschmidt Echo, Phys. Rev. Lett. **124**, 160603 (2020).

[328] J. Kurchan, Quantum Bound to Chaos and the Semiclassical Limit, J. Stat. Phys. **171**, 965–979 (2018).

[329] M. Schmitt, D. Sels, S. Kehrein, and A. Polkovnikov, Semiclassical echo dynamics in the sachdev-ye-kitaev model, Phys. Rev. B **99**, 134301 (2019).

[330] T. Scaffidi and E. Altman, Chaos in a classical limit of the sachdev-ye-kitaev model, Phys. Rev. B **100**, 155128 (2019).

[331] Y. Y. Atas, E. Bogomolny, O. Giraud, and G. Roux, Distribution of the Ratio of Consecutive Level Spacings in Random Matrix Ensembles, Phys. Rev. Lett. **110**, 084101 (2013).

[332] A. Lerose, J. Marino, B. Žunkovič, A. Gambassi, and A. Silva, Chaotic Dynamical Ferromagnetic Phase Induced by Nonequilibrium Quantum Fluctuations, Phys. Rev. Lett. **120**, 130603 (2018).

[333] D. J. Luitz and Y. Bar Lev, Information propagation in isolated quantum systems, Phys. Rev. B **96**, 020406 (2017).

[334] J. Honer, H. Weimer, T. Pfau, and H. P. Büchler, Collective Many-Body Interaction in Rydberg Dressed Atoms, Phys. Rev. Lett. **105**, 160404 (2010).

[335] T. Graß, P. Bienias, M. J. Gullans, R. Lundgren, J. Maciejko, and A. V. Gorshkov, Fractional Quantum Hall Phases of Bosons with Tunable Interactions: From the Laughlin Liquid to a Fractional Wigner Crystal, Phys. Rev. Lett. **121**, 253403 (2018).

[336] G. Pupillo, A. Micheli, M. Boninsegni, I. Lesanovsky, and P. Zoller, Strongly correlated gases of rydberg-dressed atoms: Quantum and classical dynamics, Phys. Rev. Lett. **104**, 223002 (2010).

[337] A. W. Glaetzle, R. Nath, B. Zhao, G. Pupillo, and P. Zoller, Driven-dissipative dynamics of a strongly interacting Rydberg gas, Phys. Rev. A **86**, 043403 (2012).

[338] S. Gopalakrishnan, B. L. Lev, and P. M. Goldbart, Frustration and Glassiness in Spin Models with Cavity-Mediated Interactions, Phys. Rev. Lett. **107**, 277201 (2011).

[339] P. Strack and S. Sachdev, Dicke Quantum Spin Glass of Atoms and Photons, Phys. Rev. Lett. **107**, 277202 (2011).

[340] B. Zhu, J. Marino, N. Y. Yao, M. D. Lukin, and E. A. Demler, Dicke time crystals in driven-dissipative quantum many-body systems, New J. Phys. **21**, 073028 (2019).

[341] J. Majer, J. M. Chow, J. M. Gambetta, J. Koch, B. R. Johnson, J. A. Schreier, L. Frunzio, D. I. Schuster, A. A. Houck, A. Wallraff, A. Blais, M. H. Devoret, S. M. Girvin, and R. J. Schoelkopf, Coupling superconducting qubits via a cavity bus, Nature **449**, 443–447 (2007).

[342] G. Zhu, M. Hafezi, and T. Grover, Measurement of many-body chaos using a quantum clock, Phys. Rev. A **94**, 062329 (2016).

[343] T. Onodera, E. Ng, and P. L. McMahon, A quantum annealer with fully programmable all-to-all coupling via Floquet engineering, arXiv:1907.05483 (2019).

[344] S. Genway, W. Li, C. Ates, B. P. Lanyon, and I. Lesanovsky, Generalized Dicke Nonequilibrium Dynamics in Trapped Ions, Phys. Rev. Lett. **112**, 023603 (2014).

[345] I. Bloch, J. Dalibard, and W. Zwerger, Many-body physics with ultracold gases, Rev. Mod. Phys. **80**, 885–964 (2008).

[346] M. Inguscio, W. Ketterle, and C. Salomon, eds., *Ultracold Fermi Gases, Proceedings of the International School of Physics Enrico Fermi, Course CLXIV, Varenna 2006* (IOS Press, Amsterdam, 2008).

[347] F. Böttcher, J.-N. Schmidt, M. Wenzel, J. Hertkorn, M. Guo, T. Langen, and T. Pfau, Transient supersolid properties in an array of dipolar quantum droplets, Phys. Rev. X **9**, 011051 (2019).

[348] L. Tanzi, E. Lucioni, F. Famà, J. Catani, A. Fioretti, C. Gabbanini, R. N. Bisset, L. Santos, and G. Modugno, Observation of a dipolar quantum gas with metastable supersolid properties, Phys. Rev. Lett. **122**, 130405 (2019).

[349] L. Chomaz, D. Petter, P. Ilzhöfer, G. Natale, A. Trautmann, C. Politi, G. Durastante, R. M. W. van Bijnen, A. Patscheider, M. Sohmen, M. J. Mark, and F. Ferlaino, Long-lived and transient supersolid behaviors in dipolar quantum gases, Phys. Rev. X **9**, 021012 (2019).

[350] Y. Tang, W. Kao, K.-Y. Li, S. Seo, K. Mallayya, M. Rigol, S. Gopalakrishnan, and B. L. Lev, Thermalization near integrability in a dipolar quantum newton's cradle, Phys. Rev. X **8**, 021030 (2018).

[351] A. Patscheider, B. Zhu, L. Chomaz, D. Petter, S. Baier, A.-M. Rey, F. Ferlaino, and M. J. Mark, Controlling dipolar exchange interactions in a dense three-dimensional array of large-spin fermions, Phys. Rev. Research **2**, 023050 (2020).

[352] L. Gabardos, B. Zhu, S. Lepoutre, A. M. Rey, B. Laburthe-Tolra, and L. Vernac, Relaxation of the collective magnetization of a dense 3D array of interacting dipolar $s = 3$ atoms, Phys. Rev. Lett. **125**, 143401 (2020).

[353] L. De Marco, G. Valtolina, K. Matsuda, W. G. Tobias, J. P. Covey, and J. Ye, A degenerate Fermi gas of polar molecules, Science **363**, 853–856 (2019).

[354] J. L. Bohn, A. M. Rey, and J. Ye, Cold molecules: Progress in quantum engineering of chemistry and quantum matter, Science **357**, 1002–1010 (2017).

[355] C. D. Bruzewicz, J. Chiaverini, R. McConnell, and J. M. Sage, Trapped-ion quantum computing: Progress and challenges, Appl. Phys. Rev. **6**, 021314 (2019).

[356] L. Anderegg, L. W. Cheuk, Y. Bao, S. Burchesky, W. Ketterle, K.-K. Ni, and J. M. Doyle, An optical tweezer array of ultracold molecules, Science **365**, 1156–1158 (2019).

[357] L. R. Liu, J. D. Hood, Y. Yu, J. T. Zhang, K. Wang, Y.-W. Lin, T. Rosenband, and K.-K. Ni, Molecular assembly of ground-state cooled single atoms, Phys. Rev. X **9**, 021039 (2019).

[358] J. E. Johnson and S. L. Rolston, Interactions between Rydberg-dressed atoms, Phys. Rev. A **82**, 033412 (2010).

[359] N. Henkel, R. Nath, and T. Pohl, Three-dimensional roton excitations and supersolid formation in Rydberg-excited Bose-Einstein condensates, Phys. Rev. Lett. **104**, 195302 (2010).

[360] J. B. Balewski, A. T. Krupp, A. Gaj, S. Hofferberth, R. Löw, and T. Pfau, Rydberg dressing: understanding of collective many-body effects and implications for experiments, New J. Phys **16**, 063012 (2014).

[361] E. A. Goldschmidt, T. Boulier, R. C. Brown, S. B. Koller, J. T. Young, A. V. Gorshkov, S. L. Rolston, and J. V. Porto, Anomalous broadening in driven dissipative Rydberg systems, Phys. Rev. Lett. **116**, 113001 (2016).

[362] J. A. Aman, B. J. DeSalvo, F. B. Dunning, T. C. Killian, S. Yoshida, and J. Burgdörfer, Trap losses induced by near-resonant Rydberg dressing of cold atomic gases, Phys. Rev. A **93**, 043425 (2016).

[363] Y.-Y. Jau, A. M. Hankin, T. Keating, I. H. Deutsch, and G. W. Biedermann, Entangling atomic spins with a Rydberg-dressed spin-flip blockade, Nat. Phys. **12**, 71–74 (2016).

[364] J. Zeiher, R. van Bijnen, P. Schauß, S. Hild, J.-Y. Choi, T. Pohl, I. Bloch, and C. Gross, Many-body interferometry of a Rydberg-dressed spin lattice, Nat. Phys. **12**, 1095–1099 (2016).

[365] C. Gaul, B. J. DeSalvo, J. A. Aman, F. B. Dunning, T. C. Killian, and T. Pohl, Resonant Rydberg dressing of alkaline-earth atoms via electromagnetically induced transparency, Phys. Rev. Lett. **116**, 243001 (2016).

[366] T. Boulier, E. Magnan, C. Bracamontes, J. Maslek, E. A. Goldschmidt, J. T. Young, A. V. Gorshkov, S. L. Rolston, and J. V. Porto, Spontaneous avalanche dephasing in large Rydberg ensembles, Phys. Rev. A **96**, 053409 (2017).

[367] J. Zeiher, J.-Y. Choi, A. Rubio-Abadal, T. Pohl, R. van Bijnen, I. Bloch, and C. Gross, Coherent many-body spin dynamics in a long-range interacting Ising chain, Phys. Rev. X **7**, 041063 (2017).

[368] A. Arias, G. Lochead, T. M. Wintermantel, S. Helmrich, and S. Whitlock, Realization of a Rydberg-dressed Ramsey interferometer and electrometer, Phys. Rev. Lett. **122**, 053601 (2019).

[369] V. Borish, O. Marković, J. A. Hines, S. V. Rajagopal, and M. Schleier-Smith, Transverse-field Ising dynamics in a Rydberg-dressed atomic gas, Phys. Rev. Lett. **124**, 063601 (2020).

[370] M. Mattioli, M. Dalmonte, W. Lechner, and G. Pupillo, Cluster Luttinger liquids of Rydberg-dressed atoms in optical lattices, Phys. Rev. Lett. **111**, 165302 (2013).

[371] A. Dauphin, M. Müller, and M. A. Martin-Delgado, Quantum simulation of a topological Mott insulator with Rydberg atoms in a Lieb lattice, Phys. Rev. A **93**, 043611 (2016).

[372] M. Burrello, I. Lesanovsky, and A. Trombettoni, Reaching the quantum Hall regime with rotating Rydberg-dressed atoms, Phys. Rev. Research **2**, 023290 (2020).

[373] F. Grusdt, M. Kánasz-Nagy, A. Bohrdt, C. S. Chiu, G. Ji, M. Greiner, D. Greif, and E. Demler, Parton Theory of Magnetic Polarons: Mesonic Resonances and Signatures in Dynamics, Phys. Rev. X **8**, 011046 (2018).

[374] X. Li and S. D. Sarma, Exotic topological density waves in cold atomic Rydberg-dressed fermions, Nat. Commun. **6**, 7137 (2015).

[375] B. Xiong, H. H. Jen, and D. W. Wang, Topological superfluid by blockade effects in a Rydberg-dressed Fermi gas, Phys. Rev. A **90**, 013631 (2014).

[376] W.-h. Li, T.-c. Hsieh, C.-y. Mou, and D.-w. Wang, Emergence of a metallic quantum solid phase in a Rydberg-dressed Fermi gas, Phys. Rev. Lett. **035301**, 1–5 (2016).

[377] G. De Tomasi, D. Hetterich, P. Sala, and F. Pollmann, Dynamics of strongly interacting systems: From Fock-space fragmentation to many-body localization, Phys. Rev. B **100**, 214313 (2019).

[378] Z.-C. Yang, F. Liu, A. V. Gorshkov, and T. Iadecola, Hilbert-space fragmentation from strict confinement, Phys. Rev. Lett. **124**, 207602 (2020).

[379] P. Sala, T. Rakovszky, R. Verresen, M. Knap, and F. Pollmann, Ergodicity breaking arising from Hilbert space fragmentation in dipole-conserving hamiltonians, Phys. Rev. X **10**, 011047 (2020).

[380] V. Khemani, M. Hermele, and R. Nandkishore, Localization from Hilbert space shattering: From theory to physical realizations, Phys. Rev. B **101**, 174204 (2020).

[381] R. Nandkishore and D. A. Huse, Many-body localization and thermalization in quantum statistical mechanics, Annu. Rev. Condens. Matter Phys. **6**, 15–38.

[382] D. A. Abanin, E. Altman, I. Bloch, and M. Serbyn, Colloquium: Many-body localization, thermalization, and entanglement, Rev. Mod. Phys. **91**, 021001 (2019).

[383] H. Bernien, S. Schwartz, A. Keesling, H. Levine, A. Omran, H. Pichler, S. Choi, A. S. Zibrov, M. Endres, M. Greiner, V. Vuletić, and M. D. Lukin, Probing many-body dynamics on a 51-atom quantum simulator, Nature **551**, 579–584 (2017).

[384] C. J. Turner, A. A. Michailidis, D. A. Abanin, M. Serbyn, and Z. Papić, Quantum scarred eigenstates in a Rydberg atom chain: Entanglement, breakdown of thermalization, and stability to perturbations, Phys. Rev. B **98**, 155134 (2018).

[385] L. D'Alessio, Y. Kafri, A. Polkovnikov, and M. Rigol, From quantum chaos and eigenstate thermalization to statistical mechanics and thermodynamics, Adv. Phys. **65**, 239–362 (2016).

[386] S. Weber, C. Tresp, H. Menke, A. Urvoy, O. Firstenberg, H. P. Büchler, and S. Hofferberth, Calculation of Rydberg interaction potentials, J. Phys. B At. Mol. Opt. Phys. **50**, 1–19 (2017).

[387] E. Guardado-Sanchez, P. T. Brown, D. Mitra, T. Devakul, D. A. Huse, P. Schauß, and W. S. Bakr, Probing the quench dynamics of antiferromagnetic correlations in a 2D quantum Ising spin system, Phys. Rev. X **8**, 021069 (2018).

[388] I. I. Beterov, I. I. Ryabtsev, D. B. Tretyakov, and V. M. Entin, Quasiclassical calculations of blackbody-radiation-induced depopulation rates and effective lifetimes of Rydberg nS, nP, and nD alkali-metal atoms with $n \leq 80$, Phys. Rev. A **79**, 052504 (2009).

[389] W. Li, C. Ates, and I. Lesanovsky, Nonadiabatic motional effects and dissipative blockade for Rydberg atoms excited from optical lattices or microtraps, Phys. Rev. Lett. **110**, 213005 (2013).

[390] T. Macrì and T. Pohl, Rydberg dressing of atoms in optical lattices, Phys. Rev. A **89**, 011402(R) (2014).

[391] E. Guardado-Sanchez, A. Morningstar, B. M. Spar, P. T. Brown, D. A. Huse, and W. S. Bakr, Subdiffusion and heat transport in a tilted two-dimensional Fermi-Hubbard system, Phys. Rev. X **10**, 011042 (2020).

[392] P. T. Brown, D. Mitra, E. Guardado-Sanchez, R. Nourafkan, A. Reymbaut, C.-D. Hébert, S. Bergeron, A.-M. S. Tremblay, J. Kokalj, D. A. Huse, P. Schauß, and W. S. Bakr, Bad metallic transport in a cold atom Fermi-Hubbard system, Science **363**, 379–382 (2019).

[393] A. Dauphin, M. Müller, and M. A. Martin-Delgado, Rydberg-atom quantum simulation and Chern-number characterization of a topological Mott insulator, Phys. Rev. A **86**, 053618 (2012).

[394] M. Žnidarič, T. Prosen, and P. Prelovšek, Many-body localization in the Heisenberg XXZ magnet in a random field, Phys. Rev. B **77**, 064426 (2008).

[395] J. H. Bardarson, F. Pollmann, and J. E. Moore, Unbounded growth of entanglement in models of many-body localization, Phys. Rev. Lett. **109**, 017202 (2012).

[396] M. Serbyn, Z. Papić, and D. A. Abanin, Local conservation laws and the structure of the many-body localized states, Phys. Rev. Lett. **111**, 127201 (2013).

[397] D. J. Luitz, N. Laflorencie, and F. Alet, Many-body localization edge in the random-field heisenberg chain, Phys. Rev. B **91**, 081103 (2015).

[398] M. Schecter, T. Iadecola, and S. Das Sarma, Configuration-controlled many-body localization and the mobility emulsion, Phys. Rev. B **98**, 174201 (2018).

[399] T. Rakovszky, P. Sala, R. Verresen, M. Knap, and F. Pollmann, Statistical localization: From strong fragmentation to strong edge modes, Phys. Rev. B **101**, 125126 (2020).

[400] N. Nessi, A. Iucci, and M. A. Cazalilla, Quantum quench and prethermalization dynamics in a two-dimensional Fermi gas with long-range interactions, Phys. Rev. Lett. **113**, 210402 (2014).

[401] F. Grusdt, Z. Zhu, T. Shi, and E. Demler, Meson formation in mixed-dimensional t-J models, SciPost Phys. **5**, 57 (2018).

[402] P. P. Mazza, R. Schmidt, and I. Lesanovsky, Vibrational dressing in kinetically constrained Rydberg spin systems, Phys. Rev. Lett. **125**, 033602 (2020).

[403] F. M. Gambetta, W. Li, F. Schmidt-Kaler, and I. Lesanovsky, Engineering nonbinary Rydberg interactions via phonons in an optical lattice, Phys. Rev. Lett. **124**, 043402 (2020).

[404] R. Belyansky, J. T. Young, P. Bienias, Z. Eldredge, A. M. Kaufman, P. Zoller, and A. V. Gorshkov, Nondestructive cooling of an atomic quantum register via state-insensitive Rydberg interactions, Phys. Rev. Lett. **123**, 213603 (2019).

[405] S. F. Cooper, Z. Burkley, A. D. Brandt, C. Rasor, and D. C. Yost, Cavity-enhanced deep ultraviolet laser for two-photon cooling of atomic hydrogen, Opt. Lett. **43**, 1375–1378 (2018).

[406] R. Grimm, M. Weidemüller, and Y. B. Ovchinnikov, Optical Dipole Traps for Neutral Atoms, in *Adv. At. Mol. Opt. Phys.*, Vol. 42 (Academic Press, 2000) pp. 95–170.

[407] A. G. Boetes, R. V. Skannrup, J. Naber, S. J. J. M. F. Kokkelmans, and R. J. C. Spreeuw, Trapping of Rydberg atoms in tight magnetic microtraps, Phys. Rev. A **97**, 013430 (2018).

[408] J. Fortágh and C. Zimmermann, Magnetic microtraps for ultracold atoms, Rev. Mod. Phys. **79**, 235–289 (2007).

[409] H. Labuhn, D. Barredo, S. Ravets, S. De Léséleuc, T. Macrì, T. Lahaye, and A. Browaeys, Tunable two-dimensional arrays of single Rydberg atoms for realizing quantum Ising models, Nature **534**, 667–670 (2016).

[410] V. Lienhard, S. de Léséleuc, D. Barredo, T. Lahaye, A. Browaeys, M. Schuler, L.-P. P. Henry, and A. M. Läuchli, Observing the Space- and Time-Dependent Growth of Correlations in Dynamically Tuned Synthetic Ising Models with Antiferromagnetic Interactions, Phys. Rev. X **8**, 021070 (2018).

[411] M. Saffman, Quantum computing with neutral atoms, Natl. Sci. Rev. **00**, 1–2 (2018).

[412] M. Saffman, Quantum computing with atomic qubits and Rydberg interactions: progress and challenges, J. Phys. B At. Mol. Opt. Phys. **49**, 202001 (2016).

[413] S. Zhang, F. Robicheaux, and M. Saffman, Magic-wavelength optical traps for Rydberg atoms, Phys. Rev. A **84**, 043408 (2011).

[414] J. Ye, H. J. Kimble, and H. Katori, Quantum State Engineering and Precision Metrology Using State-Insensitive Light Traps, Science **320**, 1734–1738 (2008).

[415] T. Topcu and A. Derevianko, Possibility of triple magic trapping of clock and Rydberg states of divalent atoms in optical lattices, J. Phys. B: At. Mol. Opt. Phys. **49**, 144004 (2016).

[416] T. A. Savard, K. M. O'Hara, and J. E. Thomas, Laser-noise-induced heating in far-off resonance optical traps, Phys. Rev. A **56**, R1095–R1098 (1997).

[417] D. Jaksch, J. I. Cirac, P. Zoller, S. L. Rolston, R. Côté, and M. D. Lukin, Fast Quantum Gates for Neutral Atoms, Phys. Rev. Lett. **85**, 2208–2211 (2000).

[418] M. Saffman and T. G. Walker, Analysis of a quantum logic device based on dipole-dipole interactions of optically trapped Rydberg atoms, Phys. Rev. A **72**, 022347 (2005).

[419] H. Pichler, A. J. Daley, and P. Zoller, Nonequilibrium dynamics of bosonic atoms in optical lattices: Decoherence of many-body states due to spontaneous emission, Phys. Rev. A **82**, 063605 (2010).

[420] M. Saffman, X. L. Zhang, A. T. Gill, L. Isenhower, and T. G. Walker, Rydberg state mediated quantum gates and entanglement of pairs of neutral atoms, J. Phys. Conf. Ser. **264**, 012023 (2011).

[421] A. Kumar, T.-Y. Wu, F. Giraldo, and D. S. Weiss, Sorting ultracold atoms in a three-dimensional optical lattice in a realization of Maxwell's demon, Nature **561**, 83–87 (2018).

[422] Y. Wang, A. Kumar, T.-Y. Wu, and D. S. Weiss, Single-qubit gates based on targeted phase shifts in a 3D neutral atom array, Science (80-.). **352**, 1562–1565 (2016).

[423] J. D. Thompson, T. G. Tiecke, A. S. Zibrov, V. Vuletić, and M. D. Lukin, Coherence and Raman Sideband Cooling of a Single Atom in an Optical Tweezer, Phys. Rev. Lett. **110**, 133001 (2013).

[424] A. M. Kaufman, B. J. Lester, and C. A. Regal, Cooling a Single Atom in an Optical Tweezer to Its Quantum Ground State, Phys. Rev. X **2**, 041014 (2012).

[425] P. Sompet, Y. H. Fung, E. Schwartz, M. D. J. Hunter, J. Phrompao, and M. F. Andersen, Zeeman-insensitive cooling of a single atom to its two-dimensional motional ground state in tightly focused optical tweezers, Phys. Rev. A **95**, 031403 (2017).

[426] A. J. Daley, P. O. Fedichev, and P. Zoller, Single-atom cooling by superfluid immersion: A nondestructive method for qubits, Phys. Rev. A **69**, 022306 (2004).

[427] A. Griessner, D. Jaksch, and P. Zoller, Cavity-assisted nondestructive laser cooling of atomic qubits, J. Phys. B At. Mol. Opt. Phys. **37**, 1419–1432 (2004).

[428] I. Reichenbach and I. H. Deutsch, Sideband Cooling while Preserving Coherences in the Nuclear Spin State in Group-II-like Atoms, Phys. Rev. Lett. **99**, 123001 (2007).

[429] M. D. Barrett, B. DeMarco, T. Schaetz, V. Meyer, D. Leibfried, J. Britton, J. Chiaverini, W. M. Itano, B. Jelenković, J. D. Jost, C. Langer, T. Rosenband, and D. J. Wineland, Sympathetic cooling of $^{9}\mathrm{be}^{+}$ and $^{24}\mathrm{mg}^{+}$ for quantum logic, Phys. Rev. A **68**, 042302 (2003).

[430] D. Kielpinski, B. E. King, C. J. Myatt, C. A. Sackett, Q. A. Turchette, W. M. Itano, C. Monroe, D. J. Wineland, and W. H. Zurek, Sympathetic cooling of trapped ions for quantum logic, Phys. Rev. A **61** (2002).

[431] W. M. Itano, D. J. Heinzen, J. J. Bollinger, and D. J. Wineland, Quantum Zeno effect, Phys. Rev. A **41**, 2295–2300 (1990).

[432] A. Cooper, J. Covey, I. Madjarov, and M. Endres, Alkaline earth atoms in optical tweezers, arXiv:1810.06537 .

[433] Y. Yu, N. R. Hutzler, J. T. Zhang, L. R. Liu, J. D. Hood, T. Rosenband, and K.-K. Ni, Motional-ground-state cooling outside the Lamb-Dicke regime, Phys. Rev. A **97**, 063423 (2018).

[434] T. G. Walker and M. Saffman, Consequences of Zeeman degeneracy for the van der Waals blockade between Rydberg atoms, Phys. Rev. A **77**, 032723 (2008).

[435] S. Machnes, M. B. Plenio, B. Reznik, A. M. Steane, and A. Retzker, Superfast Laser Cooling, Phys. Rev. Lett. **104**, 183001 (2010).

[436] X. Wang, S. Vinjanampathy, F. W. Strauch, and K. Jacobs, Ultraefficient Cooling of Resonators: Beating Sideband Cooling with Quantum Control, Phys. Rev. Lett. **107**, 177204 (2011).

[437] S. Machnes, J. Cerrillo, M. Aspelmeyer, W. Wieczorek, M. B. Plenio, and A. Retzker, Pulsed Laser Cooling for Cavity Optomechanical Resonators, Phys. Rev. Lett. **108**, 153601 (2012).

[438] J. T. Young, P. Bienias, R. Belyansky, A. M. Kaufman, and A. V. Gorshkov, Asymmetric blockade and multiqubit gates via dipole-dipole interactions, Phys. Rev. Lett. **127**, 120501 (2021).

[439] L. F. Buchmann, K. Mølmer, and D. Petrosyan, Creation and transfer of nonclassical states of motion using Rydberg dressing of atoms in a lattice, Phys. Rev. A **95**, 013403 (2017).

[440] F. M. Gambetta, W. Li, F. Schmidt-Kaler, and I. Lesanovsky, Engineering non-binary Rydberg interactions via electron-phonon coupling, (2019), arXiv:1907.11664 .

[441] S. Coleman, Quantum sine-Gordon equation as the massive Thirring model, Phys. Rev. D **11**, 2088–2097 (1975).

[442] P. Jentsch, R. Daviet, N. Dupuis, and S. Floerchinger, Physical properties of the massive Schwinger model from the nonperturbative functional renormalization group, Phys. Rev. D **105**, 016028 (2022).

[443] R. F. Dashen, B. Hasslacher, and A. Neveu, Particle spectrum in model field theories from semiclassical functional integral techniques, Phys. Rev. D **11**, 3424–3450 (1975).

[444] A. B. Zamolodchikov and A. B. Zamolodchikov, Factorized S-matrices in two dimensions as the exact solutions of certain relativistic quantum field theory models, Ann. Phys. **120**, 253–291 (1979).

[445] D. J. Griffiths and D. F. Schroeter, *Introduction to Quantum Mechanics*, third edition ed. (Cambridge University Press, Cambridge ; New York, NY, 2018).

[446] M. Peruzzo, F. Hassani, G. Szep, A. Trioni, E. Redchenko, M. Žemlička, and J. M. Fink, Geometric Superinductance Qubits: Controlling Phase Delocalization across a Single Josephson Junction, PRX Quantum **2**, 040341 (2021).

[447] I. Siddiqi, Engineering high-coherence superconducting qubits, Nat. Rev. Mater. **6**, 875–891 (2021).

[448] N. Y. Yao, C. R. Laumann, A. V. Gorshkov, H. Weimer, L. Jiang, J. I. Cirac, P. Zoller, and M. D. Lukin, Topologically protected quantum state transfer in a chiral spin liquid, Nat Commun **4**, 1585 (2013).

[449] J. Haegeman, C. Lubich, I. Oseledets, B. Vandereycken, and F. Verstraete, Unifying time evolution and optimization with matrix product states, Phys. Rev. B **94**, 165116 (2016).

[450] H. Suhl, Dispersion Theory of the Kondo Effect, Phys. Rev. **138**, A515–A523 (1965).

[451] P. Coleman, *Introduction to Many-Body Physics* (Cambridge University Press, 2015).

[452] M. Srednicki, *Quantum field theory* (Cambridge University Press, 2007).

[453] B. Bruognolo, A. Weichselbaum, C. Guo, J. von Delft, I. Schneider, and M. Vojta, Two-bath spin-boson model: Phase diagram and critical properties, Phys. Rev. B **90**, 245130 (2014).

[454] M. Devoret, Quantum fluctuations in electrical circuits, (Les Houches Session LXII (1997).

[455] J. Koch, T. M. Yu, J. Gambetta, A. A. Houck, D. I. Schuster, J. Majer, A. Blais, M. H. Devoret, S. M. Girvin, and R. J. Schoelkopf, Charge-insensitive qubit design derived from the cooper pair box, Phys. Rev. A **76**, 042319 (2007).

[456] G. Zhu, D. G. Ferguson, V. E. Manucharyan, and J. Koch, Circuit qed with fluxonium qubits: Theory of the dispersive regime, Phys. Rev. B **87**, 024510 (2013).

[457] L. Zhou, Z. R. Gong, Y. X. Liu, C. P. Sun, and F. Nori, Controllable scattering of a single photon inside a one-dimensional resonator waveguide, Phys. Rev. Lett. **101**, 100501 (2008).

[458] C. Eichler, D. Bozyigit, and A. Wallraff, Characterizing quantum microwave radiation and its entanglement with superconducting qubits using linear detectors, Phys. Rev. A **86**, 032106 (2012).

[459] L. Zhang, Matrix integrals over unitary groups: An application of schur-weyl duality (2014), arXiv:1408.3782 [quant-ph] .

[460] P. T. Brown, D. Mitra, E. Guardado-Sanchez, P. Schauß, S. S. Kondov, E. Khatami, T. Paiva, N. Trivedi, D. A. Huse, and W. S. Bakr, Spin-imbalance in a 2D Fermi-Hubbard system, Science **357**, 1385–1388 (2017).